1-1-2021

A NUMERICAL STUDY OF THE EFFECTS OF TIME-VARYING STREAMBED CONDUCTIVITY ON GROUNDWATER – SURFACE WATER INTERACTIONS DURING STORM EVENTS

Jiayu Fang
University of Mississippi

A NUMERICAL STUDY OF THE EFFECTS OF TIME-VARYING STREAMBED CONDUCTIVITY ON GROUNDWATER – SURFACE WATER INTERACTIONS DURING STORM EVENTS

A Dissertation
presented in partial fulfillment of requirements
for the degree of Doctor of Philosophy
in Engineering Science with Emphasis in Computational Hydroscience
The University of Mississippi

by

Jiayu Fang

December 2021

ABSTRACT

Streambed conductivity is widely recognized as a vital parameter controlling the stream-aquifer exchange. Many field measurements have revealed that temporal variation of streambed conductivity is rapid and dramatic during floods. However, previous numerical studies either assumed streambed conductivity as steady over storm events or focused on time-varying streambed conductivity during low-stage periods. This study aims at bridging this gap by both incorporating time-varying streambed conductivity into a numerical model of groundwater (GW) – surface water (SW) interactions and simulating them under different flooding conditions, making this dissertation the first modeling study to explore combined effects of high-stage events and time-varying streambed conductivity on GW-SW exchanges.

To this end, a finite element numerical model, CCHE3D-GW, which can simulate both saturated and unsaturated GW flows, was developed, and thoroughly verified in this dissertation in order to facilitate numerical studies. CCHE3D-GW was then used for the calibration of a pumping test conducted in the study area, Money experimental site in Mississippi, USA, in order to obtain the hydrogeological information.

A rapid model that can estimate time-varying streambed conductivity based on GW responses to flood-wave fluctuations was developed, and then validated with two typical synthetic cases. Its applicability to a heterogeneous aquifer was tested and confirmed as well. The sensitivity analysis showed that the rapid model was approximately linearly affected by the uncertainty of its input parameters. The rapid model was then applied to obtain the time series of the streambed

conductivity for the Money experimental site, which is near the Tallahatchie River. Three typical flooding conditions were analyzed: 1) one that consisted of multiple flood events with attenuating amplitudes, 2) one that was composed of multiple flood events with amplifying amplitudes and 3) one with a single flood event (the river stage reached a historically high value).

The estimated time-varying streambed conductivity was then imposed on CCHE3D-GW to study two commonly encountered cases of GW-SW interactions. The first case was a hypothetical riverside pump in the Money experimental site, and the second case was the dune-induced hyporheic exchange. The simulations were conducted for the aforementioned three flooding conditions with both the static (traditional manner) and time-varying streambed conductivity.

Based on the modeling results and analyses for different flooding conditions in this dissertation, it can be concluded that considering time-varying streambed conductivity is imperative for accurately understanding the evolution of the GW-SW exchange intensity and residence time of the infiltrated water. Hence, demonstrating that time-varying streambed conductivity is a critical and essential variable for accurate and robust process-based GW-SW interaction modeling, and particularly during flooding periods.

DEDICATION

This dissertation is dedicated to my parents, Mr. Xingwei Fang and Ms. Huilan Chen, for their unconditional love and endless support.

ACKNOWLEDGMENTS

I would like to sincerely express my deepest appreciation to my advisor Dr. Mohammad Al-Hamdan for his generous advice, encouragement and the support provided to me throughout my Ph.D. study at the National Center for Computational Hydroscience and Engineering (NCCHE). It was an excellent opportunity for me to work with him. I want to express my appreciation to my former advisor Dr. Yafei Jia, who became emeritus this May, for his guidance during my first 4-year Ph.D. life and his commitment to serving on my dissertation committee. I wish him a very happy and enjoyable retirement. I would also like to thank Dr. Andrew O'Reilly, Dr. Yavuz Ozeren and Dr. James Rigby for providing valuable comments and suggestions for my research and serving on my dissertation committee.

Many thanks to the former and current faculty members of NCCHE: Dr. Mohammad Al-Hamdan, Dr. Mustafa Altinakar, Dr. Xiaobo Chao, Dr. Greg Easson, Dr. Yafei Jia, Dr. Yavuz Ozeren and Dr. Yaoxin Zhang for the mentorship that I have received over the last five years and the precious knowledge I have learned from them. I would like to thank former and current staff at NCCHE: Ms. LaToya Harris, Ms. Jaclyn Montoria and Mr. Paul Smith for providing me with help with administrative paperwork and computational facility. I also appreciate the friendship I have enjoyed with my colleagues: Dr. Leili Gordji, Mr. Marcus McGrath, Dr. Nuttita Pophet, Mr. Luc Rébillout, Mr. William Rossell, and Mr. Nazim Sahin. Many thanks to my great friends, Sudeep Adhikari, Sumeet Kulkarni, Mengshen Zhao, every member of the 'Turner Center Muscle

FC’ and everyone who is working or used to work in the gyms of the Ole Miss. It is really a memorable and informative adventure and I wish you all the best.

Finally, I would like to express my deepest appreciation to my parents, Mr. Xingwei Fang and Ms. Huilan Chen for giving me life, raising me up and providing me with unconditional love and endless support. Without the love and encouragement from my family, it would be impossible for me to complete this dissertation.

Perhaps, these would be the last several inks I would drop on this dissertation, which is ironic and surreal since the ending song I wrote for this chapter in my life is the opening theme for readers. Maybe, it is indeed another overture of the next drama, the herald of an unknown future and the dawn of a charming journey until ashes to ashes and dust to dust. Coming to this world, we are all restrained by many things, such as our initial conditions (talents, nationalities, families and growing-up environments), the laws of the universe and the big picture of our contemporary era. When the stochastic and ruthless fate wants to play a trick, we would be brutally tortured. However, maybe one day, we would realize that every suffering has a meaning and it is in reality chosen by ourselves. Ultimately, the obstacle becomes the way. In this impermanent space-time, ‘fino alla fine’ and ‘負けないで’. I wish anyone who reads this dissertation well.

Financial support for this dissertation is provided by United States Department of Agriculture (USDA) - Agriculture Research Service (ARS) through Cooperative Agreement 6060-13000-028-00D between USDA-ARS-National Sedimentation Laboratory and NCCHE.

TABLE OF CONTENTS

ABSTRACT ii
DEDICATION iv
ACKNOWLEDGMENTS v
LIST OF FIGURES x
LIST OF TABLES xvii
I. INTRODUCTION 1
1.1Literature Review 3
1.1.1 Estimation of Time-varying Streambed Conductivity 3
1.1.2 Riverbank Filtration System 6
1.1.3 Hyporheic Exchange 9
1.2Research Objectives 14
1.3Dissertation Outline 16
II. DEVELOPMENT OF CCHE3D-GW 18
2.1 Governing Equation 18
2.2 Numerical Method 19
2.3 Verificaiton of CCHE3D-GW 22
III. STUDY AREA AND HYDROGEOLOGICAL SETTING 23
3.1 Description of Pumping Site 23
3.2 Conceptual Model for Calibration 25
3.3 Mesh and Boundary Conditions for Calibration 28
3.4 Calibration Results 30
IV. RAPID ESTIMATION OF TIME-VARYING STREAMBED CONDUCTIVITY 35
4.1 Objectives and Hypotheses 35
4.2 Methodology 35
4.2.1 Overview 35
4.2.2 Flood-wave Response Model 35
4.2.3 Estimation of Time-varying Streambed Conductivity 39
4.3 Validation of Estimation Model 40

4.3.1 Validation Case I 42
4.3.2 Validation Case II 45
4.4 Sensitivity Analysis of POW Size 48
4.5 Applicability of Estimation Model to Heterogeneous Aquifer 52
4.5.1 Parameters of Heterogeneous Aquifer 53
4.5.2 Analysis of Heterogeneous Aquifer-Stream Simulations 55
4.5.3 Algorithm for Equivalent Hydraulic Conductivity 57
4.5.4 Impact of Heterogeneity on Estimated Streambed Conductivity 59
4.6 Uncertainty Analysis of Estimation Model 61
4.6.1 Hydraulic Conductivity of Aquifer 62
4.6.2 Specific Yield of Aquifer 63
4.6.3 River Width 64
4.6.4 Distance between Monitoring Well and River Centerline 65
4.7 Summary and Conclusions 67
V. APPLICATION OF ESTIMATION MODEL TO STUDY AREA 69
5.1 Study Site 69
5.2 Flooding Condition 1 70
5.3 Flooding Condition 2 72
5.4 Flooding Condition 3 73
VI. NUMERICAL STUDY OF RIVERBANK FILTRATION DURING STORM EVENTS WITH TIME-VARYING STREAMBED CONDUCTIVITY 75
6.1 Objectives and Hypotheses 75
6.2 Methodology 75
6.2.1 Simulation Domain and Setting Up 75
6.2.2 Tracer Transport Model 76
6.2.3 Groundwater Age Simulation 77
6.2.4 Mean Travel Time 78
6.3 Simulation Results 79
6.3.1 Flooding Condition 1 79

6.3.2 Flooding Condition 2 87
6.3.3 Flooding Condition 3 92
6.4 Discussion 97
6.5 Summary and Conclusions 98
VII. NUMERICAL STUDY OF DUNE-INDUCED HYPORHEIC FLOW DURING STORM EVENTS WITH TIME-VARYING STREAMBED CONDUCTIVITY 101
7.1 Objectives and Hypotheses 101
7.2 Methodology 101
7.2.1 Conceptual Model 101
7.2.2 Simulation Domain and Mesh 103
7.2.3 Flow Model 103
7.2.4 Setup of Static and Time-varying Streambed Conductivity 104
7.2.5 Tracer Transport Model and Outline of Hyporheic Zone 106
7.2.6 Residence Time Model 107
7.3 Simulation Results 109
7.3.1 Flooding Condition 1 109
7.3.2 Flooding Condition 2 118
7.3.3 Flooding Condition 3 125
7.4 Discussion 133
7.4.1 Filter Function of Streambed 133
7.4.2 Importance of Time-varying Streambed Conductivity 134
7.5 Summary and Conclusions 137
VIII. SUMMARY, CONCLUSIONS AND FUTURE WORK 139
8.1 Summary and Conclusions 139
8.2 Limitations and Future Work 142
BIBLIOGRAPHY 146
LIST OF APPENDICES 159
VITA 177

LIST OF FIGURES

Figure 1.1. Outline of dissertation research objectives. 16

Figure 2.1. Mesh configuration of this model. Void circles represent the collocation nodes of the finite element mesh and solid circles are staggered nodes. Darcy velocities located on the collocation nodes and hydraulic head are located on staggered nodes. A cell consists of eight collocation nodes (void circles) and its center is the staggered node. 21

Figure 3.1. (a) Geographical position of the study area, where the white dotted rectangle delineates the boundary of simulation domain; (b) the configuration of the pumping test in Leflore County, Mississippi, USA, and (c) the layout of the measurement for sediment resistivity. 24

Figure 3.2. (a) The spatial distribution of sediment resistivity for the cross section passing the pumping well and perpendicular to the Tallahatchie River; (b) the $x - y$ plane view of the computed hydraulic conductivity from Eq. 3.1 with R_w = 10.82 Ω.m at the measured points (25.53 m deep; z = 16.0 m) and (c) the conceptualized cross section of the simulation. 28

Figure 3.3. The configuration of the mesh in x - y direction for (a) the whole simulation domain and (b) the near-well region. (c) The setup of the mesh in z direction. 30

Figure 3.4. The best-agreed simulation results (lines) at the monitoring wells in the cross section (a) perpendicular, (b) & (c) parallel to the river and (d) at ordinary locations. 32

Figure 3.5. The spatial distribution of hydraulic conductivity with R_w = 10.82 Ω.m (a) of the cross section passing the pumping well and parallel to the river (x = 0.0 m) and (b) in $x - y$ plane view at z = 21.53 m. 34

Figure 3.6. The variation of f_{RMS} with the hydraulic conductivity of the aquitard, K_u. 34

Figure 4.1. The conceptual model of the analytical solution of Zlotnik and Huang (1999). 39

Figure 4.2. Scheme of the inverse of the flood-wave responses, in which Parameter Optimization Window (POW) and POW shift are shown. The black and blue dashed rectangles are used to mark two consecutive POWs and the purple dashed line represents the GW heads computed by the analytical solution (Eq. 4.6 & 4.11). The data shown here is from USGS gaging stations near Leflore County (Money), MS, USA from January to August of 2017. 41

Figure 4.3. (a) Time series of the streambed conductivity in the synthetic case I and (b) the temporal variation of the river stage (grey line) and simulated GW hydraulic heads at the

designated monitoring well with Δx = 2.0, 1.0 and 0.5 m (black, red and blue dotted line, respectively). 44

Figure 4.4. Comparisons between the designated time-varying streambed conductivity (red dashed line) and the computed one from the estimation model (black circles) with POW size = 1.0 day and POW Shift = 0.1 day. 45

Figure 4.5. The temporal variation of (a) the flood wave (blue line, left axis) and streambed conductivity (red line, right axis) within one wavelength (10 days); (b) flood wave (blue line) and GW hydraulic head at the designated monitoring well (red line) and (c) designated (dashed line) and computed (circles, POW size = 0.8 day and POW shift = 0.1 day) streambed conductivity. 47

Figure 4.6. (a) Comparisons between the estimated temporal variations of the streambed conductivity with different POW sizes (colorful dots) and the designated variation (black solid line) and (b) the variation of the dimensionless mean residual with the ratio of POW size to the wavelength. 51

Figure 4.7. The distribution of the hydraulic conductivity of the measured cross sections, where the value is in a logarithmic scale. 54

Figure 4.8. The experimental variogram of the hydraulic conductivities (m/s) of the aquifer in logarithmic scale (circles) and the fitting variogram model (red dashed line) in two primary directions, which is (a) 45° and (b) -45° to the horizontal plane, respectively, and (c) and (d) are two representative hydraulic conductivity distributions of the near-stream aquifer among the 100 realizations. 55

Figure 4.9. (a) The simulated temporal variation of the GW hydraulic head at the designated monitoring well of each heterogeneous realization (grey line) and the ensemble results (other lines). (b) The comparisons of the simulated GW responses at the monitoring well between the ensemble result of the 100 realizations and the results simulated by a homogeneous aquifer with the hydraulic conductivity computed from different averaged algorithms. 57

Figure 4.10. The histogram of the RMS between the simulated GW hydraulic heads of the 100 heterogeneous aquifers and the homogeneous aquifer with the geometric-averaged hydraulic conductivity. 59

Figure 4.11. (a) The comparisons between the designated time-varying streambed conductivity (red dotted line) and the estimated one of each heterogeneous realization (grey line), where the ensemble result of 75 and 100 realizations is marked by the blue dashed line and the black solid line, respectively; (b) the histogram of DMS between the estimated and designated streambed

conductivity..... 61

Figure 4.12. Comparisons of the estimated time-varying streambed conductivity with different input values of (a) the aquifer hydraulic conductivity; (b) the aquifer specific yield; (c) the river width and (d) the distance between the monitoring well and river center. 66

Figure 4.13. Variation of the dimensionless mean residual (DMR) between the estimated and accurate time-varying streambed conductivity with the dimensionless input error (*IE*) of (a) the aquifer hydraulic conductivity; (b) the aquifer specific yield; (c) the river width and (d) the distance between the monitoring well and river center..... 67

Figure 5.1. The study site of the Tallahatchie River near Leflore County, Mississippi, USA. ... 70

Figure 5.2. Time series of the river stage (black solid line), GW hydraulic heads (balck dashed line), estimated static streambed conductance (blue dots) and estimated time-varying streambed conductance (red dots) during the flooding period from 2/22/2015 to 6/22/2015 in Leflore County, MS, USA. 72

Figure 5.3. Comparisons of the calculated temporal variations of the streambed conductivity with the initial condition set up at different periods prior to the starting date of flooding condition 1.. 72

Figure 5.4. Time series of the river stage (black solid line), GW hydraulic heads (black dashed line), estimated static streambed conductance (blue dots) and estimated time-varying streambed conductance (red dots) during the flooding period from 10/26/2015 to 6/16/2016 in Leflore County, MS, USA. 73

Figure 5.5. Time series of the river stage (black solid line), GW hydraulic heads (black dashed line), estimated static streambed conductance (blue dots) and estimated time-varying streambed conductance (red dots) during the flooding period from 5/7/2021 to 8/3/2021 in Leflore County, MS, USA. 74

Figure 6.1. (a) The spatial distribution of the 10 monitoring wells that were set up in the numerical pumping simulation. 80

Figure 6.2. (a) The temporal variation of the GW hydraulic head in the monitoring wells in the (a) western and (b) eastern banks during the flooding condition 1. 81

Figure 6.3. Temporal variation of the (a) river stage, (b) streambed conductivity, (c) stream depletion, (d) percentage of the pumped water from the stream and (e) travel time over the flooding condition 1, where the results under the static streambed are represented by the solid line while

those under the time-varying streambed are marked by the dashed line. 83

Figure 6.4. Snapshots of the simulated (a) concentration distribution of the conservative tracer (color map) and GW flow field (red arrows represent direction but are not to scale), and (b) distribution of the water age with the time-varying streambed conductivity at t = 50 day (starting from the formal simulation) for the flooding condition 1. 85

Figure 6.5. (a) The temporal variation of the GW hydraulic head in the monitoring wells in the (a) western and (b) eastern banks during the flooding condition 2. 88

Figure 6.6. Temporal variation of the (a) river stage, (b) streambed conductivity, (c) stream depletion, (d) percentage of the pumped water from the stream and (e) travel time over the flooding condition 2, where the results under the static streambed are represented by the solid line while those under the time-varying streambed are marked by the dashed line. 89

Figure 6.7. Snapshots of the simulated (a) concentration distribution of the conservative tracer (color map) and GW flow field (red arrows represent direction but are not to scale), and (b) distribution of the water age with the time-varying streambed conductivity at t = 50 day (starting from the formal simulation) for the flooding condition 2. 91

Figure 6.8. (a) The temporal variation of the GW hydraulic head in the monitoring wells in the (a) western and (b) eastern banks during the flooding condition 3. 93

Figure 6.9. Temporal variation of the (a) river stage, (b) streambed conductivity, (c) stream depletion, (d) percentage of the pumped water from the stream and (e) travel time over the flooding condition 3, where the results under the static streambed are represented by the solid line while those under the time-varying streambed are marked by the dashed line. 96

Figure 6.10. Snapshots of the simulated (a) concentration distribution of the conservative tracer (color map) and GW flow field (red arrows represent direction but are not to scale), and (b) distribution of the water age with the time-varying streambed conductivity at t = 50 day (starting from the formal simulation) for the flooding condition 3. 97

Figure 7.1. (a) Configuration of the dune-induced hyporheic flow in the longitudinal view; (b) conceptual model of this study. 103

Figure 7.2. Simulation Domain of the 2-D dune-induced hyporheic flow, in which the middle dune is focused in this study. 105

Figure 7.3. Temporal variation of (i) the river stage, H_S, (ii) the dynamic-head intensity, h_d, and (iii) the ratio between the time-varying (K_T) and the static streambed conductivity (K_S) for (a) the

flooding condition 1 (from February 22, 2015 to June 22, 2015), (b) flooding condition 2 (from October 26, 2015 to June 16, 2016) and (c) flooding condition 3 (from May 7, 2021 to August 3, 2021). 108

Figure 7.4. Snapshots of the flow field (red arrows represent direction but are not to scale), outline of the hyporheic zone (black solid line) and the concentration distribution of the conservative tracer (color map), in which (a) and (b) is under the static and time-varying streambed conductivity, respectively. (i), (ii) and (iii) is at t = 0.0, 0.5 and 1.0t_{total}, respectively, over the flooding condition 1..... 111

Figure 7.5. Temporal variation of the (a) depth and (b) area of the hyporheic zone for the flooding condition 1. 112

Figure 7.6. Temporal variation of the (a) dynamic-head intensity, (b) streambed conductivity, (c) and (d) mean hyporheic flux simulated with the static and time-varying streambed conductivity, respectively, and (e) and (f) mean flux-weighted residence time under the static and time-varying streambed, respectively, over flooding condition 1. 117

Figure 7.7. Snapshots of the flow field (red arrows represent direction but are not to scale), outline of the hyporheic zone (black solid line) and the concentration distribution of the conservative tracer (color map), in which (a) and (b) is under the static and time-varying streambed conductivity, respectively. (i), (ii) and (iii) is at t = 0.0, 0.5 and 1.0t_{total}, respectively, over the flooding condition 2..... 119

Figure 7.8. Temporal variation of the (a) depth and (b) area of the hyporheic zone for the flooding condition 2. 120

Figure 7.9. Temporal variation of the (a) dynamic head intensity, (b) streambed conductivity, (c) and (d) mean hyporheic flux simulated with the static and time-varying streambed conductivity, respectively, and (e) and (f) mean flux-weighted residence time under the static and time-varying streambed, respectively, over flooding condition 2. 123

Figure 7.10. Snapshots of the flow field (red arrows represent direction but are not to scale), outline of the hyporheic zone (black solid line) and the concentration distribution of the conservative tracer (color map), in which (a) and (b) is under the static and time-varying streambed conductivity, respectively. (i), (ii) and (iii) is at t = 0.0, 0.5 and 1.0t_{total}, respectively, over the flooding condition 3..... 127

Figure 7.11. Temporal variation of the (a) depth and (b) area of the hyporheic zone for the flooding condition 3. 128

Figure 7.12. Temporal variation of the (a) dynamic head intensity, (b) streambed conductivity, (c) and (d) mean hyporheic flux simulated with the static and time-varying streambed, respectively, and (e) and (f) mean flux-weighted residence time under the static and time-varying streambed, respectively, over flooding condition 3. 132

Figure 7.13. Correlation coefficient, r^2, between (a) $\bar{q}_{\mathrm{HF,Time-varying}}$ and (b) Mean $\mathrm{RT}_{\text{Time-varying}}$ with h_d and K_T. 136

Figure 7.14. Variation of correlation coefficient with lagging phase, where (a) is between $\bar{q}_{\text{HF, Time-varying}}$ and h_d, (b) is between $\bar{q}_{\text{HF, Time-varying}}$ and K_T, (c) is between Mean $\mathrm{RT}_{\text{Time-varying}}$ and h_d and (d) is between Mean $\mathrm{RT}_{\text{Time-varying}}$ and K_T. 137

Figure A.1. Comparisons between the numerical results and analytical solution for hydraulic head distributions at four vertical levels: (a) z = -0.01 m; (b) z = -0.11 m; (c) z = -0.21 m and (d) z = -0.31 m. 161

Figure A.2. Comparison between the numerical results and analytical solution for the RTD. . 162

Figure A.3. Comparisons between the simulated and analytical hydraulic head distributions for gaining condition at four vertical levels: (a) z = -0.01 m; (b) z = -0.11 m; (c) z = -0.21 m and (d) z = -0.31 m. 163

Figure A.4. Comparisons between the simulated and analytical hydraulic head distributions for losing condition at four vertical levels: (a) z = -0.01 m; (b) z = -0.11 m; (c) z = -0.21 m and (d) z = -0.31 m. 164

Figure A.5. Comparisons between the simulated and analytical hydraulic head distributions for a two-layer streambed with K_u = 65.26 m/day, K_l = 6.526 m/day, D_u = 0.16 m and D_l = 0.84 m at four levels: (a) z = -0.01 m; (b) z = -0.11 m; (c) z = -0.21 m and (d) z = -0.31 m. 166

Figure A.6. The conceptual model of Butler et al. (2001), where (a) is the view of cross section passing the pumping well and perpendicular to the river and (b) is the $x - y$ plane view. The four red dashed lines in Fig. A.6a are the representative locations for the comparisons of Fig. A.7. 167

Figure A.7. Comparisons of drawdown between the results of analytical solution (Butler et al., 2001) and CCHE3D-GW with 4 layers (black solid lines) and 12 layers (red dashed lines) in z direction when x/w (a) = 0.523 (Zone 1); (b) = -0.429 (Zone 1); (c) = -1.238 (Zone 2) and (d) = -3.425 (Zone 3). (e) Comparisons of stream depletion between the results of analytical solution (Butler et al., 2001) and CCHE3D-GW with 4 layers (2-D mode, black solid lines) and 12 layers (3-D mode, red dashed lines) in z direction with different stream leakances. 170

Figure A.8. The conceptual scheme of the 1-D infiltration case for the verification. 172

Figure A.9. Comparisons between the simulation results of Zhang and Ewen (2000) and CCHE3D-GW for (a) pressure head distribution and (b) moisture content profile after 1-day infiltration. 173

Figure A.10. Configuration of the single-well pumping case and the mesh in (a) $x - y$ coordinate and (b) $x - z$ coordinate. 174

Figure A.11. Comparisons between the simulation results of VSAFT3 (Mao et al., 2011) and CCHE3D-GW for drawdowns at different elevations when the monitoring well is (a) 5.0 m and (b) 30.0 m away from the pumping well in radial direction. 175

Figure A.12. The best-agreed simulation results (lines) under the assumption of a homogenous aquifer for the monitoring wells (a) along the transversal cross section, (b) & (c) along the longitudinal cross section and (d) at the 'ordinary' locations. The datum here is NAVD 88, which is the standard Northern American datum. 176

LIST OF TABLES

Table 3.1. The Coordinates of the Pumping Well and Monitoring Wells. 31

Table 6.1. The Coordinates of the Pumping Well and Monitoring Wells. 80

Table A.1. The Parameters of Verification Cases..... 168

CHAPTER I

INTRODUCTION

Groundwater (GW) is one of the most crucial resources for industry, agriculture, environment, and civilization. In recent decades, owing to an exponential rise in water demand, GW has undergone severe depletion on a global scale. The Mississippi Delta, which is the study area of this dissertation, is one of the most productive agricultural areas in the United States, and its crop productions heavily rely on extractions of GW from the Mississippi River Valley Alluvial Aquifer (MRVA). Due to irrigation, the MRVA has suffered from an acute GW decline. From 1900 – 2008, GW depletion of MRVA was about 150 to 400 km^3 (Konikow, 2013). To alleviate and mitigate this unsustainable trend, many attempts have been made to come up with long-term resolutions, including a pilot study of a pumping-recharging project proposed by United States Department of Agriculture (USDA) – Agricultural Research Service (ARS) (O'Reilly, 2021), which demands a better understanding of local GW flows. On the other hand, as an area with multiple alluvial rivers, the Mississippi Delta has ample surface water (SW) resources. It is therefore indispensable to study regional GW-SW interactions thoroughly to improve water resources management.

The interaction between GW and SW has long been a topic of interest due to its ubiquity and importance to the riverine ecosystem (Boano et al., 2014; Boulton et al., 2010; Brunner et al., 2017; Cardenas and Wilson, 2007a; Constantz, 2016; Gooseff, 2010; Lawrence et al., 2013). As an intermediate media between stream and aquifer, streambeds play a key role in controlling GW-

SW exchange. Its hydraulic property, streambed conductivity, has been broadly acknowledged as a critical parameter to understand hydrological processes involved with GW-SW interaction, such as hyporheic exchange (Caruso et al., 2017; Newcomer et al., 2018), riverbank filtration (RBF) system (Hiscock and Grischek 2002; Zhang et al., 2011) and river restoration projects (Constantz, 2016; Kurth and Schirmer, 2014).

Many recent researches have revealed that streambed conductivity is a time-varying variable, which is influenced by multiple processes, such as erosion and deposition of fine sediments (Coleman, 1969; Drummond et al., 2017; Jin et al., 2019; Korus et al., 2020; Levy et al., 2011; Schalchli, 1992), biofilm growth (Newcomer et al., 2016; Wang et al., 2014; Xian et al., 2019), chemical participation (Du et al., 2013; Smith and Lerner, 2008) and water temperature (Doppler et al., 2007; Wang et al., 2017). This transience in the streambed conductivity has been studied and recorded by many field measurements (e.g., Korus et al., 2020; Levy et al., 2011; Mutiti and Levy, 2010; Zhang et al., 2011). When analyzing the hydraulic property of streambed sediments before, during and after storm events at the Great Miami River Basin in Ohio, USA, Mutiti and Levy (2010) found that the streambed conductivity arose from approximately 0.005 m/d to 0.05 m/d in less than 20 days during the flood but soon dropped to a low value when the storm passed. Zhang et al. (2011) also documented a similar phenomenon of the alternation of the riverbed clogging and opening at the Russian River in Mendocino County, California, USA and suggested that this temporal variation was critical to evaluate the sustainability of the riverside pump, which is a typical scenario of GW-SW interactions. Incorporating time-varying streambed conductivity into numerical models of stream-aquifer interactions has therefore been proposed as a blueprint for future studies (Partington et al., 2017).

However, previous modeling studies either assumed streambed conductivity as steady over storm events (e.g., Singh et al., 2019 and 2020; Wu et al., 2018) or focused on time-varying streambed conductivity during low-stage periods (e.g., Newcomer et al., 2016; Xian et al., 2019). None of them considered combined effects of high-stage events and time-varying streambed conductivity on GW-SW exchanges. This dissertation aimed to bridge this gap by studying GW-SW interactions while considering time-varying streambed conductivity through conducting numerical simulations, particularly during flooding periods when the hydraulic property of the streambed changes quickly and dramatically. Hence, this dissertation is the first attempt in the research literature to numerically study combined effects of both high-stage events and time-varying streambed conductivity on GW-SW exchanges. The study area was in the Mississippi Delta and two typical GW-SW exchange cases, riverbank filtration system and dune-induced hyporheic flow, were chosen for studies. A 3-D numerical model, CCHE3D-GW, was developed based on the framework of CCHE3D, a free SW model (Jia et al., 2005; Jia et al., 2018), to facilitate numerical simulations. The details of the model can be found in Chapter 2.

1.1 Literature Review

1.1.1 Estimation of Time-varying Streambed Conductivity

In order to incorporate time-varying streambed conductivity into the numerical model, the temporal variation of the streambed conductivity must be attained first. On the one hand, the traditional approaches, e.g., seepage meters (Rosenberry, 2008; Woessner and Sullivan, 1984), permeameters (Landon et al., 2001; Lee et al., 2015) and laboratory measurements of collected soil samples (Rosenberry and Pitlick, 2009; Schalchli, 1992), are reliable but can only provide low temporal-resolution data (typically weekly or monthly) due to the limited frequency of field

campaigns. It is also hard to operate field measurements during flooding periods owing to hazardous weather. On the other hand, the demanded temporal resolution of the streambed conductivity is usually high (such as daily or hourly) in order to match the rapid dynamics of floods. As a result, field measurements are unable to obtain the desired time-varying streambed conductivity over high-stage events.

In recent years, time-series analysis has been emerging as an effective method to estimate hydraulic properties of streambeds and aquifers (e.g., Obergfell et al., 2019; von Asmuth et al., 2002; von Asmuth et al., 2008). By applying an appropriate conceptual model to represent the studied stream-aquifer system, an analytical solution or simplified numerical model can be used to compute GW responses to impulses from SW flow. An inverse problem is commonly encountered, i.e., the time series of SW and GW fluctuations are measured while certain hydraulic properties of streambed or aquifer are unknown. Those parameters can be estimated by minimizing the discrepancies between measured and calculated GW responses (Jha and Singh, 2014; von Asmuth et al., 2008). However, in the past, most of the research merely focused on the static riverbed, in which the hydraulic property of the streambed was assumed constant over the whole period. The flood-wave response model (Obergfell et al., 2016; von Asmuth et al., 2002; von Asmuth et al., 2008) and thermal transport model (Hatch et al., 2010; Mutiti and Levy, 2010) were usually implemented.

Gianni et al. (2016) was the first to extend the flood-wave response model to estimating the time-varying streambed conductivity. After disassembling the whole period of interest into multiple successive short sessions, in which the hydraulic property of streambed can be regarded as constant over time, the minimization is applied to each sub-period to calculate the corresponding

streambed conductivity. The analytical solution of Hall and Moench (1972), which was derived for an alluvial aquifer fully penetrated by a river, was adopted. The model of Gianni et al. (2016) was then applied by Zhou et al. (2018) to compute the time-varying streambed conductivity in the Schwarz Bach River, Germany, which was then incorporated into their numerical model to explore the regional GW-SW interaction. Xian et al. (2020) added a new item, the streambed buffer effect, and upgraded the optimization method from a simple gradient descent algorithm to a more stable and sophisticated trust region reflective algorithm (TRRA) (Coleman and Li, 1994, 1996) though it still targeted a fully penetrating river. In some regions, specifically the study area of this dissertation, the Mississippi Delta, an aquifer partially penetrated by a river is more prevalent, and in some extreme cases, a river almost sits on an aquifer (Ackerman, 1996), which makes the analytical solution of Hall and Moench (1972) inapplicable. Zlotnik and Huang (1999) developed an analytical solution that could compute the GW response to flood-wave fluctuations under a partially penetrated aquifer, which can be applied to cases in the Mississippi Delta.

In order to derive an analytical solution, some simplifications need to be made, and for the flood-wave response model, a homogeneous aquifer was commonly assumed (Hall and Moench, 1972; Zlotnik and Huang, 1999). However, homogeneous cases are very rare in the real world, where heterogeneity prevails among alluvial aquifers. Whether the flood-wave response model could work for the heterogeneous aquifer has not been examined yet. To apply the flood-wave response model for a heterogeneous aquifer, an equivalent value must be chosen to represent the distribution of the hydraulic conductivity of the aquifer. However, the algorithm to calculate this equivalent value has yet to be studied. Moreover, how the heterogeneity would affect the estimated time-varying streambed conductivity is unknown, and whether the error is acceptable is doubtful.

For the time series-analysis model itself, Gianni et al. (2016) found that the accuracy of the estimated streambed conductivity was affected by the size of the optimization window. Despite experimenting multiple optimization-window sizes and conducting a visual comparison, the quantitative effect of this parameter was not elaborated by Gianni et al. (2016). To the best of the author's knowledge, there has not been a consensus about how to choose the size of the optimization window.

Meanwhile, the flood-wave response model demands the information of the properties of the aquifer and river, such as the hydraulic conductivity and the specific yield of the aquifer, river width and the distance between the monitoring well and river, as input parameters. It is usually hard to guarantee that the measured data are 100% accurate, and sometimes, those values changes with time. For instance, both Gianni et al. (2016) and Xian et al. (2020) expressed their concerns about the riverbank erosion/deposition, which can change the distance between the monitoring well and the river. The uncertainty analysis of input parameters is therefore important.

Chapter 4 modifies the model of Gianni et al. (2016) by implementing the flood-wave response model of Zlotnik and Huang (1999), and then attempts to answer the aforementioned questions by examining the applicability of the flood-wave response model to heterogeneous aquifer, and conducting sensitivity analysis of the optimization window size and other input parameters.

1.1.2 Riverbank Filtration System

Riverbank filtration system (RBF) is a technique to extract water infiltrated from a riverbed and adjacent aquifer of a stream. The contents in the SW will be greatly reduced via several processes, such as physical filtration, microbial degradation, ion exchange, precipitation, sorption

and dilution as it flows through the aquifer (porous media) (Ray et al., 2002). The RBF system has been proven cost-effective in removing contaminants (Prasad et al., 2016) and virus (Derx et al., 2013) from the infiltrated SW, and widely applied in Europe over 100 years for drinking water (Tufenkji et al., 2002). In recent decades, applications of RBF have emerged in the USA (Ray et al., 2002; Jaramillo, 2012). When pumping GW near a stream, due to the increased hydraulic gradient, more purified SW can flow into the aquifer, and thus improve the local GW sustainability, which makes it a good candidate as a source for the managed aquifer recharge project (O'Reilly, 2021). To come up with an appropriate design and scheme for the RBF system, understanding its hydrological processes is crucial.

Owing to its simplicity and easiness, analytical solutions have long been used to study the RBF system. The main physical processes, the dynamics of the pump-induced GW drawdown and stream water infiltration (called stream depletion), are of prime concern. Theis (1941) was the first to propose a transient analytical model to estimate the discharge from a river to an aquifer caused by a pumping well. The river was assumed to be fully penetrating the aquifer and the hydraulic connection between river and aquifer was assumed to be perfect, i.e., the low-permeable riverbank did not exist. Although the model simplified the real problem in many aspects, it became a standard tool for water management (Jenkins, 1968). Many improvements were then made to make the model closer to real problems. For instance, Hantush (1965) improved Theis' model (1941) by considering a low-permeability layer of the aquifer near the river though it still focused on a fully penetrating river. Zlotnik et al. (1999) developed a 2D transient analytical model to estimate the stream depletion for a partially penetrating river. It was then extended by Butler et al. (2001) to consider the width of river and lateral boundary conditions. The conceptual domain was divided

into three regions based on the relative positions of river and pumping well. The transmissivity of homogeneous aquifers varies for different regions. Although these simplifications limit its applicability to more complicated problems, it is close to the field situation conceptually, and would be a basis to verify numerical models.

Physically based numerical models are more effective and applicable to handle real RBF problems, and can simulate detailed drawdown and stream depletion processes. Mas-Pla et al. (2012) developed a numerical model based on MODFLOW to study the stream-aquifer exchange induced by pumping wells in Arbúcies River Basin, Spain. The rivers were simplified to be 1-D polylines, and simulated by the STREAM routine. The stream contribution to the water budge of the basin was computed from the simulation results. When the distance between the pumping well and stream is sufficiently large, the STREAM routine works well. However, errors increase when the pumping well is close to the stream. Polomčić et al. (2012) applied MODFLOW-2000 to study the RBF pumping site in the Sava River, Belgrade, Serbia. The meandering river was discretized with multiple nodes in the horizontal plane to consider the effect of river width. Head-dependent and fixed flux boundary conditions were prescribed on the river nodes. In the vertical direction, four layers were used for the aquifer. However, for MODFLOW (Harbaugh et al., 2000), the soil retention curves were not considered, making it incapable of simulating unsaturated GW flows. Lee et al. (2018) applied FEFLOW to study stream-aquifer interactions under seasonal GW pumping and managed aquifer recharging in the Nam River, South Korean. The river was represented by the Dirichlet head boundary condition and fully incised in the aquifer. These studies have indicated the possibility and potential of physically based numerical models in simulating and managing RBF projects. All of the aforementioned works assumed a constant streambed

conductivity over the simulation period. The impact from the temporal variation of the streambed conductivity on the RBF system has yet to be studied in detail.

Since the Mississippi Delta is frequently visited by storm events, floods are commonly encountered. During high-stage events, with a higher stream-aquifer hydraulic gradient, more SW flows into the subsurface region and transports at a faster pace, which would affect the attenuation capacity of RBF system with respect to potential contamination (Hiscock and Grischek, 2002; Ray et al., 2002; Wett et al., 2002). Moreover, many field works documented that the hydraulic conductivity of the streambed increased substantially during flooding period owing to sediment erosions (e.g., Cui et al., 2021; Korus et al., 2020; Levy et al., 2011; Mutiti and Levy, 2010; Schalchli, 1992; Zhang et al., 2011). A more permeable riverbed can substantially boost SW infiltrations, which increases the uncertainty of the attenuation capacity of RBF system over storm events. For this reason, the U.S. Environmental Agencies conservatively classify many RBF systems as the GW directly influenced by the SW, which demands the same treatment processes of the SW. On the other hand, Gollnitz et al. (2005) revealed that RBF systems were efficient in cleaning the infiltrated SW, and therefore should be granted with a 3.0- or 4.0-log credit in reducing algae and diatoms. In order to evaluate the RBF system more objectively, simulating the detailed riverside pumping process during high-stage events with the consideration of the time-varying streambed conductivity, and quantifying the infiltrated SW rate and its travel time from the stream to the pumping well are necessary. To this end, numerical simulations of a hypothetical RBF pump near the Money experimental site are conducted and presented in Chapter 6.

1.1.3 Hyporheic Exchange

Driven by the SW hydraulic gradient over the sediment-water interface, in the shallow

subsurface region, SW infiltrates into the streambed in one place and emerges back in another. This circulation delimits the so-called 'Hyporheic Flow' (Jones and Mulholland, 2000; Winter et al., 1998). The hyporheic flow forms a unique zone, called hyporheic zone (Findlay, 1995). Hyporheic zone accommodates the active hydrological mixture of SW and GW, concomitant biological processes, geochemical reactions and energy exchanges, making it a 'hot spot' for ecological and biogeochemical studies (Boulton et al., 2010; Gooseff, 2010; Krause et al., 2013; Lawrence et al., 2013; Sophocleous, 2002).

The hyporheic exchange occurs in multiple scales, such as pool-riffle sequences (Tonina and Buffington, 2009a), bars (Lautz and Fanelli, 2008), dams (Sawyer et al., 2009) and dunes (Elliott and Brooks, 1997a). In this study, the dune-induced hyporheic exchange is investigated given that it is ubiquitous and most relevant for total hyporheic flux (Pryshlak et al., 2015; Stonedahl et al., 2013). When the channel flow passes over ripples or dunes, the difference of the dynamic pressure on the stoss and lee side drives the dune-scale hyporheic flow (Cardenas and Wilson, 2007a; Elliott and Brooks, 1997a&b). In general, this type of flow is majorly controlled by two factors, which are the streambed conductivity (e.g., Bardini et al., 2013; Fox et al., 2016; Laube et al., 2018; Tonina et al., 2016) and the hydraulic gradient over the sediment-water interface (e.g., Buffington and Tonina, 2009; Cardenas et al., 2004; Tonina and Buffington, 2009b). The hydraulic gradient provided by the SW flow is the hydrological driver for the hyporheic exchange, which directly initiates and maintains this system, while the streambed conductivity is the hydrological modulator for the hyporheic exchange. The streambed does not directly push the hyporheic flow, but as the medium accommodating the hyporheic zone and

facilitating the concurrent biogeochemical processes, its capacity of transmitting water and contaminants is crucial to shape hydraulic characteristics of the hyporheic flow.

Elliott and Brooks (1997a) conducted a pilot flume experiment of the dune-induced hyporheic exchange. The influences of the SW velocity, water depth, streambed sediment size and dune shapes (height and length) were studied. During the experiment, the hyporheic zone was clearly observed via the solute tracer. An analytical model was then proposed (Elliott and Brooks, 1997b), in which the infinitely thick streambed was simplified to be flat, and the hydraulic head distribution along the streambed surface was approximated as a sinusoid function. Packman et al. (2000) later improved the model by considering an alluvium of a finite thickness. The GW flow resulted from the stream-aquifer hydraulic gradient, called base flow, is often found in the field (Cardenas and Wilson, 2007b). Unlike the hyporheic flow, the base flow is unidirectional and mostly moves vertically. Situations where either the deep GW supplies a stream (gaining condition) (Harvey and Bencala, 1993) or a stream loses water to an aquifer (losing condition) (Harvey et al., 2003) were observed. By taking advantage of the linearity of the Laplace equation, Boano et al. (2008, 2009) extended the analytical solution of Elliott and Brooks (1997b) to include the base flow via the superposition method. Marzadri et al. (2016) derived an analytical solution for a finite alluvium with the base flow included. The effects of hydro morphological factors on the hyporheic zone depth, residence time and redox condition were then studied comprehensively and quantitatively (Marzadri et al., 2016).

Analytical solutions have been playing a vital role in the hyporheic flow studies, but they are often restricted by the simplifications and assumptions involved. A physically based numerical model can overcome this obstacle by using realistic physical conditions, and therefore has broader

applications. Cardenas and Wilson (2007a) coupled SW and GW models to study the dune-induced hyporheic flow numerically. The Reynolds-averaged Navier-Stokes (RANS) model was applied to simulate the stream flow over dunes to obtain the hydrodynamic pressure distribution along the streambed surface. It was then applied as a top boundary condition of the GW model. The base flow was then considered in the numerical model (Cardenas and Wilson, 2007b). The residence times of the hyporheic flow under both gaining and losing conditions were found shorter than that of the neutral condition. These conclusions were later confirmed by an experimental study (Fox et al. 2014). A reduced-complexity numerical model was proposed by Wu et al. (2018) to estimate the effect of dynamic changes of base flow on the hyporheic zone. An analytical expression of hydraulic head distributions (Elliott and Brooks, 1997b) was directly applied as the top boundary condition and only GW flow was simulated. In so doing, the computing time was significantly reduced while the simulation accuracy was preserved.

Besides the aforementioned works focusing on the homogeneous streambed, the dune-induced hyporheic exchange under a heterogeneous streambed has attracted much attention recently (e.g., Bardini et al., 2013; Fox et al., 2016; Laube et al., 2018; Salehin et al., 2004; Tonina et al., 2016). The hydraulic conductivity of the riverbed sediment was regarded as a random variable, and geostatistics model was applied to generate multiple realizations. With sufficient simulation cases, conclusions can be drawn by assembling the results through Monte-Carlo framework (Laube et al., 2018; Tonina et al., 2016). Sawyer and Cardenas (2009) studied two specific heterogeneous streambeds based on the images of climbing ripple deposits in the Brazos River and Massillon Sandstone and an outcrop analog was applied. It is generally agreed that the local-scale heterogeneity will increase the hyporheic flux and shorten the residence time, though

the magnitude of the effect varied from mild (e.g., Bardini et al., 2013; Salehin et al., 2004) to significant (Fox et al., 2016).

Aside from this spatial variation of the streambed conductivity (heterogeneity), its temporal variation has been frequently studied in recent years. With the facilitation of laboratory experiments, Fox et al. (2018) and Marttila et al. (2019) explored the clogging effect from fine sediment deposition, and concluded that this low-permeable layer would severely slow down and reduce the hyporheic exchange. Newcomer et al. (2016) developed a simplified 1-D biofilm growth model to integrate the biofilm-induced clog into the numerical study of the hyporheic flow. With both laboratory and analytical studies, Marion et al. (2008) found that an armored sediment layer could significantly boost the hyporheic flux and shorten the residence time. However, most of these works merely focused on the impact of the time-varying streambed conductivity under a steady or low-stage SW flow condition.

The hydraulic gradient provided by the SW flow is the engine to initiate and push the hyporheic exchange. The imperative of the transience in stream flow has been considered and studied in recent years (Gomez-Velez et al., 2017; Malzone et al., 2016; Trauth and Fleckenstein, 2017), particularly the impact from flood events (Wu et al., 2018; Singh et al., 2019 and 2020). With a stronger hydraulic gradient caused by peak-flow events, the hyporheic exchange can be substantially enhanced, and correspondingly, the regional biogeochemical process can be accelerated, and the whole ecosystem will therefore be altered (Gu et al., 2008; Harvey et al., 2013; Trauth and Fleckenstein, 2017). However, most of them assumed that the streambed conductivity was constant over the whole period.

Plenty of studies have revealed that the temporal variation of the streambed conductivity

is fast and dramatic during flood periods (e.g., Korus et al., 2020; Levy et al., 2011; Mutiti and Levy, 2010; Schalchli, 1992). It is therefore necessary to incorporate time-varying streambed conductivity into the study of the dune-induced hyporheic exchange during high-stage events. This objective is achieved and presented in Chapter 7.

1.2 Research Objectives

As was covered in detail in the previous section, several previous studies in the research literature have revealed that streambed conductivity is a critical parameter controlling stream-aquifer interactions and changes with time due to multiple processes, but none of these studies addressed combined effects of the high-stage event and time-varying streambed conductivity. This dissertation attempts to study combined effects of the high-stage event and time-varying streambed conductivity on GW-SW exchanges through numerical simulations. The study area is in the Mississippi Delta. To fulfill this core objective, the dissertation follows the roadmap shown in Fig. 1.1 and the following is the detailed explanation:

(1) Numerical modelling has become one of the most powerful tools for the modern scientific community since it can capture key processes of the focused problem and facilitate the study of hypothetical scenarios to enhance the understanding of certain issues, and support policy and decision-making. In this study, a finite element numerical model, CCHE3D-GW, that can simulate both saturated and unsaturated GW flows is developed and verified. It is then used as a major tool to facilitate studies of GW-SW interactions.

(2) To integrate the time-varying streambed conductivity into studies of GW-SW interactions, the first step is to obtain this temporal variation. Since field campaigns could only render a set of data with a low temporal resolution and are hard to be conducted during flooding periods, a

new method based on the GW response to the flood-wave fluctuation is developed, which is called estimation model in this dissertation. Before being applied to field cases, its validity, viability to the heterogeneous aquifer, and sensitivity to input parameters are examined in order to confirm its accuracy and efficacy.

(3) After developing the major tool (CCHE3D-GW) and obtaining the temporal variation of the streambed conductivity (via the estimation model), two typical cases of GW-SW interactions are chosen for the numerical study, which are the RBF system and the dune-induced hyporheic flow.

(3-a) USDA-ARS has proposed to apply the RBF system as a source for direct injection into the aquifer aimed at taking advantage of recharge of SW infiltrations and the filtration function of aquifer sediments. For the study area, the Mississippi Delta, it is frequently visited by storm events, so floods are commonly encountered. During flooding periods, excessive SW can flow into aquifers through RBF system due to higher stream-aquifer hydraulic gradients as well as a more permeable riverbed, which can affect the function of RBF system. It is therefore necessary to quantify the infiltrated SW rate and the travel time of the infiltrated SW from stream to the pumping well during high-stage events in order to evaluate the performance of the RBF system precisely. These objectives are fulfilled through simulations of a hypothetical RBF pump during three typical flooding conditions at Money experimental site in Mississippi (MS), USA, while considering time-varying streambed conductivity.

(3-b) Dune-induced hyporheic flow re-distributes water and nutrients, and plays a vital role in controlling biogeochemical processes in the riverine system. However, few of previous studies focused on the impacts from the combined effect of the flood event and time-varying

streambed conductivity although these two temporal variations cannot be ignored in real-world problems. To fill this gap, simulations concerning dune-induced hyporheic exchange during three typical flooding conditions with time-varying streambed conductivity are conducted.

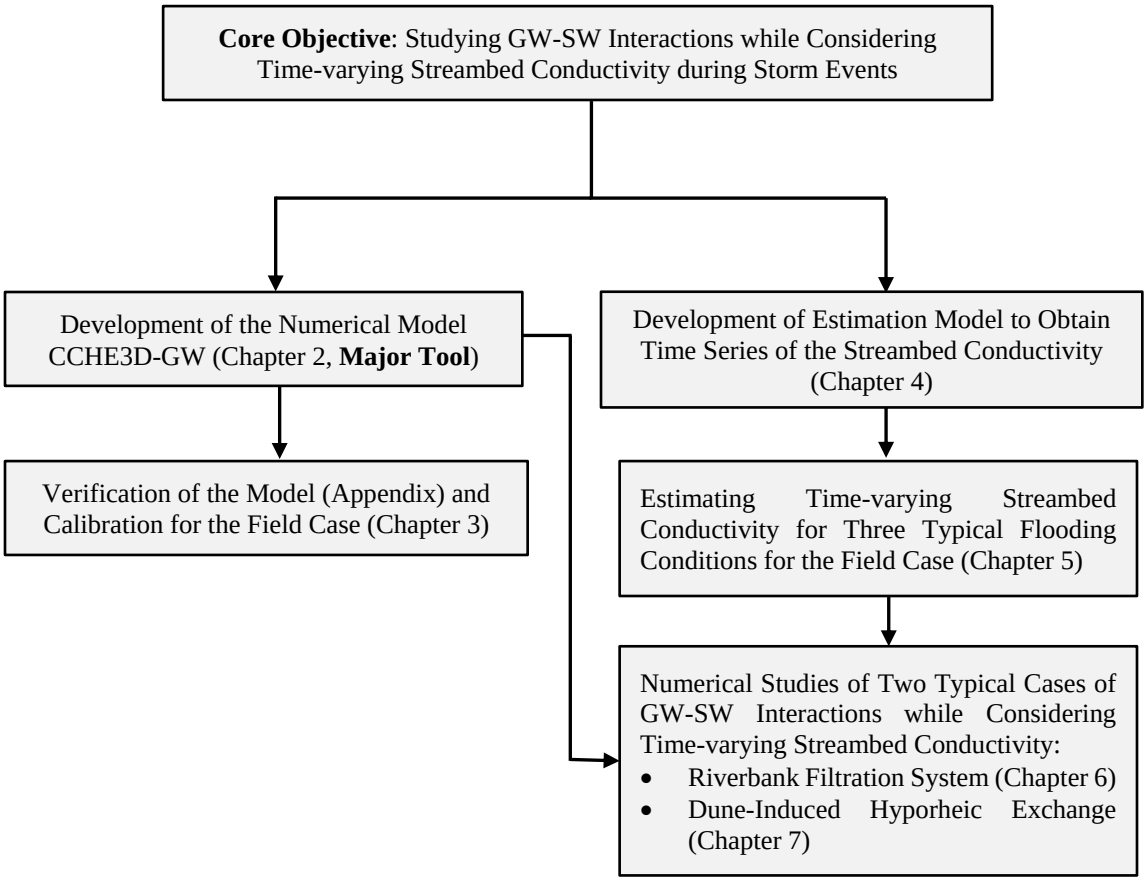

Figure 1.1. Outline of dissertation research objectives.

1.3 Dissertation Outline

Chapter 2 introduces the development of the 3-D finite element numerical model, CCHE3D-GW. Chapter 3 elaborates the calibration of the numerical model with an aquifer test conducted at Money site in Mississippi, USA, to obtain the hydrogeological information of the study area. Chapter 4 develops an estimation model to rapidly attain the temporal variation of the streambed conductivity from GW responses to flood-wave fluctuations. The validation of the

model, sensitivity analysis and its applicability to a real heterogeneous aquifer are studied as well. The estimation model is then applied to three typical flooding conditions for the Tallahatchie River near Money, Mississippi, USA, and the calculated time series of streambed conductivity are presented in Chapter 5. Chapter 6 incorporates the estimated time-varying streambed conductivity into the CCHE3D-GW to study hydrological processes of the RBF system during high-stage events with simulations of a hypothetical pump. Chapter 7 explores the combined effect from flood and time-varying streambed conductivity on the dune-induced hyporheic exchange with the simulation of CCHE3D-GW. Finally, the summary and conclusions of this dissertation, and recommendations for future research are presented in Chapter 8.

CHAPTER II

DEVELOPMENT OF CCHE3D-GW

2.1 Governing Equation

Richards Equation can be written in three forms, which are head-based, saturation-based and mixed. Among the three, the mixed-form Richards Equation can preserve mass conservation both globally and locally, and is capable of handling variably saturated GW flow (Celia et al. 1990). It is therefore used as the governing equation (Eq. 2.1) in this model.

$$\frac{\partial \theta}{\partial t} + S \cdot S_s \frac{\partial H}{\partial t} = \frac{\partial}{\partial x}\left[K_x(\psi)\frac{\partial H}{\partial x} \right] + \frac{\partial}{\partial y}\left[K_y(\psi)\frac{\partial H}{\partial y} \right] + \frac{\partial}{\partial z}\left[K_z(\psi)\frac{\partial H}{\partial z} \right] \qquad (2.1)$$

where, θ is moisture content; H is hydraulic head; ψ is pressured head (= hydraulic head – elevation); K is hydraulic conductivity; S_s is specific storativity and $S = (\theta - \theta_r)/(\theta_s - \theta_r)$ is saturation, in which θ_r is residual moisture content and θ_s is saturated moisture content. When the pressure head, ψ, is larger than the air-entry pressure head, ψ_{air}, the soil is saturated. Under this condition, the moisture content, θ, and hydraulic conductivity, K, are both of saturated values, and the saturation equals to 1. When ψ becomes lower than ψ_{air}, air enters soil, and makes it unsaturated (saturation is less than 1), which results in the reductions of θ and K values. Moisture content and hydraulic conductivity of the unsaturated soil can be estimated from pressure head based on soil retention curves, which can be obtained by fitting the measured data with theoretical models (e.g., Brooks and Corey, 1996; van Genuchten, 1980). In this study, the van Genuchten (1980) model is applied, which are:

$$\theta(\psi) = \theta_r + \frac{(\theta_s - \theta_r)}{\left[1 + (\alpha|\psi|)^{\beta}\right]^{1-1/\beta}}, \qquad \psi < 0 \tag{2.2}$$

$$K(\psi) = K_s \frac{\left[1 - (\alpha|\psi|)^{\beta-1} \cdot \left(1 + (\alpha|\psi|)^{\beta}\right)^{1/\beta - 1}\right]^2}{\left[1 + (\alpha|\psi|)^{\beta}\right]^{\frac{(1-1/\beta)}{2}}}, \qquad \psi < 0 \tag{2.3}$$

where, K_s is saturated hydraulic conductivity, α is a scaling parameter inversely related to the air-entry pressure and β is a slope parameter inversely related to the pore-size distribution.

2.2 Numerical Method

The fully implicit numerical scheme and modified Picard's iteration method (Celia et al. 1990) is used to discretize Eq. 2.1, as:

$$\frac{\theta^{m,n+1} - \theta^{n}}{\Delta t} + C^{m,n+1} \frac{H^{m+1,n+1} - H^{m,n+1}}{\Delta t} + S^{n} \cdot S_s \frac{H^{m+1,n+1} - H^{n}}{\Delta t} = \frac{\partial}{\partial x}\left[K_x^{m,n+1}(\psi) \frac{\partial H^{m+1,n+1}}{\partial x}\right] + \frac{\partial}{\partial y}\left[K_y^{m,n+1}(\psi) \frac{\partial H^{m+1,n+1}}{\partial y}\right] + \frac{\partial}{\partial z}\left[K_z^{m,n+1}(\psi) \frac{\partial H^{m+1,n+1}}{\partial z}\right] \tag{2.4}$$

where, $C = \partial\theta/\partial H$, n is time step and m is iteration step. For example, $H^{m+1,\,n+1}$ represents the hydraulic head at the iteration step m+1of the time step n+1.

A 3-D mixed form of control volume and finite element method is applied in solving Eq. 2.4 numerically. It is an extension of the 2-D method of Cumming et al. (2011). The computational domain is discretized with $N_x \times N_y \times N_z$ mesh points, in which N_x, N_y and N_z represents the number of mesh points in x, y and z direction, respectively. The number of cells (control volumes) is therefore $(N_x - 1) \times (N_y - 1) \times (N_z - 1)$. For each control volume, the volumetric integration is conducted. Using Gauss Divergence Theorem, Eq. 2.4 becomes:

$$\iiint_V \left(\frac{\theta^{m,n+1} - \theta^n}{\Delta t} + C^{m,n+1} \frac{H^{m+1,n+1} - H^{m,n+1}}{\Delta t} + S^n \cdot S_s \frac{H^{m+1,n+1} - H^n}{\Delta t} \right) dV =$$
$$\oiint_\Gamma \left[K_x^{m,n+1}(\psi) \frac{\partial H^{m+1,n+1}}{\partial x} \right] dA_x + \oiint_\Gamma \left[K_y^{m,n+1}(\psi) \frac{\partial H^{m+1,n+1}}{\partial y} \right] dA_y \qquad (2.5)$$
$$+ \oiint_\Gamma \left[K_z^{m,n+1}(\psi) \frac{\partial H^{m+1,n+1}}{\partial z} \right] dA_z$$

where, V is the control volume; A_x, A_y and A_z is the surface of V with normal of *x*, *y* and *z* direction, respectively. In CCHE3D-GW, the structure mesh is adopted. Hydraulic head (*H*), hydraulic conductivity (*K*) and moisture content (θ) are located at the center of each control volume (cell), which is called staggered node. The terms inside the surface integration, i.e., $K_x(\psi)\frac{\partial H}{\partial x}$, $K_y(\psi)\frac{\partial H}{\partial y}$ and $K_z(\psi)\frac{\partial H}{\partial z}$, are the *x*, *y* and *z* compontents of Darcy velocity (**q**). They are located at the vertex of cell called collocation node, and surrounded by eight hydraulic head nodes. The configuration is shown in Fig. 2.1, where void circles and solid circles indicate collocation nodes and staggered nodes, respectively. For clarity, only selected solid nodes are marked.

For each eight-neighbor hydraulic head nodes, the local coordinate (ξ, η and ζ) is built (as Fig. 2.1 shows) and the 3D linear interpolation function is applied:

$$N_i = \frac{1}{8}(1 + \xi_i \xi)(1 + \eta_i \eta)(1 + \zeta_i \zeta) \qquad (2.6)$$

where, *i* is the number of the hydraulic head node (from 1 to 8); N_i is the linear interpolation function for each hydraulic head node; (ξ_i, η_i, ζ_i) is the local coordinate of hydraulic head node and (ξ, η, ζ) is the local coordinate of an arbitrary point inside the unit. The hydraulic head of an arbitrary point, (ξ, η, ζ), inside the unit can be computed as:

$$H = \sum_{i=1}^{8} (N_i \cdot H_i) \tag{2.7}$$

The derivatives of hydraulic head in local coordinate can therefore be computed as:

$$\frac{\partial H}{\partial \xi} = \sum_{i=1}^{8} \left(\frac{\partial N_i}{\partial \xi} \cdot H_i \right), \quad \frac{\partial H}{\partial \eta} = \sum_{i=1}^{8} \left(\frac{\partial N_i}{\partial \eta} \cdot H_i \right), \quad \frac{\partial H}{\partial \zeta} = \sum_{i=1}^{8} \left(\frac{\partial N_i}{\partial \zeta} \cdot H_i \right) \tag{2.8}$$

The derivatives of H in global coordinate are obtained by using standard finite element transformation. In this study, these derivatives only required to be computed at velocity nodes according to Eq. 2.5, so that for each unit, the following equations can be obtained:

$$\frac{\partial H}{\partial x} = \sum_{i=1}^{8} (a_{xi} H_i), \quad \frac{\partial H}{\partial y} = \sum_{i=1}^{8} (a_{yi} H_i), \quad \frac{\partial H}{\partial z} = \sum_{i=1}^{8} (a_{zi} H_i) \tag{2.9}$$

where, a_{xi}, a_{yi} and a_{zi} are the coefficients for each hydraulic head. Each unit contains one velocity node. The coefficient of each H for computing the Darcy velocity (derivatives in the right hand side of Eq. 2.5) is then obtained.

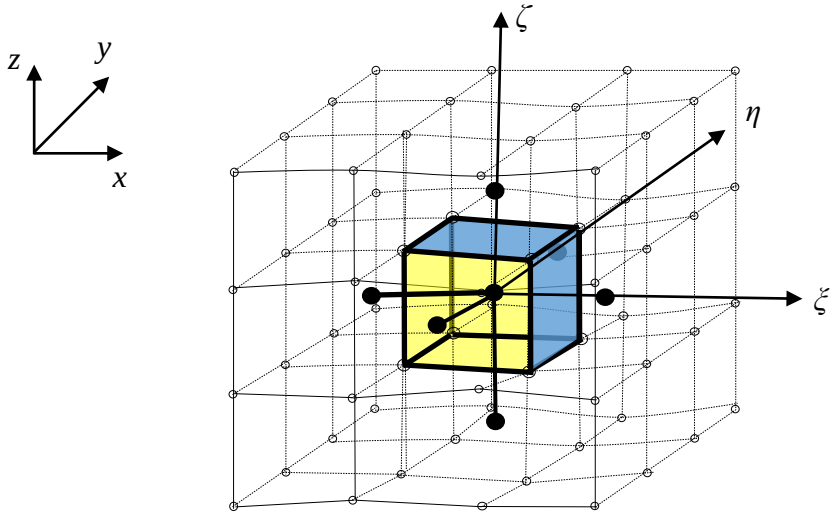

Figure 2.1. Mesh configuration of this model. Void circles represent the collocation nodes of the finite element mesh and solid circles are staggered nodes. Darcy velocities located on the collocation nodes and hydraulic head are located on staggered nodes. A cell consists of eight collocation nodes (void circles) and its center is the staggered node.

When calculating the new time step n+1, the variables (H, θ, K) at old the time step (time step n) have been obtained by the model, i.e., θ^n and S^n are known in Eq. 2.5. For the new time step n+1, iterations are applied to achieve the convergent solution. When marching on the new iteration step m+1, the values at the old step (iteration step m) have all been computed, which means, in Eq. 2.5, the values of $H^{m,n+1}$, $\theta^{m,n+1}$, $K_x^{m,n+1}$, $K_y^{m,n+1}$, $K_z^{m,n+1}$ and $C^{m,n+1}$ are all obtained, and the only unknown value is $H^{m+1,n+1}$. Eq. 2.5 is therefore a linear euqation for $H^{m+1,n+1}$ and is solved by the SIP method of Stone (1968). After getting the new value of H, the latest values of θ and K are computed from the state equations (Eq. 2.2 and Eq. 2.3). The iteration will continue to update the value of variable, H, until the convergence criterion, such as $\left|\frac{H^{m+1,n+1}-H^{m,n+1}}{H^{m,n+1}}\right|<\varepsilon$ (ε is a pre-determined small value, e.g., 1.0×10^{-6}), is satisfied. When the convergence is achieved, the computation goes on to the next time step.

2.3 Verificaiton of CCHE3D-GW

Verification is an important step to check the mathematical correctness of a newly developed model. In this dissertation, multiple analytical and numerical solutions were chosen for this purpose. To make the dissertation more focused on the major topic, which is studying the combined effect of the high-stage event and time-varying streambed conductivity on GW-SW exchanges, the verification part is attached in Appendix 1 ~ 3. In general, the simulation results of CCHE3D-GW are consistent with the published analytical and numerical solutions concerning saturated-unsaturated GW flows, riverside pumping and hyporheic exchange, indicating that CCHE3D-GW can precisely simulate the studied problems.

CHAPTER III

STUDY AREA AND HYDROGEOLOGICAL SETTING

This chapter presents the hydrogeological information of the study area of this dissertation, Money site in Mississippi, USA, which is an important experimental site for the pilot managed aquifer recharge project in the Mississippi Delta. Multiple field studies, such as measurements of sediment resistivity, were conducted by United States Geological Survey (USGS) in order to depict the geological characteristics of the site. A pumping test was carried out in 2017 by USDA-ARS, which was the basis to quantify hydrological parameters. By calibrating the simulated GW drawdowns of CCHE3D-GW with the field data, the hydraulic properties of the aquifer, aquitard and riverbed were attained. The details are elaborated in the following sections.

3.1 Description of Pumping Site

The irrigation well of the Money site was installed at longitude 90°12'44"W and latitude 33°39'24"N in Leflore County, Mississippi, USA, and it was close to the western bank of the Tallahatchie River (Fig. 3.1a and b). The depth of the well was 36.0 m, which partially penetrated the aquifer, and the well screen was from 20.0 m to 36.0 deep. 15 monitoring wells (MWs) were drilled nearby to measure the piezometer data, and their depths were all around 22.0 m underground (Fig. 3.1b). One of the MWs, MW15, was located near the eastern bank of the river while the rest, including the irrigation well, were on the western floodplain. The average width of the Tallahatchie River near the pumping site is approximately 42.0 m, and the elevation of the

riverbed is about 10.0 m beneath the land surface. To attain the hydraulic parameters of the aquifer and regional stream-aquifer connection, a three-day aquifer test was conducted by USDA-ARS from February 8, 2017 to February 11, 2017, in which the pumping rate, *Q*, was 12960.0 m^3/day.

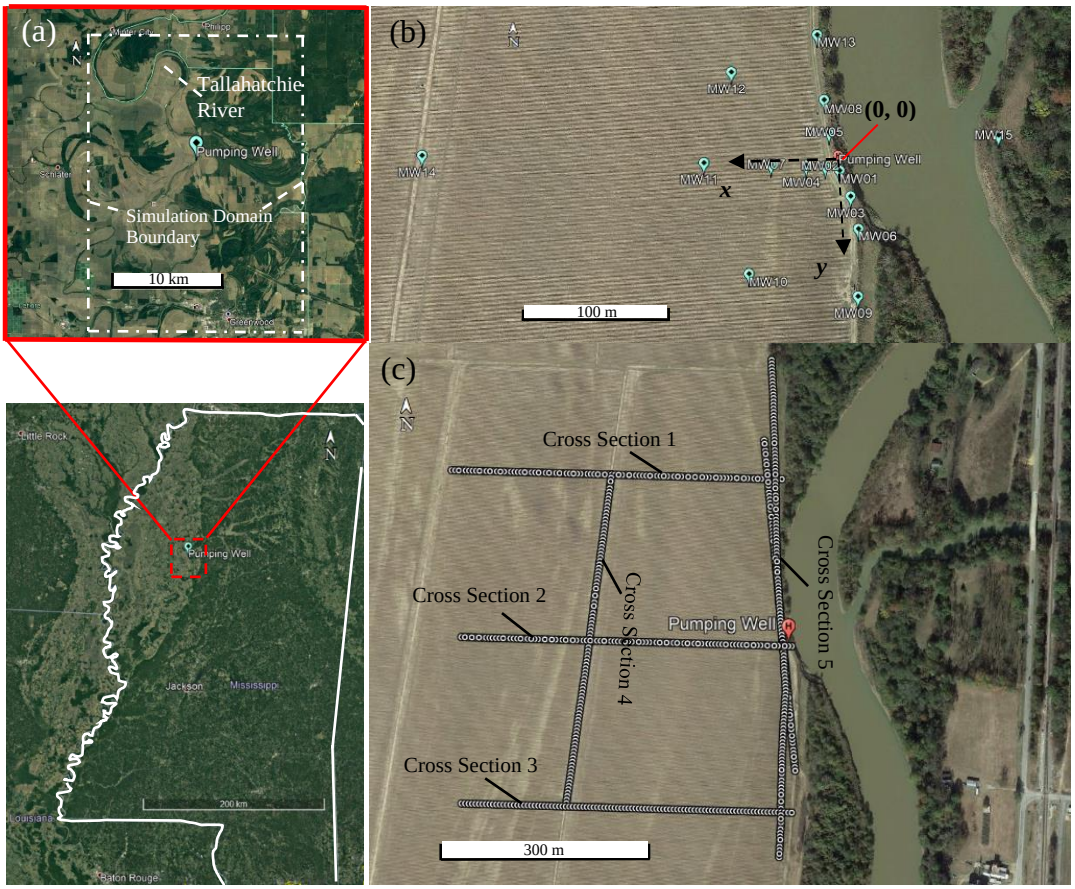

Figure 3.1. (a) Geographical position of the study area, where the white dotted rectangle delineates the boundary of simulation domain; (b) the configuration of the pumping test in Leflore County, Mississippi, USA, and (c) the layout of the measurement for sediment resistivity.

Spatial distribution of hydraulic conductivities of aquifer is an important input parameter for GW flow studies. The traditional methodology to obtain this parameter is through collecting soil samples from the field and measuring their values in the laboratory. An alternative way is to take advantage of the positive correlation between the sediment resistivity and its hydraulic conductivity. By measuring the resistivity distribution in situ and calibrating certain key

parameters of empirical formula, the hydraulic conductivity distribution can be computed. In this pumping site, the sediment resistivity data were collected at five cross sections by USGS (Bloss et al., 2019, link: https://doi.org/10.5066/P965NBFT), in which three were perpendicular and two were parallel to the stream flow direction (Fig. 3.1c). In each section, 23 layers of data, which were from the land surface (0.0 m) to 65.0 m deep, were collected.

3.2 Conceptual Model for Calibration

In this study, the meandering complex planform of the Tallahatchie River was idealized as a straight channel from North to South with a rectangular cross-section for the sake of simplicity. Given that the riverbank is usually of a low permeability, this assumption is not expected to affect the results too much. The land surface of the domain was assumed horizontal and flat considering the typical nature of the topography in the Mississippi Delta. The simulation domain was set sufficiently large (20300 m × 28600 m) to circumvent the uncertainty of the lateral boundary condition. The distance from the northern, southern, western and eastern boundary to the irrigation well was 11490.99 m, 17107.64 m, 10503.86 m and 9805.19 m, respectively.

Fig. 3.2a shows the sediment resistivity distribution of the cross-section 2 (shown in Fig. 3.1c), which passes the pumping well and is perpendicular to the Tallahatchie River. The left *y* coordinate is the elevation under the NAVD 88 datum system while the right side is the depth from the land surface. The dark blue parts are the regions without data. The sediment resistivity data illustrates that the cross section can be approximated by three layers. Among them, the top 10 m is likely to be clay owing to its small resistivity value; the resistivity data of the middle layer, which is from 10. 0 m to 50.0 m depth, is generally within a typical range of sand (Palacky, 1988) while the extremely low resistivity of the sediment below 50.0 m indicates that it is almost

impermeable, which is therefore set as a no-flux boundary in simulations. The sediment resistivity distributions of the other cross sections are congruent with this three-layer conceptual model.

An empirical formula of Salem (2001) was used to convert the sediment resistivity to hydraulic conductivity:

$$K = 7.7 \times 10^{-6} \left(\frac{R_b}{R_w} \right)^{2.09} \tag{3.1}$$

where, K (m/s) is hydraulic conductivity; R_b is measured bulk resistivity, and R_w is pore-water resistivity. In this study, R_w was a calibrated parameter. Since Eq. 3.1 does not include the effect of clay contents (Shevnin et al., 2006), the converted results for the top 10 m layer should be modified. Considering that this low-permeable layer can only transmit limited amount of water, its impact on the physical process would be minimal. Assuming this layer as a homogenous aquitard with a low hydraulic conductivity, K_u, would therefore affect the simulation results marginally but significantly simplify the problem. The value of K_u will be determined later via the calibration.

The size of the simulation domain (20300 m × 28600 m) is much larger than the region enveloped by the cross sections of the measured sediment resistivity (Fig. 3.2b), which is only around 450 m × 550 m. Our preliminary simulation results, which assumed a homogenous aquifer, revealed that the GW drawdowns were noticeable inside a 1600 m × 1100 m rectangle, in which the irrigation well was at the center. However, for the area outside this rectangle, the drawdowns were generally negligible, indicating that the heterogeneity of the aquifer in this region could have limited impacts on the GW flow. In the lateral direction, the aquifer was therefore divided into two zones. Inside the 1600 m × 1100 m rectangle frame was the near field, where the heterogeneity of the hydraulic conductivity was considered and interpolated through the sediment resistivity data.

The rest of the aquifer was categorized as the far field and assumed homogeneous with a constant hydraulic conductivity K_f, which will be determined through calibration.

For the streambed, Irvine et al. (2012) found that when it was fully saturated, its heterogeneity had a limited influence on GW-SW exchanges. Tallahatchie River is generally of abundant water supply so that an unsaturated or partially saturated streambed is rarely encountered. A homogeneous streambed was therefore assumed here to simplify the problem. Hantush (1965) found that the hydraulic effect of the streambed is correlated to streambed conductance, C, which is equal to the ratio of the hydraulic conductivity, K_r, and thickness, b', of the streambed. In this study, the value of C will be obtained through calibration as well.

With the aforementioned approximations, a typical conceptual cross section of the simulation is shown as Fig. 3.2c. From the land surface (0 m depth) to 10 m depth is a homogeneous aquitard. A non-flux boundary is placed at the bottom of the 40 m thick sandy aquifer. A heterogeneous aquifer is considered near the pumping well while the far field is approximated as homogeneous.

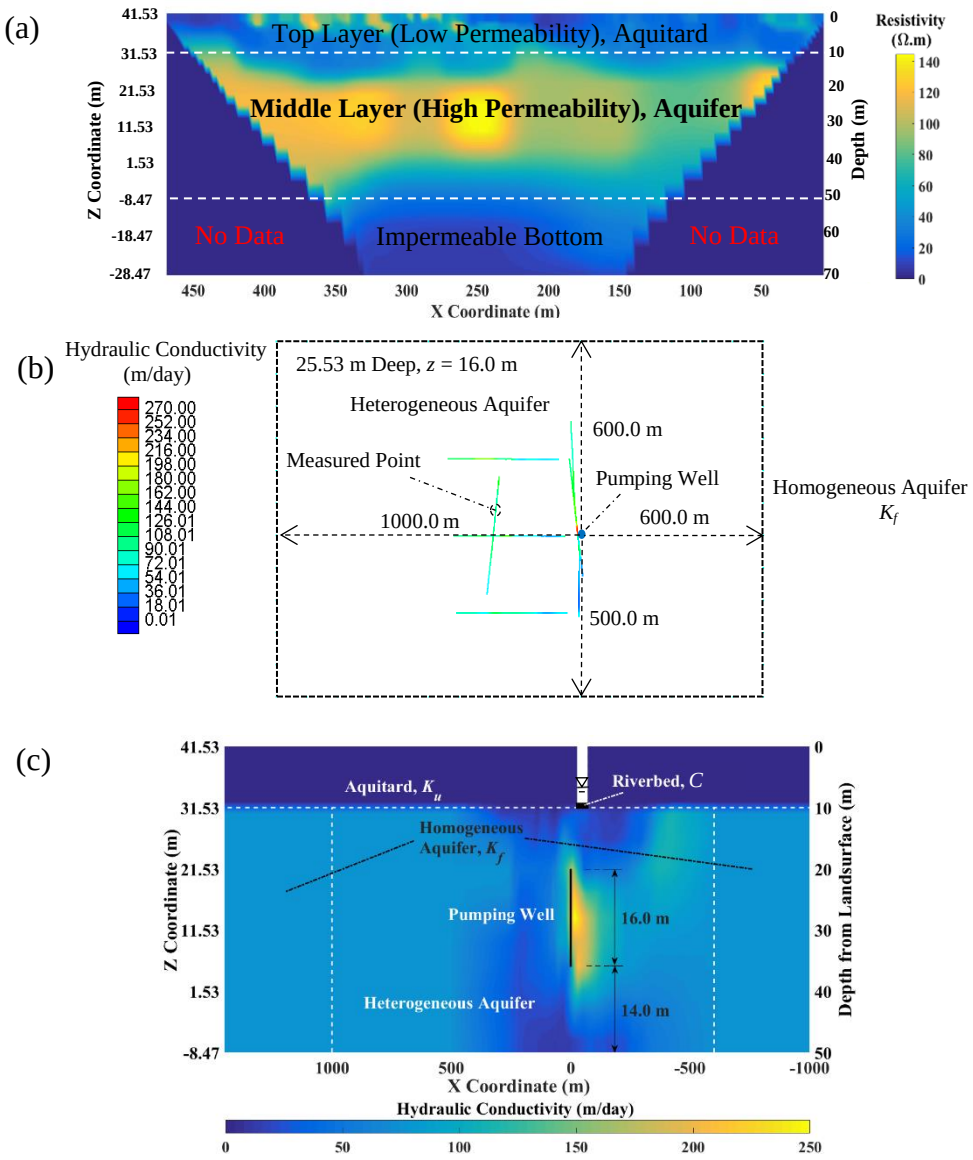

Figure 3.2. (a) The spatial distribution of sediment resistivity for the cross section passing the pumping well and perpendicular to the Tallahatchie River; (b) the $x - y$ plane view of the computed hydraulic conductivity from Eq. 3.1 with R_w = 10.82 Ω.m at the measured points (25.53 m deep; z = 16.0 m) and (c) the conceptualized cross section of the simulation.

3.3 Mesh and Boundary Conditions for Calibration

A non-uniform mesh (138 × 139 × 27 in x, y and z direction) was used to discretize the domain. The mesh origin was set at the pumping well with the x direction perpendicular to the

river (Fig. 3.1b). Fig. 3.3a and 3.3b show the configuration of the mesh in $x - y$ view. The region far from the pumping well was discretized by coarse and non-uniform meshes (Fig. 3.3a), and the near-well field was represented by fine and uniform meshes (2.0 m × 2.0 m, Fig. 3.3b). Fig. 3.3c shows the mesh distribution in z direction with the datum being NAVD 88. 12 layers were used to discretize the sandy aquifer (from z = -8.47 m to 32.53 m), and the mesh size varied from 4 m to 6 m in this region. The aquitard was represented by 15 layers. A uniform vertical grid spacing of Δz = 0.2 m was used from z = 33.63 m to 35.43 m, and a non-uniform grid spacing with an increment of 0.05 m starting with Δz = 0.05 m was used from z = 35.43 m to 41.53 m. Δz = 1.1 m was used for z = 32.53 m to 33.63 m.

The water stage of the Tallahatchie River during the pumping test, shown as a blue line in Fig. 3.4, was recorded at the USGS Money Station (USGS 07281600). The varying water stage was implemented into the simulation. The longitudinal water surface slope of the river was found to be mild (5.36×10^{-5}). Water surface elevation in the computational domain dropped about 1.5 m along the whole river channel. The initial hydraulic heads of aquifer and aquitard were both set as 35.152 m based on the field data. The lateral boundaries were all set as non-flux.

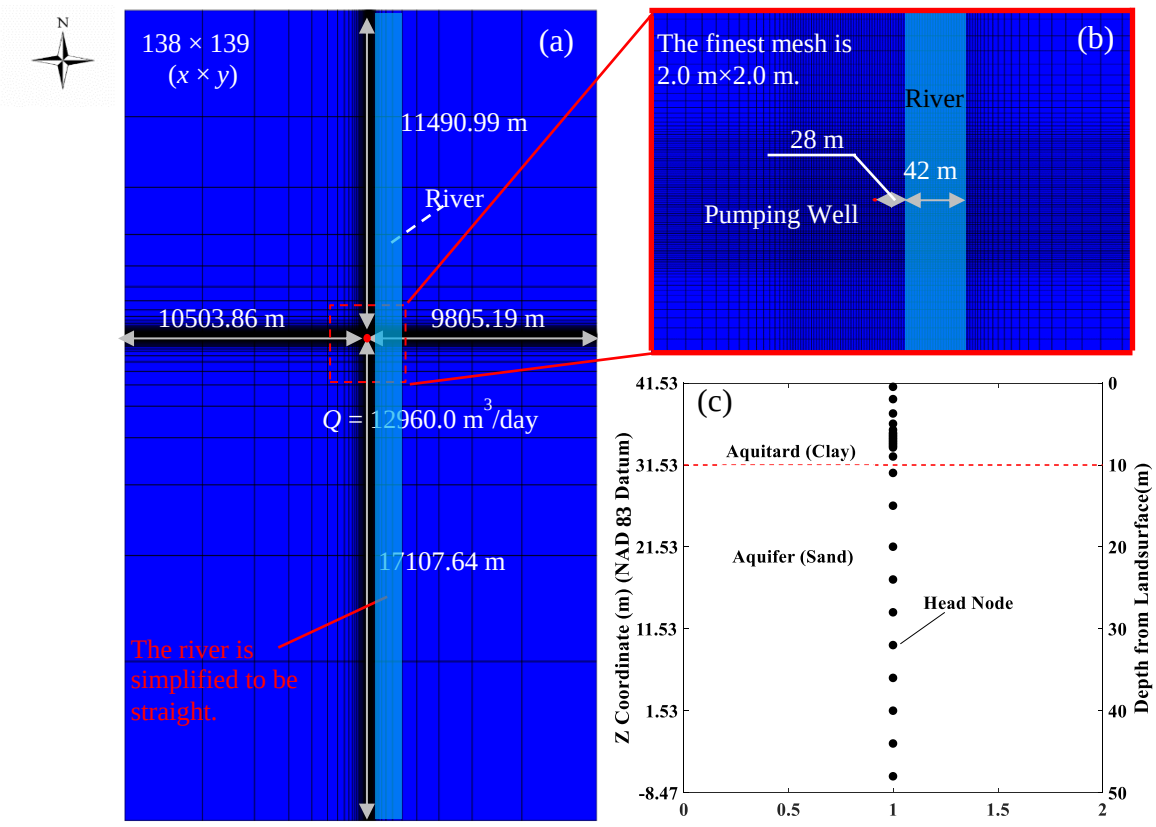

Figure 3.3. The configuration of the mesh in *x* - *y* direction for (a) the whole simulation domain and (b) the near-well region. (c) The setup of the mesh in *z* direction.

3.4 Calibration Results

To simulate the field case, four unknown parameters were required: the pore-water resistivity (R_w), hydraulic conductivities of aquitard (K_u) and far-field aquifer (K_f), and the streambed conductance (C). The GW hydraulic heads observed in the 15 monitoring wells (Fig. 3.1b) were used for comparisons in the calibration. The monitoring wells can be categorized into three groups: the ones in the cross sections perpendicular (MW02, 04, 07, 11, 14 and 15) and parallel (MW01, 03, 05, 06, 08, 09 and 13) to the Tallahatchie River, and those at ordinary locations (MW10 and 12). The coordinates of monitoring wells and their distance to the pumping wells are listed in Table 3.1.

The parameters θ_r, θ_s, α and β of soils are usually estimated by fitting the theoretical model with the measured data from the collected samples. In this study, the recommended values from USGS VS2DTI model (Hsieh et al., 2000) were applied owing to the lack of field data. Values θ_r = 0.02, θ_s = 0.375, α = 4.31 m^{-1} and β = 3.1, were adopted for the aquitard and θ_r = 0.089, θ_s = 0.43, α = 1.0 m^{-1} and β = 1.23, were used for both the near-field and far-field aquifers. The specific storativity, S_s, was set to be 0.00005.

Table 3.1. The Coordinates of the Pumping Well and Monitoring Wells

No. of Wells	Coordinate (x,y) (m)	Distance to the Pumping Well, d (m)	No. of Wells	Coordinate (x,y) (m)	Distance to the Pumping Well, d (m)
Pumping Well	(0.00, 0.00)	0.00	MW01	(0.00, 3.60)	3.60
MW02	(11.00, 0.00)	11.00	MW03	(0.00, 22.32)	22.32
MW04	(24.47, 0.00)	24.47	MW05	(0.00, -25.04)	25.04
MW06	(0.00, 46.13)	46.13	MW07	(47.72, 0.00)	47.72
MW08	(0.00, -48.56)	48.56	MW09	(0.00, 93.08)	93.08
MW10	(61.27, 78.31)	99.43	MW11	(94.51, 0.00)	94.51
MW12	(77.20, -64.98)	100.91	MW13	(0.00, -94.67)	94.67
MW14	(286.75, 0.00)	286.75	MW15	(-109.65, 0.00)	109.65

After testing several combinations of the values of calibrated parameters, it was found that the numerical results best fitted the field data with R_w = 10.82 Ω.m, K_u = 0.010 m/day, K_f = 75.0 m/day and C = 0.05 day^{-1}. The criteria for the comparison is root mean square error, f_{RMS}, computed as below:

$$f_{\mathrm{RMS}} = \sqrt{\frac{\sum \left(H_{\mathrm{sim}} - H_{\mathrm{obs}}\right)^2}{n}} \tag{3.2}$$

where, H_{sim} and H_{obs} is the simulated and measured GW hydraulic head, respectively, and n is the number of the measured data.

Fig. 3.4 shows the comparisons between the simulated (lines) and measured (crosses) declining processes of hydraulic heads during the pumping test. Fig. 3.4a is the results of the monitoring wells in the cross section perpendicular to the Tallahatchie River. Fig. 3.4b and c are for those in the cross sections parallel to the river. The results of the monitoring wells at ordinary locations are illustrated in Fig. 3.4d. The agreements between the simulation results and field data are quite good, as evidenced by the small value of f_{RMS}, which ranges from 0.017 m to 0.070 m.

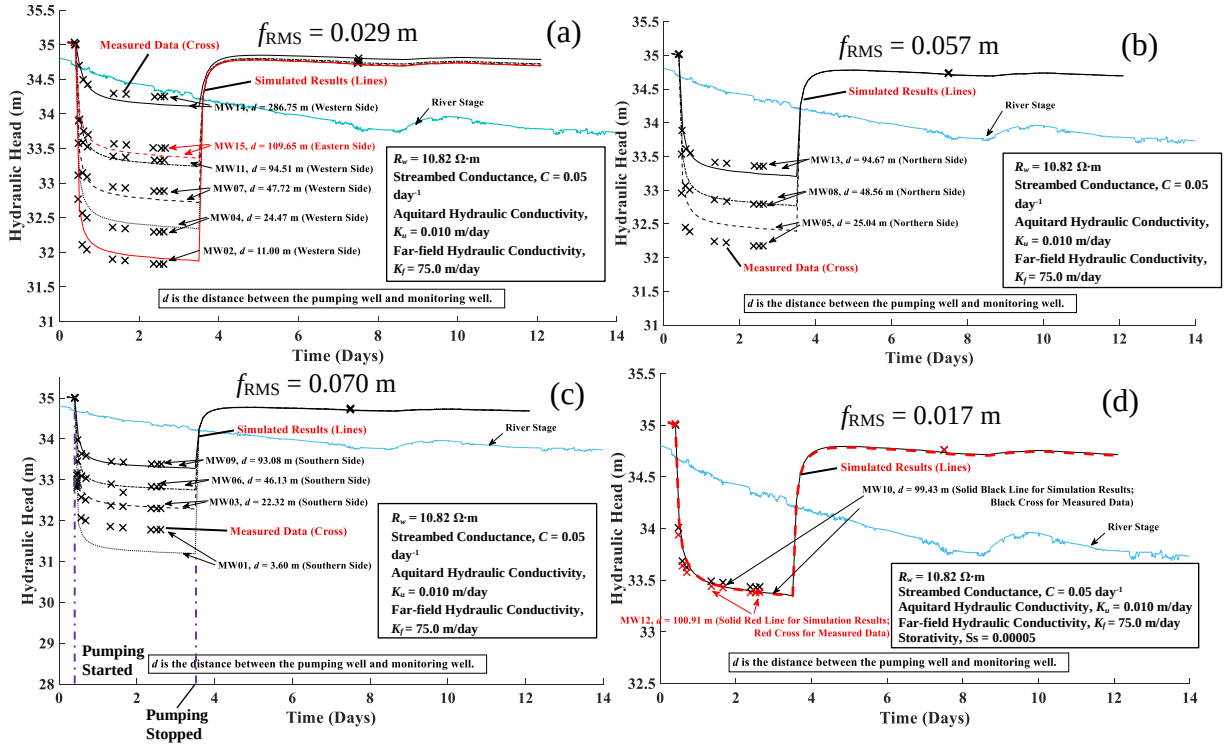

Figure 3.4. The best-agreed simulation results (lines) at the monitoring wells in the cross section (a) perpendicular, (b) and (c) parallel to the river and (d) at ordinary locations.

The hydraulic head of the aquifer was initially higher than the river stage (blue line in Fig. 3.4) but quickly dropped below that after the onset of the pump. When the extraction of GW stopped, the hydraulic head of aquifer restored quickly and surpassed the river stage almost immediately. The pumping rate was not sufficiently strong to induce sharp hydraulic head

drawdowns to desaturate the aquifer. The lowest hydraulic head collected from the monitoring wells was 31.90 m (MW01; Fig. 3.4c), which was higher than the top of aquifer (31.43 m). However, the simulation results revealed that the aquitard was in a variably saturated condition during the whole process. Some portions of the aquitard were desaturated.

The calibrated pore-water resistivity (R_w = 10.82 Ω.m) is in the typical range for aquifer, which is from 2.7 – 256.9 Ω.m (George et al., 2017). The calibrated hydraulic conductivity of the far-field aquifer, 75.0 m/day, is a typical value of sand, and that of aquitard (0.010 m/day) is in the range of clay. The calibrated spatial distribution of hydraulic conductivity is plotted in Fig. 3.5. Fig. 3.5a shows the cross section passing the pumping well and parallel to the river (x = 0.0 m). Fig. 3.5b is the result of an $x – y$ plane at z = 21.53 m. The hydraulic conductivity of the near-field aquifer varies from 10 to 200 m/day. A high-permeable zone can be clearly seen surrounding the pumping well, and the hydraulic conductivity is about 170 m/day. By considering the heterogeneity, the calibration results of hydraulic-head drawdowns, particularly for those close to the pumping well, are significantly improved compared to tests under the assumption of a homogenous aquifer (the simulations results of the homogenous aquifer are in Appendix 4).

The working hypothesis of this calibration is that the hydraulic conductivity of the aquitard has a limited impact on the simulation results. To test its validity, sensitivity analysis of K_u is conducted and presented in Fig. 3.6, which shows the variation of f_{RMS} with K_u. The minimal value of f_{RMS} is 0.048 m when K_u is the calibrated value, 0.010 m/day. When increasing K_u to 0.012 m/day or decreasing K_u to 0.008 m/day, the increment of f_{RMS} is less than 0.001 m (Fig. 3.6a), indicating a small change of the simulated GW drawdowns. When K_u further increases to 0.015 m/day or decreases to 0.005 m, f_{RMS} is found to be smaller than 0.050 m (Fig. 3.6), which is close

to the minimal f_{RMS} (= 0.048 m), proving the hypothesis that the hydraulic conductivity of aquitard does not significantly affect the pump-induced drawdown processes.

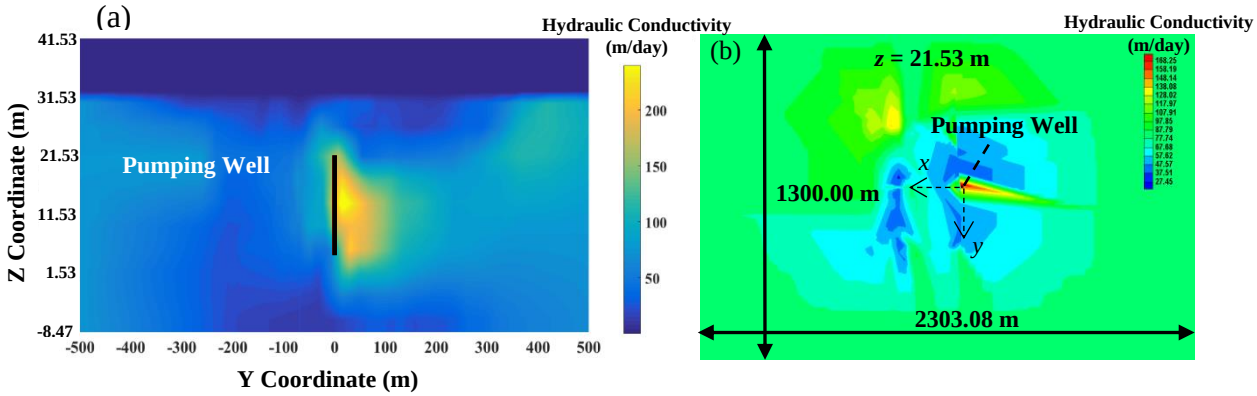

Figure 3.5. The spatial distribution of hydraulic conductivity with R_w = 10.82 Ω.m (a) of the cross section passing the pumping well and parallel to the river (x = 0.0 m) and (b) in x – y plane view at z = 21.53 m.

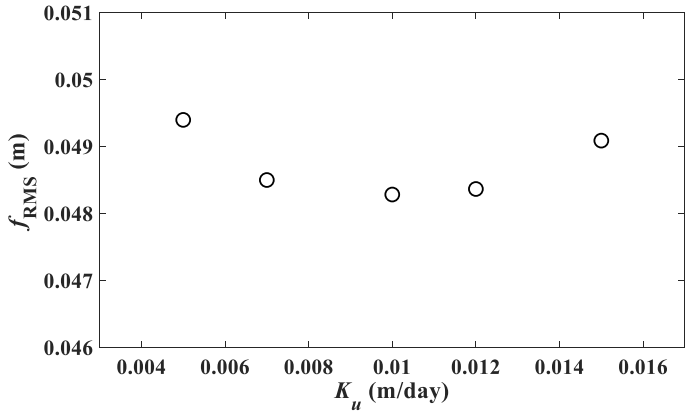

Figure 3.6. The variation of f_{RMS} with the hydraulic conductivity of the aquitard, K_u.

CHAPTER IV

RAPID ESTIMATION OF TIME-VARYING STREAMBED CONDUCTIVITY

4.1 Objectives and Hypotheses

This chapter aims at developing a model that can estimate time-varying streambed conductivity with a high temporal resolution during flooding periods. The working hypotheses are: (a) the time-varying streambed conductivity can be estimated through the inverse calculation of GW responses to flood-wave fluctuations; (b) although the estimation model is developed for a homogenous aquifer, it is still applicable to heterogeneous conditions when choosing an appropriate value to represent the heterogeneity field.

4.2 Methodology

4.2.1 Overview

The basic idea of this study's model is similar to the method described in Gianni et al. (2016) and Xian et al. (2020) though differed by the status of the stream-aquifer connection. Their models focused on an aquifer fully penetrated by an alluvial river. However, in certain areas, such as the Mississippi Delta, typically, rivers partially penetrate aquifers, and in some regions almost sit on aquifers (Ackerman, 1996), which is the case of the Money experimental site. The analytical solution of Zlotnik and Huang (1999) is therefore adopted to develop a new estimation model.

4.2.2 Flood-wave Response Model

The conceptual model is shown in Fig. 4.1, where the aquifer is divided into two zones: Zone I is the aquifer confined by the alluvial river, and Zone II is unconfined. The origin is located at the river centerline, and the coordinate is set up as Fig. 4.1 shows. Since both the domain and boundary conditions are symmetric, so is the GW flow. The analytical solution can therefore be either developed for the right or left side and then mirrored to the other. In the beginning, both the river stage and the GW hydraulic head are at the same level h_0 (initial condition). With the assumption of the Dupuit flow, GW responses to SW fluctuations can be described by a 1-D equation, which is the combination of Darcy's law and mass conservation. For Zone I, the governing equation is:

$$s\frac{\partial S_{\mathrm{I}}}{\partial t} = T_{\mathrm{I}}\frac{\partial^2 S_{\mathrm{I}}}{\partial x^2} + \frac{K_r}{b'}\left(S - S_{\mathrm{I}}\right) \qquad 0 < x < w,\ t > 0 \tag{4.1}$$

where, t is time; w is half of river width; S is river-stage change computed as $h_0 - H(t)$, in which $H(t)$ is river stage at time t; s is storativity of Zone I; T_{I} is transmissivity of Zone I; S_{I} is drawdown of Zone I that is computed as $h_0 - h_{\mathrm{I}}(t)$, where $h_{\mathrm{I}}(t)$ is GW hydraulic head of Zone I at time t; K_r is streambed conductivity and b' is streambed thickness. Since the GW flow is symmetric, the boundary condition at $x = 0$ is:

$$\frac{\partial S_{\mathrm{I}}}{\partial x}\Big|_{x=0} = 0 \tag{4.2}$$

The governing equation for Zone II is written:

$$s_y\frac{\partial S_{\mathrm{II}}}{\partial t} = T_{\mathrm{II}}\frac{\partial^2 S_{\mathrm{II}}}{\partial x^2} \qquad x > w,\ t > 0 \tag{4.3}$$

where, s_y and T_{II} are specific yield and transmissivity of Zone II, respectively. An assumption was made in the analytical model that the aquifer is infinitely long, and the far-side lateral boundary has no impact on the GW flow, so its drawdown is constantly zero:

$$S_{II} = 0 \qquad x = \infty,\ t > 0 \tag{4.4}$$

Considering the continuity of the hydraulic head and mass between Zone I and II, the boundary condition at the interface between Zone I and II is set:

$$S_I = S_{II}, T_I \frac{\partial S_I}{\partial x} = T_{II} \frac{\partial S_{II}}{\partial x} \qquad x = w,\ t > 0 \tag{4.5}$$

Zlotnik and Huang (1999) derived an analytical solution for Eqs. 4.1-4.5, where the Stehfest (1977) algorithm of numerical inverse Laplace transform was used. However, conducting a numerical inverse Laplace transform is typically not preferred owing to the concerns of numerical errors and instability. For a special case, in which the storativity of Zone I is neglected (s = 0.0), without using the Laplace transform, an exact solution of the GW head in Zone II responding to a unit step function of the river stage can be derived (Zlotnik and Huang, 1999):

$$S_{II}(\bar{x},\bar{t}) = \operatorname{erfc}\left(\frac{\bar{x}-1}{2\sqrt{\bar{t}}}\right) - \exp\left[\xi\left(\bar{x}-1\right) + t\xi^2\right]\operatorname{erfc}\left(\frac{\bar{x}-1}{2\sqrt{\bar{t}}} + \xi\sqrt{\bar{t}}\right) \tag{4.6}$$

where,

$$\bar{x} = \frac{x}{w}, \bar{t} = \frac{T_2 t}{s_y w^2}, \beta = \frac{T_I}{T_{II}}, \gamma = \frac{K_r w^2}{b' T_{II}}, \omega = \sqrt{\frac{\gamma}{\beta}} \tag{4.7}$$

and

$$\xi = \omega \tanh \omega \tag{4.8}$$

Since the storativity of the confined aquifer is usually small, which is around 10^{-5}, it is reasonable to simplify it as zero and neglect the associated terms. The impact of this simplification was found negligible when calculating the GW hydraulic heads of Zone II (Bolster et al., 2001), proving its applicability to real cases. This analytical solution (Eqs. 4.6-4.8) was therefore adopted in this study as the flood-wave response model.

In summary, six parameters are required to compute GW responses to flood waves, which are: (a) the distance between the observation well and the river centerline, *d*; (b) the transmissivity and specific yield of Zone II, T_{II}, s_y; (c) the half width of the river, *w* and (d) the hydraulic conductivity of the streambed, K_r, and its thickness, *b*'. The hydraulic properties of the streambed (pattern d) is usually represented by one parameter, streambed conductance, $C = K_r / b'$ (Hantush, 1965).

To obtain the temporal aquifer response to river-stage fluctuations, a convolution method (Hall and Moench, 1972) is adopted as:

$$S'_{II}(x,t) = \int_0^t F'(\tau) S_{II}(x, t-\tau)\, d\tau \tag{4.9}$$

where, $S'_{II}(x, t)$ is the drawdown at time *t*, S_{II} is the drawdown caused by a unit fluctuation of the river stage (Eq. 4.6), $F'(\tau)$ is the magnitude of the river-stage variation, and τ is the variable of integration. The discrete form of Eq. 4.9 is (Barlow et al., 2000):

$$S'_{II}(x, n\Delta t) = \sum_{k=1}^{n-1} \int_{k\Delta t}^{(k+1)\Delta t} F'(u) S_{II}(x, n\Delta t - u)\, du \tag{4.10}$$

where, *n* is the number of discrete time steps with a constant length Δt, *k* is the index of summation, and *u* is the variable of integration. Assuming a linear variation of the function between two successive time steps, Eq. 4.10 can be written:

$$S'_{II}(x, n\Delta t) = \sum_{k=1}^{n-1} \frac{\Delta t}{6} \left(F'_k S_{II,n-k} + F'_{k+1} S_{II,n-k+1} + 2F'_k S_{II,n-k+1} + 2F'_{k+1} S_{II,n-k} \right) \tag{4.11}$$

where, the magnitude of the river-stage variation can be computed by a finite difference scheme:

$$F'_k = \frac{F\left[(k+1)\Delta t\right] - F(k\Delta t)}{\Delta t} \tag{4.12}$$

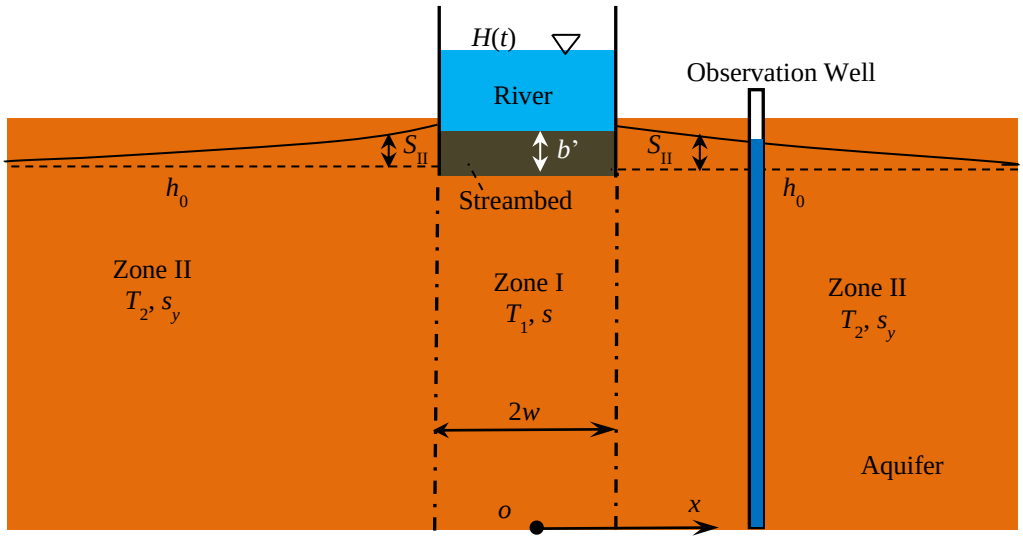

Figure 4.1. The conceptual model of the analytical solution of Zlotnik and Huang (1999).

4.2.3 Estimation of Time-varying Streambed Conductivity

For a static streambed conductivity, estimating its value can be achieved through minimizing the Sum of Square Error (SSE) between the computed GW heads from the analytical solution (Eq. 4.11) and the measured GW heads (von Asmuth et al., 2008):

$$\mathrm{SSE} = \sum_{i=1}^{n_1} \left(h_{\mathrm{obs},i} - h_{\mathrm{cal},i} \right)^2 \tag{4.13}$$

where, n_1 is the total number of the measured hydraulic head; $h_{\mathrm{obs},i}$ and $h_{\mathrm{cal},i}$ is the measured and calculated GW hydraulic head at time step i, respectively.

When encountering a time-varying streambed conductivity, prior to estimating its values through optimization, the time-series data need to be preprocessed. The principle is that although the streambed conductivity changes with time, in a certain period, the variation is so slow that it can be regarded as steady. As Fig. 4.2 shows, the whole period of concern can therefore be disassembled into several sub-periods, called Parameter Optimization Window (POW), during

which the streambed conductivity can be treated as constant. These sub-periods are consecutive while partially overlapped to have an oversampling effect. Inside each POW, the Levenberg-Marquardt Algorithm (LMA) (Levenberg, 1944; Marquardt, 1963) is applied for the minimization of the SSE value (Eq. 4.13) to obtain the corresponding streambed conductivity. The POW is then moved forward with a time step, called POW shift, to proceed with the calculation for the next sub-period. The procedure is repeated until covering the whole period. This scheme is the same as that proposed by Gianni et al. (2016) and Xian et al. (2020), where the details of the workflow can be found.

In summary, to attain the time-varying streambed conductivity through the inverse of flood-wave responses, six input parameters are required: (a) the hydraulic transmissivity and specific yield of the aquifer (aquifer properties); (b) river width; (c) measured time series of the river stage; (d) measured GW hydraulic head variations from adjacent monitoring well(s) and (e) the distance(s) between the river centerline and monitoring well(s).

4.3 Validation of Estimation Model

As a newly emerging method, the viability and accuracy of estimating time-varying streambed conductivity through the inverse of flood-wave responses needs to be validated. It is best to have a set of field measurements as a reference for such a purpose. However, either the field data was collected with a low temporal resolution, such as weekly or monthly (e.g., Korus et al., 2020), or part of the required input data, e.g., the time series of GW hydraulic heads (Mutiti and Levy, 2010; Levy et al., 2011), were not gauged.

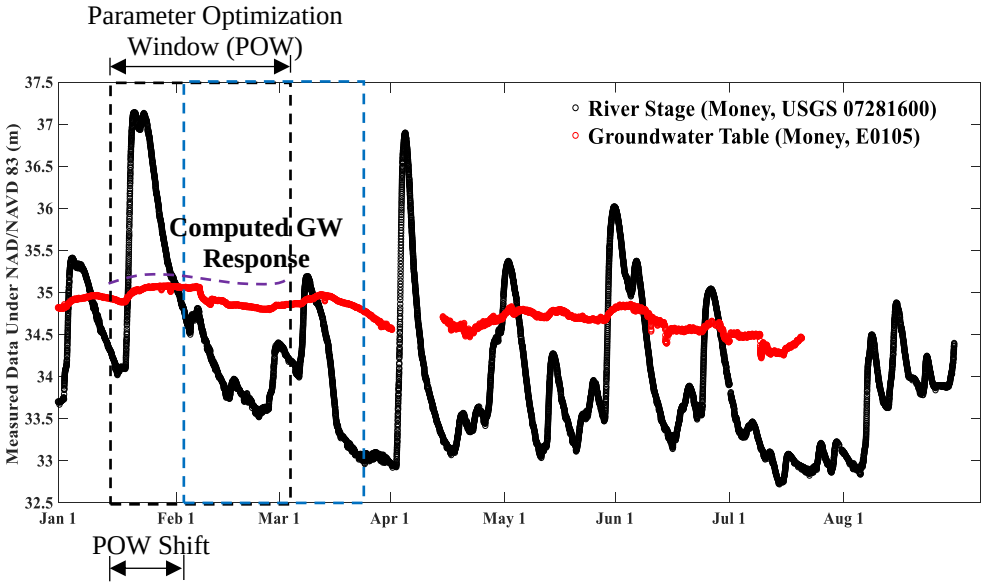

Figure 4.2. Scheme of the inverse of the flood-wave responses, in which Parameter Optimization Window (POW) and POW shift are shown. The black and blue dashed rectangles are used to mark two consecutive POWs and the purple dashed line represents the GW heads computed by the analytical solution (Eq. 4.6 & 4.11). The data shown here is from USGS gaging stations near Leflore County (Money), MS, USA, from January to August of 2017.

To circumvent this obstacle, another manner of validation was proposed and adopted by Gianni et al. (2016) and Xian et al. (2020), in which the numerical model was applied to synthesize the data for validation. By imposing a set of designated river-stage fluctuations and time-varying streambed conductivity on a numerical model, the temporal variations of the GW head at the target monitoring well(s) can be simulated. With the synthetic river stage and the simulated temporal variation of GW head as input data, the estimation model can be used to compute a time series of streambed conductivity, which will then be compared to the designated streambed conductivity to assess the accuracy of the estimation model.

In the validation part of both Gianni et al. (2016) and Xian et al. (2020), the scenario that the streambed conductivity declined from 0.1 to 0.001 $m.d^{-1}$ in 30 days while the flood wave fluctuated in 1 day was studied. The estimation model's capability in catching the transient

streambed conductivity was proven by this theoretical case. However, previous field measurements revealed that the time scales of the streambed conductivity and flood wave were close to each other (e.g., Mutiti and Levy, 2010; Levy et al., 2011; Tang et al., 2018). This was also evidenced by the calculation result of Xian et al. (2020) for the Arkansas River, in which the streambed conductivity and river stage varied at a similar pace. The estimation model's performance under this condition should be evaluated as well.

In this study, two cases were therefore chosen for the validation. The first case was similar to Gianni et al. (2016) and Xian et al. (2020), merely nuanced by the stream-aquifer connection. In the second case, the wavelengths of the flood and the streambed conductivity were both set to be 10 days. The details can be found in the following sections.

4.3.1 Validation Case I

The cross section of the validation case is the same as that conceptualized by the analytical solution (shown as Fig. 4.1). The simulation was conducted with CCHE3D-GW. Considering the symmetry of the domain and GW flow, only the right half of the aquifer was simulated. The thickness and hydraulic conductivity of Zone I was 48.0 m and 1.0 m/d, respectively, resulting in T_1 = 48.0 m^2/d, while those of Zone II was 50.0 m and 1.0 m/d, respectively, making T_2 = 50.0 m^2/d, and the river penetrate the aquifer by 2.0 m. The specific yield of Zone II, s_y, was set as 0.005. The river width was 40.0 m (w = 20.0 m), and the observation well was 40.0 m away from the river centerline. The riverbed thickness, b', was 2.0 m. The domain was set to be 5000.0 m long in the x direction, sufficing to approximate the infinite lateral extent assumption (Eq. 4.4). During the simulation period (60 days), the wavelength of the streambed conductivity was 30 days, in which the streambed conductivity decreased from 0.1 m/d to 0.001 m/d exponentially over the

first 29.99 days and then sharply leaped to the original value, 0.1 m/d, within 0.01 day (around 15 min) on the 30^{th} day, as Fig. 4.3a shows. The river stage followed a sinusoid function to fluctuate with time, where the wavelength was 1.0 day, the amplitude was 1.0 m, and the mean river stage was 52.0 m, demonstrated by the gray line in Fig. 4.3b. Initially, the stream and aquifer were at the hydrostatic equilibrium condition.

The aquifer was discretized by a three-layer mesh in the vertical (z) direction to fulfill the 1-D flow assumption. In the lateral (x) direction, three sets of uniform mesh with Δx = 2.0, 1.0 and 0.5 m were tested to achieve mesh-independent results. The simulated temporal variations of GW head were marked by the black, red and blue dotted line in Fig. 4.3b, respectively. Their fine agreements indicate that the mesh size, Δx = 1.0 m, is sufficient to produce convergent result, and therefore adopted as an input data for the estimation model. The simulation results also reveal that despite being imposed with a periodical river-stage fluctuation, GW response gradually attenuates as the streambed conductivity declines. Near the 30^{th} and 60^{th} day when the streambed is practically impermeable (1.0×10^{-3} m/d), the magnitude of the GW reaction is close to zero, illustrating that the streambed conductivity is a crucial parameter in controlling the GW-SW exchange.

After inputting the designated flood wave (grey line in Fig. 4.3b) and simulated GW responses (red dotted line in Fig. 4.3b) into the estimation model, the time-varying streambed conductivity can be computed, which is shown as black circles in Fig.4.4. The POW size and shift was set as 1.0 and 0.1 day, respectively, which were the same as the settings of Xian et al. (2020). The agreement between the estimated (black circles in Fig. 4.4) and actual time-varying streambed conductivity (red dashed line in Fig. 4.4) is quite good with a Root Mean Square Error (RMSE) of 0.0057 m/d and a Nash-Sutcliffe coefficient (NSE) of 0.94, proving the capability of the estimation

model in detecting the time-varying streambed conductivity under the circumstance considered here. Attributed to the LMA, a minimization scheme that is both robust and fast, the estimation model behaves quite well not only during the period that the streambed conductivity declines gradually and smoothly but also on the 30th day when a sudden increase takes place. This demonstrates that the model is applicable to the case that the streambed conductivity changes sharply and abruptly, which frequently occurs during storm events (Mutiti and Levy, 2010; Levy et al., 2011).

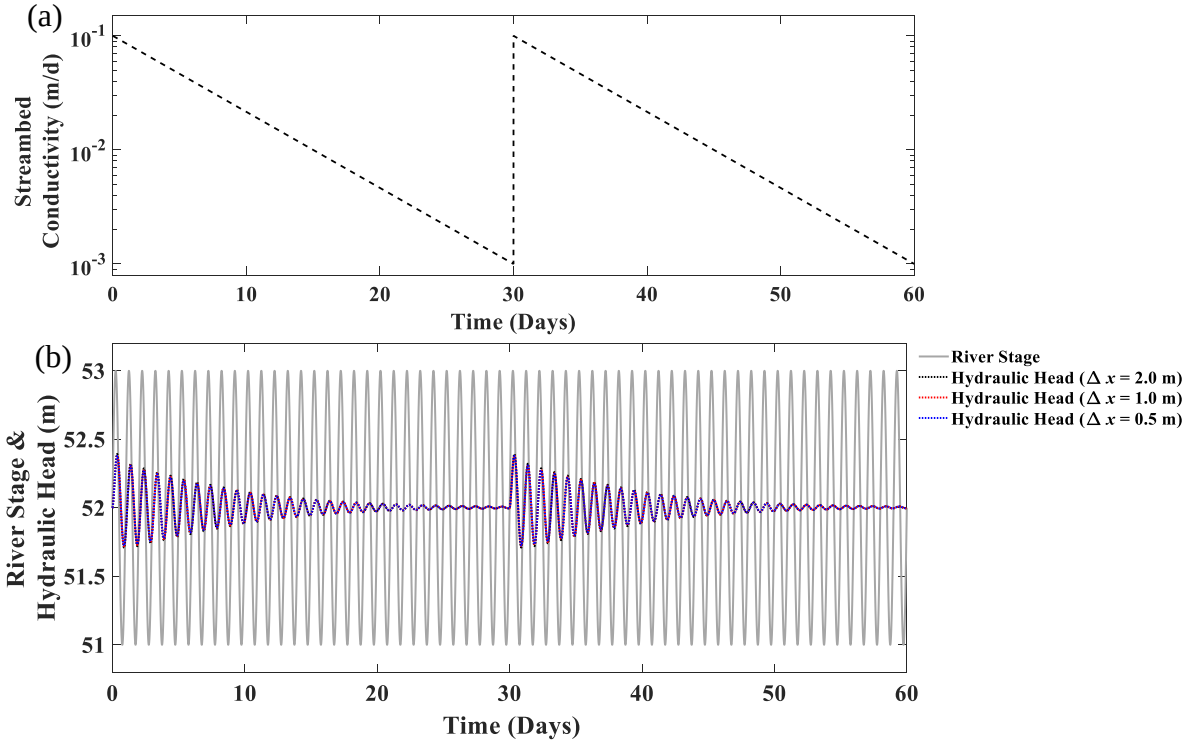

Figure 4.3. (a) Time series of the streambed conductivity in the synthetic case I and (b) the temporal variation of the river stage (grey line) and simulated GW hydraulic heads at the designated monitoring well with Δx = 2.0, 1.0 and 0.5 m (black, red and blue dotted line, respectively).

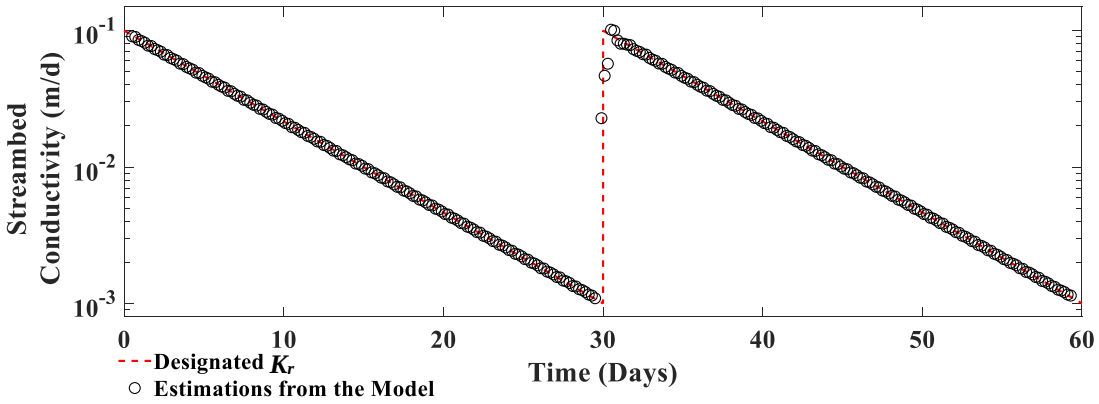

Figure 4.4. Comparisons between the designated time-varying streambed conductivity (red dashed line) and the computed one from the estimation model (black circles) with POW size = 1.0 day and POW Shift = 0.1 day.

4.3.2 Validation Case II

Case I considered a hypothetical scenario that the temporal variation of the streambed conductivity was much slower than the change of the river stage. However, in the real world, another situation that the streambed conductivity responses rapidly to the SW fluctuation has been frequently reported (e.g., Korus et al., 2020; Levy et al., 2011; Mutiti and Levy, 2010; Zhang et al., 2011). It contrasts with the assumption made by the validation case I. Validation case II is therefore dedicated to the scenario that the streambed conductivity and river stage changes at a similar pace.

To make the SW fluctuation more realistic, a formula from Cooper and Rorabaugh (1963) was applied to describe the flood wave:

$$H(t) = H_0 + H_p e^{-\delta(t-t_p)\frac{[1-\cos(\omega t)]}{[1-\cos(\omega t_p)]}} \tag{4.14}$$

where, H_0 is the river stage at low-stage condition, which is 52.0 m in this case; H_p is the maximum rise of river stage, set up as 2.0 m; t_p is the time to the peak of the flood, chosen as 5.0 days; ω is

the frequency of the flood, computed as $2\pi/t_d$, where t_d is the duration of the flood (10 days), and $\delta = \omega \cot\left(\omega t_p / 2\right)$ is the parameter controlling the degree of asymmetry of the flood.

The wavelength of the streambed conductivity was set up as 10 days as well, and the formula of calculation is similar to Eq. 4.14:

$$\log\left[K_r\left(t\right)\right] = \log\left(K_{r,0}\right) + \log\left(K_{r,p}\right) \cdot e^{-\delta\left(t-t_p\right)\frac{\left[1-\cos\left(\omega t\right)\right]}{\left[1-\cos\left(\omega t_p\right)\right]}} \tag{4.15}$$

where, the streambed conductivity during the low-stage condition, $K_{r,0}$, is 0.01 m/d; maximum rise of the order of magnitude of the streambed conductivity, $\log(K_{r,p})$, is 1; t_p is set to be 7.0 days in Eq. 4.15, reflecting the lagging phase between the spikes of the flood wave and the streambed conductivity (Drummond et al., 2017). The temporal variations of the river stage (blue line) and streambed conductivity (red line) in one wavelength (10 days) are illustrated in Fig. 4.5a.

The parameters of the aquifer, river, streambed thickness and mesh were the same as case I, and the monitoring well was located at 40.0 m away from the river centerline. The time-series variations of the imposed river stage and simulated GW responses during the whole simulation period (100 days) are shown in Fig. 4.5b, marked by the blue and red line, respectively. Aside from fluctuating in a sinusoidal shape, the temporal variation of the GW head is also found to have a general increasing trend. During the rising limb of the flood (first 5 days), the river stage is higher than the GW level, resulting in a stream-to-aquifer flow, which pushes the GW table to go up. When the flood peak passes, although the river stage starts to recede, in the early stage, the SW level is higher than the GW head, so the flow is still from the stream to aquifer. The rise of the GW head continues until the later stage of the recession when the river stage becomes lower than the GW head. Despite imposing a symmetric flood wave, within one wavelength period, the

duration that the aquifer gains water from the stream is longer than the duration it loses, which therefore causes a net increase of the GW head.

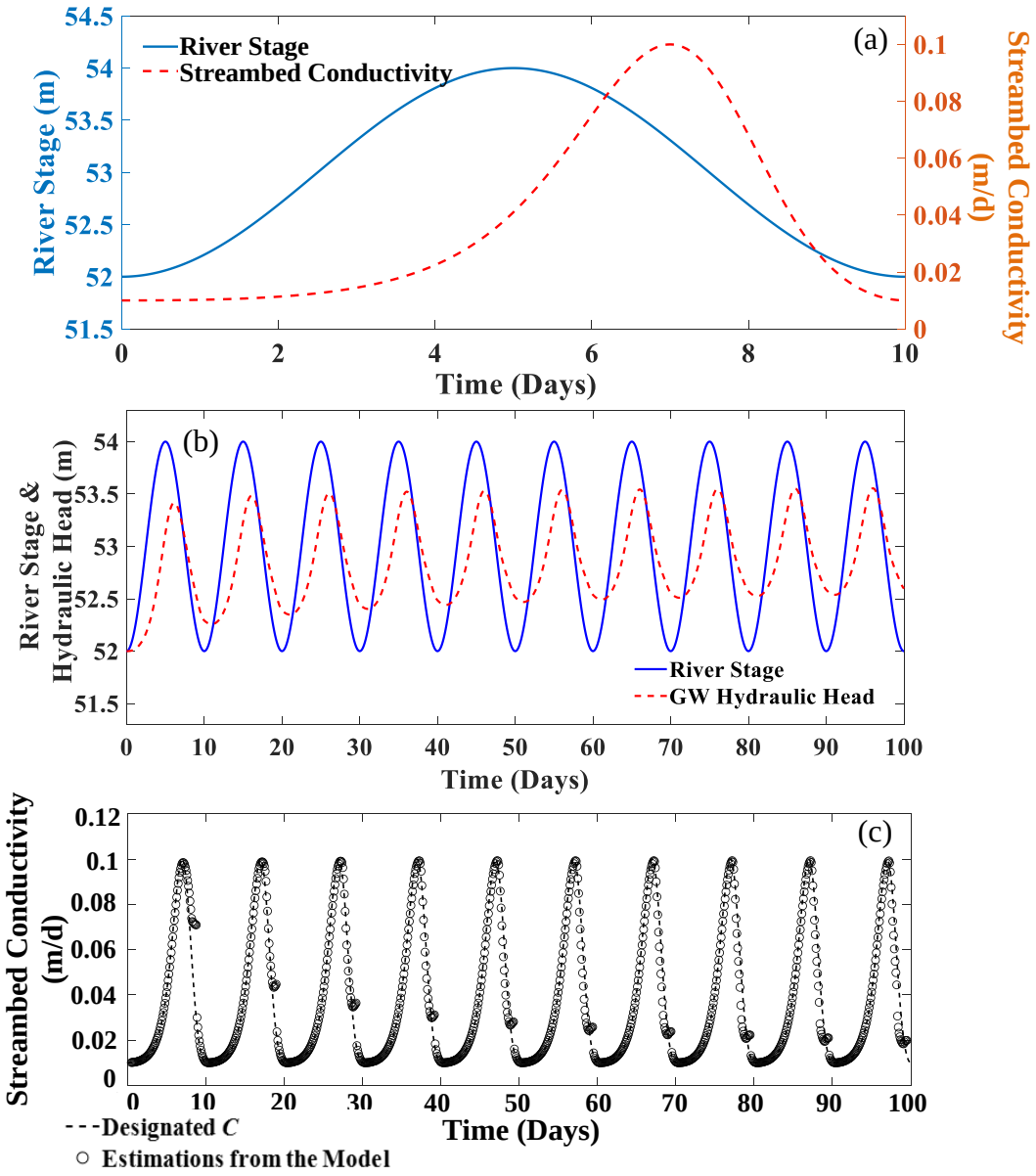

Figure 4.5. The temporal variation of (a) the flood wave (blue line, left axis) and streambed conductivity (red line, right axis) within one wavelength (10 days); (b) flood wave (blue line) and GW hydraulic head at the designated monitoring well (red line) and (c) designated (dashed line) and computed (circles, POW size = 0.8 day and POW shift = 0.1 day) streambed conductivity.

The flood wave and GW response presented in Fig. 4.5b were then imposed on the estimation model. The POW size and shift was 0.8 and 0.1 days, respectively. The comparison between the designated and computed time-varying streambed conductivity is shown as Fig. 4.5c. It can be seen that the estimated time series agree well with the actual time series with an RMSE of 0.01 m/d and an NSE of 0.88. This indicates that the estimation model is also robust and efficient for the case, where the streambed conductivity and river stage change at a similar pace. As it was elaborated by Gianni et al. (2016), the estimation model was sensitive to the POW size. The detailed sensitivity analysis is presented in the next section.

4.4 Sensitivity Analysis of POW Size

POW size is an important input parameter for the estimation model though it is determined empirically due to the lack of quantitative studies. Gianni et al. (2016) used multiple POW sizes for their validation case, and concluded that the smaller the POW size, the better the model could capture the transience in the streambed conductivity. However, the quantitative effect of the POW size on the calculation result has yet to be studied. Moreover, the sensitivity analysis of Gianni et al. (2016) focused on the case that the temporal variation of the streambed conductivity was much slower than the river-stage fluctuation. A more commonly encountered case, which is shown as the validation case II in this study, has not been analyzed. To bridge these gaps, a sensitivity analysis of the POW size devoted to the validation case II is conducted and presented here.

The basic parameters of the aquifer and river, and the time series of the river stage and GW responses were the same as those shown in section 4.3.2. 17 POW sizes, ranging from 0.1 (1% of the wavelength) to 12.0 days (120% of the wavelength) were chosen to cover a broad range of scenarios. Part of the calculation results are shown in Fig. 4.6a, where the calculated time-varying

streambed conductivities are marked by dots with different colors, and the actual streambed conductivity is represented by the black sold line. From a visual comparison, it can be found that the results with the POW size of 0.1, 0.5 and 1.0 days (black, red and blue dots in Fig. 4.6a, respectively) almost coincide with the actual variation but the results under POW size = 5.0 and 8.0 days (green and cyan dots in Fig. 4.6a, respectively) substantially deviate from the actuality. This visually shows that a smaller POW size can better detect the temporal variation of the streambed conductivity.

The estimation model assumes that the streambed conductivity is constant inside each optimization window; however, when the POW size is set too long, it cannot capture a strong temporal variation of the streambed conductivity, resulting in a large error of the calculated result. For instance, in this case, when POW size is 5.0 days, it assumes that the streambed conductivity is static during this period. However, the reality is that the variation of the streambed conductivity is so fast (red line in Fig. 4.5a) that it cannot be represented by a constant value in each 5 days. The estimated result with POW = 5.0 day is therefore highly compromised and quite dissimilar to the actual time-varying streambed conductivity.

With a smaller POW size, the details of the temporal variation of the streambed conductivity can be better traced, making the calculated result closer to the actuality. However, the oscillations of the estimated result should be concerned when applying a short optimization period. This can be observed in Fig. 4.5c (circles) that when POW size is equal to 0.8 days, some fluctuations exist in the estimated time-varying streambed conductivity though the general trend agrees well with the actual variation. The same phenomenon was reported by Gianni et al. (2016) as well, in which the estimated result from a small POW size oscillated drastically. As it was

explained by Gianni et al. (2016), the oscillation was caused by the assumption made by the convolution method but the fluctuation of the result in this study is not as strong as that of Gianni et al. (2016). One possible explanation is because of the implemented minimization algorithm. A gradient descent algorithm was adopted by Gianni et al. (2016). Although simple and easy for use, when applying this algorithm, the problem of instability and difficulty of convergence is frequently encountered, making it rarely applicable for real cases. In this study, a more sophisticated algorithm, LMA, was used. It bolsters the capability and stability of the estimation model in searching for the streambed conductivity that can minimize the SSE (Eq. 4.13), insuring the accuracy of the calculated result. When shortening the POW size, the number of measured data for the minimization reduces correspondingly, challenging the robustness of the optimization algorithm. Under this condition, a simple gradient descent algorithm would fail to converge to the minimum of SSE, resulting in a spurious oscillation, while LMA could manage this problem of convergence, attenuating the fluctuations.

To quantify the impact from the POW size on the estimation result, a dimensionless mean residual (DMR) is proposed:

$$\mathrm{DMR} = \frac{\sum_{i=1}^{M} \left| \frac{K_{r,D,i} - K_{r,E,i}}{K_{r,D,i}} \right|}{M} \tag{4.16}$$

where, M is the total number of the estimated results; $K_{r,D,i}$ and $K_{r,E,i}$ is the actual and estimated streambed conductivity at time step i, respectively.

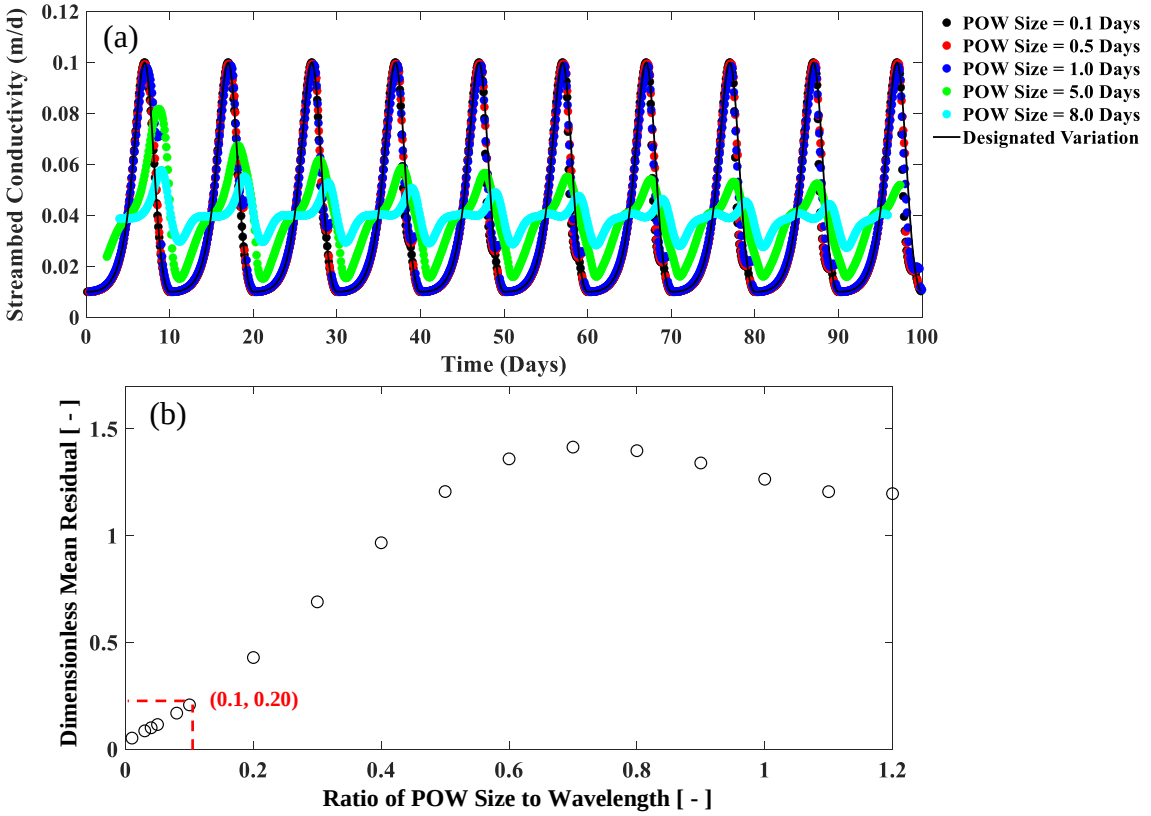

Figure 4.6. (a) Comparisons between the estimated temporal variations of the streambed conductivity with different POW sizes (colorful dots) and the designated variation (black solid line) and (b) the variation of the dimensionless mean residual with the ratio of POW size to the wavelength.

The variation of DMR with the ratio of the POW size and the wavelength is plotted as Fig. 4.6b. It could be found that DMR decreases linearly with the POW size in the region of the POW size < 70% of the wavelength, indicating that a smaller POW size will improve the general accuracy of the calculated result, and this effect is approximately linear. Another noticeable phenomenon is that DMR is generally invariant to the variation of the POW size when the optimization window is longer than 70% of the wavelength, which is because a larger POW size significantly smooths out the details of the time-varying streambed conductivity (see the results of POW size = 5.0 and 8.0 days in Fig. 6a). Once the POW size surpasses a threshold (70% of the

wavelength in this study), the smoothing effect is stabilized, resulting in an almost constant DMR value in this region, illustrated by the plateau in Fig. 4.6b.

Meanwhile, for the case studied here, it could be observed that when the POW size is 10% of the wavelength (corresponding to POW size = 1.0 day), the DMR is 0.20, meaning that on average, the estimated results deviate from the actual values for around 20%. 10% of the flood-wave length is therefore chosen as an empirical criterion to determine the POW size in this study, i.e., the POW size should be smaller than 10% of the flood-wave length.

4.5 Applicability of Estimation Model to Heterogeneous Aquifer

Although the inverse of flood-wave responses has been widely used to estimate both the steady (Obergfell et al., 2016; von Asmuth et al., 2002; von Asmuth et al., 2008) and transient (Gianni et al., 2016; Xian et al., 2020) streambed conductivity, due to the adopted 1-D analytical solution, all of them assumed a homogeneous aquifer. However, this assumption can rarely be met in the real world. Heterogeneity is a prevalent feature among alluvial aquifers, and its impact on stream-aquifer interaction has been broadly studied (Irvine et al. 2012; Laube et al., 2018; Tonina et al., 2016). For a real heterogeneous aquifer, in order to apply the flood-wave response model (Zlotnik and Huang, 1999), an equivalent value should be found to represent the distribution of the hydraulic conductivity. Meanwhile, since the flood-waver response model is developed for a homogeneous aquifer, its applicability under the heterogeneous scenario is in doubt.

This section is therefore aimed at (a) determining what hydraulic conductivity value should be used to represent a heterogeneous aquifer when using the estimation model and (b) examining the applicability of the estimation model to a real heterogeneous aquifer, and quantifying the errors resulted from the assumption of a homogeneous aquifer.

4.5.1 Parameters of Heterogeneous Aquifer

As it was elaborated in Chapter 3, the measured sediment resistivity can be transferred into its hydraulic conductivity by an empirical formula through the calibration. Fig. 4.7 shows the distribution of the converted hydraulic conductivity of the measured cross sections, which is the basis to generate the heterogeneity field.

When studying GW-SW interactions, the heterogeneity of the aquifer that is perpendicular to the SW flow direction is of primary concern (Zhou et al., 2018), so in this study, the heterogeneity of the aquifer was only considered in the *x*-*z* cross section. Along the *y* direction (the flow direction), the aquifer was assumed homogeneous. Although some errors can arise due to this assumption, the problem can be significantly simplified, and the first-order controls of the exchange process can be captured.

The experimental variograms of hydraulic conductivities (m/s) of the aquifer in logarithmic scale were plotted in two perpendicular directions, which was 45° and -45° to the horizontal plane, respectively, and shown as Fig. 4.8a and b. In general, the experimental variograms of these two directions are quite similar to each other, both of which approach to the same sill value, 1.0 m^2, at the distance of around 40.0 m, evidencing that the sediment stratification is not very strong in this region, and the variogram model can be assumed direction-independent. A spherical model is therefore used to fit both of them:

$$\gamma\left(h_{\mathrm{dis}}\right)=\frac{3}{2}\cdot\frac{h_{\mathrm{dis}}}{40.0}-\frac{1}{2}\cdot\frac{{h_{\mathrm{dis}}}^{3}}{40.0^{3}},\quad h_{\mathrm{dis}}\le 40.0\ \mathrm{m} \tag{4.17a}$$

$$\gamma\left(h_{\mathrm{dis}}\right)=1.0,\quad h_{\mathrm{dis}}>40.0\ \mathrm{m} \tag{4.17b}$$

where, $\gamma(h_{\mathrm{dis}})$ is the variogram when the distance between two points is h_{dis}. This fitted model is shown as red dashed lines in Fig. 4.8a and b.

To find an equivalent value to represent the distribution of the heterogeneous hydraulic conductivity and quantify the impact of the homogeneous assumption, the Monte Carlo (MC) approach was adopted. 100 realizations of the heterogeneous log-conductivity field were generated by the Stanford Geostatistical Modeling Software (SGeMS, Remy et al., 2011) based on sequential Gaussian simulations (SGSIM), which were then imposed on the simulation of the heterogeneous aquifer-stream interaction. Two representative distributions of the hydraulic conductivity of the near-stream aquifer are shown in Fig. 4.8c and d, where the origin of the domain is set up at the river centerline. The heterogeneity of this aquifer is relatively strong, in which the variance of the ln (K) (in m/s) is 1.0 m^2, and the alternation of sand and clay can be clearly observed in Fig. 4.8c and d.

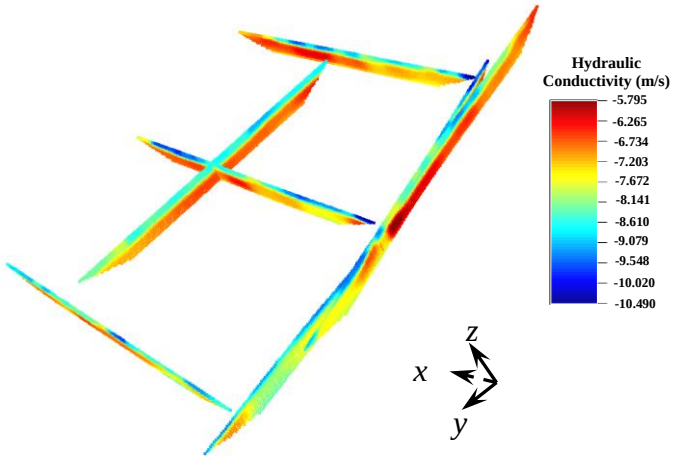

Figure 4.7. The distribution of the hydraulic conductivity of the measured cross sections, where the value is in a logarithmic scale.

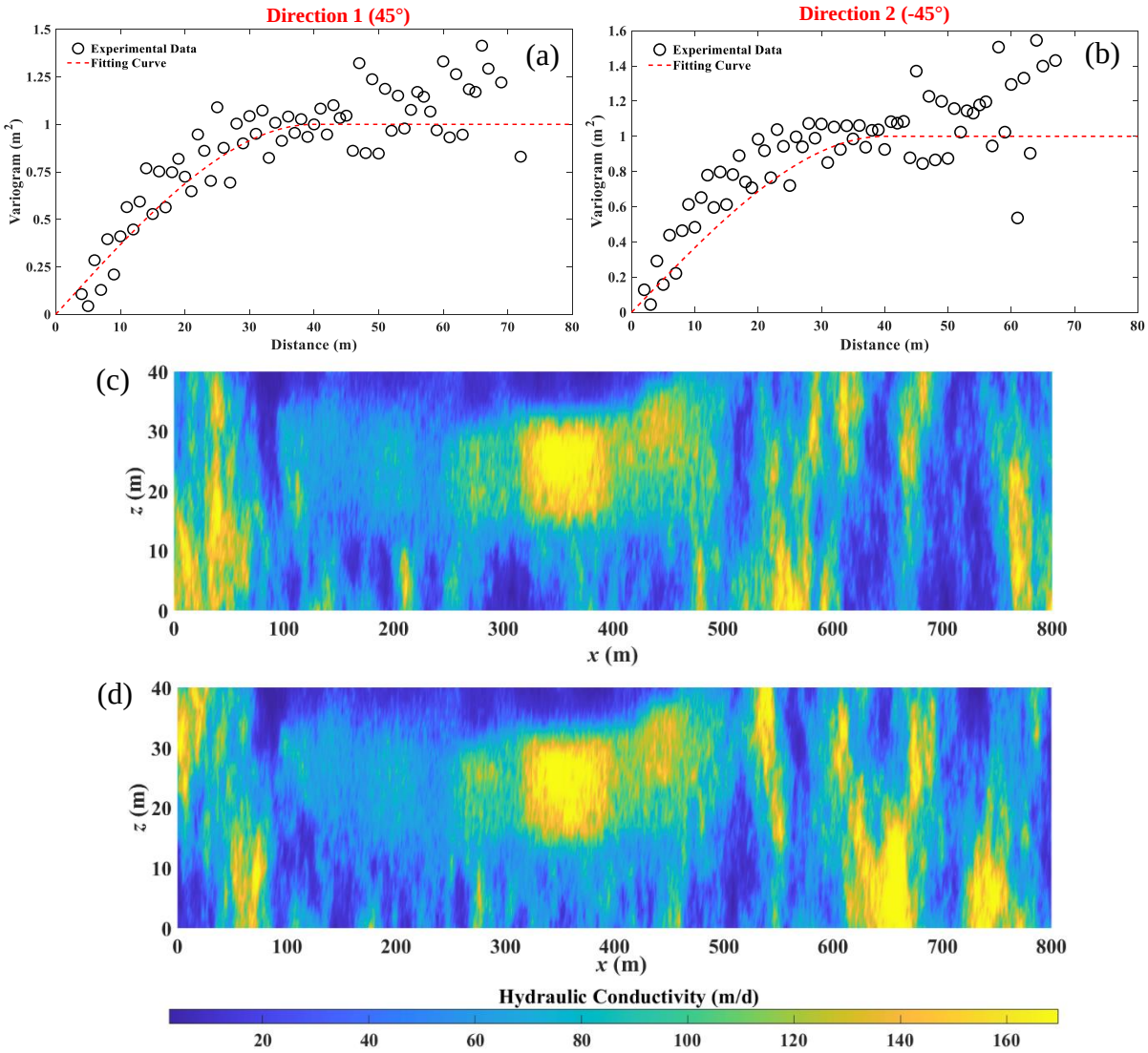

Figure 4.8. The experimental variogram of the hydraulic conductivities (m/s) of the aquifer in logarithmic scale (circles) and the fitting variogram model (red dashed line) in two primary directions, which is (a) 45° and (b) -45° to the horizontal plane, respectively, and (c) and (d) are two representative hydraulic conductivity distributions of the near-stream aquifer among the 100 realizations.

4.5.2 Analysis of Heterogeneous Aquifer-Stream Simulations

For the simulation of the heterogeneous aquifer-stream interaction, the conceptual *x*-*z* cross section is similar to the validation case II's. The aquifer and stream were set up according to the measured data and calibration results of the aquifer test shown in Chapter 3, in which the aquifer

was 40.0 m thick, its specific yield was 0.004, the river width was 42.0 m, and the monitoring well was 60.0 m to the river centerline. The heterogeneity field generated in section 4.5.1 was directly input into the numerical model to represent the distribution of the hydraulic conductivity of the aquifer. The mesh information and the imposed time series of the river stage and streambed conductivity were the same as the settings of the validation case II. The total simulation period was 60 days. The simulation was run for each realization, and the simulated time series of GW responses are illustrated by grey lines in Fig. 4.9a. It can be found that for each realization, the general trend of the simulation result is similar but the details differ.

For a Monte Carlo simulation, when assembling the results from abundant realizations, the mean value will be convergent to a constant, which is usually used as the representative result. In Fig. 4.9a, the ensemble (i.e., mean) results of 5, 25, 75 and 100 realizations (marked by the red solid, blue solid, cyan dashed and black solid lines, respectively) are presented. It could be found that the ensemble results of 75 and 100 realizations generally coincide with each other, indicating that 100 realizations are sufficient to achieve the convergence. The ensemble result of 100 realizations is therefore chosen as the basis for this analysis.

Meanwhile, it is noticeable that the simulated GW response curve of each heterogeneous realization is oscillatory but their ensemble results are generally smooth (Fig. 4.9a). When applying the inverse flood-wave response model to estimate the static streambed conductivity, a noise term rooted in the error of the measurement of the GW head has been taken into account (Von Asumth et al., 2002). The unsmooth GW response curve under a heterogeneous aquifer (grey lines in Fig. 4.9a) demonstrates that the heterogeneity would potentially be another source causing such a noise. Although not the objective of this study, the quantitative impact of the heterogeneity

on the noise would be a topic worthy of exploration.

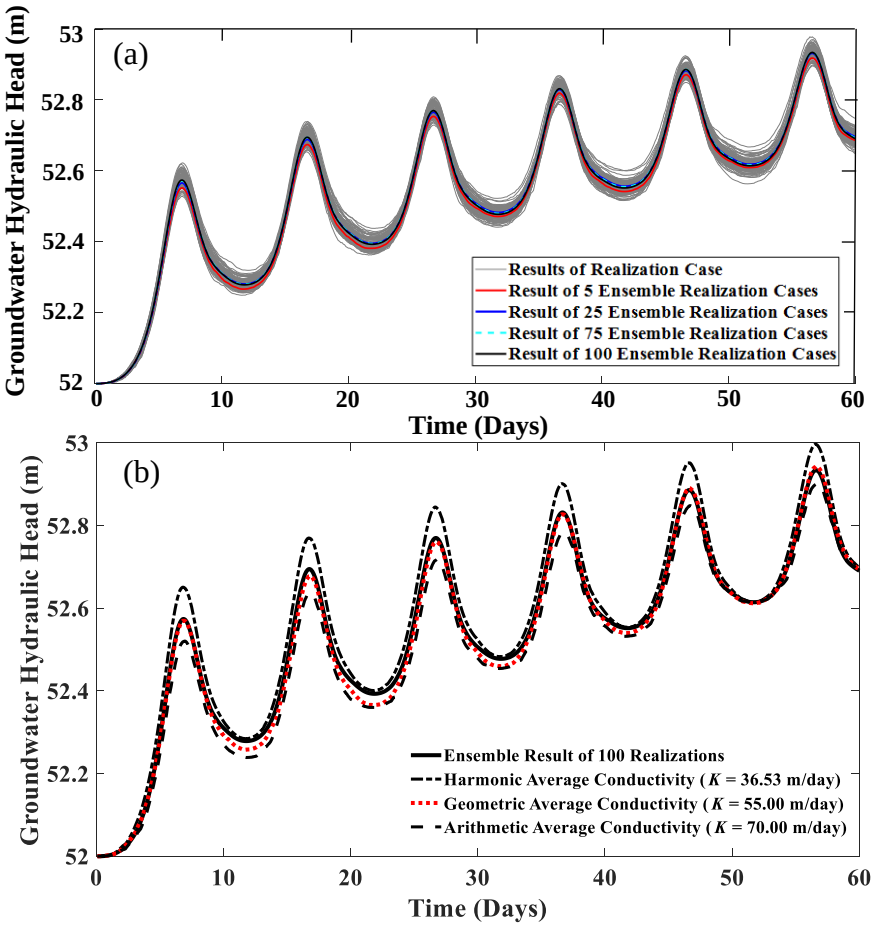

Figure 4.9. (a) The simulated temporal variation of the GW hydraulic head at the designated monitoring well of each heterogeneous realization (grey line) and the ensemble results (other lines). (b) The comparisons of the simulated GW responses at the monitoring well between the ensemble result of the 100 realizations and the results simulated by a homogeneous aquifer with the hydraulic conductivity computed from different averaged algorithms.

4.5.3 Algorithm for Equivalent Hydraulic Conductivity

In the flood-wave response model, the heterogeneity of the aquifer is not considered. An equivalent homogenous value must be chosen to represent the heterogeneous aquifer in order to apply the model. Three average algorithms that are commonly used for this purpose, which are harmonic, geometric and arithmetic averages, are examined here. It is found that the harmonic,

geometric and arithmetic-averaged hydraulic conductivity of the aquifer is 36.53, 55.00 and 70.00 m/day, respectively. They were imposed on the numerical model to simulate the GW response under the same condition as the realization cases. The results are shown in Fig. 4.9b, where the black dashed line, red dot line and black dash-dot line is used to mark the result of the harmonic, geometric and arithmetic-averaged hydraulic conductivity of the aquifer, respectively, and the black solid line denotes the ensemble result (basis result). It can be seen that among the three, the simulated GW response of the aquifer with the geometric-averaged hydraulic conductivity agrees best to the basis result, indicating that the geometric-averaged value is a better candidate to represent the heterogeneous aquifer.

To quantify the error arising from the assumption of a homogeneous aquifer, the root mean square (RMS) value between the simulated GW heads of the heterogeneous case (100 realizations) and the geometric-averaged case was computed:

$$\mathrm{RMS} = \sqrt{\frac{\sum_{i=1}^{N}\left(H_{\mathrm{realization},i} - H_{\mathrm{geometric},i}\right)^2}{N}} \tag{4.18}$$

where, N is the total number of the simulation result, and $H_{\mathrm{realization},i}$ and $H_{\mathrm{geometric},i}$ is the simulated GW hydraulic head of the realization (heterogeneous) and geometric-averaged case at time step i, respectively.

The histogram of the RMS is plotted in Fig. 4.10, which generally follows a skew normal distribution. The RMS values mainly range from 0.01 m to 0.02 m. When applying the estimation model to a field case in Switzerland, Gianni et al. (2016) chose the tolerance of SSE value (Eq. 4.13) as 0.1 m^2 for the minimization. Since their POW size was 7.0 days and temporal resolution of the measured GW head was 1 day, i.e., each optimization window included 168 measured

points, their criterion of the SSE value (0.1 m^2) is identical to 0.024 m of the RMS. It demonstrates that the vast majority of the discrepancies between the heterogeneous and homogenous (with the geometric-averaged hydraulic conductivity) results do not exceed the practical tolerance of the minimization, indicating that the errors resulted from the assumption of a homogeneous aquifer are acceptable. Hence, the inverse flood-wave response model is viable to estimate the time series of the streambed conductivity for a real heterogeneous aquifer.

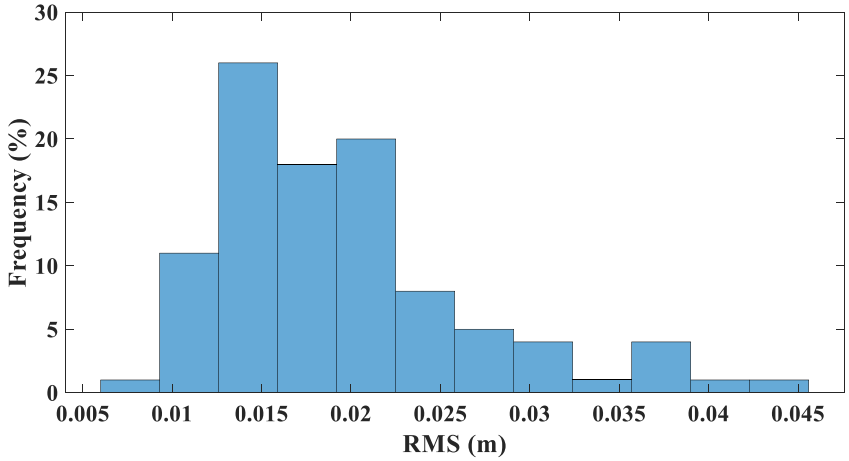

Figure 4.10. The histogram of the RMS between the simulated GW hydraulic heads of the 100 heterogeneous aquifers and the homogeneous aquifer with the geometric-averaged hydraulic conductivity.

4.5.4 Impact of Heterogeneity on Estimated Streambed Conductivity

In the previous part, it was concluded that when encountering a heterogeneous aquifer, using the geometric-averaged hydraulic conductivity to represent the aquifer in the estimation model resulted in an acceptable error. However, the question how the heterogeneity will affect the estimated streambed conductivity remains unanswered. To study this impact, the simulated GW response of each heterogeneous realization (grey line in Fig. 4.9a) and the designated river stage were imposed on the estimation model. The hydraulic conductivity of the aquifer was input as the geometric-averaged value, 55.00 m/day. The other input parameters were consistent with the

stream-aquifer simulations of section 4.5.2. The POW size was set as 0.8 days, which was smaller than 10% of the flood-wave length, and the POW shift was 0.1 days.

The estimated time-varying streambed conductivity for each heterogeneous realization is shown as grey line in Fig. 4.11a as the actual temporal variation is marked by the red dotted line. It can be found that the estimated temporal-variation curve of each heterogeneous realization is oscillatory, resulted from the fluctuations of the corresponding time series of the GW head (grey line in Fig. 4.9a). When averaging the estimated results of heterogeneous realizations, the ensemble time-varying streambed conductivity can be obtained, which is marked by the blue dashed line and the black solid line in Fig. 4.11a for 75 and 100 realizations, respectively. It can be found that the ensemble result of 75 and 100 realizations coincide very well with each other, evidencing that the convergence has been achieved. The ensemble result generally agree with the actual variation, indicating that the estimated time-varying streambed conductivity is sufficiently accurate.

To quantify the impact from the heterogeneity of the aquifer on the estimation result, the dimensionless mean residual (DMR) between the estimated and designated streambed conductivity is calculated (Eq. 4.16) as well. The histogram of DMR for all realization cases is shown in Fig. 4.11b, which generally follows a skew normal distribution and mainly locates between 0.08 and 0.14. It illustrates that the mean discrepancy between the estimated and actual time-varying streambed conductivity is smaller than 15% of the actual value. We can therefore conclude that the estimation model is applicable to the heterogeneous aquifer.

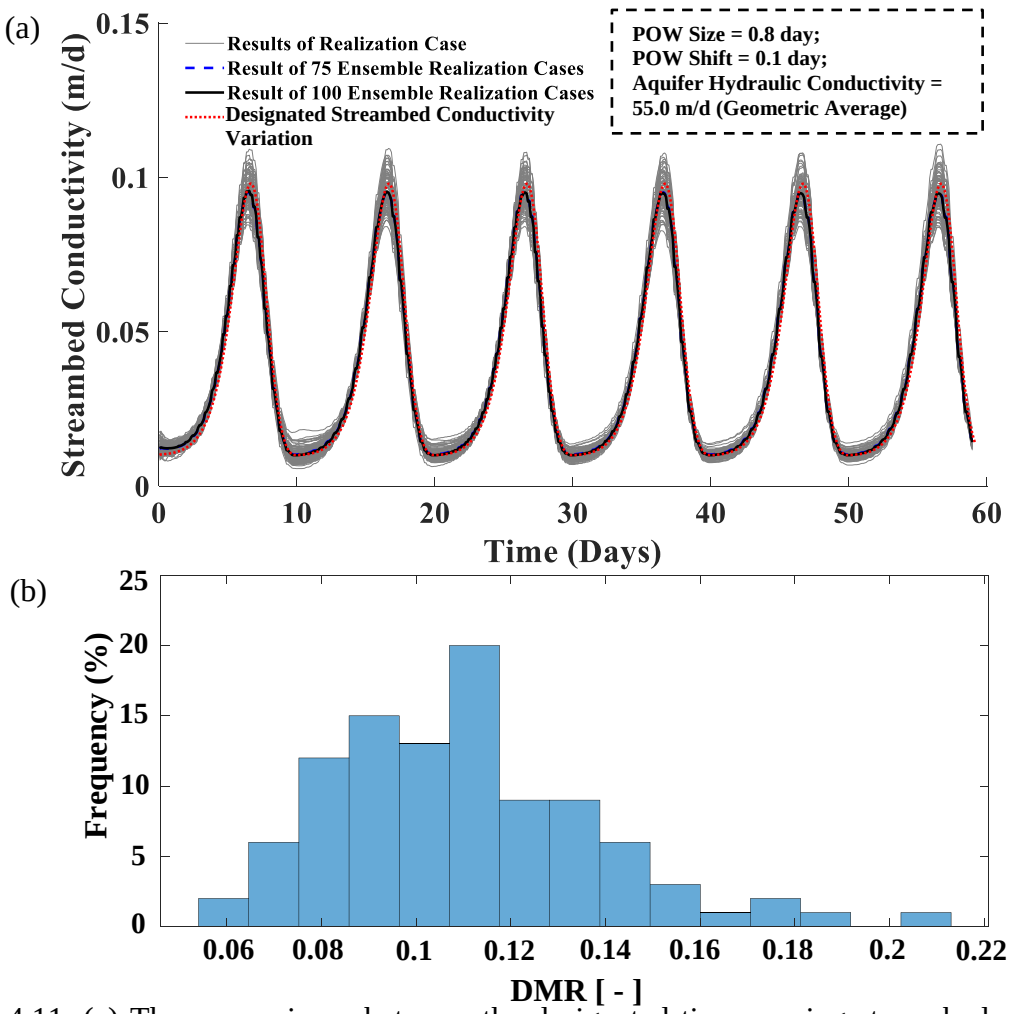

Figure 4.11. (a) The comparisons between the designated time-varying streambed conductivity (red dotted line) and the estimated one of each heterogeneous realization (grey line), where the ensemble result of 75 and 100 realizations is marked by the blue dashed line and the black solid line, respectively; (b) the histogram of DMS between the estimated and designated streambed conductivity.

4.6 Uncertainty Analysis of Estimation Model

The estimation model demands multiple input parameters pertinent to the properties of the aquifer, river and monitoring well, which would not be 100% accurate due to errors of the field measurement or laboratory analysis. As a result, the accuracy of the output, the estimated time-varying streambed conductivity, is not certain. Despite being developed and applied to field cases

(Gianni et al., 2016; Xian et al., 2020), the sensitivity of the estimation model to its input parameters has yet to be explored. To fill this gap, the uncertainty analysis was conducted in this study, in which the input data, (1) the hydraulic conductivity and (2) specific yield of the aquifer, (3) the river width and (4) the distance between the monitoring well and the river centerline, were studied. To facilitate the quantitative analysis, a parameter, dimensionless input error (IE), is proposed:

$$\mathrm{IE} = \frac{\text{Input Value} - \text{Actual Value}}{\text{Actual Value}} \tag{4.19}$$

The dimensionless IE of the aquifer hydraulic conductivity, specific yield, the river width and the distance between the monitoring well and the river centerline is denoted by IE_K, IE_{s_y}, IE_w and $\mathrm{IE}_{\mathrm{Distance}}$, respectively.

The basis for the uncertainty analysis is the hypothetical homogeneous aquifer-stream interaction shown in section 4.5, in which the geometric-averaged hydraulic conductivity was used to represent the aquifer. The imposed SW and GW fluctuations are the same, where the river stage is the blue line shown in Fig. 4.5b and the GW response is the red dotted line in Fig. 4.9b.

4.6.1 Hydraulic Conductivity of Aquifer

A broad range of the hydraulic conductivity from 5 m/d to 100 m/d was tested as the actual value was 55.0 m/d. The comparisons between the actual time-varying streambed conductivity (black solid line) and the estimated variations of four representative cases (K = 10.0, 25.0, 70.0 and 100.0 m/d) are presented in Fig. 4.12a. It can be found that when inputting a higher (or lower) value for the hydraulic conductivity of the aquifer, the estimated streambed conductivity will be larger (or smaller) than the actual value.

The ratio between the hydraulic conductivity of the streambed and the aquifer is reflected by the Grigoryev parameter, γ (Eq. 4.7), which determines the bank storage effect. Zlotnik and Huang (1999) found that the GW response to the flood wave was stronger under a higher value of γ, meaning that the estimated streambed conductivity will be increased (or decreased) correspondingly with a larger (or smaller) input aquifer hydraulic conductivity in order to keep the GW fluctuation the same.

Fig. 4.13a shows the variation of the DMR (Eq. 4.16) of the streambed conductivity with IE_K. It illustrates that in general, the estimation model is linearly sensitive to the uncertainty of the hydraulic conductivity of the aquifer. The maximum DMR is found to be around 0.5 when IE_K is -0.91 (input K = 5 m/d) or 0.82 (input K = 100 m/d).

4.6.2 Specific Yield of Aquifer

As a parameter usually assessed empirically, the precise measurement of the specific yield has long been neglected despite being frequently demanded by GW models, which in turn makes it quite uncertain. 7 sets of specific yield values, ranging from 0.001 to 0.008, were tested as the actual specific yield was 0.004.

The comparison between the actual time-varying streambed conductivity (black solid line) and the estimated results of four representative cases (s_y = 0.002, 0.003, 0.005 and 0.007) are shown in Fig. 4.12b. It can be found that when the input specific yield is larger (smaller) than the actual value, the estimation model will overestimate (underestimate) the streambed conductivity.

Specific yield is a parameter representing the storage capability of the aquifer. With a higher s_y value, the aquifer is able to accommodate the same amount of the SW infiltration/exfiltration with a smaller change of the GW head, resulting in a milder GW response.

Therefore, when the input specific yield is larger than the actual value, it demands a more permeable riverbed to push the same GW reaction, rendering an overestimated streambed conductivity. The same mechanism can be used to explain the underestimated streambed conductivity under a smaller input value of the specific yield.

Fig. 4.13b presents the variation of the DMR of the estimated and actual streambed conductivity with IE_{sy}, which generally follows a linear fashion. The maximum DMR is found to be around 0.5 when IE_{sy} is -1 or 1, i.e., when the disparity between the input and actual specific yield is 100% of the actual value, the consequential uncertainty of the estimated streambed conductivity will be 50% of the actual streambed conductivity.

4.6.3 River Width

River width is another parameter required by the estimation model. Not only would the field data contain some errors owing to the difficulty in measuring topographies, but also the dynamics of bank erosions and depositions could make the river width varied temporally. The estimation model was therefore tested with 8 sets of river-width values, covering the scenarios from 8.4 m to 75.6 m as the actual width is 42.0 m.

The comparisons between the actual time-varying streambed conductivity (black solid line) and the estimated streambed conductivities of four representative cases ($2w$ = 16.8, 33.6, 58.8 and 75.6 m) are shown in Fig. 4.12c. It can be observed that with a narrower (larger) input river width, the estimated streambed conductivity is higher (lower) than the actual streambed conductivity.

Unlike the scenario of a fully penetrating river considered by Gianni et al. (2016) and Xian et al. (2019), in our case, the river width has an impact on the intensity of the stream-aquifer interaction. When the river is wider, more aquifer areas will be confined and directly influenced

by SW fluctuations, which in turn amplifies the GW response. When imposing a larger river width on the flood-wave response model, a less permeable riverbed is sufficient to produce the same reaction of the GW head, resulting in an underestimated streambed conductivity. The same mechanism can be applied to explain the overestimated streambed conductivity under a smaller input value of the river width.

Fig. 4.13c shows the variation of the DMR between the estimated and actual streambed conductivity with the IE_w. It is generally linear while it can be seen that the slope of the line of $IE_w < 0$ is steeper than the slope of $IE_w > 0$, indicating that the estimation model is more sensitive to an under-measured river width than an over-measured river width.

4.6.4 Distance between Monitoring Well and River Centerline

Another consequence of bank erosions/depositions is the change of the distance between the monitoring well and the river centerline. This issue exists in both a fully and partially penetrated aquifer. The impact of this dynamics on the applicability of the estimation model was concerned and discussed by both Gianni et al., (2016) and Xian et al. (2019) though no quantitative analysis has been conducted. 9 sets of distance values, ranging from 30 m to 200 m, were therefore tested in this study as the actual distance was 60.0 m.

The comparisons between the actual time-varying streambed conductivity (black solid line) and the estimated streambed conductivities of four representative cases (distance = 40.0, 50.0, 100.0 and 160.0 m) are presented in Fig. 4.12d. The estimated streambed conductivities generally coincide with the actual value, indicating that the estimation model is little influenced by the river-well distance. To make this conclusion sounder, the variation of the DMR with the $IE_{Distance}$ is plotted as Fig. 4.13d. It can be observed that even when the dimensionless input error approaches

to 2.5, the DMR is still within the region of 0.10, evidencing that the distance between the monitoring well and the river centerline is not a critical input parameter for this model.

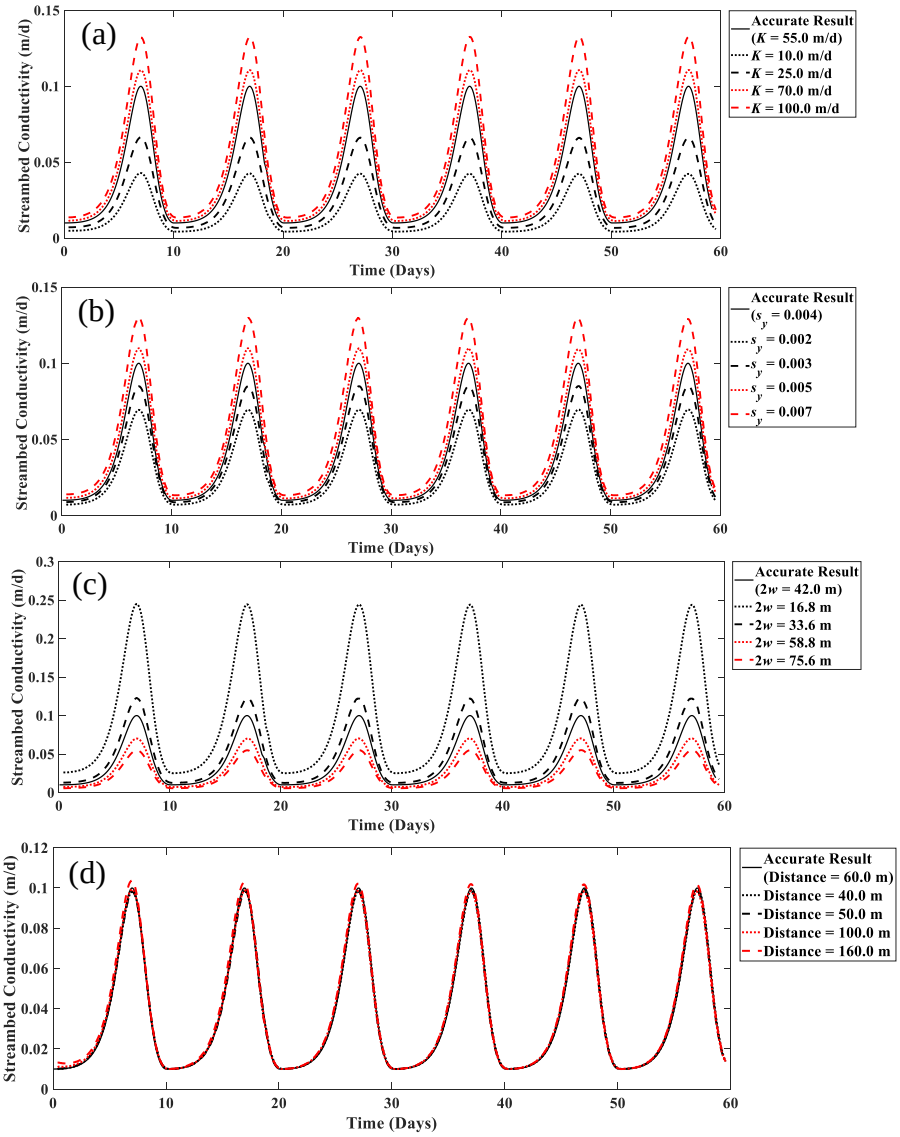

Figure 4.12. Comparisons of the estimated time-varying streambed conductivity with different input values of (a) the aquifer hydraulic conductivity; (b) the aquifer specific yield; (c) the river width and (d) the distance between the monitoring well and river center.

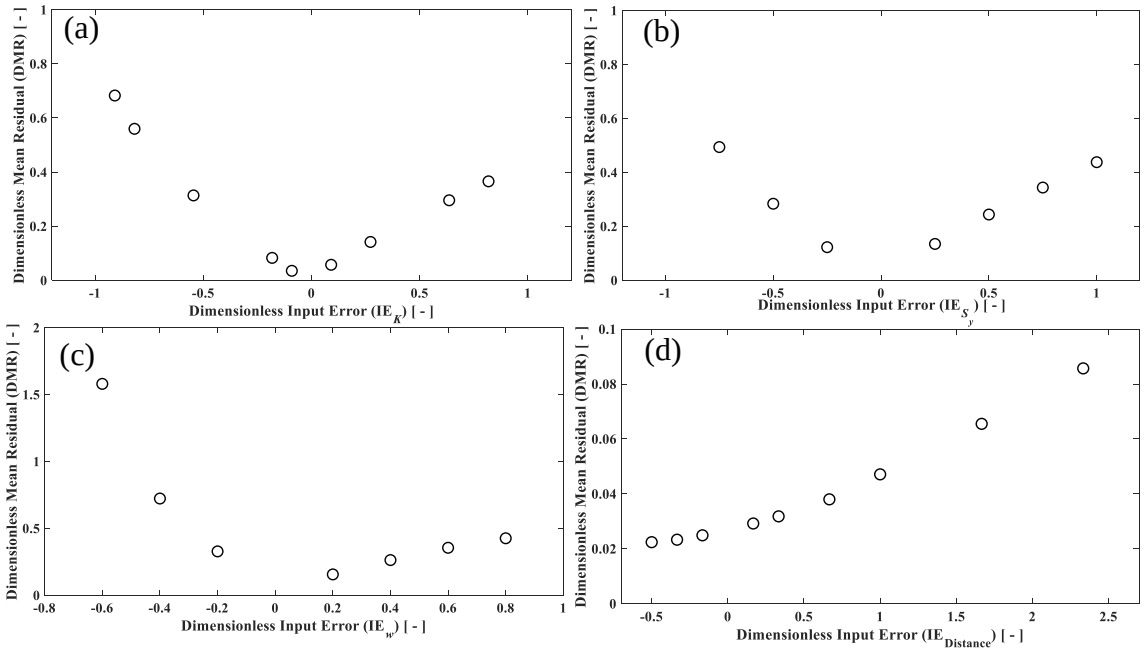

Figure 4.13. Variation of the dimensionless mean residual (DMR) between the estimated and accurate time-varying streambed conductivity with the dimensionless input error (*IE*) of (a) the aquifer hydraulic conductivity; (b) the aquifer specific yield; (c) the river width and (d) the distance between the monitoring well and river center.

4.7 Summary and Conclusions

In this chapter, a model that can rapidly estimate the time-varying streambed conductivity was developed based on a flood-wave response analytical solution. The scenario that the alluvial aquifer was partially penetrated by the river was considered.

The estimation model was then validated with two synthetic cases, one of which considered the condition in which the streambed conductivity varied much slower than the river-stage fluctuation while the other studied the scenario that the streambed conductivity and river stage changed at the same pace. For the validation case 1, the RMSE was 0.0057 m/d and the NSE was 0.94. For the validation case 2, the RMS was 0.01 m/d and NSE was 0.88, indicating that the estimation model is robust and can efficiently capture the time-varying streambed conductivity, which validates Hypothesis 1 of this chapter.

The sensitivity analysis of the estimated time-varying streambed conductivity to the optimization window size was conducted and found to be generally linear until POW size reached 70% of the flood-wave length, after which it stabilized. For the hypothetical case studied here, the results revealed that the uncertainty of the estimated streambed conductivity was less than 20% of the actual streambed conductivity when choosing a POW size that was smaller than 10% of the flood-wave length. This can be used as an empirical criterion to choose the POW size.

Meanwhile, despite the assumption made by the flood-wave response model that the aquifer was homogeneous, our study revealed that the estimation model was still applicable to heterogeneous cases. The geometric-averaged hydraulic conductivity was the most suitable value to represent the heterogeneous aquifer, and the error caused by the heterogeneity was minimal (DMR was around 0.1), which validates Hypothesis 2 of this chapter. However, it is important to mention that these findings cannot be generalized to other models, such as transport or residence time, since only the hydrological processes of GW flow were tested in this study.

The uncertainty analyses of the estimation model to its input parameters were also conducted. The results showed that approximately, the estimation model was linearly affected by the uncertainty of the aquifer hydraulic conductivity, the aquifer specific yield, and the river width. The uncertainty of the distance between the monitoring well and the river centerline was found to have minimal impacts on the estimated result.

CHAPTER V

APPLICATION OF ESTIMATION MODEL TO STUDY AREA

5.1 Study Site

The estimation model developed in Chapter 4 is applied to obtain the time-varying streambed conductivity of the Tallahatchie River near the Money experimental site. Based on the aquifer test presented in Chapter 3 and the information from Arthur (1994), the regional alluvial aquifer is generally confined by a low-permeable unit, which would substantially limit the rainfall-induced infiltration. It is therefore reasonable to believe that the fluctuation of the regional GW head is rarely associated with the surface runoff. On average, the alluvial aquifer is 40.0 m thick, located from 10 m to 50 m below the land surface. According to the aquifer test, the geometric-averaged hydraulic conductivity of the aquifer is 55.0 m/day, and the specific yield of the aquifer is set to be 0.004. The thickness of the streambed is set as 2.0 m.

Near the Money experimental site, a USGS gaging station has been installed to collect both the SW (USGS 07281600 Tallahatchie River at Money, MS) and GW (USGS 333904090123801 083E0105 Leflore (Money)) data over the last seven years. The gaging station is located at longitude 90°12'40"W and latitude 33°39'05"N, which is around 600 m to the pumping well. Their layouts can be found in Fig. 5.1. The temporal resolution of the measured data is 15 min. The monitoring well of the GW is around 60.0 m away from the river centerline as the nearby river width is approximately 42.0 m. For the estimation model, the POW size and shift is chosen as 0.8 and 0.1 days, respectively.

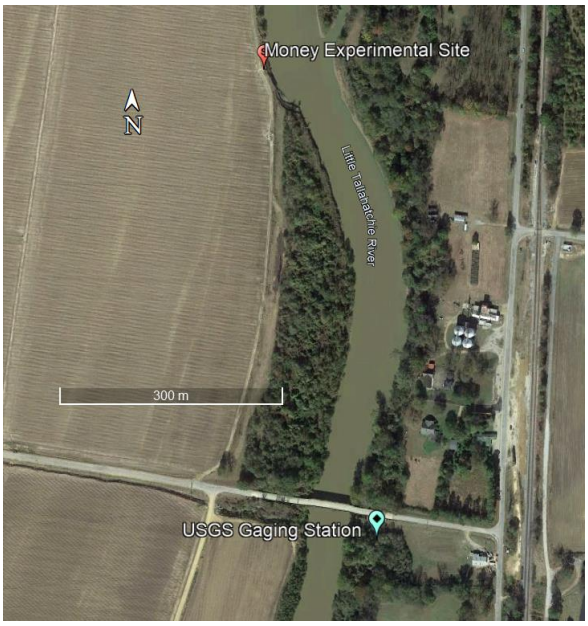

Figure 5.1. The study site of the Tallahatchie River near Leflore County, Mississippi, USA.

5.2 Flooding Condition 1

This flooding condition is from February 22, 2015 to June 22, 2015, which contains three consecutive flood events with attenuating amplitudes. The recorded river stage and GW head variations are shown in Fig. 5.2 by the black solid and dashed line, respectively, corresponding to the left *y*-axis. The estimated time-varying streambed conductance is presented as red dots, which corresponds to the right *y*-axis. Over this period, the mean SSE between the measured and calculated GW heads is 1.39×10^{-6} m^2. The static streambed conductance during this period is computed as well, which is 2.54×10^{-3} d^{-1}, and shown as the blue dots in Fig. 5.2. Generally, the static streambed conductance, which is usually used in the tradition model (e.g., Obergfell et al., 2019; von Asmuth et al., 2002; von Asmuth et al., 2008), is close to the mean (or 'equivalent') value of the time-varying conductance over the focused period. The mean SSE between the

measured and calculated GW heads under the static streambed conductance over this period is 4.17 $\times 10^{-5}$ m^2.

Since the convolution method is adopted in the estimation model developed in Chapter 4, the calculated time-varying streambed conductivity is affected by the choice of initial condition. By setting up the initial condition sufficiently long before the starting date of the formal study, the influence from the initial condition on the calculated results can be reduced and minimized. For the flooding condition 1, 4 sets of initial condition, which are 50 days, 70 days, 100 days and 150 days prior to the beginning of this flooding condition (February 22, 2015), are tested, and the comparisons are shown in Fig. 5.3. It can be found that when the initial condition is more than 70 days before the starting date, the calculated results of the time-varying streambed conductivity are generally convergent with each other (red, blue and black dots in Fig. 5.3). This agreement of the calculated results shown in Fig. 5.3 indicates that choosing the initial condition that is 100 days earlier than the formal calculation is sufficient to eliminate the major impact from the initial condition. In this study, the initial conditions are therefore all chosen to be at least 100 days before the starting date of the formal study when applying the estimation model to calculate time-varying streambed conductivity.

Prior to the commencement of the storm, in the early March of 2015, the streambed was of low permeability, and the conductance was less than 1.0×10^{-3} d^{-1}. Over the high-stage period, the streambed conductance rose persistently and reached 4.0×10^{-3} d^{-1} on June 12, 2015. The river stage returned to a low level after June 12, 2015, and the streambed conductance correspondingly reduced sharply from 4.0×10^{-3} to 1.0×10^{-3} d^{-1} (Fig. 5.2).

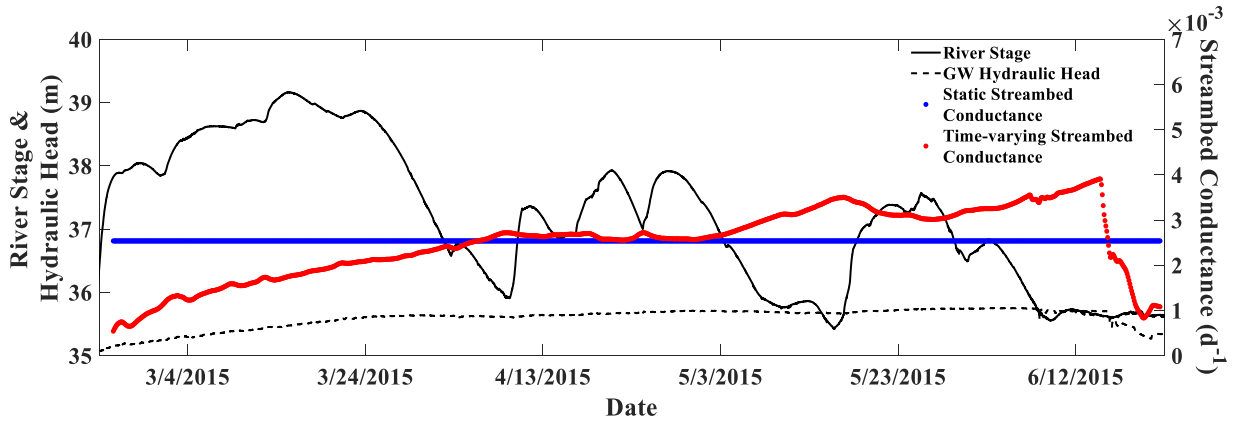

Figure 5.2. Time series of the river stage (black solid line), GW hydraulic heads (black dashed line), estimated static streambed conductance (blue dots) and estimated time-varying streambed conductance (red dots) during the flooding period from 2/22/2015 to 6/22/2015 in Leflore County, MS, USA.

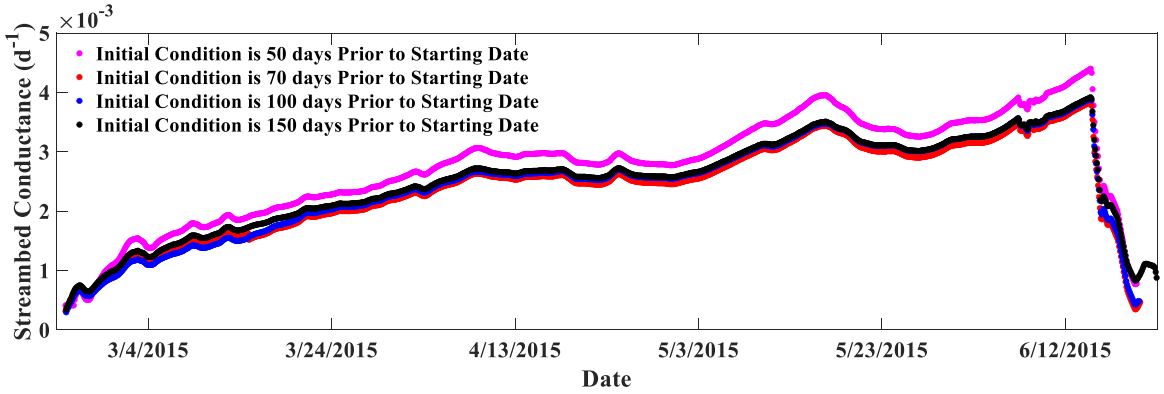

Figure 5.3. Comparisons of the calculated temporal variations of the streambed conductivity with the initial condition set up at different periods prior to the starting date of flooding condition 1.

5.3 Flooding Condition 2

This flooding condition is from October 26, 2015 to June 16, 2016, which is composed of multiple consecutive flood events with amplifying amplitudes. The recorded river stage and GW head variations are shown in Fig. 5.4 by the black solid and dashed line, respectively, corresponding to the left *y*-axis. The estimated time-varying streambed conductance is presented as red dots, which corresponds to the right *y*-axis. Over this period, the mean SSE between the

measured and calculated GW heads is 1.82×10^{-7} m^2. The static streambed conductance during this period is computed as well, which is 2.40×10^{-3} d^{-1}, shown as the blue dots in Fig. 5.4. The mean SSE between the measured and calculated GW heads under the static streambed conductance over this period is 3.25×10^{-5} m^2.

Before the onset of this flooding period, the streambed conductance was relatively high, which was around 2.5×10^{-3} d^{-1}. The streambed conductance slightly declined to 2.0×10^{-3} d^{-1} from November 19, 2015 to December 1, 2015, and then increased slowly but steadily to $2.5 \times 10^{-3} d^{-1}$ over the following high-stage period from late December 2015 to early March 2016, in which the mean river stage was around 38.0 m. As a flood with the maximum river-stage value of approximately 40.0 m arrived at this site on March 18, 2016, the streambed conductance quickly rose to around 3.5×10^{-3} d^{-1}, and remained in this high value until the end.

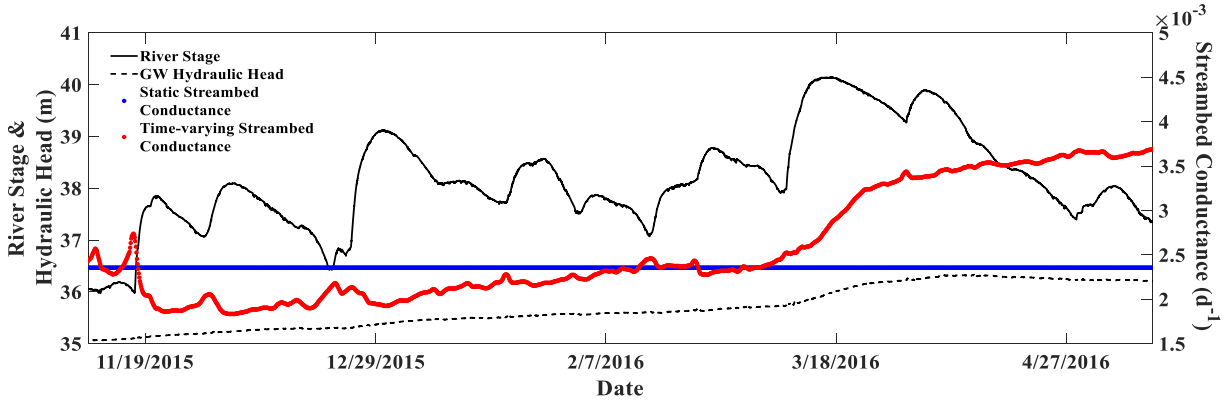

Figure 5.4. Time series of the river stage (black solid line), GW hydraulic heads (black dashed line), estimated static streambed conductance (blue dots) and estimated time-varying streambed conductance (red dots) during the flooding period from 10/26/2015 to 6/16/2016 in Leflore County, MS, USA.

5.4 Flooding Condition 3

This flooding condition is from May 7, 2021 to August 3, 2021, which contains a single flood wave. The recorded river stage and GW head variations are shown in Fig. 5.5 by the black

solid and dashed line, respectively, corresponding to the left *y*-axis. This is a peculiar flood event for the Tallahatchie River since the peak river stage approached to the record value, which was close to 41.0 m above the NAVD 88 datum. The estimated time-varying streambed conductance is presented as red dots, which corresponds to the right *y*-axis. Over this period, the mean SSE between the measured and calculated GW heads is 3.32×10^{-5} m^2. The static streambed conductance during this period is computed as well, which is 7.37×10^{-3} d^{-1}, shown as the blue dots in Fig. 5.5. The mean SSE between the measured and calculated GW heads under the static streambed conductance over this period is 3.62×10^{-3} m^2.

In May of 2021, the river stage was in decline, which dropped from 37.0 m to less than 35.0 m. The streambed conductance was correspondingly at a low value, which was around 2.50×10^{-3} d^{-1}. After the beginning of the flood on June 6, 2021, the river stage rapidly increased for around 6.0 m and the streambed conductance rocketed from less than 0.01 d^{-1} to 0.03 d^{-1}. After the peak of the flood, which was on June 15, 2021, the streambed conductance started to decline and returned to a low value, 2.50×10^{-3} d^{-1}, in early July when the SW level was in a low-stage condition.

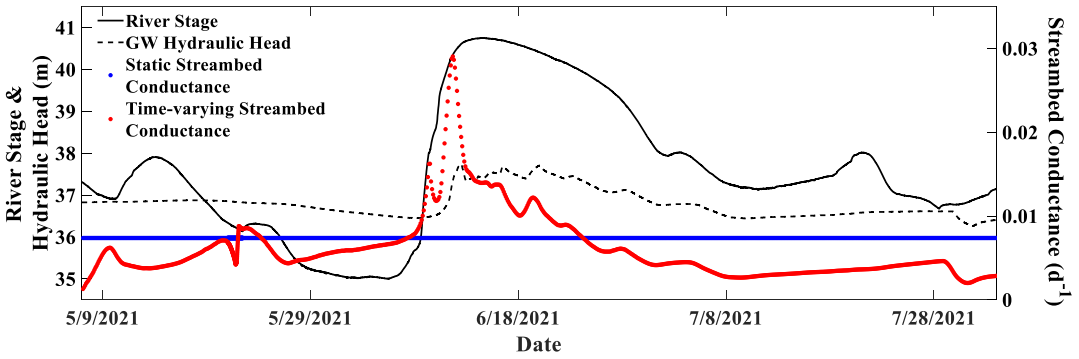

Figure 5.5. Time series of the river stage (black solid line), GW hydraulic heads (black dashed line), estimated static streambed conductance (blue dots) and estimated time-varying streambed conductance (red dots) during the flooding period from 5/7/2021 to 8/3/2021 in Leflore County, MS, USA.

CHAPTER VI

NUMERICAL STUDY OF RIVERBANK FILTRATION DURING STORM EVENTS WITH TIME-VARYING STREAMBED CONDUCTIVITY

6.1 Objectives and Hypotheses

This chapter aims at quantifying the infiltrated SW rate and the travel time of the infiltrated SW from stream to pumping well for RBF system during high-stage events with the consideration of the time-varying streambed conductivity through the simulation with CCHE3D-GW. The hypotheses of this chapter are: (a) operating riverside pumps during high-stage events results in extracting more water coming from the stream. (b) The travel time of the infiltrated water from the stream to the pumping well is shortened over storm events. (c) The evolutions of the stream depletion, the percentage of the pumped water coming from the stream and the travel time simulated with the static streambed conductivity statistically differ from the simulation results with the consideration of the time-varying streambed conductivity.

6.2 Methodology

6.2.1 Simulation Domain and Setting Up

The conceptual cross section, simulation domain, mesh and boundary conditions were the same as the calibration case shown in Chapter 3. The calibrated values of the hydraulic conductivity of the aquifer, including its heterogeneity near the pumping well, the hydraulic

conductivity of the aquitard and the storativity of the aquifer were directly implemented into the simulations in this Chapter.

Three flooding conditions, which were presented in Chapter 5, were studied. The river stage measured by the USGS gaging station (USGS 07281600 Tallahatchie River at Money, MS) was imposed on the CCHE3D-GW as the head boundary condition. Both the scenarios of the static and time-varying streambed conductivity were simulated, in which the estimated result of the streambed conductivity shown in Chapter 5 was adopted by the model. The static streambed conductivity is noted by $K_{r,S}$ while the time-varying streambed conductivity is marked by $K_{r,T}$.

6.2.2 Tracer Transport Model

During the flood event, owing to a stronger SW flow, the colmation/clogging layer of the streambed would be eroded (Cui et al., 2021; Hiscock and Grischek, 2002; Levy et al., 2011). Meanwhile, the rise of the SW level can substantially increase the hydraulic gradient between the stream and aquifer. Both of these two processes can result in an excessive infiltration of the SW to the subsurface region (Gollnitz et al., 2004). It is therefore necessary to evaluate the percentage of the pumped water that originates from the stream over flooding periods.

To achieve this goal, the transport of the conservative tracer was simulated with MT3D (Zheng and Wang, 1999) in this study. The idea is by constantly releasing conservative solutes, which can follow water particles, from top of the riverbed, the flow path of the infiltrated SW can be well tracked. In this study, only the advection is considered. As more SW flows into the aquifer and mixes with the regional GW, the concentration of the subsurface water will increase. Therefore, by recording the concentration of the pumped water, the percentage of the water coming from the stream can be computed as:

$$P_{SW} = \frac{C_{pumped}}{C_0} \tag{6.1}$$

where, P_{SW} is the percentage of the pumped water that originates from the stream, C_0 is the concentration of the released tracer in the SW, and C_{pumped} is the concentration of the pumped water.

Since the hydrological process is of primary concern in this study, only advection was simulated. The governing equation for the transport can therefore be written as:

$$\theta_n \frac{\partial C_g}{\partial t} = -\nabla \cdot (\mathbf{q} C_g) - Q_{pump} C_g \tag{6.2a}$$

$$C_g\big|_{\text{at stream}} = C_0 \tag{6.2b}$$

where, θ_n is porosity of sediment, which was chosen as 0.430 and 0.375 for the aquifer and aquitard sediment, respectively; Q_{pump} is the pumping rate (12960.0 m^3/day); C_g is concentration of conservative tracer in GW, and **q** is Darcy flux, which was provided by the simulation result of the flow model (CCHE3D-GW). Eq. 6.2b is the boundary condition that represents continually releasing tracers with a constant concentration (C_0) from the stream to the aquifer. C_0 was prescribed as 1000.0 kg/m^3 in this study. The other boundaries were all set as the no-flux condition.

Before the formal study, a spin-up simulation was conducted to reach an equilibrium initial condition, in which the GW flow field was the first-time-step simulation result with the time-varying streambed conductivity. From the experimental simulations, it was found that the concentration of the pumped water reached a constant after a 300-day spin-up pump, indicating a steady condition. The spin-up period was therefore chosen as 300 days.

6.2.3 Groundwater Age Simulation

Another highly studied item for the RBF system is the travel time of the infiltrated water

from the stream to the pumping well, which affects the chemical transformation between the infiltrated water and aquifer sediments (Schijven et al., 2003; Toze et al., 2010). Given by its importance to the whole system, travel time is usually chosen as a criterion for the design of the RBF site (Tombe et al., 2018; Mustafa et al., 2019). In this study, this parameter was obtained through the simulation of the mean water age, and the governing equation from Goode (1996) and Zhou et al. (2018) was adopted:

$$\frac{\partial(a_1)}{\partial t} = -\nabla \cdot \left(\frac{\mathbf{q}}{\theta_n} a_1 \right) + 1 - \frac{Q_{\text{pump}}}{\theta_n} a_1 \tag{6.3a}$$

$$a_1\big|_{\text{at stream}} = 0 \tag{6.3b}$$

where, a_1 is the 1st moment of the water age distribution (mean water age). Since this study only focused on the transport of the water particle, where the advection process dominates, the dispersion was therefore neglected in Eq. 6.3a. For the infiltrated SW, it is fresh when it flows into the aquifer, so its initial water age is zero, which is described by Eq. 6.3b. The other boundaries were all represented by the non-flux condition.

Before the formal study, a 300-day spin-up simulation was also conducted to achieve an equilibrium initial condition for the formal simulation, where the GW flow field was the first-time-step simulation result with the time-varying streambed conductivity.

6.2.4 Mean Travel Time

The age of the pumped water, which is marked by $a_{1,\text{pumped}}$, was recorded during the simulation period. It is an average value of the mean travel time of the pumped SW and the aquifer water age, which can be represented as:

$$a_{1,\text{pumped}} = \text{Percentage of Water Pumped from Aquifer} \times \text{Aquifer Water Age} + \text{Percentage of Water Pumped from Stream} \times \text{Mean Travel Time} \quad (6.4)$$

For the items inside the Eq. 6.4, the percentage of the water pumped from the aquifer and stream can be obtained through the simulation of the conservative tracer shown in 6.2.2. The water age of the aquifer GW is identical to the simulation time step. The only unknown item, the mean travel time of the pumped SW (T_{Travel}), can therefore be computed as:

$$T_{\text{Travel}} = \frac{a_{1,\text{pumped}} - \text{Percentage of Water Pumped from Aquifer} \times \text{Aquifer Water Age}}{\text{Percentage of Water Pumped from Stream}} \quad (6.5)$$

The dimensionless travel time, T^*_{Travel} is defined as:

$$T^*_{\text{Travel}} = \frac{T_{\text{Travel}}}{T_{\text{Travel, Initial}}} \quad (6.6)$$

where, $T_{\text{Travel, Initial}}$ is the travel time at $t = 0$ (initial value of the formal simulation).

6.3 Simulation Results

6.3.1 Flooding Condition 1

6.3.1.1 Hydrological Processes

The drawdown of the GW hydraulic head is highly focused for the RBF system since it reflects the impact of the irrigation on the regional GW resource. 10 observation wells were set up in the numerical model to observe this process, and their spatial distributions are shown in Fig. 6.1. Table 6.1 lists their detailed coordinates.

Fig 6.2a and b shows the simulated temporal variation of the GW hydraulic head in the monitoring wells on the western and eastern bank of the Tallahatchie River, respectively, during the flooding condition 1. The red dashed lines and black solid lines mark the simulation results with the static and time-varying streambed conductivity, respectively. In general, the drawdown

curves in all monitoring wells are smooth and flat, and almost uninfluenced by the fluctuations of the river stage. Once the pump was started, the GW hydraulic head dropped immediately and sharply, which was more than 1.0 m on average according to the data shown in Fig. 6.2. However, the drawdown was soon stabilized, and the GW only declined slightly over the rest of the flooding period, which was less than 0.5 m for all monitoring wells. It could be found that the simulated drawdown curves with the static streambed conductivity are generally in line with the simulation results under the time-varying scenario, indicating that the assumption of a static streambed can produce a reasonable result for the GW drawdown process.

Table 6.1. The Coordinates of the Pumping Well and Monitoring Wells

No. of Wells (Western Bank)	Coordinate (x,y) (m)	Distance to the Pumping Well (m)	No. of Wells (Eastern Bank)	Coordinate (x,y) (m)	Distance to the Pumping Well (m)
MW-W1	(10.00, 0.00)	10.00	MW-E1	(-99.51, 0.00)	99.51
MW-W2	(30.00, 0.00)	30.00	MW-E2	(-189.79, 0.00)	189.79
MW-W3	(50.00, 0.00)	50.00	MW-E3	(-263.99, 0.00)	263.99
MW-W4	(100.00, 0.00)	100.00	MW-E4	(-380.00, 0.00)	380.00
MW-W5	(210.00, 0.00)	210.00	MW-E5	(-484.43, 0.00)	484.43

Figure 6.1. (a) The spatial distribution of the 10 monitoring wells that were set up in the numerical pumping simulation.

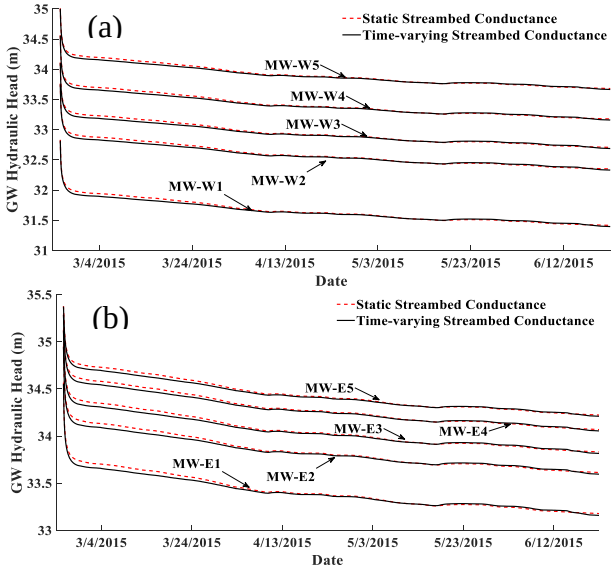

Figure 6.2. (a) The temporal variation of the GW hydraulic head in the monitoring wells in the (a) western and (b) eastern banks during the flooding condition 1.

Fig. 6.3c presents the temporal variation of the stream depletion during the flooding condition 1, in which the solid and dashed line represents the simulation result with the static and time-varying streambed conductivity, respectively. Generally, both the simulated stream-depletion curves of the static and time-varying streambed conductivity follow the river-stage fluctuation (Fig. 6.3a), in which three crests can be clearly observed. However, when comparing the detailed processes, differences can be observed. The first flood visited the site from early March to early April of 2015, in which the value of the static streambed conductivity was higher than the corresponding time-varying streambed conductivity, reflected by $K_{r,T}/K_{r,S} < 1$ over this period (Fig. 6.3b). The stream depletion estimated from the static streambed conductivity is therefore larger than that from the time-varying scenario. The second flood event occurred from April 13 to May 15, 2015, in which $K_{r,T}/K_{r,S}$ was generally in the region of 1.0, causing the depletion curve under the static streambed conductivity (solid line, Fig. 6.3c) to be almost identical to that under the time-varying condition (dashed line, Fig. 6.3c). Over the last flood wave, from May 23 to June

12 of 2015, $K_{r,T}/K_{r,S}$ was generally larger than 1.0, rendering the stream depletion under the time-varying streambed conductivity higher than that of the static scenario. Hence, it can be concluded that the evolution of the stream depletion is tightly associated with the streambed conductivity. Detailed processes would be missed if the temporal variation of the streambed conductivity were not considered. A *t* test indicated that mean difference of the stream depletions simulated with the static and time-varying streambed conductivity over flooding condition 1 was statistically significant ($P < 0.01$).

6.3.1.2 Percentage of Pumped Water from Stream

As it has been elaborated in the Methodology section, in this study, the percentage of the pumped water that originates from the stream is obtained through the simulation of the conservative tracer. Fig. 6.4a shows the simulated concentration distribution of the tracer with the time-varying streambed conductivity at $t = 50.0$ day, in which the red arrows are used to indicate the GW flow direction but not to scale. It can be clearly observed that tracers follow the infiltrate water to transport from the streambed to the pumping well.

Since the hydraulic conductivity of the streambed is much smaller than that of the aquifer, for the area near the riverbed, it is much harder for the GW to flow vertically than horizontally, which results in a predominantly horizontal GW flow. With this GW flow field (shown in Fig. 6.4a), when the SW infiltrates into the aquifer, it first flows horizontally and interacts with the shallow GW. This is reflected by a high-concentration plume of the tracer in the shallow layer of the aquifer (Fig. 6.4a). When the infiltrated water progresses to the region close to the pumping well, owing to a strong vertical hydraulic gradient caused by the irrigation, downward flow becomes dominant, and the tracer plume therefore starts to move towards the pumping well.

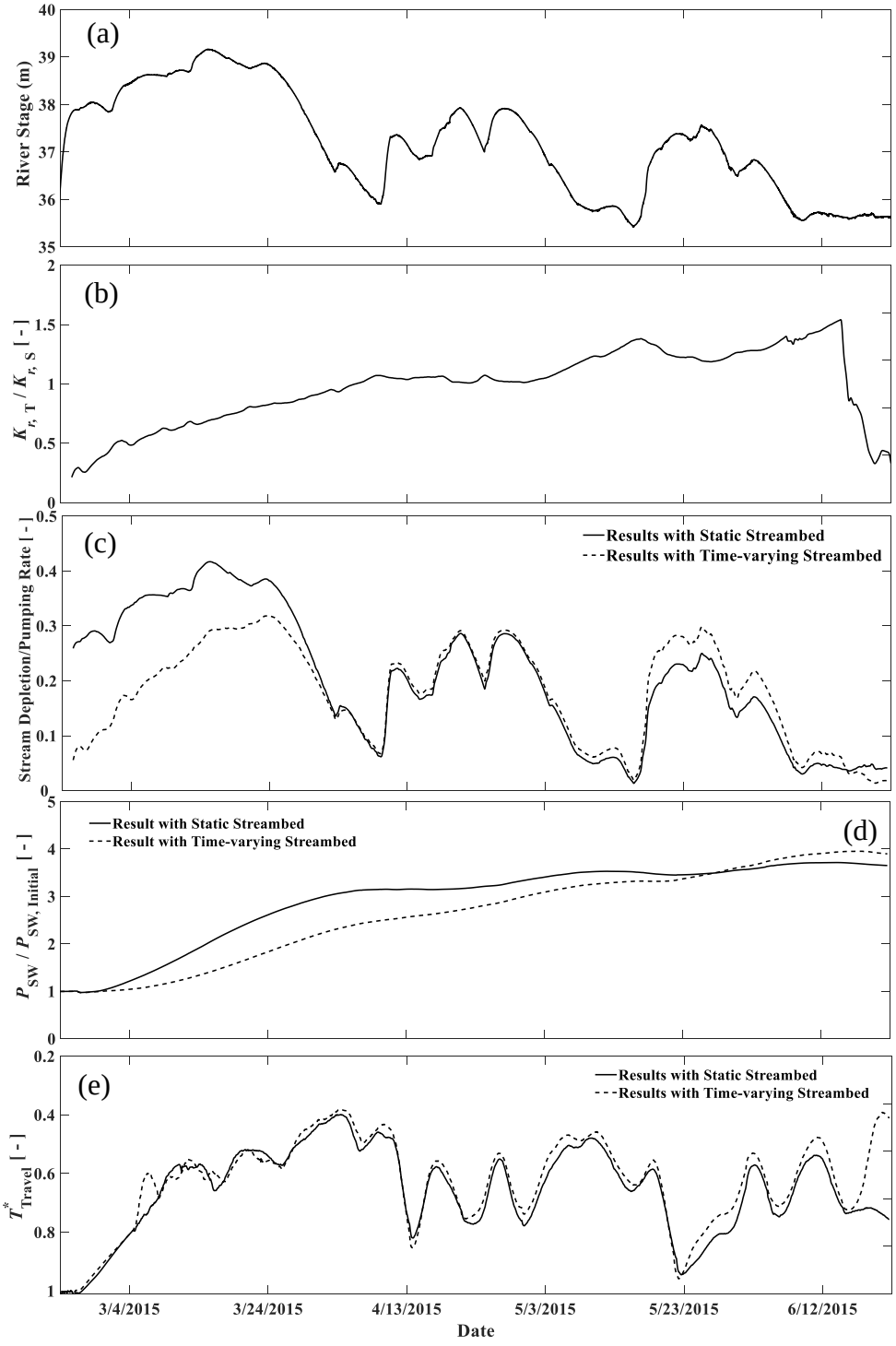

Figure 6.3. Temporal variation of the (a) river stage, (b) streambed conductivity, (c) stream depletion, (d) percentage of the pumped water from the stream and (e) travel time over the flooding condition 1, where the results under the static streambed are represented by the solid line while those under the time-varying streambed are marked by the dashed line.

Fig. 6.3d shows the temporal variation of $P_{SW}/P_{SW,\ Initial}$ during this flooding condition, where $P_{SW,\ Initial}$ is the percentage of the pumped water from the stream at $t = 0$ (initial value of the formal simulation). It could be seen that both the simulation results with the static (solid line) and time-varying (dashed line) streambed conductivity follow a similar trend and are generally not affected by the river-stage fluctuations. Both of them gradually climbed from 1.0 to around 3.5 at the end of the simulation, revealing that owing to the flood events, more SW was pumped, and it was 2.5 times more than that of the low-stage period. In the early stage (from early March to late May of 2015), since the static streambed conductivity was higher than the time-varying streambed conductivity ($K_{r,T}/K_{r,S} < 1$, Fig. 6.3b), the simulated $P_{SW}/P_{SW,\ Initial}$ of the static streambed (solid line Fig. 6.3d) was consistently larger than that under the time-varying condition. However, in the late stage, owing to $K_{r,T}/K_{r,S} > 1$ (Fig. 6.3b), this situation is reversed. A *t* test indicated that mean difference of the percentages simulated with the static and time-varying streambed conductivity over flooding condition 1 was statistically significant ($P < 0.01$).

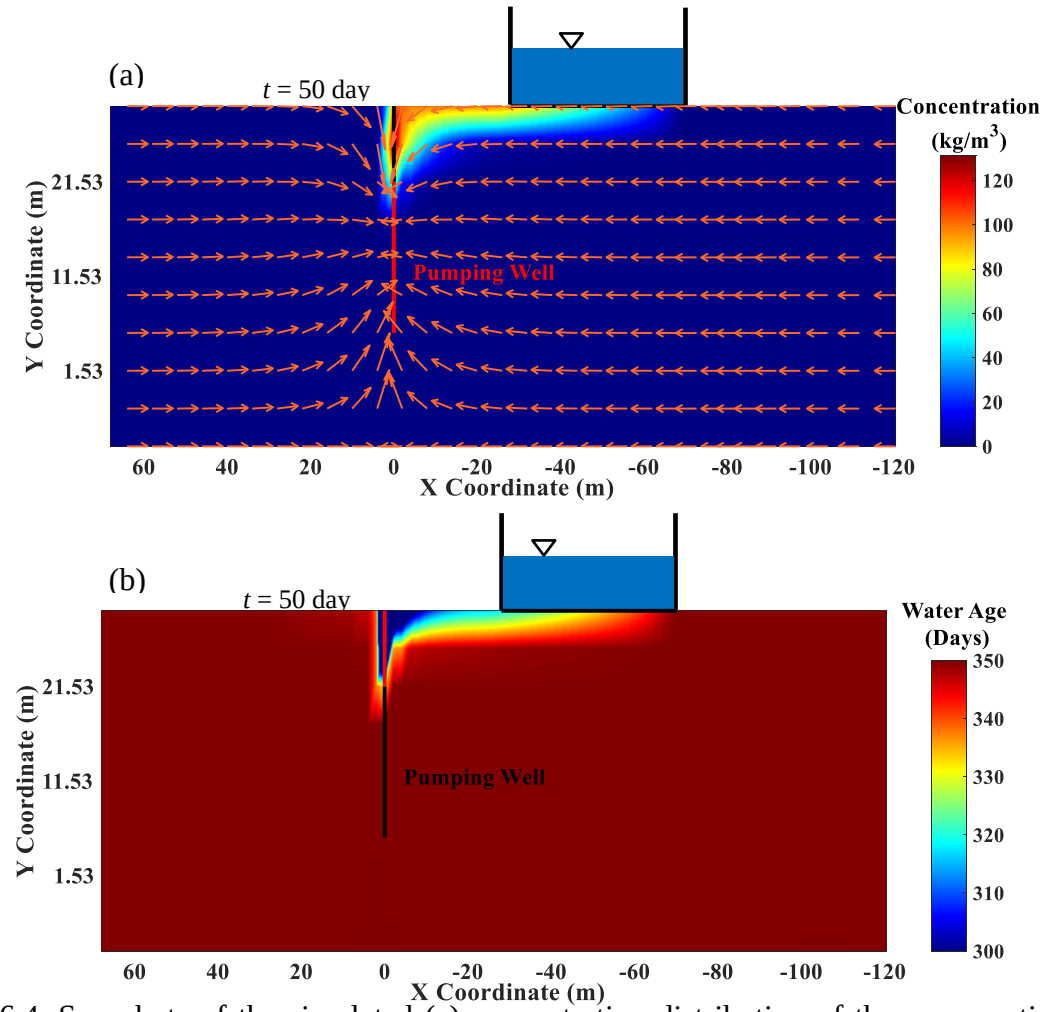

Figure 6.4. Snapshots of the simulated (a) concentration distribution of the conservative tracer (color map) and GW flow field (red arrows represent direction but are not to scale), and (b) distribution of the water age with the time-varying streambed conductivity at t = 50 day (starting from the formal simulation) for the flooding condition 1.

6.3.1.3 Mean Travel Time of SW

Fig. 6.4b shows the simulated distribution of the mean water age with the time-varying streambed conductivity at t = 50.0 day of the flooding condition 1, which is generally in line with concentration distribution (Fig. 6.4a). Since the SW is younger than the GW, the more infiltrated SW to the aquifer, the younger the age of the regional GW. After obtaining the value of the mean pumped water age, the travel time of the infiltrated SW to the pumping well can be computed from

Eq. 6.5.

Fig. 6.3e presents the temporal variation of the dimensionless travel time over this flooding period, in which the solid and dashed line marks the result under the static and time-varying streambed conductivity, respectively. The *y* coordinate is reverse aimed at better comparing the dimensionless travel time with the other parameters. In general, T^*_{Travel} follows the trend of the river stage to vary with time. With a higher river stage, the stream-aquifer hydraulic gradient increases, so GW flows are accelerated, resulting in a shorter travel time between the stream and the pumping well. The simulated travel times under the static and time-varying streambed conductivity are generally close to each other. The only exception is in late June 2015, in which the simulated travel time under the static streambed (black line in Fig. 6.3e) became stable with the river stage returning to a low level while the travel time under the time-varying streambed condition (dashed line in Fig. 6.3e) declined dramatically. It is pertinent to the continuous increase of the streambed conductivity, $K_{r,\text{T}}$, over the early June (Fig. 6.3b), which pushed the infiltrated SW to flow at a faster velocity, and therefore shortened the transport time between the streambed and the pumping well. Once these infiltrated waters arrived at the pumping site in late June, the mean travel time was substantially reduced. Over this flooding condition, the minimum T^*_{Travel} was around 0.4, i.e., the minimum travel time over this high-stage event was 40% of the travel time in the low-stage condition. A *t* test indicated that mean difference of the travel times simulated with the static and time-varying streambed conductivity over flooding condition 1 was statistically significant ($P < 0.01$).

6.3.2 Flooding Condition 2

6.3.2.1 Hydrological Processes

Fig. 6.5a shows the temporal variation of the GW hydraulic head in the five monitoring wells on the western bank of the Tallahatchie River over the flooding condition 2 while Fig. 6.5b illustrates the five on the eastern bank, where the red dashed lines and black solid lines represent the results under the static and time-varying streambed conductivity, respectively. Similar to the findings of the flooding condition 1, the drawdown curves are all flat and smooth despite the river-stage fluctuation (Fig. 6.6a). The GW drawdowns simulated with the static (red dashed lines) and time-varying streambed conductivity (black solid lines) generally agree with each other.

Fig. 6.6c shows the temporal variation of the stream depletion during this period, in which the dashed and solid line is used to represent the results with the static and time-varying streambed conductivity, respectively. The stream-depletion curve generally follows the trend of the river stage (Fig. 6.6a) to fluctuate, and their crests and troughs almost occur at the same time. With a higher SW level, the hydraulic gradient between the stream and aquifer increases, which therefore pushes more SW to recharge GW, resulting in a higher stream-depletion rate.

When comparing the stream depletion simulated with the static (solid line in Fig. 6.6c) and time-varying streambed conductivity (dashed line in Fig. 6.6c), the whole period can be divided into two stages. The first stage is from the beginning to the middle of March 2015. During this period, the time-varying streambed conductivity was slightly smaller than the static value, reflected by Fig. 6.6b as $K_{r,\mathrm{T}}/K_{r,\mathrm{S}} < 1$. The stream depletion simulated by the static streambed conductivity was therefore higher than the simulation result with the time-varying condition. However, as the streambed consistently became more permeable, in the second stage (from March

18, 2015 to the end), the stream depletion simulated with the time-varying streambed conductivity was higher than the result under the static condition. A *t* test indicated that mean difference of the stream depletions simulated with the static and time-varying streambed conductivity over flooding condition 2 was statistically significant ($P < 0.01$).

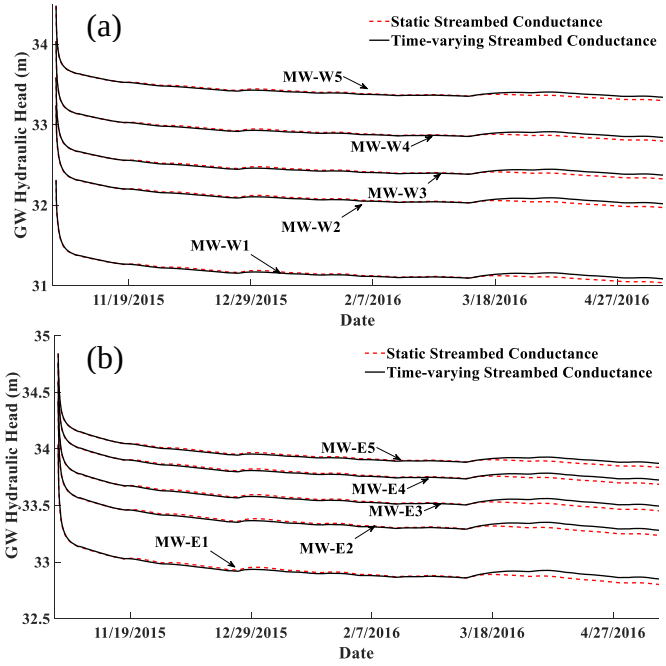

Figure 6.5. (a) The temporal variation of the GW hydraulic head in the monitoring wells in the (a) western and (b) eastern banks during the flooding condition 2.

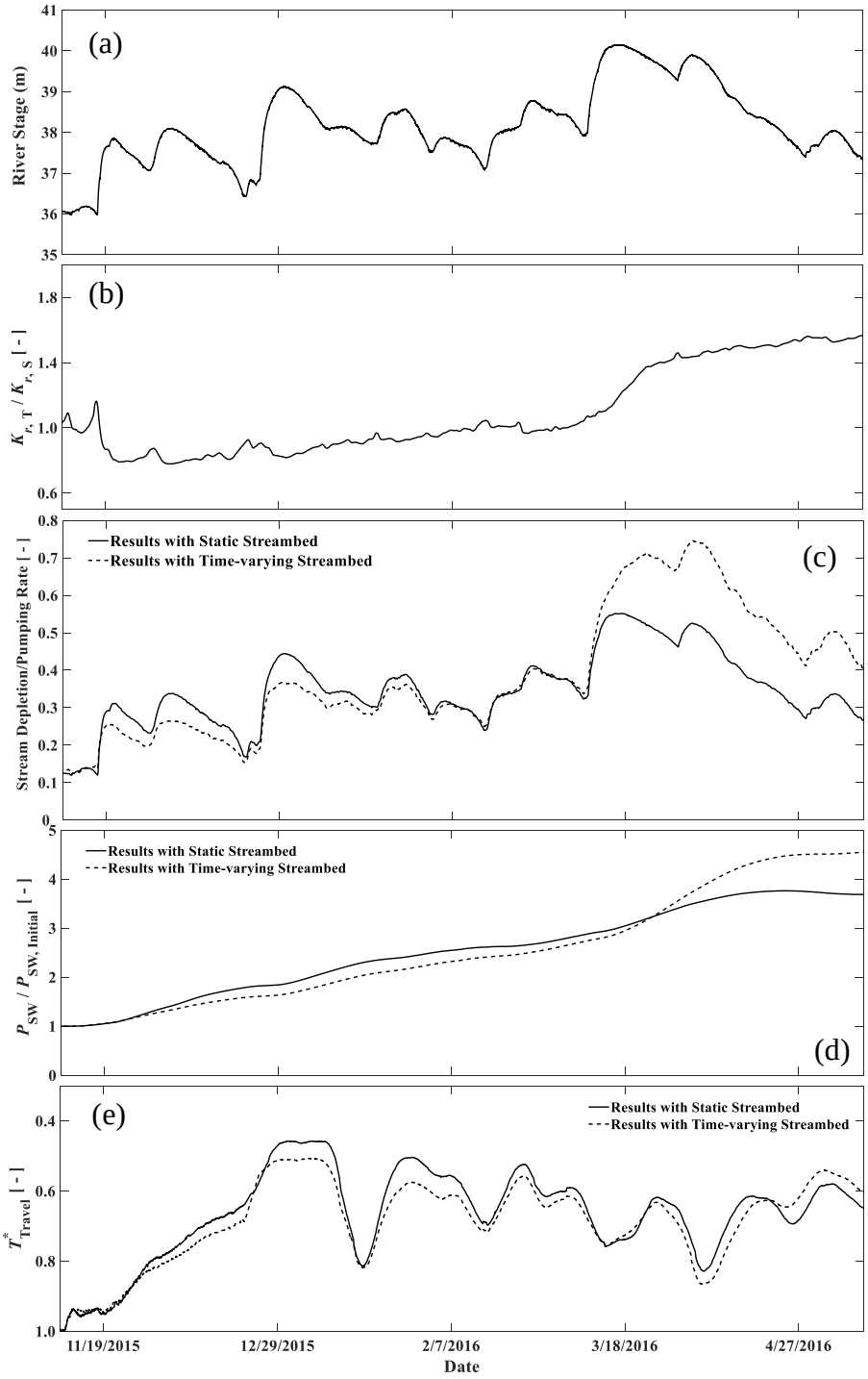

Figure 6.6. Temporal variation of the (a) river stage, (b) streambed conductivity, (c) stream depletion, (d) percentage of the pumped water from the stream and (e) travel time over the flooding condition 2, where the results under the static streambed are represented by the solid line while those under the time-varying streambed are marked by the dashed line.

6.3.2.2 Percentage of Pumped Water from Stream

Fig. 6.7a shows the concentration distribution of the tracer simulated with the time-varying streambed conductivity at t = 50.0 day of the flooding condition 2, in which the red arrows are used to indicate the GW flow direction but not to scale. The GW flow field and the shape of the tracer plume are similar to the results of the flooding condition 1 shown in Fig. 6.4a, and the mechanisms are the same.

Fig. 6.6d presents the temporal variation of $P_{SW}/P_{SW,\,Initial}$ during the flooding condition 2. It can be seen that in the early stage (before April 2016), the simulation result with the static streambed conductivity (solid line) is generally close to the result under the time-varying condition (dashed line), both of which gradually climbed from 1.0 to 3.0. However, with the substantial increase of the streambed conductivity during the last flood event, in which starting from March 18, 2016, $K_{r,T}/K_{r,S}$ jumped from 1.0 to 1.4 in half a month (Fig. 6.6b), the simulated $P_{SW}/P_{SW,\,Initial}$ under the time-varying streambed conductivity became higher than the result under the static condition. At the end of this period, $P_{SW}/P_{SW,\,Initial}$ of the static and time-varying streambed conductivity was 3.8 and 4.2, respectively, indicating that the amount of the pumped water coming from the stream was approximately 3.0 times more than that of the low-stage period. A t test indicated that mean difference of the percentages simulated with the static and time-varying streambed conductivity over flooding condition 2 was statistically significant ($P < 0.01$).

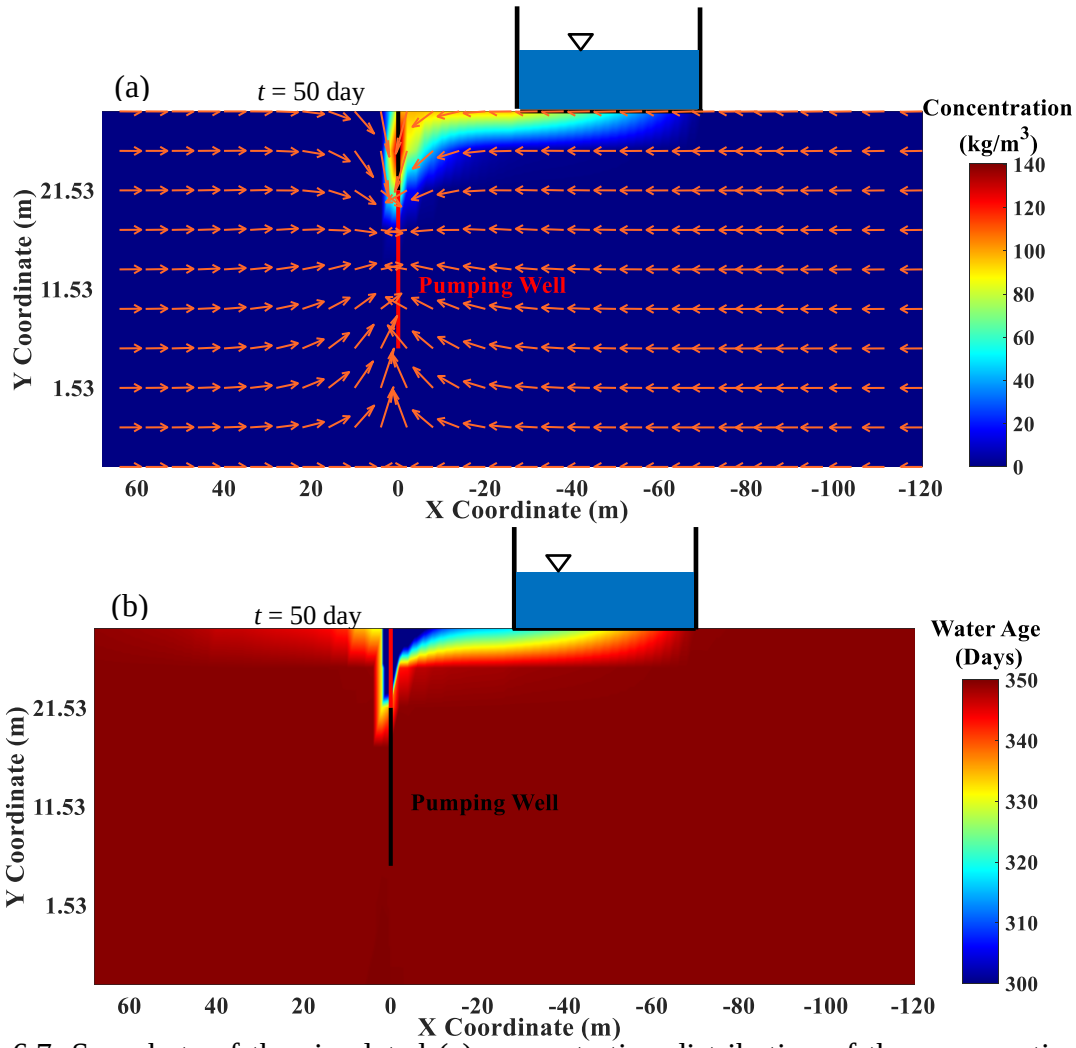

Figure 6.7. Snapshots of the simulated (a) concentration distribution of the conservative tracer (color map) and GW flow field (red arrows represent direction but are not to scale), and (b) distribution of the water age with the time-varying streambed conductivity at t = 50 day (starting from the formal simulation) for the flooding condition 2.

6.3.2.3 Mean Travel Time of SW

Fig. 6.7b shows the distribution of the mean water age simulated with the time-varying streambed conductivity at t = 50.0 day of the flooding condition 2, which is generally consistent with the concentration distribution (Fig. 6.7a).

Fig. 6.6e presents the temporal variation of the dimensionless travel time over the flooding condition 2, in which the result under the static and time-varying streambed conductivity is

represented by the solid and dashed line, respectively, and the direction of *y* coordinate is flipped. Generally, the simulated T^*_{Travel} under both the static and time-varying scenarios followed the river stage to fluctuate with time. In the early stage (before April 2016), T^*_{Travel} simulated with the static streambed conductivity was consistently shorter than T^*_{Travel} under the time-varying condition because $K_{r,\text{T}}$ was generally smaller than $K_{r,\text{S}}$ over this period (Fig. 6.6b). With the considerable increase of $K_{r,\text{T}}/K_{r,\text{S}}$ during the flood event that occurred from late March to early April 2016 (Fig. 6.6b), the travel time simulated with the time-varying streambed conductivity became smaller than the simulation result under the static condition. Over this flooding condition, the minimum T^*_{Travel} was around 0.45, i.e., the minimum travel time over this high-stage event was 45% of the travel time in the low-stage condition. A *t* test indicated that mean difference of the travel times simulated with the static and time-varying streambed conductivity over flooding condition 2 was statistically significant ($P < 0.01$).

6.3.3 Flooding Condition 3

6.3.3.1 Hydrological Processes

Fig 6.8a and b shows the simulated drawdown processes of the GW hydraulic head in the monitoring wells on the western and eastern bank of the Tallahatchie River, respectively, during the flooding condition 3. The simulation results with the static and time-varying streambed conductivity are marked by the red dashed lines and black solid lines, respectively. For this case, a peculiar phenomenon that the GW hydraulic heads increase during the pumping session is observed. After the river stage jumped for around 6 m, and arrived at a record-high value in early June 2021 (Fig. 6.9a), the stream-aquifer hydraulic gradient was substantially enlarged, which pushed excessive SW to infiltrate into the aquifer, resulting in the rise of the GW level even though

the aquifer was stressed by the pumping well. For the simulation considering the time-varying streambed conductivity, the increase of the GW hydraulic head was sharp, and a spike could be clearly observed (Fig. 6.8), which was caused by the rise of both the river stage and streambed conductivity. However, this phenomenon could not be captured by the simulation with the static streambed conductivity, in which the rise was smooth, and its value was noticeably smaller than that of the time-varying condition (Fig. 6.8).

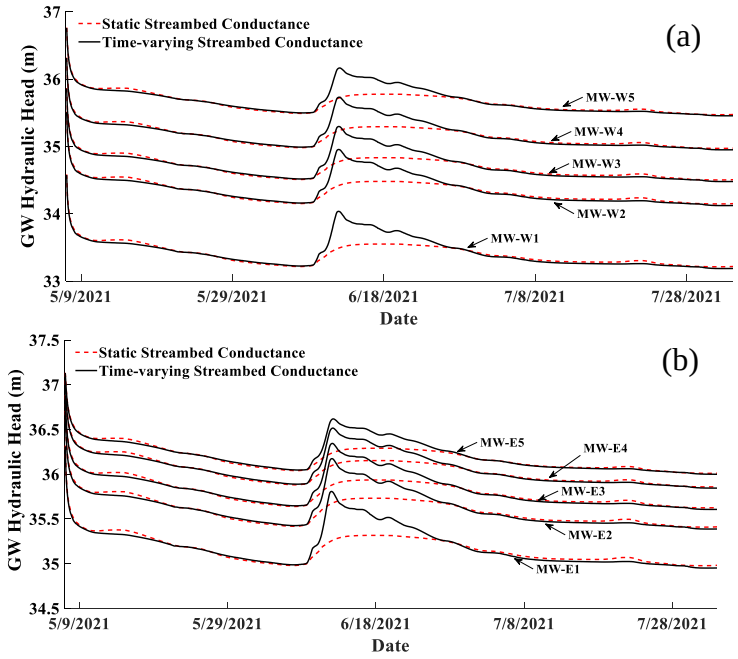

Figure 6.8. (a) The temporal variation of the GW hydraulic head in the monitoring wells in the (a) western and (b) eastern banks during the flooding condition 3.

Fig. 6.9c presents the temporal variation of the stream depletion during the flooding condition 3 with the solid and dashed line representing the simulation results under the static and time-varying streambed conductivity, respectively. When assuming a static streambed conductivity, the stream-depletion curve generally followed the trend of the river stage to vary with time. However, with the consideration of the time-varying streambed conductivity, owing to the increase of both the river stage and streambed conductivity at the peak of the flood, the

simulated stream depletion experienced a spike correspondingly, which could not be captured by the simulation with the static streambed conductivity. For both the static and time-varying scenarios, the ratio between the stream depletion and the pumping rate was larger than 1.0 during the crest of the flood, indicating that the recharge from the stream exceeded the irrigation, which was the reason of the rise of the GW heads during the pumping period. A *t* test indicated that mean difference of the stream depletions simulated with the static and time-varying streambed conductivity over flooding condition 3 was statistically significant ($P < 0.05$).

6.3.3.2 Percentage of Pumped Water from Stream

Fig. 6.10a shows the concentration distribution of the tracer simulated with the time-varying streambed conductivity at $t = 50.0$ day of the flooding condition 3, in which the red arrows are used to indicate the GW flow direction but not to scale. The GW flow field and the shape of the tracer plume are similar to the results of the flooding conditions 1 and 2 shown in Fig. 6.4a and 6.7a, which are caused by the same mechanism.

Fig. 6.9d presents the temporal variation of $P_{SW}/P_{SW,Initial}$ during the flooding condition 3, which reveals that for both the static (solid line) and time-varying (dashed line) simulations, the percentage of the pumped water coming from the stream raises substantially over this high-stage event. The maximum value of $P_{SW}/P_{SW,Initial}$ simulated with the time-varying streambed conductivity was around 13.0, i.e., the amount of the pumped water coming from the stream was 12.0 times more than that of the low-stage period, while the maximum $P_{SW}/P_{SW,Initial}$ simulated with the static streambed conductivity was 9.8. The difference of the maximum $P_{SW}/P_{SW,Initial}$ simulated with the time-varying and static streambed conductivity is because the static assumption severely underestimates the streambed conductivity during the peak of the flood, which is

evidenced in Fig. 6.9b as $K_{r,T}/K_{r,S} = 4$. A *t* test indicated that mean difference of the percentages simulated with the static and time-varying streambed conductivity over flooding condition 3 was statistically significant ($P < 0.05$).

6.3.3.3 Mean Travel Time of SW

Fig. 6.10b shows the distribution of the mean water age simulated with the time-varying streambed conductivity at $t = 50.0$ day of the flooding condition 3, which is generally in line with concentration distribution (Fig. 6.10a).

Fig. 6.9e presents the temporal variation of the dimensionless travel time during this 88.4-day hypothetical pumping simulation, in which the solid and dashed line is used to mark the result simulated with the static and time-varying streambed conductivity, respectively, and the *y* coordinate is reversed. It can be found that after the start of the storm, the simulated travel time was shortened substantially for both the static and time-varying streambed scenarios, especially when the flood peak arrived. Over this period, the decline of the travel time simulated with the time-varying streambed conductivity was larger than that under the static condition, which was related to the sudden increase of the streambed conductivity at the peak of the flood. The minimum T^*_{Travel} simulated with the time-varying streambed conductivity was around 0.20, i.e., the minimum travel time over this high-stage event was 20% of the travel time in the low-stage condition. After the SW returned to the low-stage condition, the travel time began to increase. A *t* test indicated that mean difference of the travel times simulated with the static and time-varying streambed conductivity over flooding condition 3 was statistically significant ($P < 0.05$).

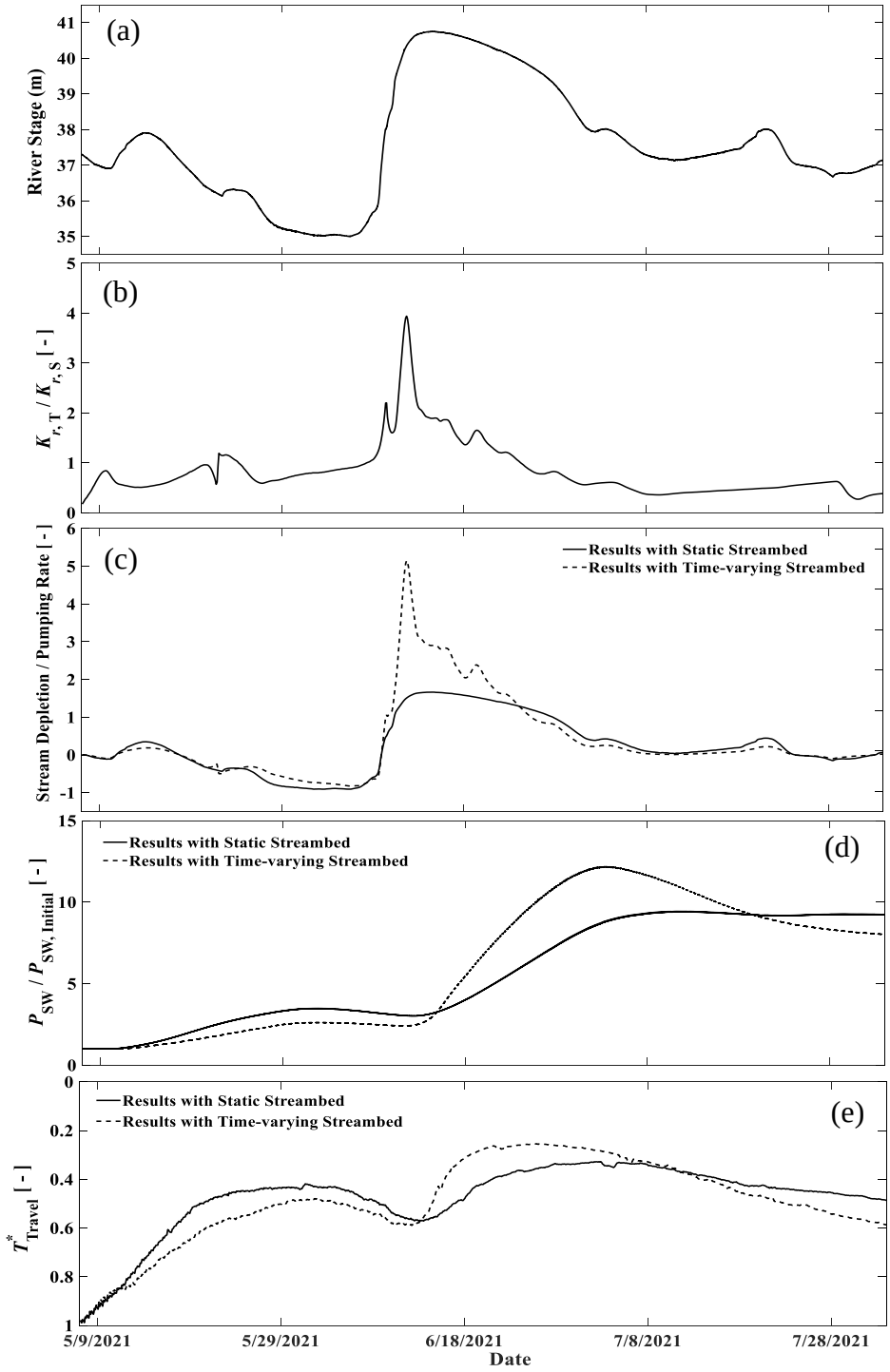

Figure 6.9. Temporal variation of the (a) river stage, (b) streambed conductivity, (c) stream depletion, (d) percentage of the pumped water from the stream and (e) travel time over the flooding condition 3, where the results under the static streambed are represented by the solid line while those under the time-varying streambed are marked by the dashed line.

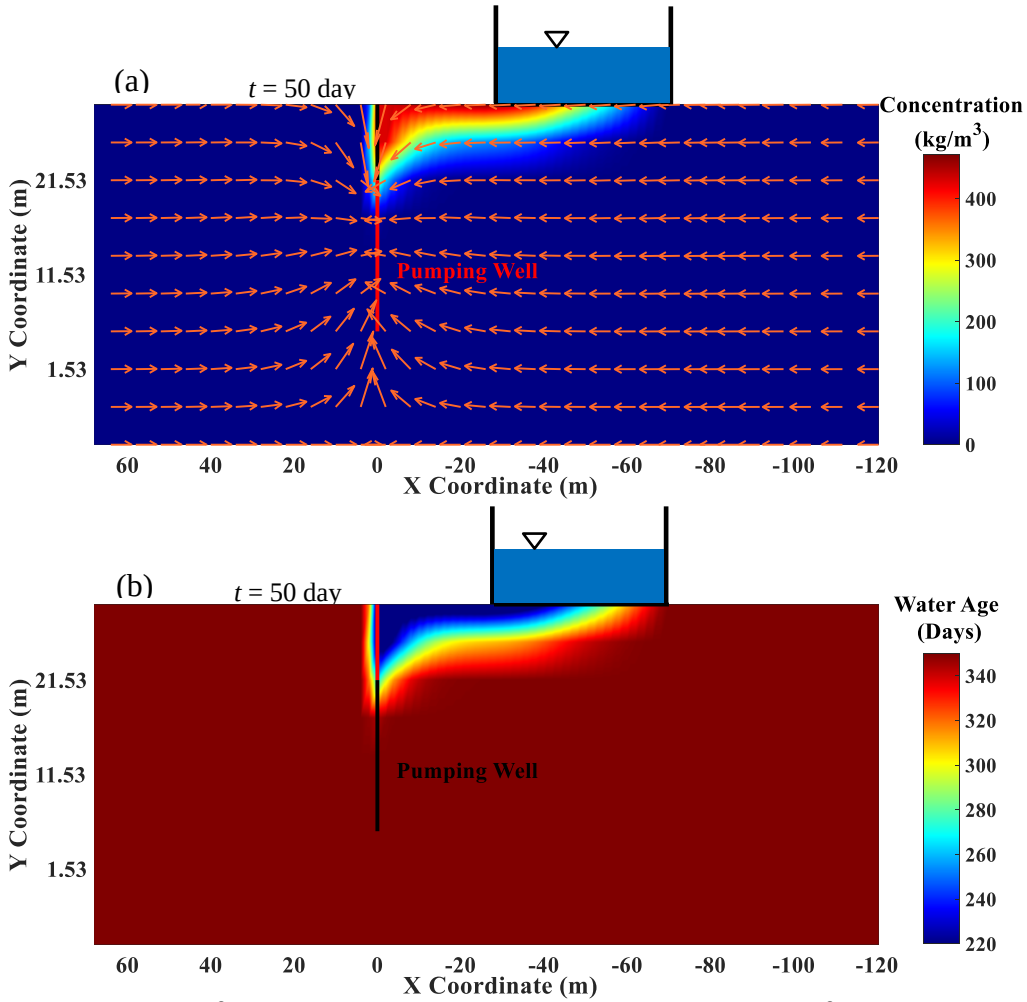

Figure 6.10. Snapshots of the simulated (a) concentration distribution of the conservative tracer (color map) and GW flow field (red arrows represent direction but are not to scale), and (b) distribution of the water age with the time-varying streambed conductivity at t = 50 day (starting from the formal simulation) for the flooding condition 3.

6.4 Discussion

In the traditional numerical study of GW-SW interactions, the streambed conductivity was usually assumed to be constant over time. However, during the flooding period, owing to the dynamic change of the SW flow, erosions and depositions of streambed sediments would be swiftly altered, resulting in a rapid temporal variation of the streambed conductivity. In this chapter, with the facilitation of the estimation model developed in Chapter 4, the time-varying

streambed conductivity was incorporated into the numerical model, and its impact on the RBF system over high-stage events was then studied as well as compared with the simulation conducted with the static streambed conductivity. It was found that over the low-stage period, simulation results with the static and time-varying streambed conductivity generally agreed with each other. For the high-stage period in the flooding condition 1 and 2, the maximum river stage was lower than 40.0 m. The general trends of simulation results with the static and time-varying streambed conductivity were consistent, though discrepancies could be observed. For the flooding condition 3, where the peak of the river stage was higher than 41.0 m, the results simulated with the static streambed conductivity noticeably differed from the results simulated with the time-varying streambed conductivity. It can therefore be concluded that the assumption of a static streambed conductivity can produce a reasonable result under low-stage periods. However, during storm events, the temporal variation of the streambed conductivity must be considered.

6.5 Summary and Conclusions

This chapter investigated hydrological processes of the RBF system in the Money experimental site near the Tallahatchie River in MS, USA, during the flooding periods with the consideration of the time-varying streambed conductivity. The numerical model, CCHE3D-GW, was used to conduct numerical simulations. Three typical flooding conditions were studied, and the time series of the streambed conductivity were obtained by the estimation model developed in Chapter 4. Cases of the static and time-varying streambed conductivity were both simulated. Four items were analyzed, which were the drawdown of the GW hydraulic head, stream depletion, the percentage of the pumped water from the stream, and the mean travel time of the infiltrated SW.

GW heads were found to be almost uninfluenced by the temporal variation of the river stage and streambed conductivity during flooding conditions 1 and 2, in which the maximum river stage was lower than 40.0 m, but experiencing a rise over the flooding condition 3, in which the peak of the river stage was 41.0 m above NAVD 88 datum. Stream depletions simulated with the time-varying and static streambed conductivity were found to be noticeably different over flooding periods, particularly at the crest of the flood wave.

The simulation results revealed that for the flooding conditions 1 and 2, the amount of the pumped water coming from the stream was approximately 3.0 times more than the low-stage period. For the flooding condition 3, the maximum percentage of the pumped water coming from the stream was ten times more than the low-stage period. These comparisons indicate that operating RBF pump during high-stage events results in extracting more water coming from the stream, validating Hypothesis 1 of this chapter. For all three flooding conditions, the maximum percentage simulated with the static streambed conductivity was smaller than the simulation result with the consideration of the time-varying streambed conductivity.

The simulated travel time of the infiltrated SW from the stream to the pumping well was found to be substantially shorter over high-stage events than the low-stage period. For the flooding conditions 1 and 2, the minimum travel time was approximately 40% of the travel time during low-stage period; for the flooding condition 3, the minimum travel time was around 20% of that over the low-stage event, validating Hypothesis 2 of this chapter. The travel time simulated with the static streambed conductivity was generally consistent with the simulation result with the consideration of the time-varying streambed conductivity over low-stage events, but the disparity became clear over flooding periods.

From the *t* tests conducted in this study for comparing the simulation results of the static verses the time-varying streambed conductivity cases, all *P* values were found to be smaller than 0.05, indicating a significant statistical difference between the two simulation scenarios, which validates Hypothesis 3 of this chapter. Thus, these results also indicate the importance of incorporating the time-varying streambed conductivity in studies related to GW-SW interactions, particularly during flooding periods.

CHAPTER VII

NUMERICAL STUDY OF DUNE-INDUCED HYPORHEIC FLOW DURING STORM EVENTS WITH TIME-VARYING STREAMBED CONDUCTIVITY

7.1 Objectives and Hypotheses

This chapter aims at exploring combined effects of the high-stage event and time-varying streambed conductivity on the dune-induced hyporheic flow through numerical simulations with CCHE3D-GW. The hypothesis is that temporal variation of streambed conductivity statistically significantly affects the evolution of hyporheic exchange intensity and mean residence time during high-stage events.

7.2 Methodology

7.2.1 Conceptual Model

Dune is one of the primary topographies in accommodating hyporheic exchange (Bhaskar et al., 2012; Stonedahl et al., 2013). When SW flow passes over a dune, the divergence and re-convergence of stream flow cause difference in the dynamic pressure between the stoss and lee side of the dune, activating the hyporheic flow (Fig. 7.1a). In this study, for simplicity, only a vertical 2-D case was considered, where the effects from the transverse direction of the channel were ignored. Elliott and Brooks (1997a, 1997b) found that the dynamic pressure along the 2-D natural triangular dune generally followed a sinusoidal distribution, and the sediment-water interface (SWI) could be simplified as flat given that the dune height is typically small compared

to the SW depth. The dune-induced hyporheic flow is therefore conceptualized as Fig. 7.1b. The distribution of the hydraulic head over the SWI, h_{SWI}, can be represented as:

$$h_{SWI}(x,t) = -sx + H_S(t) + h_d(t)\cos(\lambda x) \tag{7.1}$$

where, t is time; λ is the wavenumber of a dune and computed as $2\pi/L$ (L is the wavelength of the dune); s is the streambed slope; H_S (t) is the time-varying SW depth and h_d (t) is the intensity of the dynamic head fluctuation, which is computed as (Shen et al., 1990):

$$h_d(t) = 0.28\frac{U_S(t)^2}{2g}\begin{cases}\left(\dfrac{\Delta}{0.34H_S(t)}\right)^{3/8}, & \text{if } \dfrac{\Delta}{H_S(t)} \le 0.34 \\ \left(\dfrac{\Delta}{0.34H_S(t)}\right)^{3/2}, & \text{if } \dfrac{\Delta}{H_S(t)} > 0.34\end{cases} \tag{7.2}$$

where, Δ is the dune height; g is the gravitational acceleration (= 9.81 m/s) and U_s (t) is the mean SW velocity.

The floods studied in this chapter were from the experimental site in Money, Mississippi, USA, which is near the Tallahatchie River. The detailed information of the study site can be found in Chapter 3 and 5. The cross section was idealized as a rectangle with a river width of 42.0 m and the streambed slope (s) was approximated as 0.001, a typical value for an alluvial river. The wavelength (L) and height (Δ) of the dune was set as 1.0 m and 0.10 m, respectively. In Eq. 7.2, the time series of the SW depth, H_S (t), can be directly obtained from the nearby USGS gaging station (USGS 07281600 Tallahatchie River at Money, MS). The discharge of the river is measured by the gaging station every 15 min as well, so the time series of the mean SW velocity, U_S (t), can be attained as $= \frac{\text{River Discharge }(t)}{\text{River Width} \times H_S(t)}$. With these parameters set up, the time varying hydraulic head over the SWI, h_{SWI} (x, t), can be computed through Eq. 7.1 and 7.2, and then imposed on the numerical simulation. This type of reduced-complexity model has been widely

applied in the study of the dune-induced hyporheic flow, particularly for the numerical simulation under the storm event (Wu et al., 2018; Singh et al., 2019, 2020).

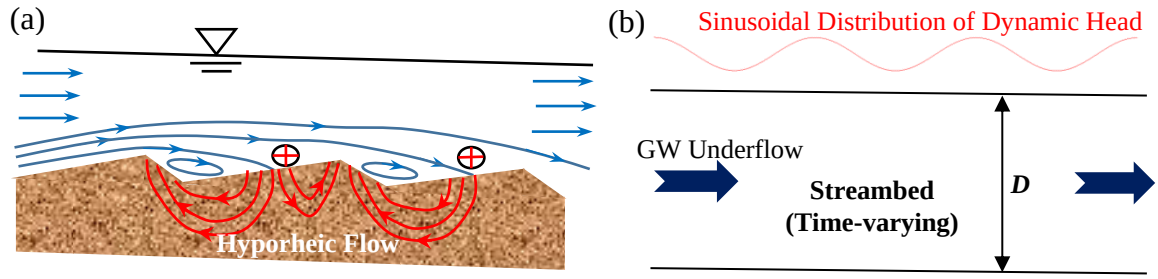

Figure 7.1. (a) Configuration of the dune-induced hyporheic flow in the longitudinal view; (b) conceptual model of this study.

7.2.2 Simulation Domain and Mesh

In the vertical direction (z), the thickness of the domain (D) was set to be 1.0 m, which sufficed to cover the hyporheic zone in order avoid the influence from the bottom boundary. The datum (z = 0) was located at the SWI, and the positive direction was upward. In the longitudinal direction (x), three dunes were covered, resulting in a 3.0 m long domain, and the results of the middle dune were chosen for analysis to minimize possible lateral boundary effects. The origin (x = 0) was set in the middle. A uniform mesh with $\Delta x = \Delta z = 0.005$ m was applied, i.e., the domain was discretized by 601 × 201 nodes.

7.2.3 Flow Model

Since the GW flow in the hyporheic zone is fully saturated, the storage term of the aquifer can be neglected (e.g., Singh et al., 2019; Su et al., 2018; Wu et al., 2018). By combining Darcy's law and the continuity equation, the governing equation of the flow can be written as:

$$\nabla \cdot \left[K(\nabla H) \right] = 0 \tag{7.3a}$$

$$\left. \frac{\partial H}{\partial x} \right|_{x=-1.5L} = -s; \left. \frac{\partial H}{\partial x} \right|_{x=1.5L} = -s \tag{7.3b}$$

$$\left.\frac{\partial H}{\partial z}\right|_{z=-D} = 0 \tag{7.3c}$$

where, H is the hydraulic head of the GW, and K is the hydraulic conductivity. In this study, the aquifer sediment is assumed isotropic, so K is a scalar rather than a tensor. The Darcy velocity, **q**, can be computed as $K(\nabla H)$.

Fig. 7.2 summarizes the configuration of the numerical simulation. The datum (z = 0 m) was set at the streambed surface. The top boundary condition was the prescribed distribution of the hydraulic head shown as Eq. 7.1, and the lateral boundary condition was Eq. 7.3b, representing the GW underflow. In this study, only neutral base flow condition was considered, which is represented by Eq. 7.3c. This simplification is the same as the work of Singh et al. (2019, 2020), which is a limitation since the regional base flow (gaining/losing) would potentially affect the hyporheic exchange (Wu et al., 2018). By implementing a more realistic base flow condition, the simulation result can be further improved. However, since the influence from base flow is not the objective of this study, a simplified bottom boundary condition (Eq. 7.3c) is adopted.

7.2.4 Setup of Static and Time-varying Streambed Conductivity

The traditional estimation model can only render an 'equivalent' streambed conductivity since it assumes that the hydraulic property of the streambed is constant over the whole period of concern (e.g., Obergfell et al., 2019; von Asmuth et al., 2002; von Asmuth et al., 2008). By applying this type of model to a flooding period, a static streambed conductivity, K_S, could be computed, which is the value that is usually adopted by previous studies of GW-SW interactions. With the estimation model developed in Chapter 4, the time series of the streambed conductivity, $K_T(t)$, can be obtained, which is incorporated into the numerical model aimed at studying the impact from the time-varying streambed conductivity on the dune-induced hyporheic exchange.

In this study, numerical simulations were conducted with both the static and time-varying streambed conductivity for the sake of comparison, and the streambed was assumed homogeneous and isotropic for each scenario. Three typical flooding conditions were studied and the temporal variations of H_S, h_d and K_T/K_S are shown in Fig. 7.3.

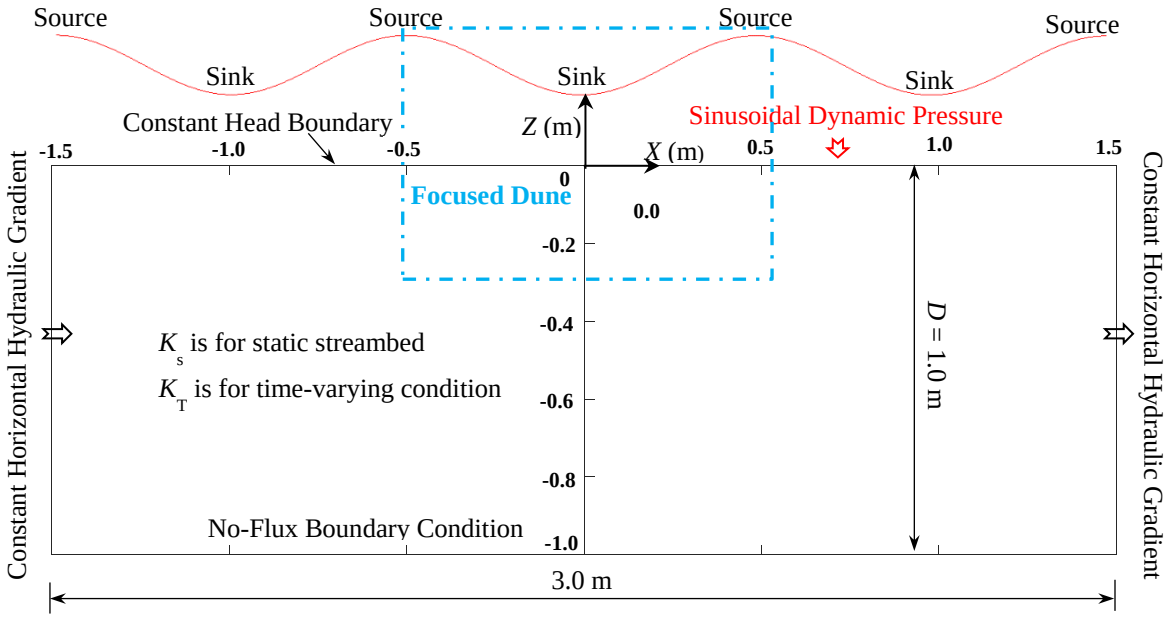

Figure 7.2. Simulation Domain of the 2-D dune-induced hyporheic flow, in which the middle dune is focused in this study.

The flooding condition 1 is from February 22, 2015 to June 22, 2015, which represents the scenario for multiple consecutive flood waves with attenuating amplitudes. For this case, the streambed conductivity increased monotonically during the whole flooding period and then started to drop dramatically when the SW returned to the low-stage condition (the 160th day) (Fig. 7.3 a, iii). The flooding condition 2 is from October 26, 2015 to June 16, 2016, which represents the scenario for multiple consecutive flood events with amplifying amplitudes. The streambed conductivity rose steadily but slowly in the first half of this period. However, after the arrival of a larger flood on the 130th day, it experienced a leap and then stayed at a high value until the 200th

day when it started to decline (Fig. 7.3 b, iii). The flooding condition 3 is from May 7, 2021 to August 3, 2021, which represents the scenario with a single flood wave. For this case, the streambed conductivity jumped to a very high level during the peak of the flood but soon dropped to a low value when the SW returned to the low-stage condition (Fig. 7.3 c, iii). The detailed information of these time-varying processes can be found in Chapter 5.

7.2.5 Tracer Transport Model and Outline of Hyporheic Zone

In order to detect and delineate the hyporheic zone, the transport of conservative tracer was simulated with MT3D (Zheng and Wang, 1999) in this study. The principle is by releasing conservative solutes, which can follow water particles, from the SWI, the hyporheic flow path can be tracked and the extent of the hyporheic zone can therefore be outlined. Since the hydrological process is of primary concern here, only advection was simulated. The governing equation for the transport can therefore be written as:

$$\theta_n \frac{\partial C_g}{\partial t} = -\nabla \cdot \left(\mathbf{q} C_g \right) \tag{7.4a}$$

$$C_g\big|_{z=0} = C_0 \tag{7.4b}$$

where, θ_n is porosity of sediment, which was 0.375 in this study; C_g is concentration of conservative tracer and **q** is the Darcy flux, which was provided by the simulation result of the flow model (CCHE3D-GW). Eq. 7.4b is the top boundary condition that represents a constant concentration of the released tracer (C_0), which was prescribed as 100.0 kg/m^3 in this study. The biogeochemical definition of the hyporheic zone (Triska et al., 1989; Gomez-Velez et al., 2014, 2017) is adopted, in which the subsurface area of $C_g \geq 0.9C_0$ is defined as the hyporheic zone, i.e., at least 90% of the pore water is from the SW. Before the formal study, a 150-day spin-up simulation with the GW flow field of the first time step was conducted to have an equilibrium

initial condition.

7.2.6 Residence Time Model

Residence time is how long the hyporheic flow stays in the subsurface region, which has been frequently studied owing to its tight association with the biogeochemical process (Briggs et al., 2013; Zarnetske et al., 2011), particularly its dynamics during flooding periods (Wu et al. 2018; Singh et al., 2019, 2020). In this study, the governing equation of the mean residence time from Gomez-Velez and Wilson (2013), and Gomez-Velez et al. (2017) was adopted, in which the dispersion process was neglected since the hydrological transport was the priority:

$$\frac{\partial(a_1)}{\partial t} = -\nabla \cdot \left(\frac{\mathbf{q}}{\theta_n} a_1 \right) + 1 \tag{7.5a}$$

$$a_1(x,t)\big|_{z=0} = 0 \ \text{ on } \partial\Omega_{\text{IN}}; \ \left.\frac{\partial a_1}{\partial z}\right|_{z=0} = 0 \ \text{ on } \partial\Omega_{\text{OUT}} \tag{7.5b}$$

$$a_1(x = -1.5L, z) = a_1(x = 1.5L, z) \tag{7.5c}$$

$$\left.\frac{\partial a_1}{\partial z}\right|_{z=-D} = 0 \tag{7.5d}$$

where, a_1 is the 1st moment of the residence time distribution (mean residence time). Eq. 7.5b is used to represent the top boundary condition, where Ω_{IN} and Ω_{OUT} is the inflow and outflow of the SWI, respectively. The physical meaning of Eq. 7.5b is that for the SW flowing into the streambed (from Ω_{IN}), its residence time is zero ($a_1 = 0$). Eq. 7.5c is for the periodical lateral boundary condition and the bottom boundary is non-flux. Similar to the conservative tracer, prior to the formal study, a 150-day spin-up simulation with the GW flow field of the first time step was conducted to make the system reach an equilibrium condition.

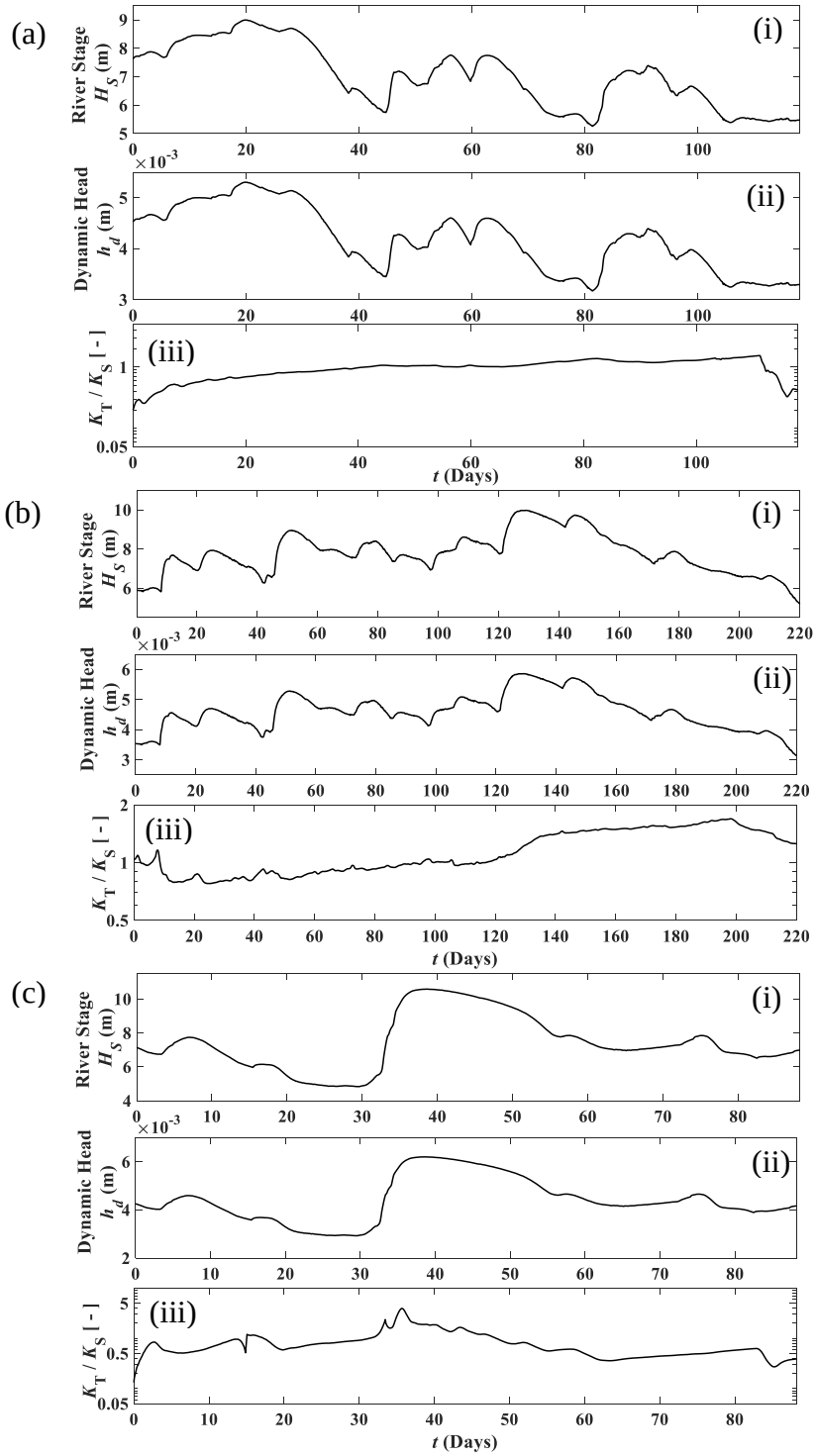

Figure 7.3. Temporal variation of (i) the river stage, H_S, (ii) the dynamic-head intensity, h_d, and (iii) the ratio between the time-varying (K_T) and the static streambed conductivity (K_S) for (a) the flooding condition 1 (from February 22, 2015 to June 22, 2015), (b) flooding condition 2 (from October 26, 2015 to June 16, 2016) and (c) flooding condition 3 (from May 7, 2021 to August 3, 2021).

7.3 Simulation Results

7.3.1 Flooding Condition 1

7.3.1.1 Hyporheic Zone Depth and Area

Fig. 7.4a and b shows the evolution of the hyporheic zone simulated with the static and time-varying streambed conductivity, respectively, over this flooding period, in which three representative time steps, t = 0.0, 0.5t_{total} and 1.0t_{total}, are chosen for presentation and labeled by (i), (ii) and (iii), respectively. Red arrows are used to represent the direction of the GW flow but not to scale. From the flow field, the flow paths that originate from the SW, pass through the streambed and emerge back to the stream can be clearly detected and derived. They are the so-called hyporheic flows. With these circular streamlines, the hyporheic zone is formed, where the SW and GW actively interact with each other. The color map is the concentration distribution of the conservative tracer, from which the hyporheic zone can be delineated as the black solid line shown in Fig. 7.4. In general, the hyporheic zone is confined in the shallow streambed sediment layer and the deep aquifer is hardly reached by the conservative tracers that are released from the stream.

Fig. 7.5a and b shows the simulation result of the temporal variation of the depth (D_{HF}) and area ($Area_{HF}$) of the hyporheic zone during the flooding condition 1, respectively. It can be found that both D_{HF} and $Area_{HF}$ approach to a constant value after the 150-day spin-up simulation, indicating that the system has achieved an equilibrium condition. After the spin-up period, D_{HF} simulated with the time-varying streambed (black line in Fig. 7.5a) is slightly smaller than D_{HF} simulated with the static streambed (red line in Fig. 7.5a) because at the first time step, K_T is lower than K_S, evidenced by $K_T/K_S < 1.0$ at t = 0 shown in Fig. 7.3 (a, iii). However, when entering into

the formal simulation, D_{HF} simulated with the time-varying streambed conductivity gradually increases and after 20 days, it becomes almost identical to D_{HF} of the static streambed (Fig. 7.5a). For both the static and time-varying scenarios, D_{HF} is found to fluctuate mildly during this flooding period, which is associated with the dynamics of the SW flow. With the risings and fallings of flood waves, the energy of driving the hyporheic flow, the dynamic-head intensity (Fig. 7.3 a, ii), is correspondingly altered, which therefore changes the hyporheic zone depth. However, the simulation result reveals that this variation is small. The same phenomenon can be observed for $Area_{HF}$ (Fig. 7.5b), indicating that under this circumstance, the extent of the hyporheic zone is minimally affected by the temporal variations of both the dynamic-head intensity and streambed conductivity. This finding can also be illustrated by Fig. 7.4, from which it can be observed that the shape of the hyporheic zone (dark red in Fig. 7.4) generally does not differ too much at the three representative time steps despite some slight variations of its outline (black line in Fig. 7.4).

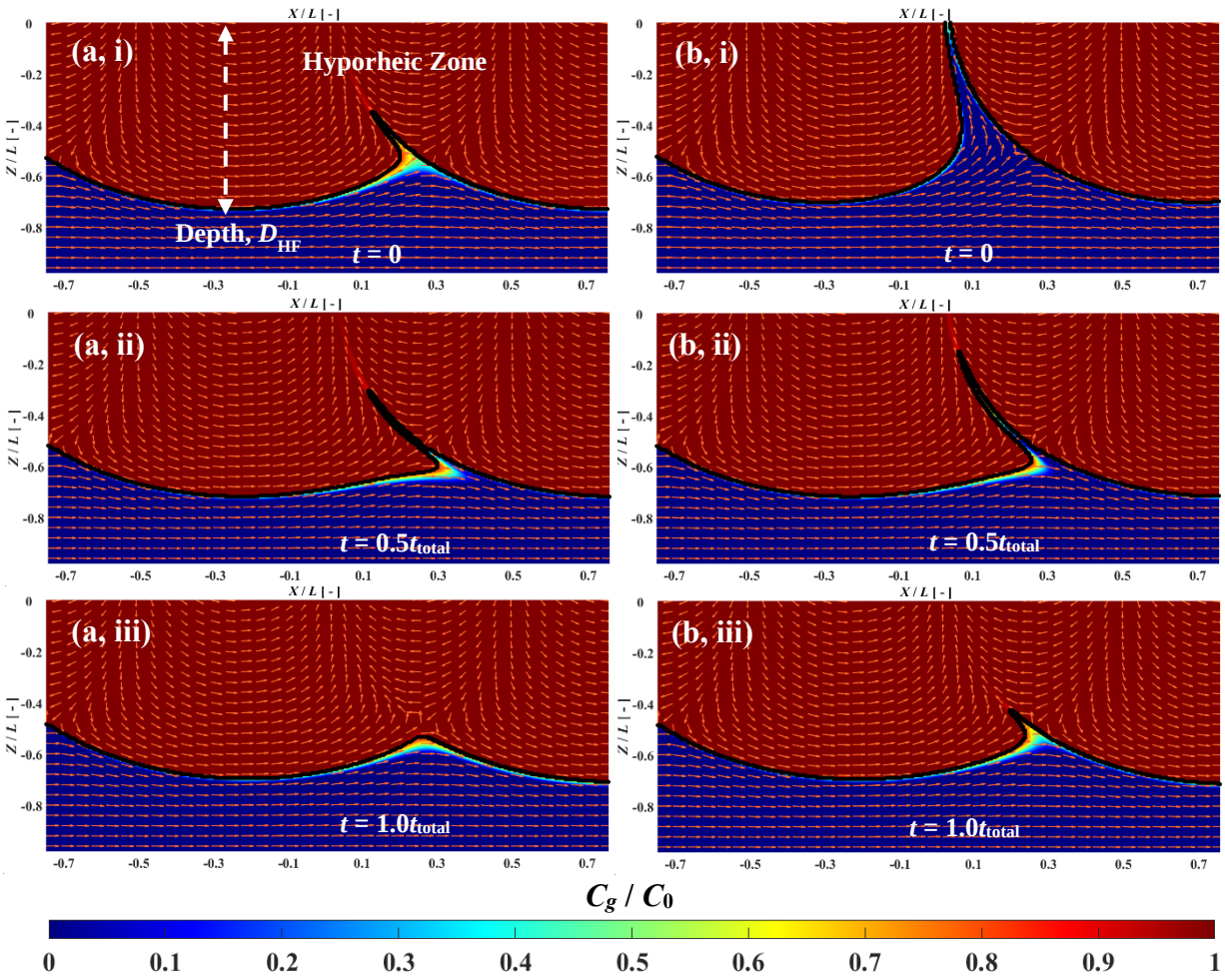

Figure 7.4. Snapshots of the flow field (red arrows represent direction but are not to scale), outline of the hyporheic zone (black solid line) and the concentration distribution of the conservative tracer (color map), in which (a) and (b) is under the static and time-varying streambed conductivity, respectively. (i), (ii) and (iii) is at t = 0.0, 0.5 and 1.0t_{total}, respectively, over the flooding period 1.

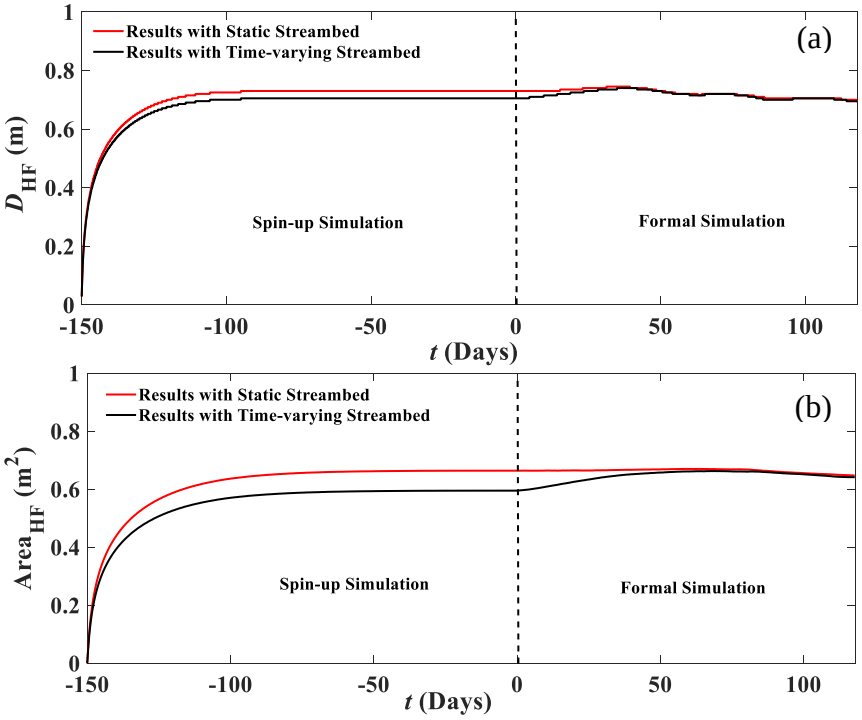

Figure 7.5. Temporal variation of the (a) depth and (b) area of the hyporheic zone for the flooding period 1.

7.3.1.2 Mean Hyporheic Flux

The hyporheic flow is the circulated exchange between SW and GW, i.e., it flows from SW to GW and then returns to stream. Under the neutral condition, the streambed is of mass balance, i.e., the inflow from the stream to streambed is equal to the outflow. Either the influx or outflux of the SWI is identical to the hyporheic flux (Su et al. 2018). The mean hyporheic flux over a dune, $\overline{q}_{\mathrm{HF}}$, can therefore be obtained from the simulation result as:

$$\overline{q}_{\mathrm{HF}} = \frac{1}{L}\int_0^L \left(v_{\mathrm{outflow}}\big|_{z=0} \right) dx \tag{7.6}$$

where, v_{outflow} is the seepage velocity of the outflow at the streambed surface. The dimensionless form of the mean hyporheic flux $\overline{q}^*_{\mathrm{HF}}$ is computed as:

$$\bar{q}^{*}_{\mathrm{HF}} = \frac{\bar{q}_{\mathrm{HF}}}{\bar{q}_{\mathrm{HF,S}}\big|_{t=0}} \tag{7.7}$$

where, $\bar{q}_{\mathrm{HF,S}}\big|_{t=0}$ is the mean hyporheic flux simulated with the static streambed conductivity at t = 0. In this study, $\bar{q}^{*}_{\mathrm{HF,S}}$ and $\bar{q}^{*}_{\mathrm{HF,T}}$ is used to represent the dimensionless hyporheic flux under the static and time-varying streambed conductivity, respectively.

Fig. 7.6c shows the temporal variation of the mean hyporheic flux simulated with the static streambed conductivity during the flooding condition 1. The shape of this curve is similar to the dynamic-head intensity (Fig. 7.6a), in which their fluctuations follow the same trend and occur at the same time. However, the temporal variation of the mean hyporheic flux simulated with the time-varying streambed conductivity (Fig. 7.6d) is dissimilar to the temporal variation of the dynamic-head intensity. Instead, it more resembles the curve of the time-varying streambed conductivity (Fig. 7.6b).

The first flood event occurred from 0 to 0.35t_{total}, in which h_d gradually increased from 4.51 × 10^{-3} m to 5.35 × 10^{-3} m from 0 to 0.20t_{total} and soon dropped to less than 3.5 ×10^{-3} m in the following 0.10t_{total} (Fig. 7.6a). Correspondingly, $\bar{q}^{*}_{\mathrm{HF,S}}$ slightly climbed from 1.0 to 1.2 during the rising limb of the flood while decreased to less than 0.8 after the recession (Fig. 7.6c). When considering the time-varying streambed conductivity, since the streambed was of low permeability prior to the onset of the storm (Fig. 7.6b), $\bar{q}^{*}_{\mathrm{HF,T}}$, which was only 0.25 (Fig. 7.6d), was much smaller than $\bar{q}^{*}_{\mathrm{HF,S}}$ in the beginning. Due to the consistent increase of the streambed conductivity as well as the stronger dynamic-head intensity over the rising limb, $\bar{q}^{*}_{\mathrm{HF,T}}$ incremented substantially and approached to 1.0 on 0.20t_{total} (Fig. 7.6d). During the recession period, despite the decline of the river stage, the streambed conductivity was still in a session of a persistent rise. Influence by the

conflict between a weaker dynamic-head intensity and a more permeable streambed, $\bar{q}^*_{\mathrm{HF,S}}$ decreased slightly but then generally stabilized at 0.8 from 0.20 ~ 0.35t_{total}, which was unlike the swift drop of $\bar{q}^*_{\mathrm{HF,S}}$ over the same period.

The second flood event was from 0.38t_{total} to 0.70t_{total}, which was composed of three flood waves. Compared to the first flood event, this one was relatively weak, where the peak value of h_d was around 4.8×10^{-3} m (Fig. 7.6a). For the static streambed simulation, the temporal variation of the mean hyporheic flux generally followed the trend of the dynamic-head intensity, in which three waves can be clearly observed (Fig. 7.6c). Around the same period, $K_{\mathrm{T}}/K_{\mathrm{S}}$ generally remained at 1.0 according to the estimation result (Fig. 7.6b), so the variation of $\bar{q}^*_{\mathrm{HF,T}}$ followed the dynamic-head intensity as well (Fig. 7.6d). This phenomenon can be more clearly seen in the 'close-up' figure that is marked by the red dashed rectangle in Fig. 7.6d, in which the three waves are noticeable in the curve of $\bar{q}^*_{\mathrm{HF,T}}$. For this flood event, since the value of the time-varying streambed conductivity was close to the static value, $\bar{q}^*_{\mathrm{HF,T}}$ and $\bar{q}^*_{\mathrm{HF,S}}$ were generally at the same level.

The third flood event took place from 0.7t_{total} to 0.90t_{total}. The peak value of h_d was around 4.4×10^{-3} m, which occurred at 0.78t_{total} (Fig. 7.6a), indicating that this storm was weaker than the previous two. The temporal variation of $\bar{q}^*_{\mathrm{HF,S}}$ followed the same trend of h_d and the maximum value of $\bar{q}^*_{\mathrm{HF,S}}$ was1.0. After the flood passed, the stream came to the low-stage condition (from 0.90t_{total} to final step), so $\bar{q}^*_{\mathrm{HF,S}}$ correspondingly dropped to a low value of approximately 0.70 and remained constant until the end of this simulation period (Fig. 7.6c). However, when the time-varying streambed conductivity was considered, owing to the continuous increase of the streambed conductivity over this period, $\bar{q}^*_{\mathrm{HF,T}}$ stayed at a high value (1.2) despite the decline of h_d. When t = 0.92t_{total}, the streambed conductivity started to drop dramatically (Fig. 7.6b), resulting in a sharp

drop of $\bar{q}^{*}_{\mathrm{HF,T}}$ (Fig. 7.6d). A *t* test indicated that mean difference of the hyporheic flux simulated with the static and time-varying streambed conductivity over flooding condition 1 was statistically significant ($P < 0.01$).

7.3.1.3 Mean Residence Time

Residence time is the duration that the hyporheic flow stays in the subsurface region. With a stronger dynamic-head intensity or/and a higher permeable streambed, the GW flow will be accelerated, resulting in a shorter residence time. The flux-weighted mean residence time of the hyporheic flow, Mean $\mathrm{RT_{HF}}$, is analyzed here and the method of calculation is the same as the work of Singh et al. (2019) and Wu et al. (2018). The dimensionless flux-weighted mean residence time, Mean $\mathrm{RT^{*}_{HF}}$ is defined:

$$\text{Mean } \mathrm{RT^{*}_{HF}} = \frac{\text{Mean } \mathrm{RT_{HF}}}{\text{Mean } \mathrm{RT_{HF,S}}\big|_{t\,=\,0}} \tag{7.8}$$

where, $\text{Mean } \mathrm{RT_{HF,S}}\big|_{t\,=\,0}$ is the flux-weighted mean residence time of the hyporheic flow simulated with the static streambed conductivity at $t = 0$. Mean $\mathrm{RT^{*}_{HF,S}}$ and Mean $\mathrm{RT^{*}_{HF,T}}$ is used to denote the dimensionless flux-weighted mean residence time under the static and time-varying streambed conductivity, respectively.

Fig. 7.6e and f shows the temporal variation of the simulated Mean $\mathrm{RT^{*}_{HF,S}}$ and Mean $\mathrm{RT^{*}_{HF,T}}$ during the flooding condition 1, respectively, in which the direction of the *y* coordinate is reversed to better present and compare the results. In general, the temporal variation of Mean $\mathrm{RT^{*}_{HF,S}}$ is similar to the temporal variation of the dynamic-head intensity (Fig. 7.6a) with respect to the shape though smoother. The temporal variation of Mean $\mathrm{RT^{*}_{HF,T}}$ generally follows the trend of the time-varying streambed conductivity (Fig. 7.6b).

During the rising limb of the first flood event, owing to a stronger dynamic-head intensity, the hyporheic flow was pushed to move faster in the subsurface region, causing Mean $RT^*_{HF,S}$ to decline from 1.0 to 0.90. During the recession period, the dynamic-head intensity, which drives the hyporheic flow, was substantially weakened. It therefore took a longer time for the hyporheic flow to pass through the streambed, resulting in an increasing Mean $RT^*_{HF,S}$, which was around 1.12 at the end of this flood event ($t = 0.35t_{total}$). On the other hand, when incorporating the time-varying streambed conductivity into the numerical model, due to the low-permeable condition of the streambed before the storm event, Mean $RT^*_{HF,T}$, which was more than 2.5, was much longer than Mean $RT^*_{HF,S}$ in the beginning. It reveals that when neglecting the temporal variation of the streambed conductivity, for the low-stage period, the frequency of the hyporheic exchange would be overestimated, which would in turn misevaluate the dominant biogeochemical process in this region. For instance, the mean residence time of the hyporheic flow has been found to be a crucial parameter in determining whether the streambed system is of a net nitrate production or net uptake (Briggs et al., 2013; Marzadri et al., 2011; Zarnetske et al., 2011). A wrong calculation of this value would result in an erroneous assessment of the general behavior of the riverine system. With the consistent increase of the streambed conductivity, Mean $RT^*_{HF,T}$ was shortened persistently from 0 to $0.35t_{total}$ despite the risings and fallings of the dynamic-head intensity. At the end of the first flood event, Mean $RT^*_{HF,T}$ declined to 1.0.

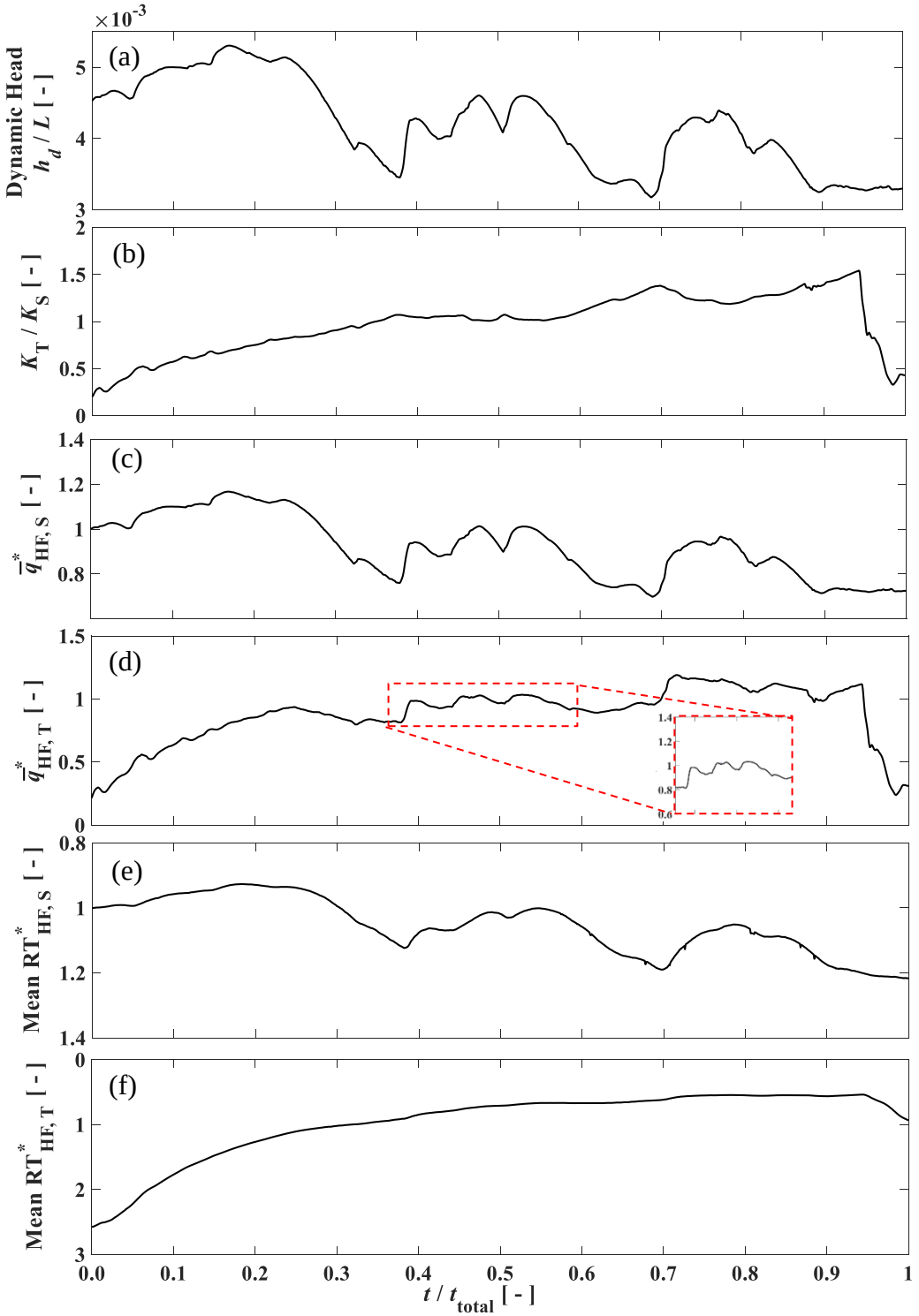

Figure 7.6. Temporal variation of the (a) dynamic-head intensity, (b) streambed conductivity, (c) and (d) mean hyporheic flux simulated with the static and time-varying streambed conductivity, respectively, and (e) and (f) mean flux-weighted residence time under the static and time-varying streambed, respectively, over flooding period 1.

The second flood event consisted of three flood waves from 0.38 ~ 0.70t_{total} (Fig. 7.6a). The general trend of the temporal variation of Mean $RT^*_{HF,S}$ is similar to the dynamic-head intensity, in which three waves can be observed (Fig. 7.6e). However, unlike the sharp fluctuation of h_d shown in Fig. 7.6a, the curve of Mean $RT^*_{HF,S}$ (Fig. 7.6e) oscillated mildly and was much smoother. Around the same period, owing to the slow but steady rise of the streambed conductivity, Mean $RT^*_{HF,T}$ was gradually shortened from 1.0 to 0.5 (Fig. 7.6e). The temporal variation of Mean $RT^*_{HF,T}$ was found invariant to the fluctuation of the dynamic-head intensity over this period.

During the third flood event, which was from 0.7 ~ 0.90t_{total}, the temporal variation of Mean $RT^*_{HF,S}$ only followed the general rising and falling trend of the dynamic-head intensity while small fluctuations were all smoothed. After the flood passed, the stream returned to the low-stage condition and Mean $RT^*_{HF,S}$ slowly climbed to 1.22. However, with the consideration of the time-varying streambed conductivity, due to the consistent increase of the streambed conductivity over this period, Mean $RT^*_{HF,T}$ almost remained at a constant, 0.5, despite the variation of the dynamic-head intensity. When $t = 0.92t_{total}$, the streambed conductivity started to drop dramatically, causing Mean $RT^*_{HF,T}$ to rise to 1.0 at the end of the simulation. A *t* test indicated that mean difference of the mean residence time simulated with the static and time-varying streambed conductivity over flooding condition 1 was statistically significant ($P < 0.01$).

7.3.2 Flooding Condition 2

7.3.2.1 Hyporheic Zone Depth and Area

Fig. 7.7a and b shows the temporal variation of the hyporheic zone shape simulated with the static and time-varying streambed conductivity, respectively, over the flooding condition 2, in which the meanings of the labels are the same as them in Fig. 7.4. The red arrows indicate the

direction of the GW flow but are not to scale. Through the simulated concentration distribution of the tracer, which is represented by the color map, the outline of the hyporheic zone can be attained and is marked by the black solid line in Fig. 7.7. From visual comparisons, for both the static and time-varying scenarios, the shape and extent of the hyporheic zone (dark red in Fig. 7.7) generally does not change too much at the three representative time steps though some subtle variations could be observed.

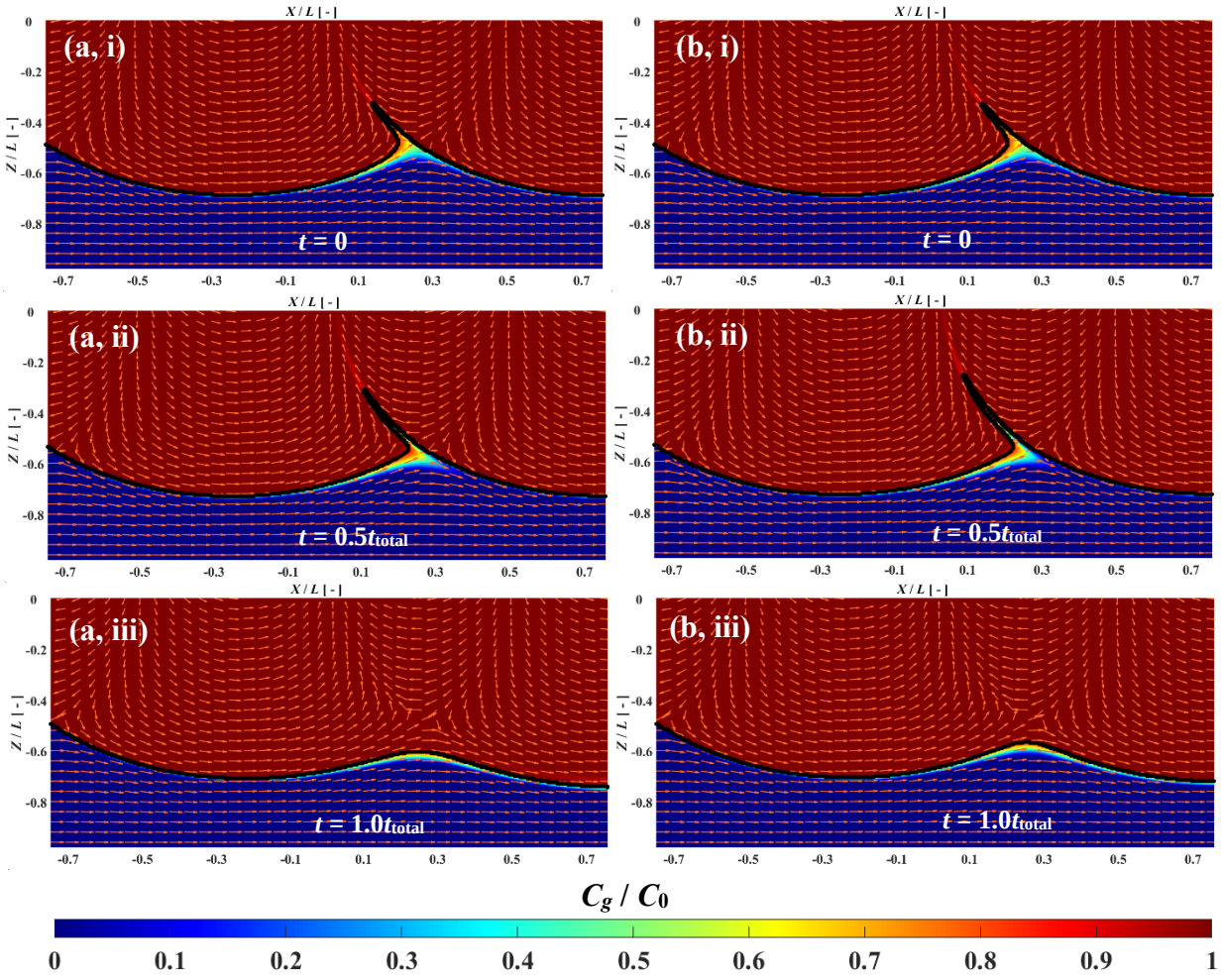

Figure 7.7. Snapshots of the flow field (red arrows represent direction but are not to scale), outline of the hyporheic zone (black solid line) and the concentration distribution of the conservative tracer (color map), in which (a) and (b) is under the static and time-varying streambed conductivity, respectively. (i), (ii) and (iii) is at t = 0.0, 0.5 and 1.0t_{total}, respectively, over the flooding period 2.

Fig. 7.8a and b shows the simulation result of the temporal variation of the depth (D_{HF}) and area ($Area_{HF}$) of the hyporheic zone during the flooding condition 2, respectively. After the 150-day spin-up simulation, both D_{HF} and $Area_{HF}$ reach a constant value, indicating an equilibrium initial condition for the formal simulation. Similar to the flooding condition 1, for this case, the depth and area of the hyporheic zone are generally not influenced by the temporal variation of both the dynamic-head intensity and streambed conductivity. For both D_{HF} and $Area_{HF}$, the simulation results under the static and time-varying streambed conductivity are close to each other, which can be concluded from the almost coincident black and red curves show in Fig. 7.8.

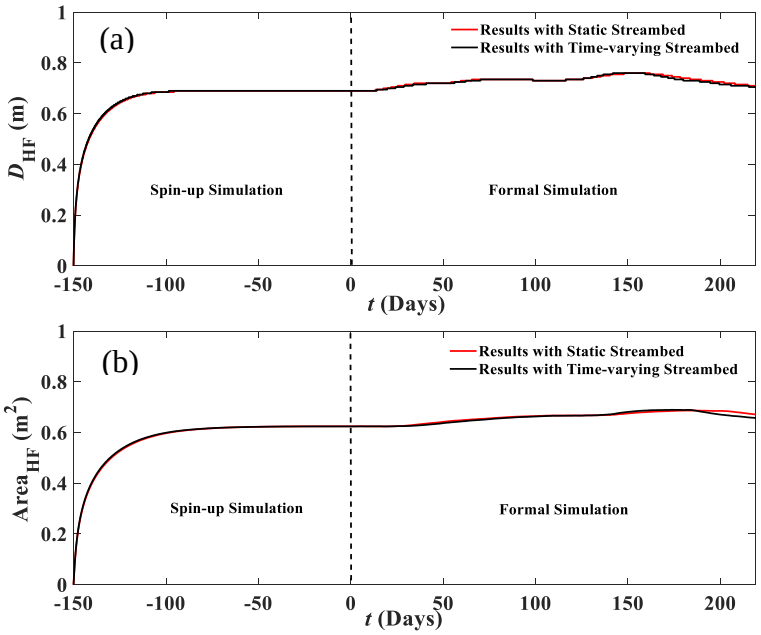

Figure 7.8. Temporal variation of the (a) depth and (b) area of the hyporheic zone for the flooding condition 2.

7.3.2.2 Mean Hyporheic Flux

Fig. 7.9c shows the temporal variation of the simulated mean hyporheic flux under the static streambed conductivity during the flooding condition 2, which generally follows fluctuations of h_d (Fig. 7.9a). When considering the time-varying streambed conductivity, the temporal

variation of the simulated mean hyporheic flux becomes more intricate, which is shown in Fig. 7.9d. In general, the whole process can be divided into two stages. From t = 0 to 0.55t_{total}, owing to a relatively low-permeable streambed, $\bar{q}^*_{\text{HF,T}}$ varied in the range of 0.8 to 1.8, which was at the same scale of $\bar{q}^*_{\text{HF,S}}$ (Fig. 7.9c). However, after t = 0.55t_{total}, with a considerable rise of the streambed conductivity, $\bar{q}^*_{\text{HF,T}}$ increased substantially and reached its peak value of 2.5 (Fig. 7.9d), which was higher than the peak value of $\bar{q}^*_{\text{HF,S}}$ ($\approx$ 1.6) at the same period (Fig. 7.9c). As the flood passed and streambed conductivity started to decline, $\bar{q}^*_{\text{HF,T}}$ dropped rapidly.

For this case, according to the estimation result of the time-varying streambed conductivity (Fig. 7.9b), in the low-stage period before the onset of the flood (from 0.0 to 0.05t_{total}), the permeability of the streambed was relatively high and its hydraulic conductivity was close to the static value ($K_{\text{T}}/K_{\text{S}} \approx 1$). The value of $\bar{q}^*_{\text{HF,T}}$ was therefore almost identical to $\bar{q}^*_{\text{HF,S}}$ over the same period. From t = 0.05t_{total} to 0.55t_{total}, this site was consecutively visited by several floods and peak values of the dynamic-head intensity were in the region of 5.0×10^{-3} m. Correspondingly, $\bar{q}^*_{\text{HF,S}}$ followed the same trend to fluctuate, in which the minimum value was 1.0 as the maximum was less than 1.6. However, when considering the impact from the time-varying streambed conductivity, the temporal variation of $\bar{q}^*_{\text{HF,T}}$ becomes different and complicated. $\bar{q}^*_{\text{HF,T}}$ first decreased from 1.2 to 1.0 from 0.50t_{total} to 0.80t_{total} owing to the decline of the streambed conductivity (Fig. 7.9b). After that, the streambed conductivity went up slowly but steadily, resulting in an upward tendency of $\bar{q}^*_{\text{HF,T}}$. Aside from that, the temporal variation of $\bar{q}^*_{\text{HF,T}}$ also exhibited strong oscillations during this period, which can be clearly observed in the 'close-up' figure that is marked by the red dashed rectangle in Fig. 7.9d. In general, since $K_{\text{T}}/K_{\text{S}}$ was close to 1.0 at this stage, $\bar{q}^*_{\text{HF,S}}$ and $\bar{q}^*_{\text{HF,T}}$ were at the same scale.

A flood with an amplitude that was larger than the previous flood waves arrived at the site at $0.60t_{\text{total}}$, in which the peak value of the dynamic-head intensity was 6.0×10^{-3} m. It pushed $\bar{q}^*_{\text{HF,S}}$ to increase from 1.2 to 1.6 immediately. During the recession of the flood, $\bar{q}^*_{\text{HF,S}}$ gradually decreased owing to the weaker dynamic-head intensity and at the end of this period, it became less than 1.0. Meanwhile, when considering the time-varying streambed conductivity, due to the rapid rise of both h_d and K_{T}, $\bar{q}^*_{\text{HF,T}}$ leaped from less than 1.5 to around 2.3 at $0.60t_{\text{total}}$. This indicates a strong intensification of the hyporheic exchange, which cannot be captured by the simulation of the static streambed conductivity. During the flooding recession, due to the continuous rise of the streambed conductivity from $0.70t_{\text{total}}$ to $0.90t_{\text{total}}$, $\bar{q}^*_{\text{HF,T}}$ only declined slightly. However, after $t = 0.90t_{\text{total}}$, with the decrease of both the dynamic-head intensity and streambed conductivity, $\bar{q}^*_{\text{HF,T}}$ began to drop. A *t* test indicated that mean difference of the hyporheic flux simulated with the static and time-varying streambed conductivity over flooding condition 2 was statistically significant ($P < 0.01$).

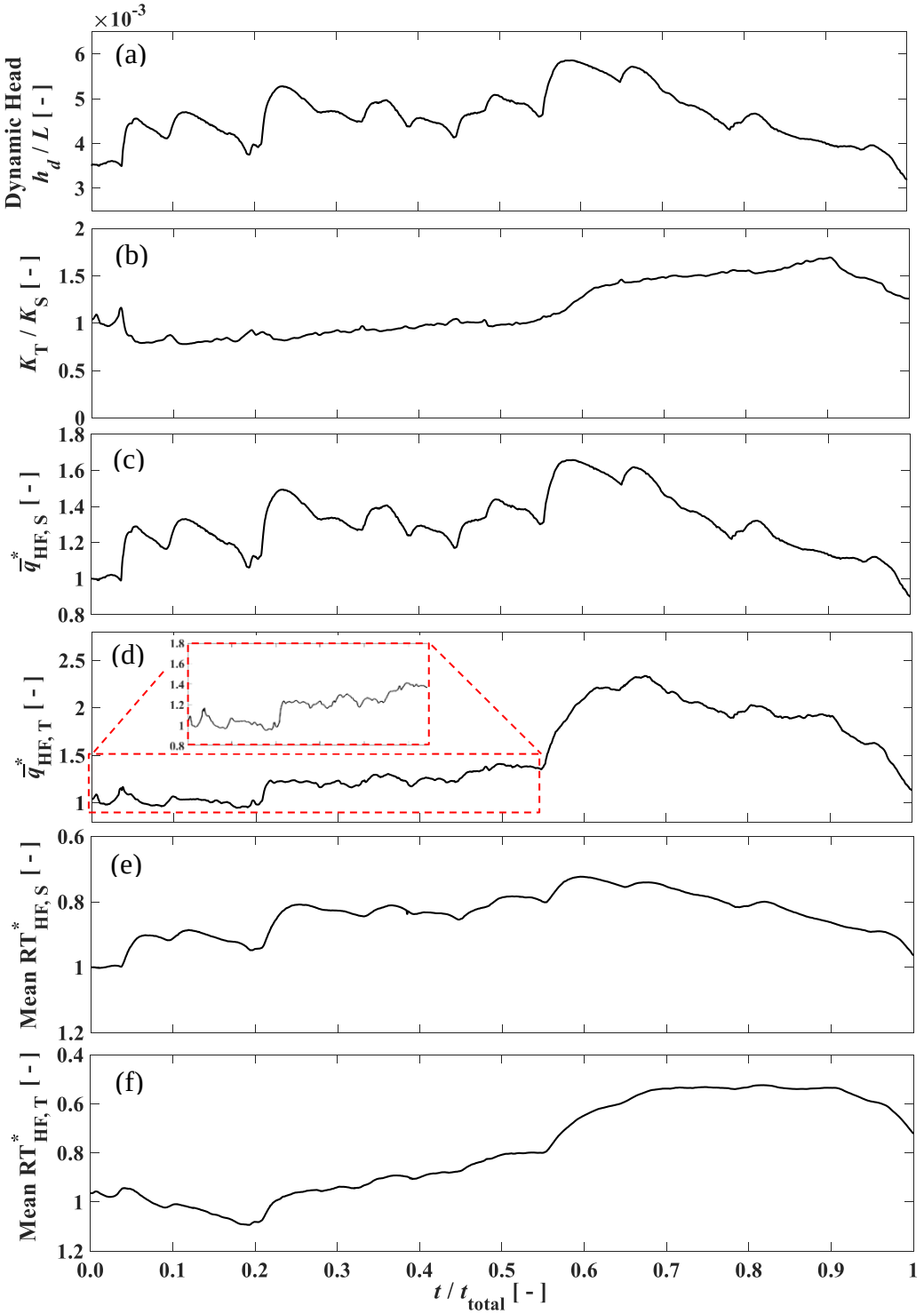

Figure 7.9. Temporal variation of the (a) dynamic head intensity, (b) streambed conductivity, (c) and (d) mean hyporheic flux simulated with the static and time-varying streambed conductivity, respectively, and (e) and (f) mean flux-weighted residence time under the static and time-varying streambed, respectively, over flooding period 2.

7.3.2.3 Mean Residence Time

Fig. 7.9e and f presents the temporal variation of the dimensionless flux-weighted mean residence time simulated with the static and time-varying streambed conductivity during the flooding condition 2, respectively. The *y* coordinate is reversed aimed at better exhibiting the comparisons of the results. Generally, under the static streambed condition, the simulated Mean $RT^*_{HF,S}$ follows the tendency of the dynamic-head intensity (Fig. 7.9a) to vary with time though it is much smoother. With the consideration of the time-varying streambed conductivity, the temporal variation of the simulated Mean $RT^*_{HF,T}$ is similar to the shape of the streambed-conductivity curve (Fig. 7.9b) despite being slightly affected by the oscillation of the dynamic-head intensity.

In the early stage of this case (before $0.55t_{total}$), owing to the flood waves, the dynamic-head intensity was in fluctuation, which in turn made Mean $RT^*_{HF,S}$ oscillate simultaneously (Fig. 7.9e). Over the same period, the dynamic-head intensity was also experiencing an overall trend of increase, causing Mean $RT^*_{HF,S}$ to decline from 1.0 to 0.8 generally (noticing that the *y* coordinate in Fig. 7.9e is reversed). However, when the time-varying streambed conductivity was considered, the mean residence time varied in a different manner. In Fig. 7.9f, it could be found that from $0.05t_{total}$ to $0.20t_{total}$, due to the decreasing streambed conductivity (Fig. 7.9b), Mean $RT^*_{HF,T}$ was on the rise, which was from around 0.95 to more than 1.0, despite the arrival of the first flood wave at $0.10t_{total}$. From $0.20t_{total}$ to $0.55t_{total}$, Mean $RT^*_{HF,T}$ was shortened constantly due to the incremental streambed conductivity. At the same time, some fluctuations could be observed in the curve of Mean $RT^*_{HF,T}$ (Fig. 7.9f), which were associated with the dynamic-head intensity, though they were much smaller than the fluctuations in the curve of Mean $RT^*_{HF,S}$.

Starting from $t = 0.55t_{total}$ to $0.65t_{total}$, with the arrival of a strong flood and a huge increase of the streambed conductivity, the GW flow in the hyporheic zone were significantly accelerated, resulting in a substantial reduction of the mean residence time. From Fig. 7.9f, it could be found that Mean $RT^*_{HF,T}$ dropped from 0.8 to less than 0.6, indicating a much more active hyporheic exchange. On the other hand, the reduction of the mean residence time simulated with the static streambed conductivity was not as large as that under the time-varying scenario, in which the corresponding minimum value of Mean $RT^*_{HF,S}$ was around 0.7 (Fig. 7.9e). During the recession of the last flood (from $0.65t_{total}$ to the end), following in the trend of a weaker dynamic-head intensity, Mean $RT^*_{HF,S}$ consistently augmented, illustrating that the hyporheic zone was becoming inactive. However, for Mean $RT^*_{HF,T}$, due to the continuous increment of the streambed conductivity until $0.90t_{total}$, it was kept at a low value, 0.55 (Fig. 7.9f), indicating that the hyporheic zone remained in an active status, which was diametrically opposite to the result of the static streambed simulation. After $0.90t_{total}$, with the decline of both the streambed conductivity and dynamic-head intensity, Mean $RT^*_{HF,T}$ started to increase. A *t* test indicated that mean difference of the mean residence time simulated with the static and time-varying streambed conductivity over flooding condition 2 was statistically significant ($P < 0.01$).

7.3.3 Flooding Condition 3

7.3.3.1 Hyporheic Zone Depth and Area

Fig. 7.10a and b shows the temporal evolution of the hyporheic zone simulated with the static and time-varying streambed conductivity, respectively, over flooding condition 3, in which the meanings of the labels are the same as them of Fig. 7.4. The red arrows indicate the direction of the GW flow while they are not to scale. Through the simulated concentration distribution of

the tracer (represented by the color map), the extent of the hyporheic zone can be detected, of which the outline is depicted by the black solid line in Fig. 7.10. From the visual comparisons, the area of the hyporheic zone under the time-varying streambed conductivity (Fig. 7.10b) is slightly smaller than the area simulated with the static streambed conductivity (7.10a). To quantify this difference, the temporal variation of the simulated depth (D_{HF}) and area ($Area_{HF}$) of the hyporheic zone during this flooding condition is plotted as Fig. 7.11a and b, respectively.

From Fig. 7.11, it can found that after the 150-day spin-up simulation, both D_{HF} and $Area_{HF}$ arrive at a constant value, indicating an equilibrium condition. In the early stage of the formal study, both D_{HF} and $Area_{HF}$ simulated with the time-varying streambed conductivity (black line in Fig. 7.11) are smaller than that under the static condition (red line in Fig. 7.11) because K_T is lower than K_S over this period (Fig. 7.3c, iii). However, with a more permeable streambed, D_{HF} and $Area_{HF}$ simulated with the time-varying streambed conductivity gradually increase and ultimately become close to their counterpart of the static scenario (Fig. 7.11). D_{HF} and $Area_{HF}$ simulated with both the static and time-varying streambed conductivity are found to fluctuate mildly during the flood crest (Fig. 7.11). However, in general, the variation is marginal, which indicates that for this case, the influences from the temporal variation of both the dynamic-head intensity and streambed conductivity on the extent of the hyporheic zone are minimal.

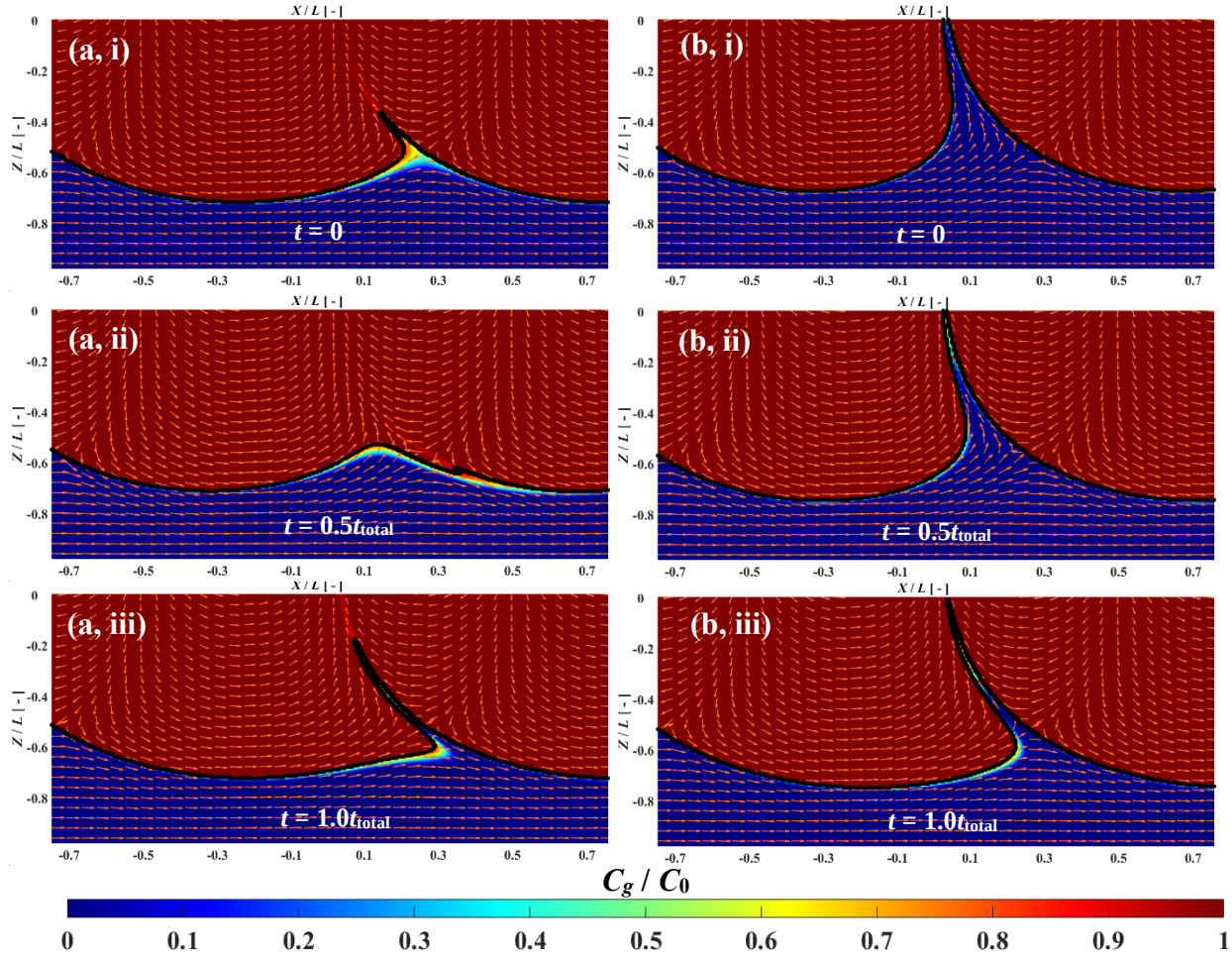

Figure 7.10. Snapshots of the flow field (red arrows represent direction but are not to scale), outline of the hyporheic zone (black solid line) and the concentration distribution of the conservative tracer (color map), in which (a) and (b) is under the static and time-varying streambed conductivity, respectively. (i), (ii) and (iii) is at t = 0.0, 0.5 and 1.0t_{total}, respectively, over the flooding period 3.

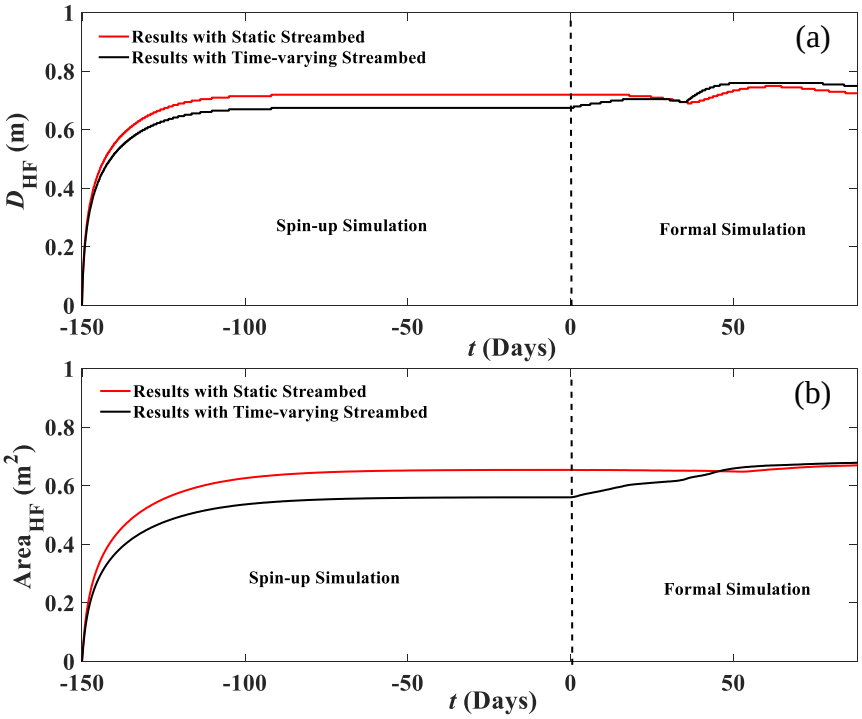

Figure 7.11. Temporal variation of the (a) depth and (b) area of the hyporheic zone for the flooding period 3.

7.3.3.2 Mean Hyporheic Flux

Fig. 7.12c shows the temporal variation of the simulated mean hyporheic flux under the static streambed conductivity during the flooding condition 3, which generally follows the temporal variation of the dynamic-head intensity (Fig. 7.12a). With the consideration of the time-varying streambed conductivity, however, the temporal variation of the simulated mean hyporheic flux is more similar to the curve of the streambed conductivity (Fig. 7.12b) while is independent of fluctuations of the dynamic-head intensity.

Before the onset of this flood event, the river stage experienced a continuous decline (shown in Fig. 7.3. i, c), causing h_d to decrease from more than 4.0×10^{-3} m to lower than 3.0×10^{-3} m between t = 0 to $0.32t_{\text{total}}$. For the static streambed scenario, it resulted in a significant inactivation of the hyporheic exchange, reflected by the drop of $\bar{q}^{*}_{\text{HF,S}}$ from 1.0 to 0.6 over this

period. However, when incorporating the time-varying streambed conductivity into the simulation, the outcome becomes different. Since the streambed was of low permeability in the beginning according to the estimation result (Fig. 7.12b), the initial value of $\bar{q}^*_{\mathrm{HF,T}}$ was low, which was less than 0.20. Due to the swift rise of the streambed conductivity from 0 to $0.05t_{\mathrm{total}}$, $\bar{q}^*_{\mathrm{HF,T}}$ soon jumped to the region of 0.6. Unlike the constant reduction of $\bar{q}^*_{\mathrm{HF,S}}$ before the arrival of the flood, $\bar{q}^*_{\mathrm{HF,T}}$ was generally intensified owing to the upward trend of the streambed conductivity, which could be more clearly observed from the 'close-up' figure that is marked by the red dashed rectangle in Fig. 7.12d. For this process, it could be seen that without considering the temporal variation of the streambed conductivity, an opposite evolutionary trend of the regional GW-SW exchange rate was obtained.

A flood visited the site from $0.35t_{\mathrm{total}}$ to $0.60t_{\mathrm{total}}$, in which the peak was reached at $0.40t_{\mathrm{total}}$, leading to the maximum value of h_d as 6.0×10^{-3} m. It induced an increase of the hyporheic flux for the circumstance of both the static and time-varying streambed conductivity. Owing to an increase of the streambed conductivity as the flood wave approaching to the crest (Fig. 7.12a and b), $\bar{q}^*_{\mathrm{HF,T}}$ rocketed from 0.6 to 5.8 within $0.05t_{\mathrm{total}}$ (Fig. 7.12d), indicating a significant intensification of the hyporheic exchange. However, for $\bar{q}^*_{\mathrm{HF,S}}$, the increment was relatively small, which was only from 0.6 to 1.4 (Fig. 7.12c). For this process, without considering the temporal variation of the streambed conductivity, it cannot precisely capture the dynamic and sharp variation of the hyporheic flux. During the recession of the flood, $\bar{q}^*_{\mathrm{HF,S}}$ followed the dynamic-head intensity to gradually decline while $\bar{q}^*_{\mathrm{HF,T}}$ sharply dropped to a low level due to the rapid decrease of the streambed conductivity (from $0.50t_{\mathrm{total}}$ to $0.70t_{\mathrm{total}}$). In the final stage of this period (from $0.70t_{\mathrm{total}}$ to the end), the SW returned to a low-stage condition. The dynamic-head intensity

and streambed conductivity were therefore stabilized at a low value, resulting in a general constant hyporheic flux (both $\bar{q}^*_{\mathrm{HF,S}}$ and $\bar{q}^*_{\mathrm{HF,T}}$) with slight fluctuations. A *t* test indicated that mean difference of the hyporheic flux simulated with the static and time-varying streambed conductivity over flooding condition 3 was statistically significant ($P < 0.01$).

7.3.3.3 Mean Residence Time

Fig. 7.12e and f demonstrates the temporal variation of the simulated dimensionless flux-weighted mean residence time under the static and time-varying streambed conductivity during the flooding condition 3, respectively, where the *y* coordinate is reversed to facilitate the comparisons of the results. In general, under the static streambed conductivity, the curve of the simulated mean residence time (Fig. 7.12e) resembles the variation of the dynamic-head intensity (Fig. 7.12a) though smoother. When considering the time-varying streambed conductivity, the evolution of the residence time becomes much more complex and the curve (Fig. 7.12f) is a blend of the temporal variations of the dynamic-head intensity and streambed conductivity.

Before the start of this flood event, with a constant decline of the river stage, the hyporheic zone was provided with a weaker energy (smaller h_d), which in turn slowed down the hyporheic flow and rendered a longer mean residence time when the streambed conductivity was assumed static (Fig. 7.12e). Between $t = 0$ to $0.32t_{\mathrm{total}}$, Mean $\mathrm{RT}^*_{\mathrm{HF,S}}$ rose from 1.0 to 1.2, demonstrating that the hyporheic zone was becoming inactive. With the consideration of the time-varying streambed conductivity, the whole process becomes diametrically different. In the beginning ($t = 0$), due to an extremely low-permeable streambed (Fig. 7.12b), the hyporheic flow was at a low speed. This resulted in a long residence time, which is reflected by a large value (5.0) of Mean $\mathrm{RT}^*_{\mathrm{HF,T}}$ in Fig. 7.12f. Owing to the continuous increase of the streambed conductivity, Mean

$RT^*_{HF,T}$ was shortened substantially, signaling that the hyporheic zone is becoming more active, which is opposite to the trend of Mean $RT^*_{HF,S}$. However, it should be noted that Mean $RT^*_{HF,T}$ was still much longer than $RT^*_{HF,S}$ over this period ($0 \sim 0.32t_{total}$) since K_T/K_S was generally smaller than 1.0 (Fig. 7.12b).

With the arrival of the flood, the dynamic-head intensity became higher, which accelerated the hyporheic exchange, resulting in a considerable reduction of both Mean $RT^*_{HF,S}$ and Mean $RT^*_{HF,T}$. For Mean $RT^*_{HF,S}$, it decreased from 1.2 to 0.8 while Mean $RT^*_{HF,T}$ dropped from 2.0 to 0.9 due to an extra support from the increase of the streambed conductivity (Fig. 7.12b). With a more permeable streambed, the hyporheic flow can pass through the subsurface region at a faster speed and the residence time is therefore substantially shortened. For this process, the change of the streambed conductivity significantly bolstered the activation of the hyporheic exchange, which can further intensify regional biogeochemical processes and ultimately alter the riverine system (Marzadri et al., 2016; Wu et al., 2018).

During the flood recession, caused by the smaller dynamic-head intensity, both Mean $RT^*_{HF,S}$ and Mean $RT^*_{HF,T}$ experienced a steady increase. However, the decline of Mean $RT^*_{HF,S}$ was mild, which was from 0.8 to 1.0, while that of Mean $RT^*_{HF,T}$ was severe (from 0.8 to 2.0) owing to an acute decline of the streambed conductivity (Fig. 7.12b). In the final stage of this period (from $0.70t_{total}$ to the end), with the SW returning to the low-stage condition, both Mean $RT^*_{HF,S}$ and Mean $RT^*_{HF,T}$ were stabilized. A *t* test indicated that mean difference of the mean residence time simulated with the static and time-varying streambed conductivity over flooding condition 1 was statistically significant ($P < 0.01$).

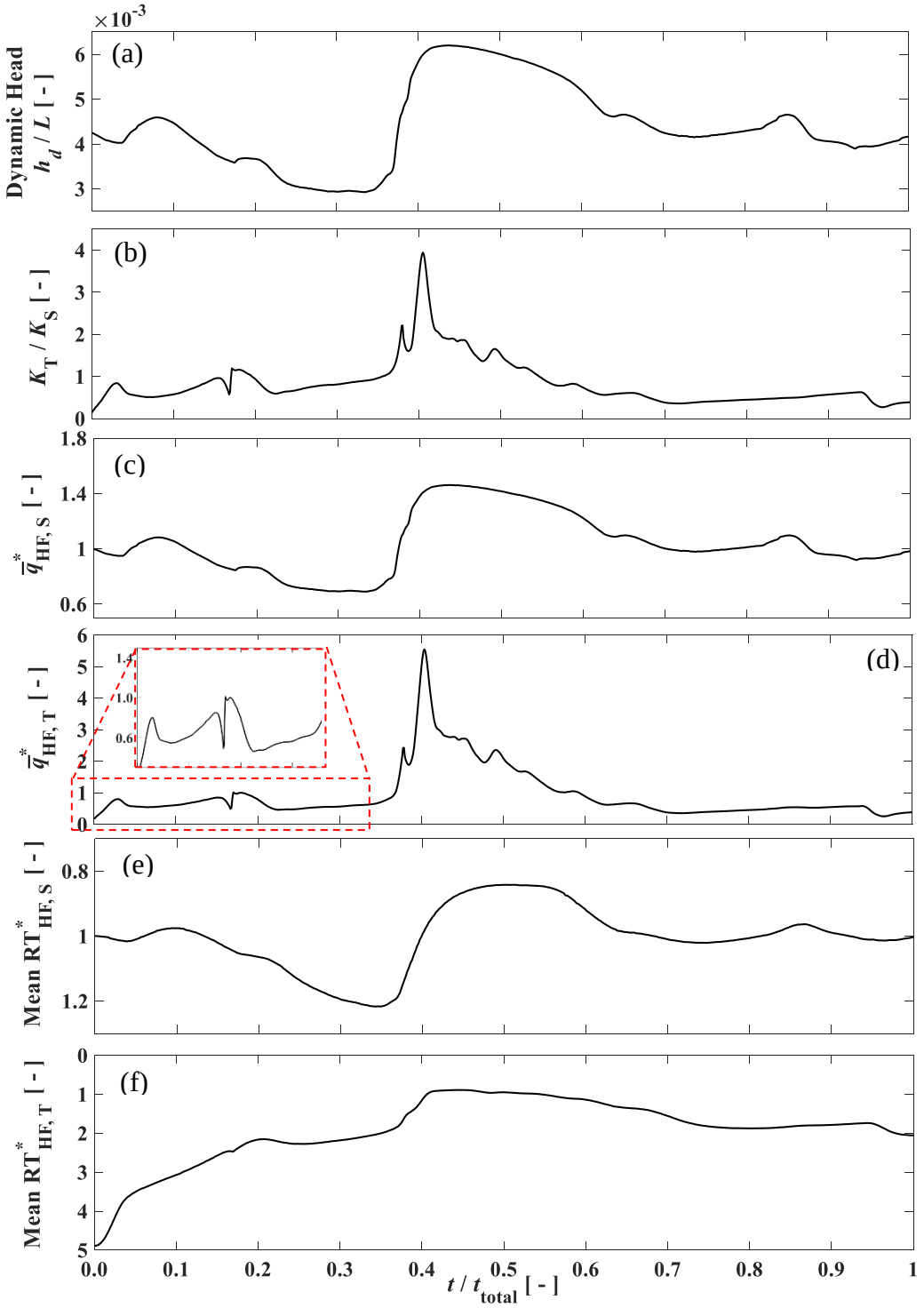

Figure 7.12. Temporal variation of the (a) dynamic head intensity, (b) streambed conductivity, (c) and (d) mean hyporheic flux simulated with the static and time-varying streambed, respectively, and (e) and (f) mean flux-weighted residence time under the static and time-varying streambed, respectively, over flooding period 3.

7.4 Discussion

7.4.1 Filter Function of Streambed

It has been widely reported that porous media can act as a low-pass filter to attenuate high-frequency input signals and produce relatively smooth responses (O'Reilly, 2004, 2007). As a porous medium that is composed of sediments, streambed is playing this role for the dune-induced hyporheic exchange. When the fast-flowing SW infiltrates into the subsurface region, it slows down significantly owing to the friction from the solid matrix, which substantially reduces and delays the reaction of GW to fluctuations of SW flow. The storage properties of the porous media enhance this 'filter' function as well.

Although the variation of the dynamic-head intensity changes the amount and speed of the hyporheic exchange, the shape of the hyporheic zone evolves at a mild and slow pace due to the attenuating and delaying effects from the streambed. This is evidenced by Fig. 7.4, 7.7 and 7.10, in which the hyporheic zone is generally stable at different time steps. The depth and area of the hyporheic zone are therefore minimally impacted by the fluctuations of the SW flow.

However, as a parameter that is determined by the streambed conductivity and the hydraulic gradient over the sediment-water interface, the hyporheic flux is tightly associated with the strength of the SW flow, which is represented by the dynamic-head intensity in this study. When the streambed conductivity is constant over time, the hyporheic exchange is completely controlled by the energy provided by the SW, causing the hyporheic flux to follow the fluctuations of the dynamic-head intensity. With the consideration of the time-varying streambed conductivity, the temporal variations of both the dynamic-head intensity and the streambed conductivity affect the evolution of the hyporheic flux based on the simulation results.

For the mean residence time, it is impacted by the hydraulic property of the streambed as well as the energy that drives the hyporheic exchange. With a more permeable streambed and/or a higher dynamic-head intensity over the sediment-water interface, the hyporheic flow moves at a faster speed, and its residence time is therefore shortened. Hence, similar to the mean hyporheic flux, the mean residence time is closely correlated with the streambed conductivity and dynamic-head intensity. Since residence time represents how long the infiltrated SW stays in the subsurface region, the filter function of the streambed sediment acts on this parameter as well, which is the reason why the curve of the residence time is much smoother than the temporal variation of the dynamic-head intensity.

7.4.2 Importance of Time-varying Streambed Conductivity

From the simulation results of this study, it can be concluded that the time-varying streambed conductivity is a decisive parameter for the evolution of the dune-induced hyporheic exchange. Without considering this factor, the detailed temporal variation of the exchange intensity and residence time cannot be captured, according to the comparisons between the results simulated with static and time-varying streambed conductivity.

To quantify the correlation between the simulation results and input parameters, the correlation coefficient (lagging phase = 0), r^2, was calculated for both mean hyporheic flux and residence time, which is shown as Fig. 7.13a and b, respectively. Only the simulation results under the time-varying streambed conductivity were analyzed. The blue and yellow bar represents the r^2 value of the simulation results with the dynamic-head intensity and streambed conductivity, respectively. Fig. 7.14 shows the variation of the correlation coefficient with lagging phase, from which it can be generally found that the maximum absolute value of r^2 appears at lag = 0, indicating

that the r^2 values shown in Fig. 7.13 are appropriate for the correlation analysis.

Since a stronger hydraulic gradient and/or a more permeable streambed can boost the hyporheic flux, theoretically, the r^2 values of $\bar{q}_{\mathrm{HF,Time-varying}}$ with h_d and K_T should both be positive. From Fig. 7.13a, it can be found that the r^2 values between $\bar{q}_{\mathrm{HF,Time-varying}}$ and K_T are all above 0.70, indicating a strong correlation. When comparing the blue and yellow bars in Fig. 7.13a, it can be concluded that the temporal variation of $\bar{q}_{\mathrm{HF,Time-varying}}$ is more correlated with K_T than h_d, demonstrating the importance of the time-varying streambed conductivity to the hyporheic exchange rate.

With a stronger hydraulic gradient and/or a more permeable streambed, the hyporheic flow is accelerated, so the residence time is shortened. The r^2 values of Mean $RT_{\text{Time-varying}}$ with h_d and K_T should therefore be both negative in theory. From Fig. 7.13b, it could be found that for the flooding conditions 1 and 2, both of which are composed of multiple flood waves, the temporal variation of Mean $RT_{\text{Time-varying}}$ is more correlated with K_T than h_d, and their correlation (Mean $RT_{\text{Time-varying}}$ & K_T) is strong ($|r^2| > 0.90$). A positive value of r^2 between Mean $RT_{\text{Time-varying}}$ and h_d can be found for the flooding condition 1, which contrasts to the theoretical analysis. It is because h_d has a general downward trend (Fig. 7.6a) while over the same period, Mean $RT_{\text{Time-varying}}$ is generally shortened due to the more permeable streambed (Fig. 7.6b and f). For the flooding condition 3, in which only one flood wave is involved, the r^2 values reveal that Mean $RT_{\text{Time-varying}}$ is weakly correlated with both h_d and K_T ($|r^2| < 0.60$). Given the general close correlation between Mean $RT_{\text{Time-varying}}$ and K_T, it is necessary to incorporate the time-varying streambed conductivity into the studies of the hyporheic exchange.

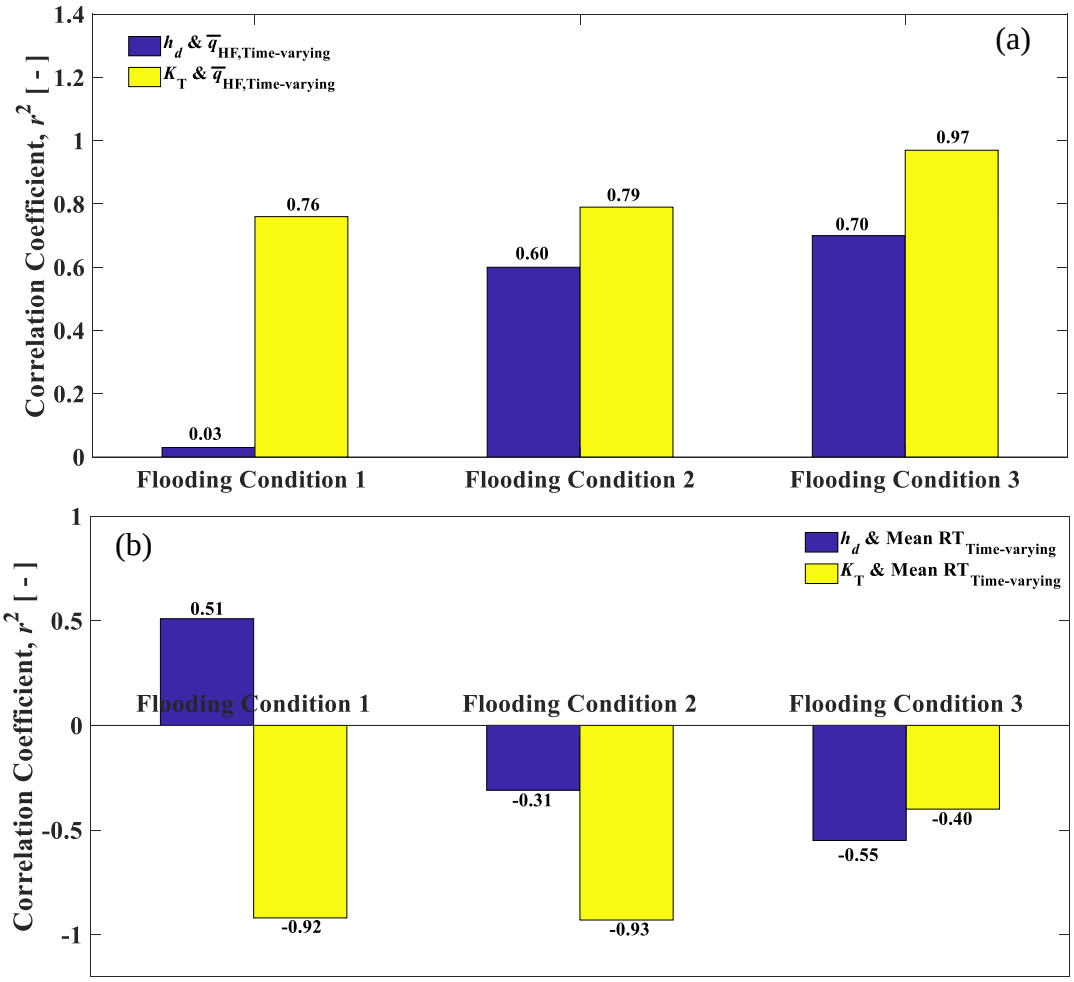

Figure 7.13. Correlation coefficient, r^2, between (a) $\overline{q}_{HF,\,Time\text{-}varying}$ and (b) Mean $RT_{Time\text{-}varying}$ with h_d and K_T.

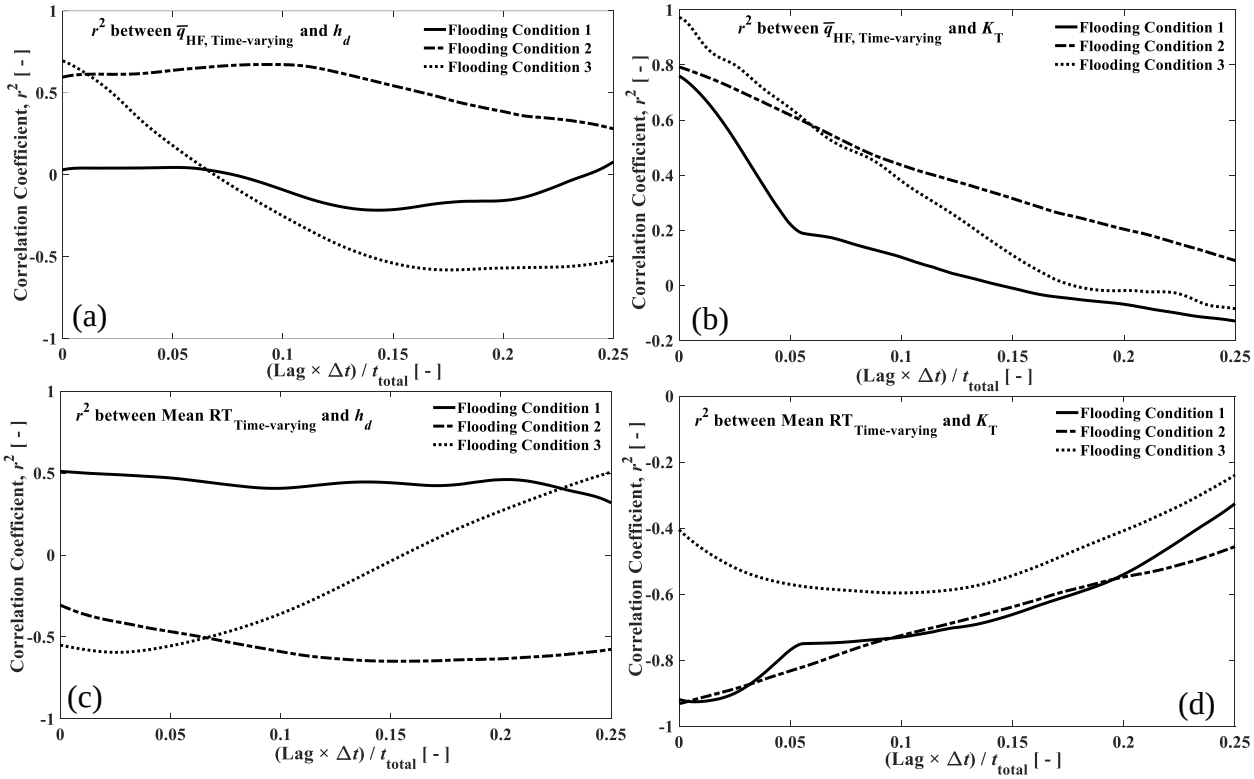

Figure 7.14. Variation of correlation coefficient with lagging phase, where (a) is between $\overline{q}_{\text{HF, Time-varying}}$ and h_d, (b) is between $\overline{q}_{\text{HF, Time-varying}}$ and K_{T}, (c) is between Mean $\text{RT}_{\text{Time-varying}}$ and h_d and (d) is between Mean $\text{RT}_{\text{Time-varying}}$ and K_{T}.

7.5 Summary and Conclusions

This chapter investigated the dune-induced hyporheic exchange affected by the time-varying streambed conductivity through the numerical model, CCHE3D-GW. The study area was the Money experimental site near the Tallahatchie River in Mississippi, USA. Three typical flooding conditions were studied. Simulations were conducted with both the static and time-varying streambed conductivity. Three items of the hyporheic exchange were analyzed, which were the extent of the hyporheic zone, mean hyporheic flux and the flux-weighted mean residence time.

The extent of the hyporheic zone was found to be almost uninfluenced by the temporal variation of the dynamic-head intensity and streambed conductivity, indicating that the conclusions from the previous studies, which mainly considered the steady condition, can be directly applied to compute the depth and area of the hyporheic zone.

Under the static streambed conductivity, the simulated mean hyporheic flux and residence time generally followed the fluctuations of the dynamic-head intensity to vary temporally. However, with the consideration of the time-varying streambed conductivity, the temporal variations of the hyporheic flux and residence time were found affected by the time-varying streambed conductivity as well as the dynamic-head intensity. From the *t* test conducted in this study for comparing the simulation results of the static verses the time-varying streambed conductivity cases, all *P* values were found to be smaller than 0.05, indicating a significant statistical difference between the two simulation scenarios, which validates Hypothesis of this chapter. The correlation analysis revealed that for the simulations conducted with the time-varying streambed conductivity, the mean hyporheic flux and residence time were generally more correlated with the temporal variation of the streambed conductivity than the dynamic-head intensity.

CHAPTER VIII

SUMMARY, CONCLUSIONS AND FUTURE WORK

8.1 Summary and Conclusions

This dissertation focused on studying GW-SW interactions while considering time-varying streambed conductivity during storm events, in which two commonly encountered scenarios, RBF and dune-induced hyporheic exchange, were studied. The study area was in Money, Mississippi, USA, which was an experimental site for a managed aquifer recharge project in the Mississippi Delta. The influences from the time-varying streambed conductivity on stream-aquifer exchanges were explored through simulations of multiple hypothetical cases. To the best of the author's knowledge, this is the first attempt in the research literature to numerically study the GW-SW interactions during different flooding conditions with time-varying streambed conductivity.

Considering the complexity of the investigated problems, a 3-D finite element GW model, CCHE3D-GW, was developed. The mixed form of the Richards' equation was adopted so that the model can handle saturated-unsaturated GW flows. Before the application, the newly developed numerical model was vigorously verified with comprehensive analytical and numerical solutions, and was then used as a major tool for this study.

Sponsored by a pilot study of a managed aquifer recharge project in the Mississippi Delta, a 3-day pumping test was conducted by the USDA-ARS in February of 2017 in Leflore County (Money), Mississippi, USA, to obtain the hydrogeological information of the regional aquifer and riverbed. By calibrating the simulated drawdowns of GW head with the measured data in the

monitoring wells, the hydraulic conductivities of the aquifer, aquitard and streambed were attained. The calibrated model of the Money pumping site was the basis for simulations in this study.

In order to consider the time-varying streambed conductivity in the numerical study of GW-SW interactions during storm events, its time series must be obtained in advance and the required temporal resolution is high. An estimation model was therefore developed based on a flood-wave response analytical solution. The scenario that an alluvial aquifer was partially penetrated by a river was considered given that it was the feature in the study area. The estimation model was then validated with two synthetic cases, one of which was that the streambed conductivity changed much slower than the flood-wave fluctuation while the other considered the situation that the streambed conductivity and flood wave varied at the same pace. The fine agreements between the estimated and actual time-varying streambed conductivity validated the model. The viability of the estimation model to heterogeneous aquifer was also tested and confirmed. The geometric-averaged hydraulic conductivity was found most suitable to represent the heterogeneity of the aquifer when applying the estimation model. The comprehensive uncertainty analysis of the estimation model to its input parameters was conducted as well. The results revealed that the estimation model was approximately linearly influenced by the uncertainty of its input parameters.

The developed and validated estimation model was then applied to attain the time series of the streambed conductivity for the Tallahatchie River near the Money pumping site, Mississippi, USA. Three typical flooding conditions were analyzed: 1) one that consisted of multiple flood events with attenuating amplitudes, 2) one that was composed of multiple flood events with amplifying amplitudes, and 3) one with a single flood event (the river stage reached a historically

high value, 41.0 m above NAVD 88 datum).

The estimated temporal variations of the streambed conductivity were then implemented into the numerical model, CCHE3D-GW, to study two typical cases of GW-SW interactions during flooding periods. The first application was the RBF system of the Money experimental site near the Tallahatchie River, MS, USA. The simulations were conducted for the aforementioned three flooding conditions with both static (the traditional method to study GW-SW interactions) and time-varying streambed conductivity. Four items were analyzed, which were the drawdowns of GW head, stream depletion, percentage of the pumped water coming from the stream and the mean travel time of the infiltrated water. GW heads were found generally uninfluenced by the temporal variations of both the river stage and streambed conductivity over the flooding condition 1 and 2, where the maximum river stage was lower than 40 m. However, for the flooding condition 3, the simulated GW heads experienced an increase during the peak of the flood. The stream depletions simulated with the time-varying and static streambed conductivity were found noticeably different over flooding periods, particularly at the peak of the flood wave. The simulation also revealed that for the flooding condition 1 and 2, the maximum amount of the pumped water coming from the stream was approximately three times more than the value of the low-stage period. For the flooding condition 3, the maximum percentage of the pumped water coming from the stream was ten times more than that over the low-stage condition. The simulated travel time of the infiltrated SW from the stream to the pumping well during high-stage events was found to be substantially shortened compared to the low-stage condition. For the flooding condition 1 and 2, the minimum travel time was approximately 40% of the travel time during the low-stage period. For the flooding condition 3, the minimum travel time was around 20% of that during the low-stage period. The results

simulated with the static and time-varying streambed conductivity were found close during low-stage conditions, but differences became clear during high-stage events.

The second case is the dune-induced hyporheic exchange under storm events. Similar to the study of the RBF system, three flooding conditions were explored, and simulations were conducted with both static and time-varying streambed conductivity. Three items of the hyporheic exchange were analyzed, which were the extent of the hyporheic zone, mean hyporheic flux and flux-weighted mean residence time. The extent of the hyporheic zone was found almost uninfluenced by the fluctuation of the dynamic-head intensity and streambed conductivity. The simulated evolutions of mean hyporheic flux and residence time during flooding conditions were all found affected by the time-varying streambed conductivity as well as the dynamic-head intensity. The correlation analysis revealed that the simulated mean hyporheic flux and residence time were more correlated with the temporal variation of the streambed conductivity than the dynamic-head intensity. When comparing the results simulated with the static and time-varying streambed conductivity, the discrepancies were clearly observed, indicating that it is indispensable to consider the time-varying streambed conductivity to capture the detailed evolution of the hyporheic flow.

Thus, based on the modeling results and analyses for different flooding conditions in this study, it can be concluded that considering time-varying streambed conductivity is imperative for accurately understanding the evolution of the GW-SW exchange intensity and residence time of the infiltrated water. Hence, demonstrating that time-varying streambed conductivity is a critical and essential variable for accurate and robust process-based GW-SW interaction modeling.

8.2 Limitations and Future Work

Based on the research conducted in this dissertation, I would recommend the following research directions to improve the current work and further enhance our understandings of GW-SW interactions:

(1) The present estimation model has been validated with two sets of synthetic data. The accuracy and efficacy of the model were proven but it is always better to have a set of field data for validation. Field data can also help explain the mechanism of the temporal variation of the streambed conductivity, such as sediment transport, biomass growth, other physical chemical and biological processes or threshold effect (O'Reilly et al., 2020). It is therefore suggested to conduct multiple field campaigns in the future to measure the temporal variation of the infiltration rate or permeability of the streambed sediments before and right after flood events in order to enhance the understanding of the clogging/flushing processes.

(2) In this study, for the riverside pump simulation, the SW was represented by a head boundary condition and the measured temporal variation of the river stage was implemented into CCHE3D-GW. Only the GW flow was simulated. The simulation results could be more realistic when the GW model is coupled with a SW model, such as CCHE2D, and the dynamics of the stream flow is simulated as well.

(3) For the dune-induced hyporheic flow, the bottom boundary condition was simplified to be no flux to represent the neutral base flow, which was also adopted by Singh et al. (2019, 2020) when studying the impact of floods on the hyporheic exchange. This simplification was applied in this dissertation to avoid complicated boundary conditions, and emphasize the core objective, i.e., studying combined effects of the time-varying streambed conductivity and the high-stage event on GW-SW interactions. However, for the real-world scenario, base flow

exists and varies with time owing to the temporal variation of the stream-aquifer hydraulic gradient. The simulation results can become more realistic if the dynamics of the base flow is considered in the bottom boundary condition.

(4) Considering that CCHE3D-GW is a process-based numerical model, it is generally applicable to any region as long as the required hydrogeological data are obtained. However, this dissertation focused on a specific study site, so similar studies in the future need to be conducted for other study areas with different soil conditions and geographic features in order to further generalize findings and conclusions.

BIBLIOGRAPHY

BIBLIOGRAPHY

Ackerman, D.J. (1996). Hydrology of the Mississippi River Valley Alluvial Aquifer, South-Central United States. U.S. Geological Survey Professional Paper 1416-D. Available at: https://pubs.er.usgs.gov/publication/pp1416D. Accessed October 17, 2017.

Adams, R.F., Miller, B.V., and Kress, W.H. (2019). Waterbone Resistivity Inverted Models, Mississippi Alluvial Plain, 2016-2018: U.S. Geological Survey data release, https://doi.org/10.5066/P9WQPRFB.

Arthur, J.K. (1994). Thickness of the upper and lower confining units of the Mississippi River Alluvial Aquifer in Northwest Mississippi. USGS Water Resources Investigations Report: 94-4172.

Bardini, L., Boano, F., Cardenas, M., Sawyer, A., Revelli, R., and Ridolfi, L. (2013). Small-scale permeability heterogeneity has negligible effects on nutrient cycling in streambeds. *Geophysical Research Letters*, 40(6): 1118-1122.

Barlow, P.M., DeSimone, L.A., Moench, A.F. (2000). Aquifer response to stream-stage and recharge variations. II. Convolution method and applications. *Journal of Hydrology*, 230(3-4): 211-229. Doi: 10.1016/s0022-1694(00)00176-1.

Beller, M., Ellis, A., Lee, S.H., Drebot, M.A., Jenkerson, S.A., Funk, E., et al. (1997). Outbreak of viral gastroenteritis due to a contaminated well: International Consequences. *JAMA*, 278(7): 563-568. Doi: 10.1001/jama.1997.03550070055038

Bhaskar, A.S., Harvey, J.W., and Henry, E.J. (2012). Resolving hyporheic and groundwater components of streambed water flux using heat as a tracer. *Water Resources Research*, 48(8): 1076.

Bloss, B.R., Pace, M.D.M., Thayer, D.C., White, E.A., Johnson, C.D., Adams, R.F., Smith, D.C., Bolton, W.J., and Minsley, B.J., 2019, Ground-based time-domain electromagnetic data and resistivity models for the Mississippi Alluvial Plain Project: U.S. Geological Survey data release, https://doi.org/10.5066/P965NBFT.

Boano, F., et al. (2015). Hyporheic flow and transport process: mechanisms, models, and biogeochemical implications. *Reviews of Geophysics*, 52(4): 603-679.

Boano, F., Harvey, J.W., Marion, A., Packman, A.I., Revelli, R., Ridolfi, L., and Wörman, A. (2014). Hyporheic flow and transport processes: mechanisms, models, and biogeochemical implications. *Reviews of Geophysics*, 52: 603–679. Doi: 10.1002/2012RG000417.

Boano, F., Revelli, R., and Ridolfi, L.A. (2008). Reduction of the hyporheic zone volume due to

the stream-aquifer interaction. *Geophysical Research Letters*, 35(9): 250-258.

Boano, F., Revelli, R., and Ridolfi, L.A. (2009). Quantifying the impact of groundwater discharge on the surface-subsurface exchange. *Hydrological Process*, 23(15): 2108-2116.

Boano, F., Revelli, R., and Ridolfi, L.A. (2010). A linear model for the coupled surface-subsurface flow in a meandering stream. *Water Resource Research*, 46: W07535.

Bolster, C.H., Genereux, D.P., and Saiers, J.E. (2001). Determination of specific yield for the Biscayne Aquifer with a canal-drawdown test. *Ground water*, 39(2): 768-777.

Boulton, A.J., Datry, T., Kasahara, T., Mutz, M., and Stanford, J.A. (2010). Ecology and management of the hyporheic zone: stream-groundwater interactions of running waters and their floodplains. *Journal of the North American Benthological Society*, 29(1): 26-40.

Briggs, M.A., Lautz, L.K., and Hare, D.K. (2013). Residence time control on hot moments of net nitrate production and uptake in the hyporheic zone. *Hydrological Processes*, 28(11): 3741-3751.

Brooks, R.H., and Corey, A.T. (1966). Hydraulic properties of porous media. Hydrology Paper no. 3, Civil Engineering Dep., Colorado State Univ., Ft. Collins, Co.

Brunner, P., Therrien, R., Renard, P., Simmons, C.T., and Franssen, H.-J.H. (2017). Advances in understanding river-groundwater interactions. *Reviews of Geophysics*, 55: 818–854. Doi: 10.1002/2017RG000556.

Buffington, J.M., and Tonina, D. (2009). Hyporheic exchange in Mountain Rivers II: Effects of channel morphology on mechanics, scales and rates of exchange. *Geography Compass*, 3(3): 1038-1062. Doi: 10.1111/j.1749-8198.2009.00225.x

Bulter, J.J., Zlotnik, V.A., and Tsou, M. (2001). Drawdown and stream depletion produced by pumping in the vicinity of a partially penetrating stream. *Ground Water*, 39(5): 651-659. Doi: 10.1111/j.1745-6584.2006.00169.x

Cardenas, M.B., Wilson, J., and Zlotnik, V.A. (2004). Impact of heterogeneity, bed forms, and stream curvature on subchannel hyporheic exchange. *Water Resources Research*, 40(8): W08307. Doi: 10.1029/2004WR003008

Cardenas, M.B., and Wilson, J.L. (2007a). Dunes, turbulent eddies, and interfacial exchange with permeable sediments. *Water Resources Research*, 43(8): W08412.

Cardenas, M.B., and Wilson, J.L. (2007b). Exchange across a sediment-water interface with ambient groundwater discharge. *Journal of Hydrology*, 346(3): 69-80.

Caruso, A., Boano, F., Ridolfi, L., Chopp, D.L., and Packman, A. (2017). Biofilm-induced bioclogging produces sharp interfaces in hyporheic flow, redox conditions, and microbial community structure. *Geophysics Research Letter*, 44, 4917–4925. Doi: 10.1002/2017GL073651.

Celia, M.A., Bouloutas, E.T., and Zarba, R.L. (1990). A general mass-conservative numerical solution for the unsaturated flow equation. *Water Resources Research*, 26(7): 1483-1496. Doi:

10.1029/90WR00196

Coleman, J.M. (1969). Brahmaputra river: Channel processes and sedimentation. *Sediment Geology*, 3(2-3): 129-239.

Coleman, T.F., and Li, Y. (1994). On the convergence of interior-reflective Newton methods for nonlinear minimization subject to bounds. *Mathematical Programming*, 67 (1-3): 189-224. Doi: 10.1007/BF01582221.

Coleman, T.F., and Li, Y. (1996). A reflective Newton method for minimizing a quadratic function subject to bounds on some of the variables. *SIAM Journal on Optimization*, 6(4): 1040–1058. Doi: 10.1137/S1052623494240456.

Constantz, J. (2016). Streambeds merit recognition as a scientific discipline. *WIREs Water*, 3 (1), 13–18. Doi: 10.1002/wat2.1119.

Cooper, H. H., and Rorabaugh, M. I. (1963). Ground-water movements and bank storage due to flood stages in surface streams. Ground Water Hydraulics, Water Supply Paper 1536-J, US Geological Survey.

Cui, G., Su, X., Liu, Y., and Zheng, S. (2021). Effect of riverbed sediment flushing and clogging on river-water infiltration rate: a case study in the Second Songhua River, Northeast China. *Hydrogeology Journal*, 29(2): 551-565. Doi: 10.1007/s10040-020-02218-7

Cumming, B., Moroney, T., and Turner, I. (2011). A mass-conservative control volume-finite element method for solving Richards' equation in heterogeneous porous media. *BIT Numerical Mathematics*, 51(4): 845-864. Doi: 10.1007/s10543-011-0335-3.

Derx, J., Blaschke, A.P., Farnleitner, A.H., Pang, L., Blöschl, G., and Schijven, J.F. (2013). Effects of fluctuations in river water level on virus removal by bank filtration and aquifer passage — A scenario analysis. *Journal of Contaminant Hydrology*, 147:34-44. Doi: 10.1016/j.jconhyd.2013.01.001

Doppler, T., Franssen, H.J.H., Kaiser, H.P., Kuhlman, U., and Stauffer, F. (2007). Field evidence of a dynamic leakage coefficient for modelling river-aquifer interactions. *Journal of Hydrology*, 347 (1–2): 177–187. Doi: 10.1016/j.jhydrol.2007.09.017.

Drummond, J. D., Larsen, L.G., González-Pinzón, R., Packman, A.I., and Harvey, J.W. (2017). Fine particle retention within stream storage areas at base flow and in response to a storm event. *Water Resources Research*, 53, 5690–5705. Doi: 10.1002/ 2016WR020202.

Du, X. Q., Wang, Z.J., and Ye, X.Y. (2013). Potential clogging and dissolution effects during artificial recharge of groundwater using potable water. *Water Resources Management*, 27(10): 3573–3583.

Elliott, A.H., and Brooks, N.H. (1997a). Transfer of nonsorbing solutes to a streambed with bed forms: Laboratory experiments. *Water Resources Research*, 33(1): 137-151.

Elliott, A.H., and Brooks, N.H. (1997b). Transfer of nonsorbing solutes to a streambed with bed forms: Theory. *Water Resources Research*, 33(1): 123-136.

Findlay, S. (1995). Importance of surface-subsurface exchange in stream ecosystems: The hyporheic zone. *Limnology and Oceanography*, 40(1): 159-164.

Fox, A., Boano, F., and Arnon, S. (2014). Impact of losing and gaining streamflow conditions on hyporheic exchange fluxes induced by dune-shaped bed forms. *Water Resources Research*, 50(3): 1895-1907.

Fox, A., Laube, G., Schmidt, C., Fleckenstein, J.H., and Arnon, S. (2016). The effect of losing and gaining flow conditions on hyporheic exchange in heterogeneous streambeds. *Water Resources Research*, 52(9): 7460-7477.

Fox, A., Packman, A.I., Boano, F., Phillips, C.B., and Arnon, S. (2018). Interactions between suspended Kaolinite deposition and hyporheic exchange flux under losing and gaining flow conditions. *Geophysical Research Letters*, 45(9): 4077-4085.

George, N.J., Ekanem, A.M., Ibanga, J.I., Udosen, N.I. (2017). Hydrodynamic implications of aquifer quality index (AQI) and flow zone indicator (FZI) in groundwater abstraction: a case study of coastal hydro-lithofacies in South-eastern Nigeria. *Journal of Coastal Conservation*, 21(6): 759-776.

Gianni, G., Richon, J., Perrochet, P., Vogel, A., Brunner, P. (2016). Rapid identification of transience in streambed conductance by inversion of floodwave responses. *Water Resources Research*, 52: 2647–2658. Doi: 10.1002/2015WR017154.

Gollnitz, W.D., Clancy, J.L., McEwen, J.B., and Garner, S.C. (2005). Riverbank filtration for IESTWR compliance. *Journal of the American Water Works Association*, 97, 64e76.

Gomez, J., and Wilson, J. (2013). Age distributions and dynamically changing hydrologic systems: Exploring topography-driven flow. *Water Resources Research*, *49*, 1503–1522.

Gomez-Velez, J. D., Krause, S., and Wilson, J. L. (2014). Effect of low-permeability layers on spatial patterns of hyporheic exchange and groundwater upwelling. *Water Resources Research*, 50: 5196–5215. Doi: 10.1002/2013WR015054

Gomez-Velez, J. D., Wilson, J. L., Cardenas, M. B., and Harvey, J. W. (2017). Flow and residence times of dynamic river bank storage and sinuosity-driven hyporheic exchange. *Water Resources Research*, 53: 8572–8595. Doi: 10.1002/2017wr021362

Goode, D. J. (1996). Direct simulation of groundwater age. *Water Resources Research*, 32(2): 289-296.

Gooseff, M.N. (2010). Defining hyporheic zones – advancing our conceptual and operational definitions of where stream water and groundwater meet. *Geography Compass*, 4(8): 945-955.

Gu, C., Hornberger, G. M., Herman, J. S., and Mills, A. L. (2008). Effect of freshets on the flux of groundwater nitrate through streambed sediments. *Water resources research*, 44, W05415. Doi: 10.1029/2007WR006488

Hall, F. R., Moench, A.F. (1972). Application of convolution equation to stream-aquifer relationships. *Water Resources Research*, 8(2): 487–493.

Hantush, M.S. (1965). Well near streams with semi pervious beds. *Journal of Geophysics Research*, 70(12): 2829-2838. Doi: 10.1029/JZ070i012p02829

Harbaugh, A.W., Banta, E.R., Hill, M.C., and McDonald, M.G. (2000). MODFLOW-2000: The U.S. Geological Survey modular groundwater model: user guide to modularization concepts and the groundwater flow process. *US Geological Survey Open-File Report*, 00-92, 121 pp.

Harvey, J.W., and Bencala, K.E. (1993). The effect of streambed topography on surface-subsurface water exchange in mountain catchments. *Water Resources Research*, 29(1): 89-98.

Harvey, J.W., Conklin, M.H., and Koelsch, R.S. (2003). Predicting changes in hydrologic retention in an evolving semi-arid alluvial stream. *Advances in Water Resources*, 26(9): 930-950.

Harvey, J. W., Bohlke, J. K., Voytek, M. A., Scott, D., and Tobias, C. R. (2013). Hyporheic zone denitrification: Controls on effective reaction depth and contribution to whole-stream mass balance. *Water Resources Research*, 49: 6298–6316. Doi: 10.1002/wrcr.20492

Hatch, C.E., Fisher, A.T., Ruehl, C.R., and Stemler, G. (2010). Spatial and temporal variations in streambed hydraulic conductivity quantified with time-series thermal methods. *Journal of Hydrology*, 389(3): 276-288.

Hiscock, K.M., and Grischek, T. (2002). Attenuation of groundwater pollution by bank filtration. *Journal of hydrology (Amsterdam)*, 266(3):139-44.

Hsieh, P.A., Wingle, W., Healy, R.W., et al. (2000). VS2DI-a graphical software package for simulating fluid flow and solute or energy transport in variably saturated porous media. *USGS Water-Resources Investigations Report*, 99-4130.

Irvine, D.J., Brunner, P., Franssen, H., and Simmons, C.T. (2012). Heterogeneous or homogeneous? implications of simplifying heterogeneous streambeds in models of losing streams. *Journal of Hydrology*, 424–425, 16–23. Doi: 10.1016/j.jhydrol.2011.11.051.

Jarmillo, M. (2012). Riverbed filtration: an efficient and economical drinking-water treatment technology. *DYNA*, 79(171): 148-157.

Jenkins, C.T. (1968). Techniques for computing rate and volume of stream depletion by wells. *Groundwater water*, 6(2): 37-46. Doi: 10.1111/j.1745-6584.1968.tb01641.x

Jha, M. K., and Singh, A. (2014), Application of genetic algorithm technique to inverse modeling of tide-aquifer interaction. *Environmental Earth Sciences*, 71(8): 3655–3672.

Jia, Y., Altinakar, M., and Guney, M.S. (2018). Three-dimensional numerical simulations of local scouring around bridge piers. *Journal of Hydraulic Research*, 56(3): 351-366. Doi: 10.1080/00221686.2017.1356389

Jia, Y., Scott, S., Xu, Y., and Huang, S. (2005). Three-dimensional numerical simulation and analysis of flows around a submerged weir in a channel bendway. *Journal of Hydraulic Engineering*, 131(8): 628-693. Doi: 10.1061/(ASCE)0733-9429(2005)131:8(682).

Jin, G., Chen, Y., Tang, H., Zhang, P., Li, L., and Barry, D.A. (2019). Interplay of hyporheic exchange and fine particle deposition in a riverbed. *Advances in Water resources*, 128: 145-

157.

Jones, J.B., and Mulholland, J. (2000). Streams and ground waters. *Journal of the North American Benthological Society*, 19(4): 760-761.

Kollet, S. J., and Zlotnik, V.A. (2007). Evaluation of the streambed leakage concept in analytical models using data from three pumping tests. *Hydrogeology Journal*, 15(6): 1051–1062.

Konikow, L.F. (2013). Groundwater depletion in the United States (1900-2008). *U.S. Geological Survey Scientific Investigations Report* 2013-5079, 63p.

Korus, J.T., Fraundorfer, W.P., Gilmore, T.E., and Karnik, K. (2020). Transient streambed hydraulic conductivity in channel and bar environments, Loup River, Nebraska. *Hydrological Processes*, 34(14): 3061-3077.

Krause, S., Tecklenburg, C., Munz, M., and Naden, E. (2013). Streambed nitrogen cycling beyond the hyporheic zone: flow controls on horizontal patterns and depth distribution of nitrate and dissolved oxygen in the upwelling groundwater of a lowland river. *Journal of Geophysical Research: Biogeosciences*, 118(1): 54-67.

Kurth, A. M., and Schirmer, M. (2014). Thirty years of river restoration in Switzerland: implemented measures and lessons learned. *Environmental Earth Sciences*, 72(6): 2065–2079.

Landon, M. K., Rus, D.L., and Harvey, F.E. (2001). Comparison of instream methods for measuring hydraulic conductivity in sandy streambeds. *Ground Water*, 39(6): 870–885.

Laube, G., Schmidt, C., and Fleckenstein, J.H. (2018). The systematic effect of streambed conductivity heterogeneity on hyporheic flux and residence time. *Advances in Water Resources*, 122: 60-69.

Lautz, L.K., and Fanelli, R.M. (2008). Seasonal biogeochemical hotspots in the streambed around restoration structures. *Biogeochemistry*, 91(1): 85-104.

Lawrence, J.E., Skold, M.E., Hussain, F.A., Silverman, D.R., Resh, V.H., Sedlak, D.L., Luthy, R.G., and McCray, J.E. (2013). Hyporheic zone in urban streams: A review and opportunities for enhancing water quality and improving aquatic habitat by active management. *Environmental Engineering Science*, 30(8): 480-501.

Lee, B. J., Lee, J.H., Yoon, H., and Lee, E. (2015). Hydraulic experiments for determination of in-situ hydraulic conductivity of submerged sediments. *Scientific Reports*, 5(1): 7917.

Lee, H., Koo, M., and Oh, S. (2019). Modeling stream-aquifer interactions under seasonal groundwater pumping and managed aquifer recharge. *Groundwater*, 57(2): 216-225.

Levenberg, K. (1944). A Method for the Solution of Certain Non-linear Problems in Least Squares. *Quarterly of Applied Mathematics*, 2 (2): 164 – 168. Doi: 10.1090/qam/10666.

Levy, J., Birck, M.D., Mutiti, S., Kilroy, K.C., Windeler, B., Idris, O., and Allen, L.N. (2011). The impact of storm events on a riverbed system and its hydraulic conductivity at a site of induced infiltration. *Journal of Environmental Management*, 92(8): 1960–1971.

Malzone, J. M., Anseeuw, S. K., Lowry, C. S., and Allen-King, R. (2016). Temporal hyporheic zone response to water table fluctuations. *Groundwater*, *54*(2), 274–285. Doi: 10.1111/gwat.12352

Mao, D., Wan, L., Yeh, T.-C.J., Lee, C.-H., Hsu, K.-C., Wen, J.-C., and Lu, W. (2011). A revisit of drawdown behavior during pumping in unconfined aquifer. *Water Resources Research*, 47, W05502, Doi: 10.1029/2010WR009326.

Marion, A., Packman, A.I., Zaramella, M., and Bottacin-Busolin A. (2008). Hyporheic flows in stratified beds. *Water Resources Research*, 44(9):W09433.

Marquardt, D. (1963). An algorithm for least-squares estimation of nonlinear parameters. *SIAM journal on Applied Mathematics*, 11 (2): 431 – 441. Doi: 10.1137/0111030.

Marttila, H., Tammela, S., Mustonen, K.-R., Louhi, P., Muotka, T., Mykrä, H., and Kløve, B. (2019). Contribution of flow conditions and sand addition on hyporheic zone exchange in gravel beds. *Hydrology Research*, 50(3): 878-885.

Marzadri, A., Tonina, D., and Bellin, A. (2011). A semianalytical three-dimensional process-based model for hyporheic nitrogen dynamics in gravel bed rivers. *Water Resources Research*, 47(11): W11518.

Marzadri, A., Tonina, D., Bellin, A., and Valli, A. (2016). Mixing interfaces, fluxes, residence times and redox conditions of the hyporheic zones induced by dune-like bedforms and ambient groundwater flow. *Advances in Water Resources*, 88: 139-151.

Mas-Pla, J., Font, E., Astui O, Menció, A., Rodríguez-Florit, A., Folch, A., et al. (2012). Development of a stream-aquifer numerical flow model to assess river water management under water scarcity in a Mediterranean basin. *Science of the Total Environment*, 440: 204-218. Doi: 10.1111/gwat.12799

Mustafa, S., Darwish, M., Bahar, A., and Aziz, Z.A. (2019). Analytical modeling of well design in riverbank filtration systems. *Groundwater*, 57(5):756-63.

Mutiti, S., and Levy, J. (2010). Using temperature modeling to investigate the temporal variability of riverbed hydraulic conductivity during storm events. *Journal of Hydrology*, 388(3-4): 321–334.

Newcomer, M.E., Hubbard, S.S., Fleckenstein, J.H., Maier, U., Schmidt, C., Thullner, M., et al. (2016). Simulating bioclogging effects on dynamic riverbed permeability and infiltration. *Water Resources Research*, 52: 2883–2900. Doi: 10.1002/2015WR018351.

Newcomer, M.E., Hubbard, S.S., Fleckenstein, J.H., Maier, U., Schmidt, C., Thullner, M., et al. (2018). Influence of hydrological Perturbations and Riverbed Sediment Characteristics on Hyporheic Zone Respiration of CO_2 and N_2. *Journal of Geophysical Research. Biogeosciences*, 123(3): 902-22.

Obergfell, C.C.A, Bakker, M., and Maas, K. (2016). A time-series analysis framework for the flood-wave method to estimate groundwater model parameters. *Hydrogeology Journal*, 24(7): 1807 – 1819.

Obergfell, C.C.A, Bakker, M., and Maas, K. (2019). Estimation of average diffuse aquifer recharge using time series modeling of groundwater heads. *Water Resources Research*, 55(3): 2194-2210.

O'Reilly, A. M. (2004). *A method for simulating transient ground-water recharge in deep water-table settings in central Florida by using a simple water-balance/transfer-function model* (Scientific Investigations Report 2004-5195). Reston, VA: U.S. Geological Survey.

O'Reilly, A. M. (2007). *Effects of the temporal variability of evapotranspiration on hydrologic simulation in central Florida* (Scientific Investigations Report 2007-5100). Reston, VA: U.S. Geological Survey.

O'Reilly, A.M., Holt, R.M., Davidson, G.R., Patton, A., and Rigby, J.R. (2020). A dynamic water balance/nonlinear reservoir model of a perched phreatic aquifer-river systems with hydrogeologic threshold effects. *Water Resources Research*, 56(6).

O'Reilly, A. M. (2021). USDA Agricultural Research Service, 'Managed Aquifer Recharge for Sustainable Groundwater-irrigated Agroecosystems: Objectives, Construction, and Preliminary Performance of a Pilot Facility in the Delta Region of Mississippi'. *2021 Virtual Annual Water Resources Conference*, American Water Resources Association, link: https://www.awra.org/Members/Events_and_Education/Events/2021_Annual_Conference/2021_Annual_Conference_Program/2021_Annual_Conference_Session_Nov_10_3.aspx.

Packman, A.I., Brooks, N.H., and Morgan, J.J. (2000). A physicochemical model for colloid exchange between a stream and a sand streambed with bed forms. *Water Resources Research*, 36(8): 2351-2361.

Palacky, G.J. (1988). Resistivity characteristics of geologic targets. Investigations in Geophysics vol. 3: Electromagnetic methods in applied geophysics-theory, vol. 1, edited by M.N. Nabighian, *Soc. Expl. Geophys.*, 53-129.

Partington, D., Therrien, R., Simmons, C.T., and Brunner, P. (2017). Blueprint for a coupled model of sedimentology, hydrology, and hydrogeology in streambeds. *Reviews of Geophysics*, 55. Doi: 10.1002/2016RG000530.

Pollock, D.W. (2017). MODPATH v7.2.01: A particle-tracking model for MODFLOW: U.S. Geological Survey Software Release, 15 December 2017.

Polomčić, D., Hajdin, B., Stevanović, Z., Bajić, D., and Hajdin, K. (2013). Groundwater management by riverbank filtration and an infiltration channel: the case of Obrenovac, Serbia. *Hydrogeology Journal*, 21(7): 1519-1530. Doi: 10.1007/s10040-013-1025-9

Prasad, K.S., Ojha, C.S.P., Nirala, R.K., and Sharma, D. (2016). Optimal well location in a river bank filtration system: sensitivity to aquifer characteristics and decay rate. *Journal of Hazardous, Toxic and Radioactive Waste*, 20(3): 4016001.

Pryshlak, T.T., Sawyer, A.H., Stonedahl, S.H., and Soltanian, M.R. (2015). Multiscale hyporheic exchange through strongly heterogeneous sediments. *Water resources research*, 51(11): 9127-40.

Ray, C., Grischek, T., Schubert, J., Wang, J.Z., and Speth, T.F. (2002). A perspective of riverbank filtration. *Journal American Water Works Association (AWWA)*, 94(4): 149-160.

Reba, M.L., Massey, J.H., Adviento-Borbe, M.A., Leslie, D., Yaeger, M.A., Anders, M., et al. (2017). Aquifer depletion in the Lower Mississippi River Basin: challenges and solutions. *Journal of Contemporary Water Research & Education*, 162(1): 128-139. Doi: 10.1111/j.1936-704X.2017.03264.x

Remy, N., Boucher, A., and Wu, J. (2009). *Applied geostatistics with SGeMS: a user's guide*. New York: Cambridge University Press.

Rosenberry, D. O. (2008). A seepage meter designed for use in flowing water. *Journal of Hydrology*, 359(1–2): 118–130.

Rosenberry, D. O., and Pitlick, J. (2009). Effects of sediment transport and seepage direction on hydraulic properties at the sediment-water interface of hyporheic settings. *Journal of Hydrology (Amsterdam)*, 373(3–4): 377–391.

Salehin, M., Packman, A.I., and Paradis, M. (2004). Hyporheic exchange with heterogeneous streambeds: Laboratory experiments and modeling. *Water Resources Research*, 40(11): W11504 – W1150416.

Salem, H.S. (2001). Modelling of lithology and hydraulic conductivity of shallow sediments from resistivity measurements using Schlumberger vertical electrical soundings. *Energy Sources*, 23(7): 599-618. Doi: 10.1080/00908310119202

Sawyer, A.H., Cardenas, M.B. (2009). Hyporheic flow and residence time distributions in heterogeneous cross-bedded sediment. *Water Resources Research*, 45(8): W08406.

Sawyer, A.H., Cardenas, M.B., Bomar, A., and Mackey, M. (2009). Impact of dam operations on hyporheic exchange in the riparian zone of a regulated river. *Hydrological Processes*, 23(15): 2129-2137.

Schalchli, U. (1992). The clogging of coarse gravel river beds by fine sediment. *Hydrobiologia*, 235: 189–197.

Shen, H.W., Fehlman, H.M., and Mendoza, C. (1990). Bed Form Resistances in Open Channel Flows. *Journal of Hydraulic Engineering*, 116(6): 799-815.

Shevnin, V., Delgado-Rodríguez, O., Mousatov, A., and Ryjov, A. (2006). Estimation of hydraulic conductivity on clay content in soil determined from resistivity data. *Geofisica Internacional*, 45(3): 195-207.

Schijven, J., Berger, P., and Miettinen, I. (2003). Removal of pathogens, surrogates, indicators, and toxins using riverbank filtration. In: Ray, C., Melin, G., and Linsky, R. B. (2003). *Riverbank filtration :Improving source-water quality*. Dordrecht; Boston: Kluwer Academic.

Singh, T., Wu, L., Gomez-Velez, J.D., Lewandowski, J., Hannah, D.M., and Krause, S. (2019). Dynamic hyporheic zones: Exploring the role of peak flow events on bedform-induced hyporheic exchange. *Water Resources Research*, 55(1):218-35.

Singh, T., Gomez-Velez, J.D., Wu, L., Wörman, A., Hannah, D.M., and Krause, S. (2020). Effects of successive peak flow events on hyporheic exchange and residence times. *Water Resources Research*, 56(8): n/a.

Smith, J. W. N., and Lerner, D.N. (2008). Geomorphologic control on pollutant retardation at the groundwater-surface water interface. *Hydrological Processes*, 22(24): 4679–4694.

Sophocleous, M. (2002). Interactions between groundwater and surface water: the state of the science. *Hydrogeology Journal*, 10(2): 348.

Stehfest, H. (1970). Numerical inversion of Laplace transforms. *Communication of the ACM*, 13(1): 47-49.

Stone, H.L. (1968). Iterative solution of implicit approximation of multidimensional partial differential equations. *SIAM (Society Industrial Applied Mathematics) Journal of Numercial Analysis*, 5(3): 530-558. Doi: 10.1137/0705044

Stonedahl, S.H., Harvey, J.W., and Packman, A.I. (2013). Interactions between hyporheic flow produced by stream meanders, bars, and dunes. *Water Resources Research*, 49(9): 5450-5461.

Su, X., Shu, L., and Lu, C. (2018). Impact of a low-permeability lens on dune-induced hyporheic exchange. *Hydrological Sciences Journal*, 63(5): 818-835.

Tang, Q., Schilling, O.S., Kurtz, W., Brunner, P., Vereecken, H., and Hendricks Franssen, H. (2018). Simulating flood-induced riverbed transience using unmanned aerial vehicles, physically based hydrological modeling, and the ensemble Kalman filter. *Water Resources Research*, 54(11): 9342–9363. Doi: 10.1029/2018WR023067.

Theis, C.V. (1941). The effects of a well on the flow of a nearby stream. *Transactions of the American Geophysical Union*, 22(3): 734-738. Doi: 10.1029/TR022i003p00734

Tombe, B.F., Bakker, M., Schaars, F., van der, Made., and Kees, Jan. (2018). Estimating travel time in bank filtration systems from a numerical model based on DTS measurements. *Groundwater*, 56(2): 288-99.

Tonina, D., and Buffington, J.M. (2009a). A three-dimensional model for analyzing the effects of salmon redds on hyporheic exchange and egg pocket habitat. *Canadian Journal of Fisheries and Aquatic Sciences*, 66(12): 2157-2173.

Tonina, D., and Buffington, J.M. (2009b). Hyporheic exchange in mountain rivers I: Mechanics and environmental effects. *Geography Compass*, 3(3): 1063–1086.

Tonina, D., de Barros, F.P., Marzadri, A., Bellin, A. (2016). Does streambed heterogeneity matter for hyporheic residence time distribution in sand-bedded streams? *Advance Water Resources*, 96: 120–126. Doi: 10.1016/j.advwatres.2016.07.009.

Toze, S., Bekele, E., Leviston, Z., and Patterson, B. (2010). Recycling water via infiltration galleries in urban groundwater. *Water (Melbourne)*, 37(2): 58-61.

Trauth, N., and Fleckenstein, J. H. (2017). Single discharge events increase reactive efficiency of the hyporheic zone. *Water Resources Research, 53*: 779–798. Doi: 10.1002/2016WR019488

Triska, F. J., Kennedy, V. C., Avanzino, R. J., Zellweger, G. W., and Bencala, K. E. (1989). Retention and transport of nutrients in a third-order stream in northwestern California: Hyporheic processes. *Ecology*, *70*: 1893–1905.

Tufenkji, N., Ryan, J.N., and Elimelech, M. (2002). The promise of bank filtration. *Environmental Science and Technology*, 36(21): 422A-428A.

United States Department of Agriculture. (2013). Farm and Ranch Irrigation Survey (2013). Volume 3, Special Studies, Part 1: 6p.

Van Genuchten, M.T. (1980), A closed-form equation for predicting the hydraulic conductivity of unsaturated soils. *Soil Science Society of America Journal*, 44(5): 892-898. Doi: 10.2136/sssaj1980.03615995004400050002x

von Asmuth, J. R., Maas, K., and Bierkens, M. F. P. (2002). Transfer function-noise modeling in continuous time using predefined impulse response functions. *Water Resources Research*, 38(12): 1287. Doi: 10.1029/2001WR001136.

von Asmuth, J. R., Maas, K., Bakker, M., and Petersen, J. (2008). Modeling time series of ground water head fluctuations subjected to multiple stresses. *Ground Water*, 46(1): 30-40. Doi: 10.1111/j.1745-6584.2007.00382.x

Wang, P., Pozdniakov, S.P., and Vasilevskiy, P.Y. (2017). Estimating groundwater-ephemeral stream exchange in hyper-arid environments: field experiments and numerical simulations. *Journal of Hydrology*, 555: 68–79. Doi: 10.1016/j.jhydrol.2017.10.004.

Wang, T. Z., Li, Y.K., Liang, M.C., Yang, P.L., and Bai, Z.H. (2014). Biofilms on the surface of gravels and aquatic plants in rivers and lakes with reusing reclaimed water. *Environmental Earth Sciences*, 72(3): 743–755.

Wett, B., Jarosch, H., Ingerle, K., 2002. Flood induced infiltration affecting a bank filtrate well at the River Enns, Austria. *Journal of Hydrology*, 266: 222-234.

Winter, T. C., Harwey, J.W., Franke, O.L., and Alley, W.M. (1998). Ground water and surface water: A single resource. *U.S. Geological Survey Circulation*, 1139: 79.

Woessner, W. W., and Sullivan, K. E. (1984). Results of seepage meter and mini-piezometer Study, Lake Mead, Nevada. *Ground Water*, 22(5): 561–568.

Wu, L., Singh, T., Gomez-Velez, J., Nützmann, G., Wörman, A., Krause, S., et al. (2018). Impact of dynamically changing discharge on hyporheic exchange processes under gaining and losing groundwater conditions. *Water Resources Research*, 54(12): 10,076-10,093.

Xian, Y., Jin, M., Zhan, H., and Liu, Y. (2019). Reactive transport of nutrients and bioclogging during dynamic disconnection process of stream and groundwater. *Water Resources Research*, 55(5): 3882-3903. Doi: 10.1029/2019WR024826.

Xian, Y., Jin, M., and Zhan, H. (2020). Buffer effect on identifying transient streambed hydraulic conductivity with inversion of flood wave responses. *Journal of Hydrology (Amsterdam)*, 580: 124261. Doi: 10.1016/j.jhydrol.2019.124261

Zarnetske, J.P., Haggerty, R., Wondzell, S.M., and Baker, M.A. (2011). Dynamics of nitrate production and removal as a function of residence time in the hyporheic zone. *Journal of Geophysical Research: Biogeosciences*, 116(1).

Zhang, X., and Ewen, J. (2000). Efficient method for simulating gravity-dominated water flow in unsaturated soil. *Water Resources Research*, 36 (9): 2777-2780.

Zhang, Y., Hubbard, S., Finsterle, S. (2011). Factors governing sustainable groundwater pumping near a river. *Groundwater*, 49 (3): 432–444. Doi: 10.1111/j.1745-6584.2010.00743.x.

Zheng, C., and Wang, P.P. (1999). MT3DMS: A modular three-dimensional multispecies transport model for simulation of advection, dispersion, and chemical reactions of contaminants in groundwater systems; documentation and user's guide, Contract Report SERDP-99-1, U.S. Army Engineer Research and Development Center, Vicksburg, MS.

Zhou, D., Zhang, Y., Gianni, G., Lichtner, P., and Engelhardt, I. (2018). Numerical modelling of stream–aquifer interaction: Quantifying the impact of transient streambed permeability and aquifer heterogeneity. *Hydrological Processes*, 1–14. Doi: 10.1002/hyp.13169.

Zlotnik, V.A., Huang, H. (1999). Effect of shallow penetration and streambed sediments on aquifer response to stream stage fluctuations (analytical model). *Ground water*, 37(4):599-605.

Zlotnik, V.A., Huang, H., and Bulter, J.J. Jr. (1999). Evaluation of Stream Depletion Considering Finite Stream Width, Shallow Penetration and Properties of Streambed Sediments. In Proceedings of Water 99, Joint Congress, 221-226. Brisbane, Australia.

LIST OF APPENDICES

LIST OF APPENDICES

It is an important step to verify a newly developed numerical model with analytical solutions to insure its correctness. It is preferable if the analytical solutions are similar to the real world problems under investigation. In so doing, not only the correctness of mathematics but also of boundary conditions can be verified. The numerical model, CCHE3D-GW, has been strictly verified with analytical models of the (1) dune-induced hyporheic flow; (2) pumping in a phreatic aquifer near an alluvial river, and (3) unsaturated GW flow simulation to justify its application to the problems studied in this dissertation. This Chapter is divided into three parts, in which each one corresponds to the aforementioned case, respectively.

A.1 Verification of Dune-Induced Hyporheic Flow

The conceptual domain, assumptions and simplifications are the same as those mentioned in Chapter 7. Three sub-cases were selected for verification.

Case I: Head Differential

Packman et al. (2000) derived an analytical solution for the hyporheic flow driven by the head differential, where the alluvium is of finite thickness. The streambed is simplified as flat, and the hydraulic head distribution over a dune is approximated to follow a sinusoidal function:

$$H(x,0) = H_d \cos(\lambda x) \tag{A.1}$$

where, λ is the wavenumber of a dune and equals to $2\pi/L$ (L is the wavelength of a dune); H_d is the amplitude of the hydraulic head distribution and can be computed by the empirical formula (Shen et al., 1990):

$$h_d = 0.28\frac{{U_S}^2}{2g}\begin{cases}\left(\dfrac{\Delta}{0.34H_S}\right)^{3/8}, & \text{if } \dfrac{\Delta}{H_S} \le 0.34 \\ \left(\dfrac{\Delta}{0.34H_S}\right)^{3/2}, & \text{if } \dfrac{\Delta}{H_S} > 0.34\end{cases} \tag{A.2}$$

The meanings of the symbols are the same as them in Chapter 7. The other boundary conditions are given as:

$$\left.\frac{\partial H}{\partial x}\right|_{x=-1.5L} = 0; \quad \left.\frac{\partial H}{\partial x}\right|_{x=1.5L} = 0 \tag{A.3a}$$

$$\left.\frac{\partial H}{\partial z}\right|_{z=-D} = 0 \tag{A.3b}$$

The analytical solution of the hydraulic head in the underneath alluvium is:

$$H(x,z) = H_d \cos(\lambda x)\left[\tanh(\lambda D)\cdot\sinh(\lambda z) + \cosh(\lambda z)\right] \tag{A.4}$$

where, D is the thickness of alluvium. For this verification case, the dune wavelength (L) is 1.0 m and height (Δ) is 0.08 m. The alluvium thickness (D) was 1.0 m, and the streambed slope (s) was 0.01%. The simulation domain was set up as 3.0 m (x) × 1.0 m (z), which covered three dunes. The results of the middle dune were chosen for analysis to minimize possible boundary effects. A uniform mesh with $\Delta x = \Delta z = 0.005$ m was applied, i.e., the domain was discretized by 601× 201 nodes. The steady mean stream velocity was set as 0.129 m/s. The stream water depth (H_s) was 0.4 m. The amplitude of the sinusoidal hydraulic head distribution (H_d) was therefore computed to be 0.0134 m from Eq. A.2.

Fig. A.1 shows the comparisons between the simulation results (red lines) and analytical solution (Eq. A.4, black lines) for the hydraulic head distributions at different depths. It can be found that the agreements are good, indicating the accuracy of the CCHE3D-GW. The hydraulic

head at the shallow layer (Fig. A.1a) is close to that at the streambed interface but weakens downward dramatically (Fig. A.1b – d).

Elliott and Brooks (1997) derived an analytical solution for the residence time distribution (RTD) under an infinitely thick alluvium. Although this idealized condition cannot be exactly reproduced by the numerical model, the results would be similar when the alluvium is set up sufficiently thick. In this study, the thickness, 1.0 m, is found to be sufficient to fulfill this requirement, so the analytical solution of RTD can be applied for verification:

$$t = \frac{2\cos^{-1}\bar{R}}{\bar{R}\cdot\lambda^2 K H_d}\cdot n_s \tag{A.5}$$

where, n_s is the porosity, which is 0.325 in this study.

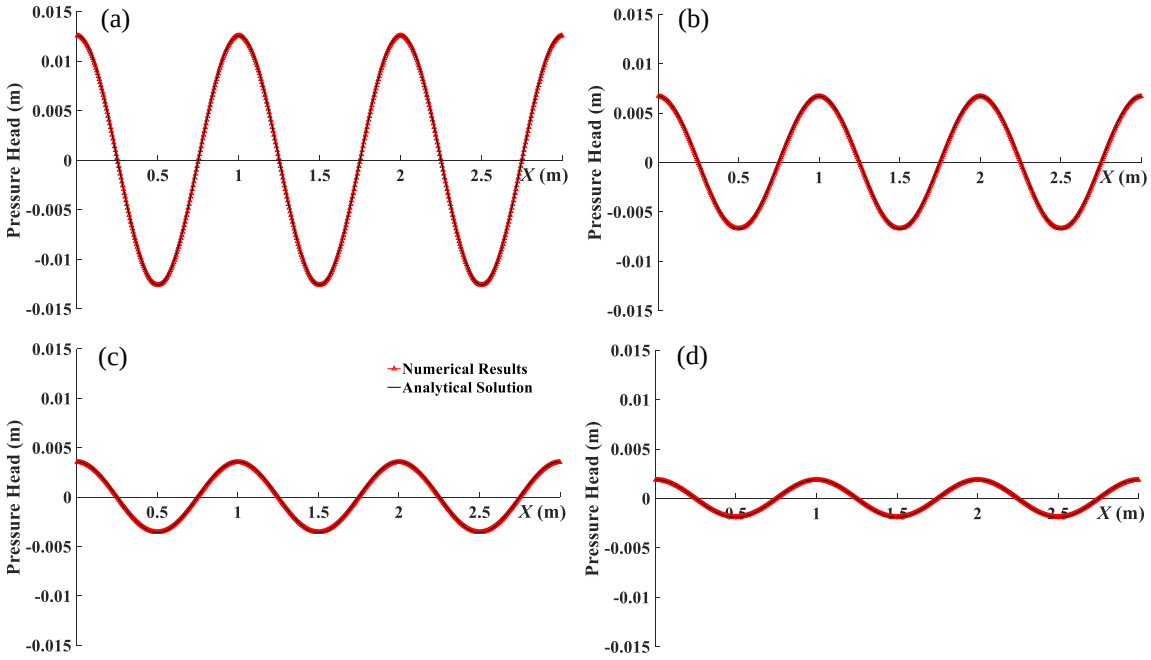

Figure A.1. Comparisons between the numerical results and analytical solution for hydraulic head distributions at four vertical levels: (a) z = -0.01 m; (b) z = -0.11 m; (c) z = -0.21 m and (d) z = -0.31 m.

The method to derive the RTD from the simulation results is by releasing 2000 particles from the 'source' part of the sediment-water interface and tracking them through the simulations by MODPATH (Pollock, 2016). Fig. A.2 shows the comparison between the numerical results (red dashed line) and analytical solution (black solid line), where the fine agreement indicates the models and method applied in this study can reproduce an accurate RTD.

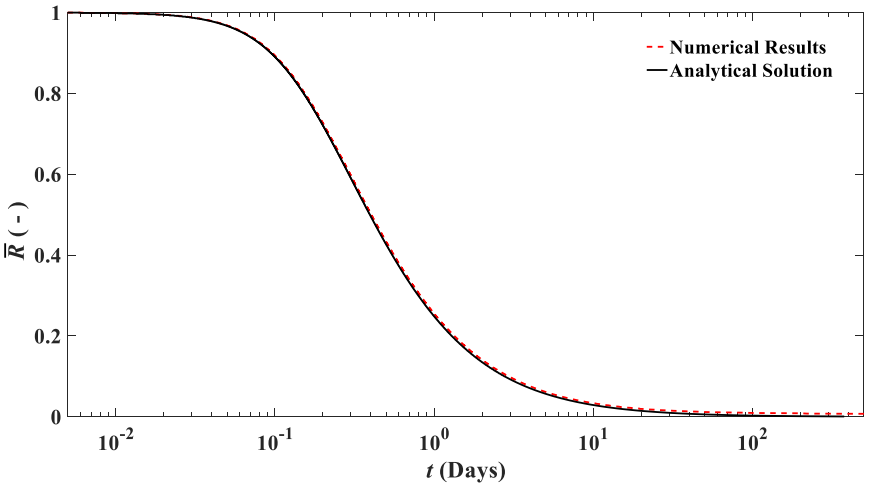

Figure A.2. Comparison between the numerical results and analytical solution for the RTD.

Case II: Head Differential and Basal Flow

The ambient groundwater, such as the underflow and basal flow, often accompanies the hyporheic flow. Open channel flow is driven by the energy slope, and it may propagate and conduct in the shallow alluvial aquifer, and result in a general horizontal GW flow, called underflow. The hydraulic gradient between the SW and surrounding GW pushes the basal flow. For a vertical 2D model, the basal flow is typically simplified to be upward or downward with a constant flow rate (Marzadri et al., 2016; Wu et al., 2018). An analytical solution including both underflow and basal flow in the dune scale was derived by Marzadri et al. (2016) with boundary conditions:

$$H(x,0) = H_d \cos(\lambda x) - sx \tag{A.6a}$$

$$\left.\frac{\partial H}{\partial x}\right|_{x=-1.5L} = -s; \quad \left.\frac{\partial H}{\partial x}\right|_{x=1.5L} = -s \tag{A.6b}$$

$$\left.\frac{\partial H}{\partial z}\right|_{z=-D} = \mp\frac{q_b}{K} \tag{A.6c}$$

The analytical solution is:

$$H(x,z) = H_d \cos(\lambda x)\left[\tanh(\lambda D)\sinh(\lambda z) + \cosh(\lambda z)\right] - sx \mp \frac{q_b}{K} z \tag{A.7}$$

The meanings of the notations are the same as them in Chapter 7. The basal flow rate, q_b, was chosen as 0.020 m/d, and the other parameters are the same as verification case I.

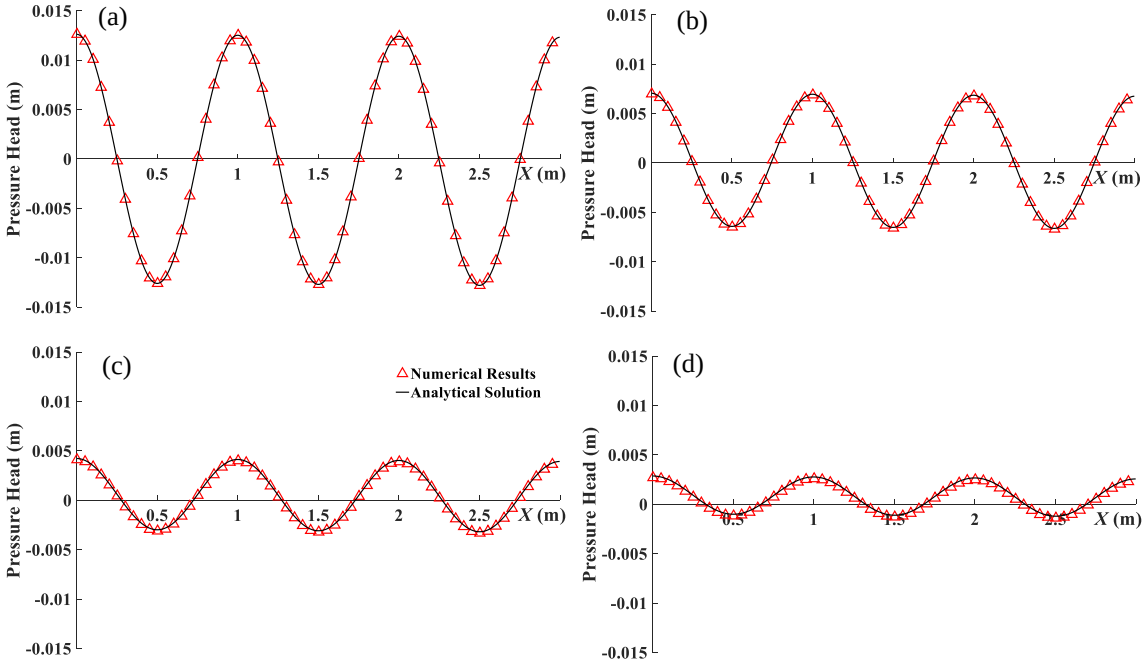

Figure A.3. Comparisons between the simulated and analytical hydraulic head distributions for gaining condition at four vertical levels: (a) z = -0.01 m; (b) z = -0.11 m; (c) z = -0.21 m and (d) z = -0.31 m.

Fig. A.3 and A.4 show the comparisons between the simulated (red triangles) and analytical (solid black lines) hydraulic head distributions under the gaining and losing condition, respectively. The good agreements demonstrate the capability of CCHE3D-GW in handling the

basal flow boundary conditions. The analytical solution of RTD under this condition is not available, so it is not for verification.

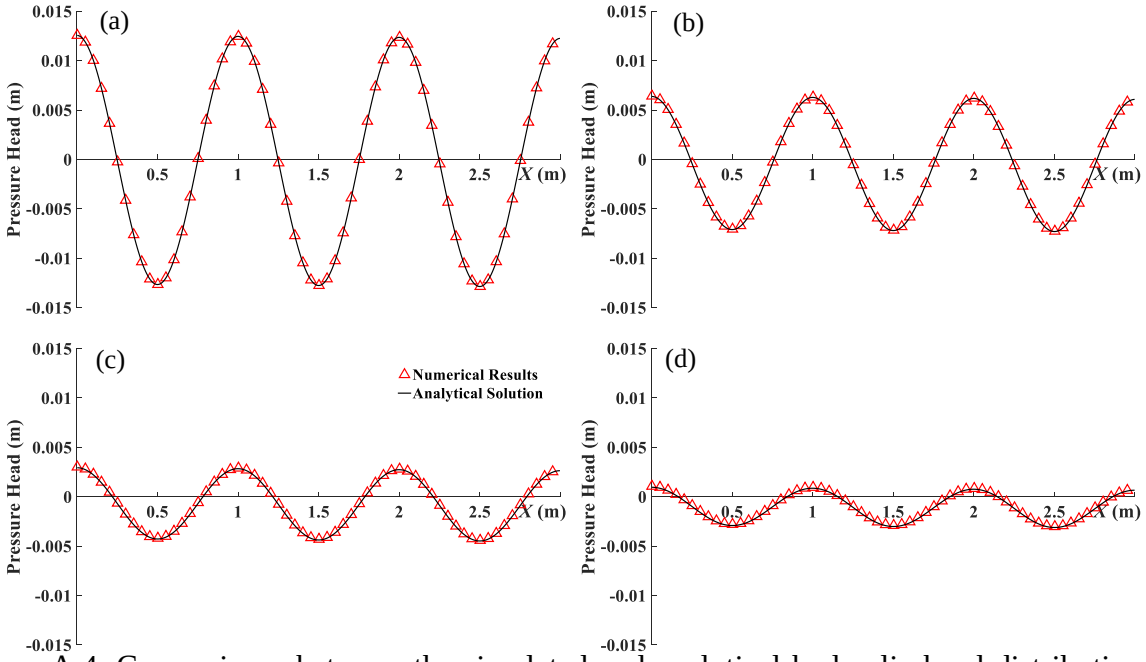

Figure A.4. Comparisons between the simulated and analytical hydraulic head distributions for losing condition at four vertical levels: (a) z = -0.01 m; (b) z = -0.11 m; (c) z = -0.21 m and (d) z = -0.31 m.

Case III: Hyporheic Flow under a Two-layer Bed

Marion et al. (2008) derived an analytical solution for a two-layer streambed to study the effects from an armorer layer. The ambient groundwater was neglected, so the boundary conditions are the same as Case I. The alluvium is consist of two layers: an upper layer with a thickness D_u and hydraulic conductivity K_u, and a lower layer with a thickness D_l and hydraulic conductivity K_l. The analytical solution reads:

$$H(x,z) = H_d \cos(\lambda x) \frac{\sinh\left[\lambda(D_u + z)\right] - h_{12}/H_d \sinh(\lambda z)}{\sinh(\lambda D_u)}, \quad -D_u < z < 0 \tag{A.8a}$$

$$H(x,z) = H_{12} \cos(\lambda x) \frac{\cosh\left[\lambda(D_u + D_l + z)\right]}{\cosh(\lambda D_l)}, \quad -(D_u + D_l) < z < -D_u \tag{A.8b}$$

where, H_{12} is the 'intermediate' hydraulic head to compute the hydraulic head of the upper layer (Eq. A.8a) and lower layer (Eq. A.8b), and it is expressed as:

$$H_{12} = H_d \frac{\operatorname{csch}(\lambda D_u)}{\coth(\lambda D_u) + K_l/K_u \tanh(\lambda D_l)} \tag{A.9}$$

In this study, K_u and K_l is set to be 65.26 m/day and 6.526 m/day, respectively. D_u and D_l is set to be 0.16 m and 0.84 m, respectively. The other parameters are set to be the same as the verification case I.

Fig. A.5 shows the comparisons between the simulated (red triangles) and analytical hydraulic head distributions, where Figs. A.5a & b are for the upper layer, and c & d are for the lower layer. The great agreements in Fig. A.5 reveal that the model is able to simulate the GW flow under a two-layer streambed. The analytical solution of RTD is also unavailable for this case, so it is not included in the verification.

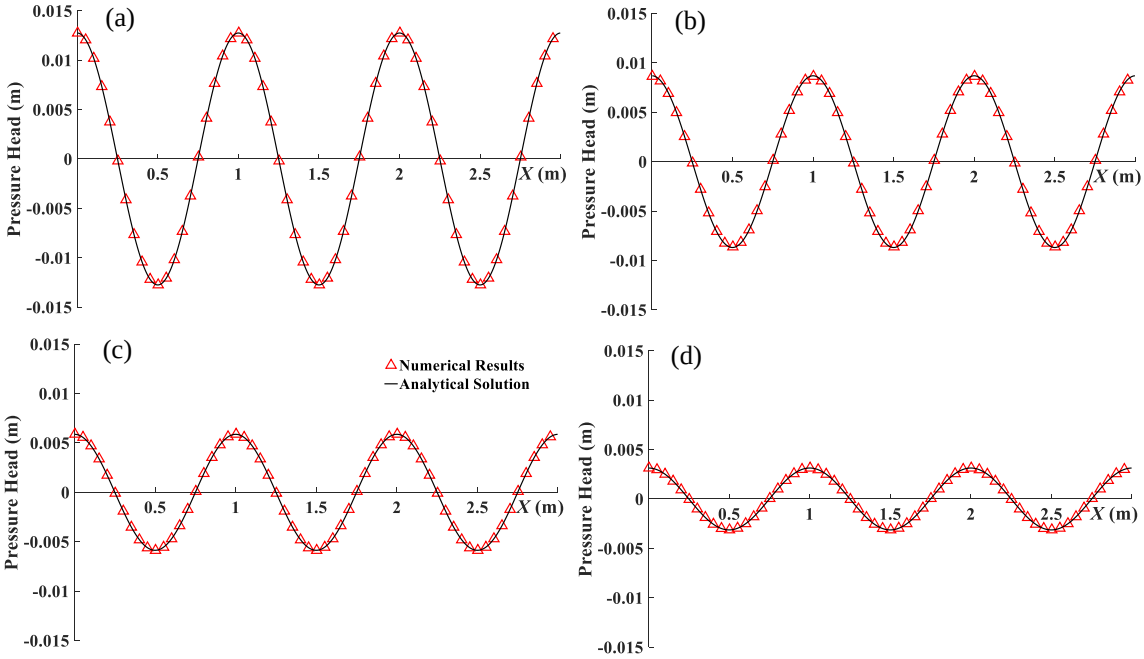

Figure A.5. Comparisons between the simulated and analytical hydraulic head distributions for a two-layer streambed with K_u = 65.26 m/day, K_l = 6.526 m/day, D_u = 0.16 m and D_l = 0.84 m at four levels: (a) z = -0.01 m; (b) z = -0.11 m; (c) z = -0.21 m and (d) z = -0.31 m.

A.2 Verification of Pump near Alluvial River

The analytical solution of Butler et al. (2001) was chosen to verify the numerical model given by its similarity to the pumping test in Leflore County, MS.

Fig. A.6 shows the conceptual model of the depth-averaged 2D analytical solution: a pumping well is placed near an alluvial river with an idealized rectangular cross section. The riverbank is impermeable but the riverbed is permeable. The river is simplified to be a constant head boundary condition. The effect of aquitard was represented as an impermeable confining unit (Fig. A.6a). Flow properties in the vertical direction were assumed uniform, and the vertical flow was neglected. The pumping well fully penetrates the aquifer. The domain is divided into three zones: Zone 1 is the aquifer on the left of the river containing the pumping well; Zone 2 is the aquifer beneath the riverbed, and Zone 3 is the aquifer on the right side. T_i and S_i were used to

represent the hydraulic properties, transmissivity and storativity, respectively, of these zones. The properties of these zones can be different, but each of them must be homogeneous in one zone. Fig. A.6b shows the coordinate system: the origin is located at the pumping well.

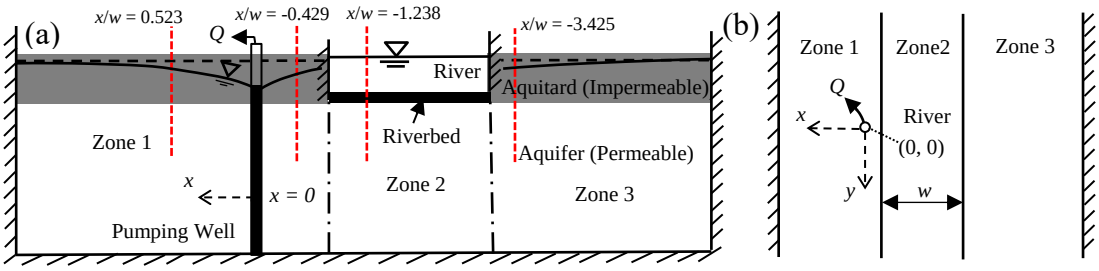

Figure A.6. The conceptual model of Butler et al. (2001), where (a) is the view of cross section passing the pumping well and perpendicular to the river and (b) is the $x - y$ plane view. The four red dashed lines in Fig. A.6a are the representative locations for the comparisons of Fig. A.7.

The domain of the verification cases was 20300 m × 28600 m, discretized by a non-uniform mesh (138 × 139 in x and y direction). Coarser meshes were applied to the region far from the pumping well, and the near field was represented by fine and uniform meshes (2 m × 2 m). The width of river, w, was 42 m, and the thickness of riverbed, b', was assumed 2 m. The pumping well was set fully penetrating the aquifer, and the pumping rate, Q, was 12960.0 m^3/day. The aquifer was 40 m thick. The transmissivities of the three zones, T_1, T_2 and T_3, were all assumed 2400 m^2/day, and aquifer storativity (S_1, S_2 and S_3) was 0.12 m. The relative permeability of riverbed was reflected by a dimensionless parameter, stream leakance, B:

$$B = \frac{K_r \cdot w^2}{b' \cdot T_2} \tag{A.10}$$

where, K_r is hydraulic conductivity of riverbed.

Multiple scenarios were simulated to cover a variety of parameters. The riverbed hydraulic conductivity, K_r, listed in Table A.1, was computed using Eq. A.10 and other known parameters. For each case, the initial time step, Δt, was 0.001 days, and it was increased by a factor of 1.1 in each step. The total simulation time was 138 days. The initial hydraulic head of the aquifer was set as 50 m to ensure the aquifer was fully saturated during the pumping process. The river stage was set to be constant, 50 m, in all simulations.

CCHE3D-GW was verified using a 4-layer mesh and a 12-layer mesh. With more layers in z direction, 3D groundwater flow features can be better simulated. The setup of the 4-layer mesh fits exactly as that of the depth-averaged analytical solution, since the vertical flow in the solution is technically minimal. When the 12-layer mesh was tested, the hydraulic conductivity in z direction (K_z) was set much larger than those of the horizontal directions (K_x, K_y), so that the vertical component moved fast in the close vicinity of the pumping well. The simulated GW flow behaves like 2D because the vertical components vanished rapidly away from the well. In this study, K_x and K_y were both 60 m/day, i.e., the transmissivity of aquifer was still 60 m/day × 40 m = 2400 m^2/day, while K_z was set to be 2000 m/day.

Table A.1. The Parameters of Verification Cases

	Stream Leakance, B [-]	Riverbed Conductivity, k_r (m/day)
Case 1	0.001 (Theis, 1935)	0.00272
Case 2	0.1	0.272
Case 3	1.0	2.72
Case 4	10.0	27.2
Case 5	100.0	272

Two parameters, dimensionless drawdown, Φ, and stream depletion, ΔQ:

$$\Phi_i = \frac{s_i \cdot T_i}{Q} \tag{A.11}$$

$$\Delta Q = \frac{\Delta q}{Q} \tag{A.12}$$

were used for comparisons between the simulation and analytical results. Where, s_i is drawdown in Zone i ($H - H\big|_{t=0}$), and Δq is the discharge from river to aquifer.

Fig. A.7a – d are the comparisons of the simulated and analytical drawdown curves at four representative locations (red dashed lines in Fig. A.6a) in the cross section passing the pumping well and perpendicular to the river. Each of the sub-figures has five groups of curves, representing the five cases in Table A.1, computed by 4-layer mesh, 12-layer mesh and the analytical model. Fig. A.7e shows the comparisons for the dimensionless stream depletion. The black solid lines and red dashed lines are the simulation results of 4-layer and 12-layer mesh, respectively. The scatter points are the analytical solutions. Fine agreements are found between the numerical solutions and the analytical solutions, and between the results of the 4-layer and 12-layer meshes (Fig. A.7).

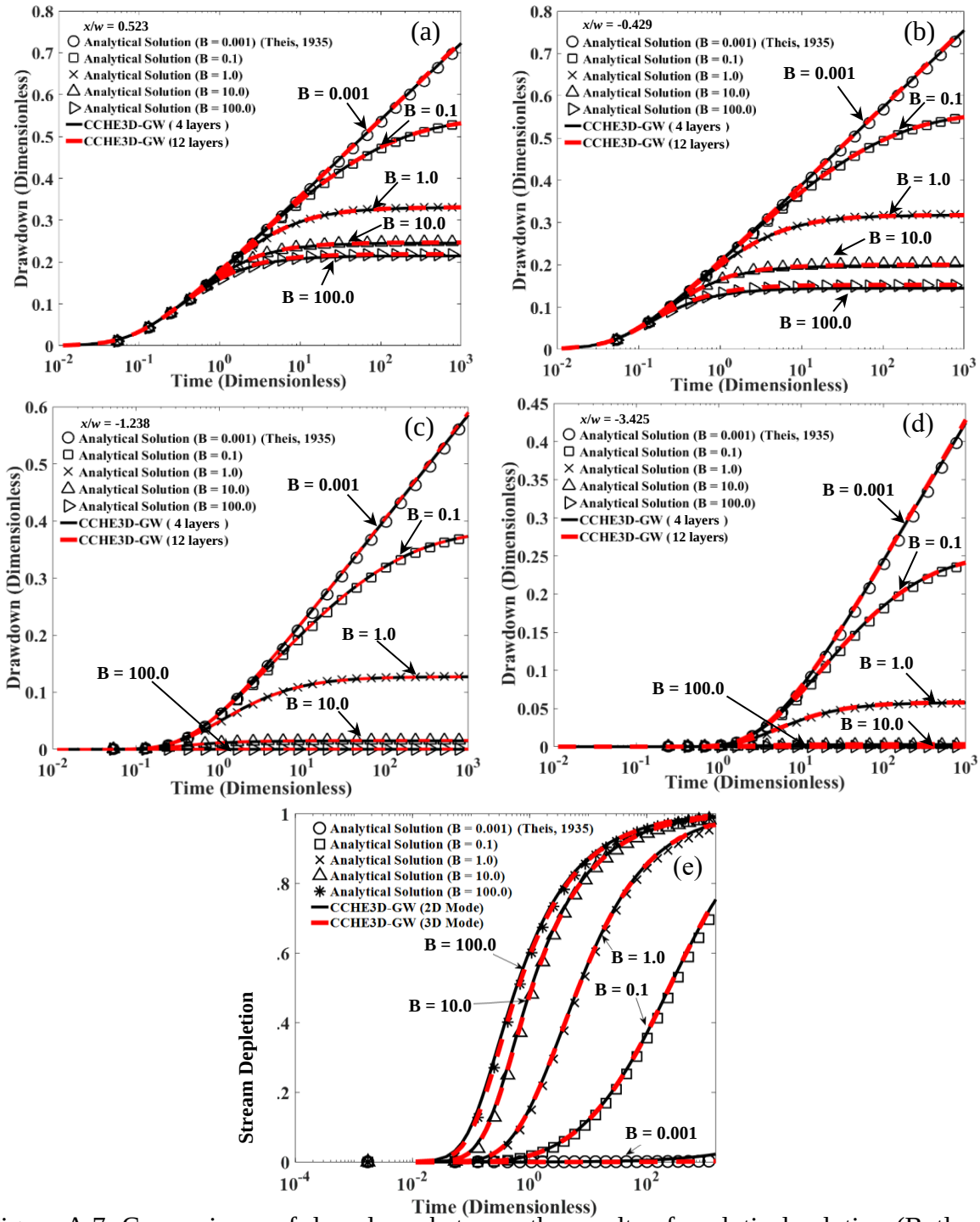

Figure A.7. Comparisons of drawdown between the results of analytical solution (Butler et al., 2001) and CCHE3D-GW with 4 layers (black solid lines) and 12 layers (red dashed lines) in *z* direction when *x*/*w* (a) = 0.523 (Zone 1); (b) = -0.429 (Zone 1); (c) = -1.238 (Zone 2) and (d) = -3.425 (Zone 3). (e) Comparisons of stream depletion between the results of analytical solution (Butler et al., 2001) and CCHE3D-GW with 4 layers (2-D mode, black solid lines) and 12 layers (3-D mode, red dashed lines) in *z* direction with different stream leakances.

When the riverbed is almost impermeable (B = 0.001, Case 1), the river does not respond much to the pumping, and the solution becomes identical to that of Theis (1935), i.e., the drawdown increases and approaches to infinite with the pumping time. Under this circumstance, the stream depletion keeps minimal during the whole process (Fig. A.7e). With a permeable riverbed (Case 2 - 5), the drawdown will increase at the beginning but slow down at a certain time (Fig. A.7a - 2d). Under these conditions, the stream depletion would grow with different rates depending on the values of riverbed permeability (Fig. A.7e). When the stream depletion approaches to 1, the extracted water is completely balanced by the discharge from river and the drawdown of aquifer ceases. With the increase of the stream leakance (from Case 2 to 5), the equilibrium condition is achieved earlier, and the stabilized drawdown value is smaller (Fig. A.7).

A.3 Verification of Unsaturated GW Flow

The analytical solution of Butler et al. (2001) only considered fully saturated GW flow but the unsaturated zone clearly exists fin our field case. The model must be further verified for its capability in handling the flow in the vadose zone. Given by the complexity of the unsaturated GW flow, the analytical solution available for verification is hard to find. Typical scenarios simulated by well-accepted numerical models were therefore selected, which were a 1-D infiltration and a sing-well pump.

Case I: 1-D Infiltration

Infiltration is a prevailing phenomenon and commonly encountered for the unsaturated soil. A simple 1-D infiltration was chosen for verification. The scheme of the case is shown in Fig. A.8, where the domain is a 1-D soil column of 4.0 m thickness and discretized by 200 uniform meshes (Δz = 0.02 m). The initial pressure head for the whole soil is -100 m, and the z coordinate

was setup downward with the origin at the land surface. Van Genuchten model was applied here to describe the soil characteristic curve, in which n = 3.45, α = 1.5, θ_s = 0.45, θ_r = 0.05 and K_s = 0.8 m/day. Two time steps, Δt = 0.005 and 0.01 days, were tested. The total infiltration period is 1.2 days. The comparisons with the simulations of Zhang and Ewen (2000) for pressure head and moisture content distribution after 1-day infiltration were shown in Fig. A.9 (a) & (b), respectively, in which the results from this study and Zhang and Ewen (2000) were marked by lines and circles, respectively. It can be observed that the agreements between the results of CCHE3D-GW and Zhang and Ewen (2000) are very good, indicating that the newly developed model is capable in simulating the 1-D infiltration process, particularly it can precisely capture the infiltration front. Meanwhile, the fine agreement of the results with Δt = 0.005 and 0.01 days reveals the insensitivity of the simulation to the time step under this setup.

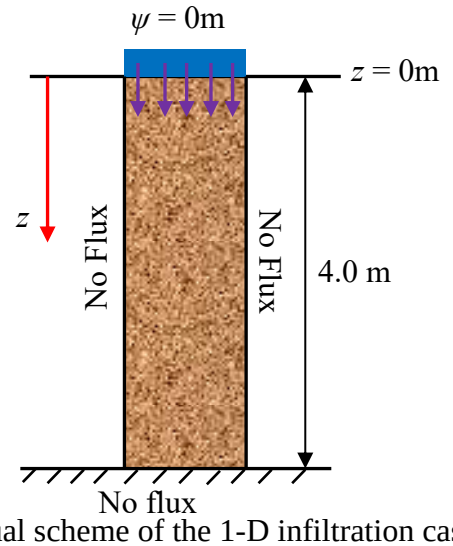

Figure A.8. The conceptual scheme of the 1-D infiltration case for the verification.

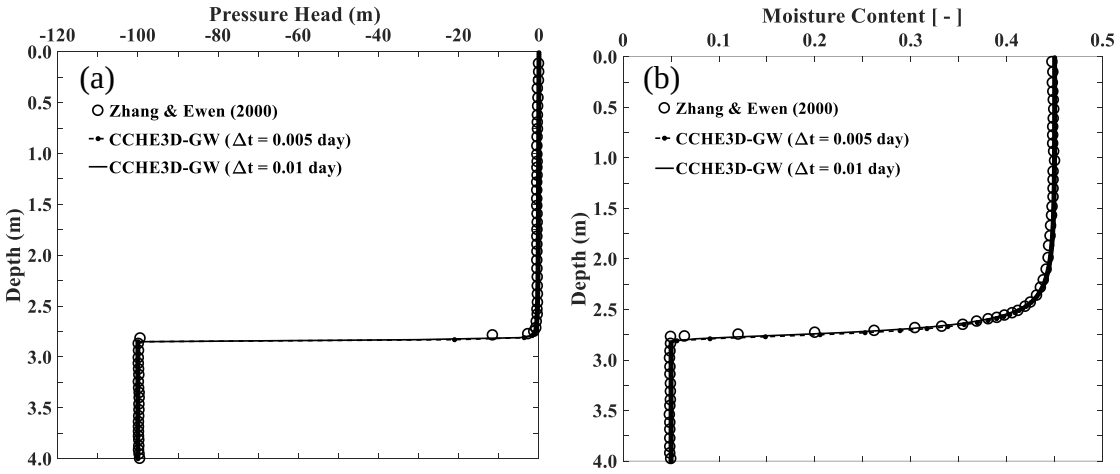

Figure A.9. Comparisons between the simulation results of Zhang and Ewen (2000) and CCHE3D-GW for (a) pressure head distribution and (b) moisture content profile after 1-day infiltration.

Case II: Sing-well Pump

The field case in the Leflore County, MS, is a 3-D pump-induced flow, and the irrigation well partially penetrated the aquifer. From the measured data, it could be interpreted that the unsaturated soil roughly existed in the first 10 m depth layer. It is necessary to verify the ability of the model in handling the pump with the presence of the vadose zone. Although much simpler than our case, Mao et al. (2011) did a numerical simulation of a hypothetical single-well pump with VSAFT3. The domain was a rectangle homogenous aquifer with both the length and width of 200 m (Fig. A.10a), and was 9 m thick (Fig. A10b). The pumping well was located at the center of the domain, and the origin was set up at this point (Fig. A10a). After locating the datum at the bottom of the domain, the pumping well was from z = 0 m to 4 m (partially penetrating the aquifer), and the pumping rate was 0.06 m^3/min (Fig. A10b). The initial water table was at z = 6.7 m. The soil characteristic curve was represented by Gardner model (1958):

$$K(\psi) = K_s \exp(\alpha\psi) \tag{A.13}$$

$$\theta(\psi) = \theta_r + (\theta_s - \theta_r)\exp(\beta\psi) \tag{A.14}$$

where, α and β are pore size distribution parameters, and were both set as 4.0 m^{-1} in this study. K_s is the saturated hydraulic conductivity, which is set as 0.00396 m/min. The saturated and residual moisture content, θ_s and θ_r, was 0.37 and 0.07, respectively here.

A non-uniform mesh (136 ×136 ×24) was applied in CCHE3D-GW, and the scheme is shown in Fig. A.10. In x – y direction, a uniform mesh with $\Delta x = \Delta y = 0.5$ m was applied in the near-well area, which was from x (or y) = -24 m to 24 m, and $\Delta x = \Delta y = 4.0$ m was used for the other parts (Fig. A.10a). In z direction, from 6.1 m to 7.5 m, where the vadose zone mostly located, a fine uniform mesh with $\Delta z = 0.2$ m was implemented while the other aquifer was discretized with $\Delta z = 0.5$ m (Fig. A.10b). The initial time step was 0.001 min and amplified by a factor of 1.1 if the Modified Picard iteration could be convergent in 5 steps. The total simulation time is 2000 min.

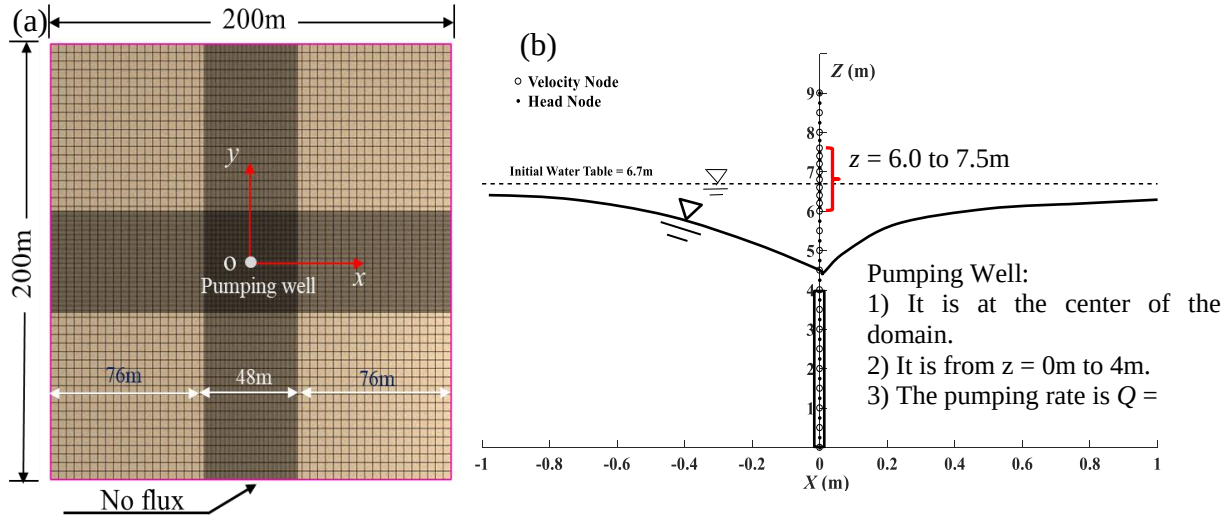

Figure A.10. Configuration of the single-well pumping case and the mesh in (a) x – y coordinate and (b) x – z coordinate.

The simulated drawdown processes of CCHE3D-GW and VSAFT3 (Mao et al., 2011) at two monitoring wells, which is 5.0 m and 30.0 m away from the pumping well in radial driection, are compared in Fig. A.11 (a) and (b), respectively. For each monitoring well, three elevations, z = 1.5 m, 3.0 m and 6.0 m, are chosen for the comparison. It can be found that the simulation results of CCHE3D-GW (lines in Fig. A.11) agree very well with the ones of VSAFT3 (scatters in Fig. A.11), validating the newly developed model for this topic. The drawndown curves of both the saturated (z = 1.5 m and 3.0 m) and vadose zones (z = 6.0 m) follow a three-phase shape. The drawdown of the saturated zone is larger than the unsaturated zone while inside the saturated zone, the drawdowns are generally the same when comparing z = 1.5 m and 3.0 m.

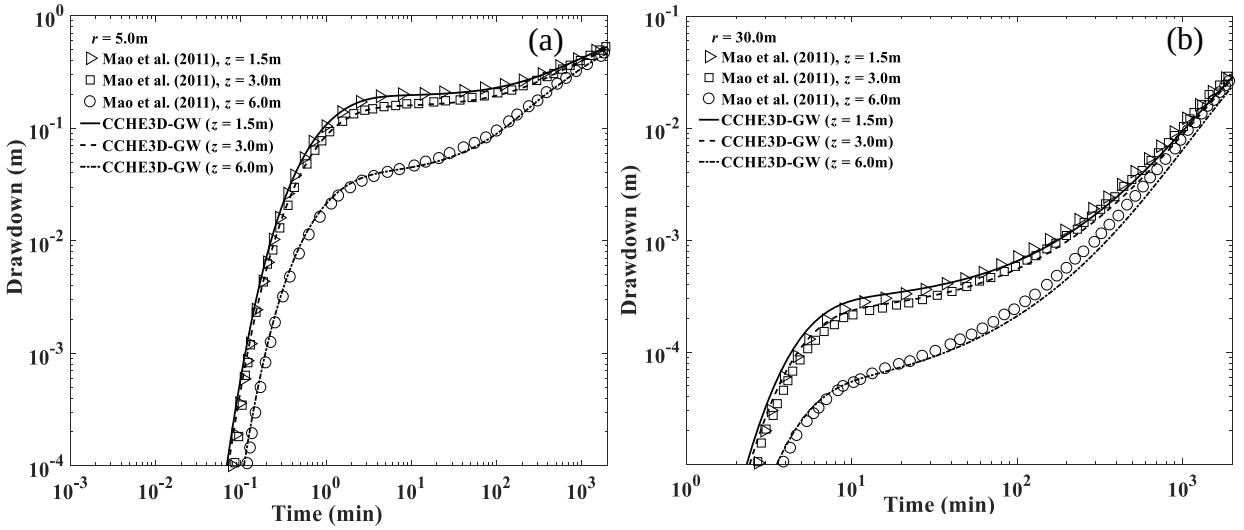

Figure A.11. Comparisons between the simulation results of VSAFT3 (Mao et al., 2011) and CCHE3D-GW for drawdowns at different elevations when the monitoring well is (a) 5.0 m and (b) 30.0 m away from the pumping well in radial direction.

A.4 Simulation Results of a Homogenous Aquifer

Prior to the simulation shown in Chapter 4 that considered the heterogenity of the aquifer, a case in which the aquifer was assumed homogenous was run. The calibration found that the best-

fitted parameters were K_u = 0.010 m/day, K_r = 0.10 m/day and the aquifer hydraulic conductivity 75.0 m/day. The comparisons between the simulation and measurement are shown in Fig. B.1, in which the root mean square error is also calculated. In general, the agreements are good except for the observation well close to the pumping well (MW01), in which a significant improvement can be found when considering the heterogenity of the aqufier. From the measured resistivity data (Fig. 4.3), it can be seen that the sediment near the pumping well is of a higher permeability than the other regions, i.e., only a smaller near-pumping-well hydraulic gradient can fulfill the pumping rate for the real case than the assumed homogenous aquifer. When neglecting this factor, a large error will be induced.

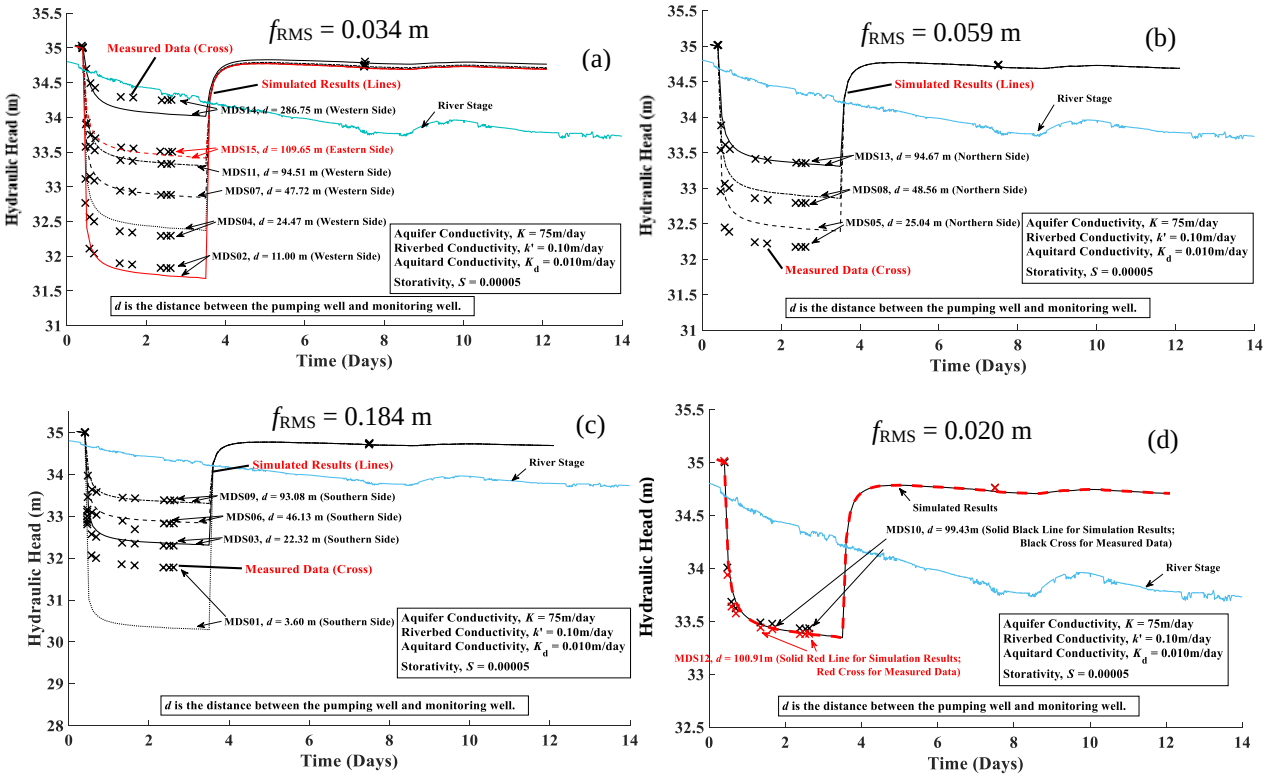

Figure A.12. The best-agreed simulation results (lines) under the assumption of a homogenous aquifer for the monitoring wells (a) along the transversal cross section, (b) & (c) along the longitudinal cross section and (d) at the 'ordinary' locations. The datum here is NAVD 88, which is the standard Northern American datum.

VITA

Jiayu Fang was born on December 31, 1991 in Wuhu City, Anhui Province, China. He received the degree of Bachelor of Engineering from Hohai University, China in June 2014. He entered the National Center for Computational Hydroscience and Engineering at The University of Mississippi for the degree of Doctor of Philosophy in January 2017.